# Chalcogenide Glass Materials for Integrated Infrared Photonics

by

Vivek Singh

B.S. Materials Science and Engineering
Columbia University, 2009

Submitted to the Department of Materials Science and Engineering in Partial Fulfillment of the Requirements for the Degree of

DOCTOR OF PHILOSOPHY
at the
MASSACHUSETTS INSTITUTE OF TECHNOLOGY

September 2015



Signature of Author:_____

Department of Materials Science and Engineering
July 20, 2015

Certified by:_____

Lionel C. Kimerling
Thomas Lord Professor of Materials Science and Engineering
Thesis Supervisor

Certified by:_____

Anuradha M. Agarwal
Principal Research Scientist, Materials Processing Center
Thesis Supervisor

Accepted by:_____

Donald Sadoway
Chair, Departmental Committee on Graduate Students

**Chalcogenide Glass Materials for Integrated Infrared Photonics**

**by**

Vivek Singh

Submitted to the Department of Materials Science and Engineering on July 20, 2015 in Partial Fulfillment of the Requirements for the Degree of Doctor of Philosophy in Materials Science and Engineering

# Abstract

Chalcogenide glasses (ChGs) are amorphous compounds containing the chalcogen elements (S, Se, Te) and exhibit wide infrared transparency windows. They are easy to synthesize in bulk and thin film forms and their compositional flexibility allows tuning of optical properties such as refractive index making them ideal for infrared photonics. We have studied the material attenuation in ChGs that arises due to the presence of impurities in the raw materials and established UV photolithography-based process flows that enable fabrication of chalcogenide glass waveguides and microresonators for near- and mid-IR wavelength ranges.

Waveguides and optical resonators are key microphotonic elements for many on-chip applications such as telecommunications and chemical sensing. In this thesis, we show that scattering losses dominate in our ChG microphotonic devices while material attenuation from impurities is low. We demonstrate resonators coated with nanoporous polymers to improve their selectivity against target analytes for sensing applications. We exploit the photosensitivity of $As_2S_3$ glass to build silicon-based tunable photonic devices that offer post-fabrication tuning to optimize performance. Resonators also serve as a test platform for studying the effects of radiation on silicon and chalcogenide materials systems.

Further, we propose new mid-IR microphotonic device designs using ChG materials and the challenges associated with measuring mid-IR devices along with solutions to address them. We employ input-to-output offsets, standard tapered waveguides, and a fiber collimator to improve mid-IR measurements and demonstrate transparent ChG waveguides with losses as low as 2.5 dB/cm.

Finally, we propose a novel design that integrates PbTe detectors with ChG waveguides for on-chip mid-IR detection. Our simulations show that the use of a low-index spacer layer leads to a well-distributed field along the width of the detector due to a reduction in the effective index of the structure. We develop a fabrication process for waveguide-integrated detector designs and fabricate prototype structures that exhibit attenuation at telecom and mid-IR wavelengths. Such an integrated sensor design will enable the creation and deployment of low-cost remote sensor arrays with small footprints, and ultimately lead to "lab-on-a-chip" structures.

Thesis Supervisors:

Lionel C. Kimerling
Title: Thomas Lord Professor of Materials Science and Engineering

Anuradha M. Agarwal
Title: Principal Research Scientist, Materials Processing Center

# Acknowledgements

I distinctly remember the day in January 2009 when I received an email saying that I had been accepted to MIT and it took a few minutes for the news to sink in. Growing up in India, I had heard many great things about MIT but I never imagined that I would one day graduate with a degree from MIT. It has been a long journey and I want to recognize all those who had a hand in helping me get to this point.

I wish to start by thanking my parents. It could not have been easy for them to let their only child jet off to a foreign land on his own but they have always supported me with everything. I would not be here if it were not for their love and encouragement over the years.

My thesis advisors, Prof. Lionel C. Kimerling ("Kim") and Dr. Anu Agarwal, welcomed me into the electronic materials research group ("EMAT") during my first semester and I will forever be grateful for it. I could always count on Kim to provide meaningful solutions to problems that I ran into during my thesis work and lead me down paths I would not have conceived of on my own. His intuitive understanding of photonics and materials science is inspiring and he can always break down a problem into simpler parts to help me focus better. Anu has been my day-to-day advisor in EMAT since I started and this thesis would not exist without all her support and guidance through the years. She is always approachable and easy to talk to which led to many long conversations about not just my research but other topics as well.

The EMAT mentor list would be incomplete if I did not include Dr. Jurgen Michel. Although I did not get a chance to work with him directly until the last few months of my

research, I always appreciated his honesty, practical advice, and humor during group meeting presentations.

I would also like to thank my committee members, Prof. Silvija Gradecak and Prof. Caroline Ross for their helpful suggestions and direction during committee meetings and the preparation of this thesis.

Prof. Juejun "JJ" Hu, was my post-doctoral mentor when I joined EMAT and he has taught me much about photonics and chalcogenide glasses since then. Even after he left EMAT to teach at the University of Delaware, he was always available for discussions regarding my work over email and phone. His suggestions over the years and experimental assistance from his group members have been vital in the completion of this thesis work.

I have been extremely fortunate to collaborate with a number of brilliant scientists and engineers during the course of my Ph.D. Prof. Kathleen Richardson (University of Central Florida), Prof. Igor Luzinov (Clemson University) and Dr. Joel Hensley (Physical Sciences, Inc.) have been a part of our chalcogenide glass team since the beginning of my time here and it has been wonderful working with their respective research groups. Many of the important achievements in this thesis would not have been possible without their direction. EMAT has also played host to visiting scholars and I had the pleasure of working with Dr. Stefano Grillanda and Dr. Davide Bianchi from Politecnico di Milano on various projects.

I want to thank the staff at MIT's shared facilities (MTL/CMSE) for training me on a number of instruments and for being patient with my questions. In particular, Paul Tierney and Kurt Broderick at MTL provided wonderful guidance when I was trying to design new process flows and were always available to answer my questions. Dr. Charlie Settens' assistance at the CMSE XRD Lab was also very important. I wish to express my gratitude to Dr. Piotr Becla for helping with PbTe thin film measurements and Dr. Nilanjan

Chatterjee in the Department of Earth, Atmospheric & Planetary Sciences for his help with WDS data collection for my thin films.

I want to thank Kim's assistant, Ms. Lisa Sinclair, for all her help with scheduling meetings with Kim, administrative concerns, and most importantly, her delicious cakes! She keeps the group functioning smoothly and EMAT is lucky to have her onboard. I extend my sincere thanks to Ms. Angelita Mireles and Ms. Elissa Haverty at the DMSE administrative office as well as the staff at the International Students Office for their assistance during my time.

Many former and current members of EMAT have formed an important part of my time at MIT: Dr. Timothy Zens, Neil Patel, Zhaohong Han, Brian Albert, Dr. Vivek Raghunathan, Dr. Michiel Vanhoutte, Dr. Yan Cai, Dr. Jianfei Wang, Dr. Jing Cheng, Dr. Rodolfo Camacho-Aguilera, Corentin Monmeyran, Brian Pearson, Dr. Kevin McComber, Dr. Xing Sheng, Dr. Kazumi Wada, Wei Yu, Dr. Lirong Zheng-Broderick, Dr. Jonathan Bessette, Dr. Jifeng Liu, Louisa Chiao, Dr. Pao Tai Lin, Dr. Lin Zhang, Dr. Clara Dimas, and Dr. Jianwei Mu. I had the pleasure of working directly with many of them on collaborative research projects within EMAT and I enjoyed the lively discussions we had on a variety of subjects. I want to extend a special thank you to Neil, Corentin, and Yan for helping me prepare for my oral exam.

I am grateful to Prof. Joshua Grossman (now at University of Maryland) and Prof. James Im (Columbia), my undergraduate advisors, for giving me opportunities to conduct research in their labs and learn valuable skills that have helped me during my time at MIT.

Finally, I wish to thank the rest of my family back in India for their love and support through the years. My friends, both at MIT and outside of it, played an important role in keeping me sane through these years by helping me take my mind off work

I dedicate this thesis to my maternal grandmother and a dear friend who unfortunately passed away during the course of my Ph.D.

# Table of Contents

# Chapter 1: Introduction & Motivation

## 1.1 Chip-scale photonics

Photonics is the science and technology of generating, controlling, and detecting photons[1] across many regions of the electromagnetic spectrum such as visible, infrared (IR), ultraviolet (UV), and even X-rays. Photonics has found widespread use in many areas such as telecommunications, lighting, medical instrumentation, and personal electronics such as smartphones. Integrated, on-chip photonic devices present a compelling solution to several technical challenges due to their small footprint, low fabrication cost, and immunity to electromagnetic interference. In addition to shrinking macroscale photonics to "small footprint," on-chip photonics enables new applications. Electronic-photonic integration on silicon CMOS (complementary metal oxide semiconductor) platforms can provide energy-efficient, scalable pathways that can enhance interconnection bandwidth and bridge the gap between traditional CMOS devices and fiber optics.

Integrated photonics is also poised to play a prime role in the emerging field of on-chip biological and chemical sensing. Changes in the real and imaginary parts of the complex refractive index can be used to rapidly detect the presence of biological and chemical species with high sensitivity. In particular, the mid-IR wave band (2.5 to 12 μm) represents a strategically important spectral regime for photonic sensing applications, as characteristic absorption fingerprints of most molecules reside here.

## 1.2 Infrared spectroscopy

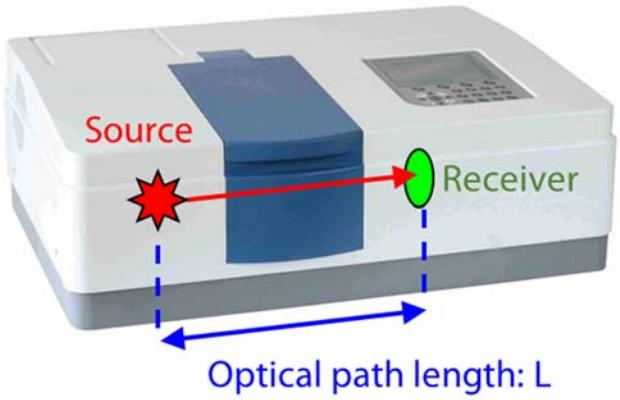


**Figure 1.1:** A typical absorption-based spectrometer. A broadband light source sweeps through a pre-determined range of wavelengths, passes through a sample with an optical path length of L, and the detector at the other end records a transmission spectrum. The limit of detection depends on the sensitivity of the detector, the absorption strength of the sample, and the optical path length through the sample.

The measurement and analysis of characteristic absorption spectra (IR spectroscopy) has been widely used to gather information about the structure and composition of several chemical and biological species in applications such as environmental monitoring[2], medical diagnoses[3], forensic analysis[4], and pharmaceutical manufacturing[5]. Traditional IR spectrometers employ free-space geometry, and measure absorbance from a single pass-through of the light within an absorption chamber as shown in Figure 1.1. According to the Beer-Lambert Law,

$$\Delta I\% = 1 - \exp(-\alpha L) \approx \alpha L \tag{1}$$

the measured change in intensity depends on the absorption of the sample as well as the optical path length in the spectrometer. To achieve high detection sensitivity from a single pass, a large optical path length is used in the spectrometer (e.g., a Fourier Transform Infrared (FTIR) spectrometer) making it a bulky instrument with a large footprint. This

prevents such spectrometers from being used out in the field and in remote detection scenarios critical for chemical warfare and safety applications.

IR spectroscopy for the identification of biological and chemical agents is usually performed in the "fingerprint" midwave-infrared (MWIR) bands from 3-5 μm and 8-12 μm where most molecules show characteristic vibrational absorption features. Rapid sensing and detection with high sensitivity in a small footprint can be achieved by the integration of various functional elements (mid-IR light source, sensing element, detector, and read-out circuits) onto a monolithic, planar silicon platform. Smaller device footprints can lead to new and important applications such as remote deployment of arrays of integrated mid-IR sensor devices that can record and relay data from sensing events without human intervention.

## 1.3 Planar sensors

Microfabrication technology and materials development have enabled planar microphotonic and plasmonic devices for chem-bio sensing, demonstrating higher sensitivity in a smaller footprint compared to bulk spectrometers[6-10]. Furthermore, monolithic integration of required sensor components onto a silicon platform will allow for rapid sensing.

Surface Plasmon Resonance (SPR) is a well-developed technique used for label-free detection of biological and chemical species with high sensitivity[8, 11]. However, the plasmon wave has high attenuation over a short distance and SPR sensors are not sensitive to changes in optical absorption, thus precluding their use in mid-IR absorption sensing. A planar micro-resonator sensor device can offer fundamentally higher sensitivity and is limited only by the wavelength resolution of the light source and detector[12, 13]. A micro-resonator increases optical path length and hence sensitivity due to enhanced photon-matter interactions from spatial light confinement over a longer period of time. Prior work in the

Kimerling group has demonstrated a process for fabricating planar ChG-based photonic devices such that it is also Si-CMOS-compatible, which is invaluable for low cost mass production and scalability[14]. In addition, such devices open up routes to fabricate resonator arrays that can be used for parallelized detection of multiple species while maintaining a small footprint. Additionally, optical resonators offer a versatile device platform that can operate in two separate modes to detect sensing events as illustrated in Figure 1.2. In the first mode, called *cavity-enhanced absorption spectroscopy*, sensing events are identified by a change in the extinction ratio of a resonant peak. The second mode, *refractive index spectroscopy*, utilizes a shift in the resonant wavelength due to a change in the effective refractive index of the resonator mode to indicate a sensing event. Successful demonstration of both modes of sensing can be found in the literature[15, 16].

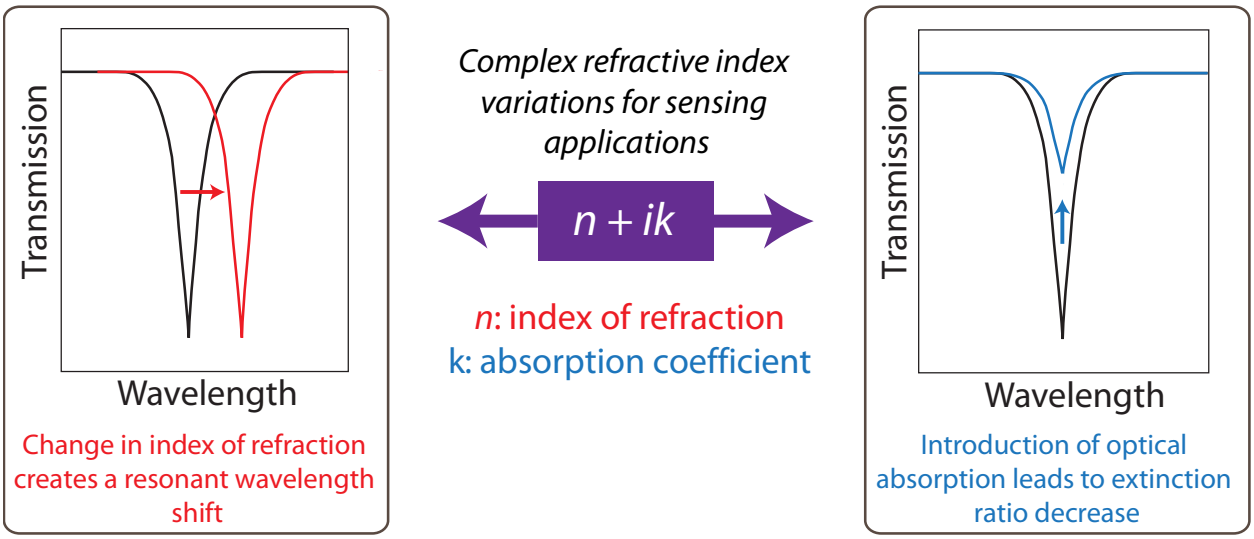


**Figure 1.2:** Schematic showing the two modes of monitoring changes in the complex refractive index.

## 1.4 Mid-infrared materials

A diverse range of material systems have been explored for passive mid-IR waveguide and resonator fabrication. In addition to silicon-on-insulator (SOI) devices operating at up to 4.4 µm[17-20], the examples include suspended silicon[21, 22], silicon on sapphire[23-25], III-V

semiconductors[26, 27], silicon on porous silicon[28], silver halides[29], and non-oxide glasses[30, 31]. Material selection criteria for passive mid-IR photonic applications may be vastly different from the conventional standards we take for granted in optimizing near-IR materials operating in the telecommunication bands. For example, silicon-on-insulator (SOI) and silica-on-silicon have been the dominant material platforms for integrated photonic devices operating in the near-IR. However, their transmission window in the mid-IR is limited until 4.0 μm wavelength due to the onset of phonon absorption in silica (the absorption coefficient of fused silica glass is as high as ~40 dB/cm at 4.5 μm[32]). Further, while processing compatibility with mature CMOS manufacturing can prove to be a major advantage for photonics in the telecom wavebands, such benefits are lacking for mid-IR photonics. Our argument is based on several distinctive features of mid-IR photonics versus its near-IR counterpart. First, applications of integrated mid-IR photonics mostly focus on fragmented niche market needs, which negate potential cost benefits associated with high-volume CMOS production[33]. Second, unlike near-IR devices which can readily leverage mature CMOS material platforms and fabrication process flows, mid-IR (> 4.5 μm) photonic device fabrication often necessitate specialized processing steps (e.g., thick cladding layer deposition or deep undercut etching to isolate guided modes from silicon dioxide), which largely prohibits the use of shuttle runs sharing CMOS foundry infrastructures[34]. The much larger feature size of mid-IR devices also relieves the fabrication tolerance requirement as well as the dependence on state-of-the-art CMOS foundry lines. Last but not least, most mid-IR light sources such as quantum cascade lasers are demonstrated on non-silicon platforms to date[35, 36]. Therefore, instead of emphasizing compatibility with standard CMOS processes, we argue that performance-driven material optimization and versatility of material/device processing to meet highly diverse end user application-needs are likely to be among the key requirements for mid-IR photonic materials and systems development.

In addition to silicon (transparent up to 7 µm wavelengths), the dominant material for micro-electronics and integrated photonics, amorphous materials such as silicon nitride[37, 38] and non-silicate glasses including transition metal oxides[39] and chalcogenides[40, 41] offer unique performance and processing advantages for passive mid-IR photonics. These materials have reduced phonon energy compared to silica and thus possess broad transmission windows in the mid-IR. Silicon nitride and transition metal oxides are typically transparent from visible to about 7 µm wavelength, and tellurium-based chalcogenide glasses are known to exhibit optical transparency up to 25 µm wavelength[42]. Very low optical attenuation ($< 0.1$ dB/m) in the glass materials has been theoretically established[43] and experimentally validated through optical fiber measurements[31]. Unlike crystalline materials with narrowly defined stoichiometry, amorphous compounds, in particular chalcogenides and some transition metal oxides (e.g. $TiO_2$-$ZrO_2$[39] have a large capacity for composition alloying without sacrificing their structural stability. The wide range of property tuning is critical for mid-IR applications: for example, mid-IR transparent core and cladding layers with high index contrast ($\Delta n > 1$) can be realized in a single amorphous alloy system, which significantly facilitate photonic integration. Most importantly, the amorphous nature and low deposition temperature of these materials allows monolithic deposition on virtually any substrates free of lattice-matching constraints, enabling several applications including mid-IR laser source integration[31].

Chalcogenide glasses (ChGs) are inorganic, amorphous compounds of chalcogen elements (sulfur, selenium, and/or tellurium) with other metal or non-metal elements, and have been recognized as a material of choice for infrared (IR) applications due to their wide optical transparency in the mid- and far-infrared wavelength regions. Although ChG films have been widely used as phase change materials for optical discs and non-volatile random access memories[44, 45], these materials exhibit other properties such as high optical

nonlinearities and low linear and nonlinear loss that make them attractive for integrated device applications. ChGs offer the ability to tune optical properties such as refractive index and photosensitivity through doping and/or compositional alloying in the bulk. High refractive index ChG materials have led to the development of compact, planar devices that can operate over a wide wavelength range extending to the far-infrared, for example the fabrication of optical resonant cavities with ultra-high quality (Q) factors[14, 30, 46, 47]. Low optical loss can be realized in planar ChG photonic devices by post-fabrication reduction of sidewall roughness[48], a unique advantage over crystalline materials. Their IR transparency window covers the characteristic absorption wavebands for many chemical and biological species, making ChGs an ideal material for chem-bio sensing applications. Finally, room-temperature ChG thin film deposition on virtually any substrate using low-cost techniques such as evaporation and sputtering make device fabrication processing of ChGs a Si-CMOS-compatible one, facilitating a very desirable monolithically integrated mid-IR Chalcogenide Glass on Silicon (ChG-OS) platform.

In this thesis, we will design, fabricate, and test near- and mid-IR devices built from chalcogenide glasses and silicon-based material systems. We also develop new characterization methodologies for mid-IR devices to demonstrate transparent waveguides at longer wavelengths.

## 1.5 Mid-infrared detectors

As our target wavelengths lie in the mid-infrared regime, few materials systems prove to be viable choices for integrated detectors. For photodetection in the mid-IR wavelength regime, semiconductor materials with small, direct band gaps (typically $< 0.4$ eV) are necessary. Mercury cadmium telluride (HgCdTe) and III-V compounds such as InAs and InSb are typically used for mid-IR detection and spectroscopy applications but are obtained

by high-cost growth techniques such as metal organic chemical vapor deposition (MOCVD) or Molecular Beam Epitaxy (MBE)[49] that also inhibit monolithic integration unless all components are grown together. Lead salts or lead chalcogenides such as PbTe, PbSe, and PbS form another set of materials suitable for this wavelength range and mid-IR detectors based on single-crystalline PbSe and PbS are commercially available[50]. PbTe is a promising candidate for low cost and robust IR detection technology due to its superior chemical stability and the ease of deposition[51, 52]. Single crystal PbTe has been studied for the fabrication of IR photodetectors and long wavelength laser devices[53]. Epitaxial PbTe detectors integrated with mid-IR filters have demonstrated enhanced photoresponsivity at room temperature[54]. Alloying PbTe with tin telluride (SnTe) to form $Pb_xSn_{1-x}Te$ offers the ability to tune the optical band gap of the material.

High detectivity has also been obtained with polycrystalline PbTe films[55]. We have previously conducted systematic studies of the structural, electrical, and optical properties of polycrystalline PbTe films obtained from single source thermal evaporation[52, 53, 55, 56]. Our fabrication process has yielded stoichiometric, polycrystalline films with a rock salt structure and grain sizes on the order of 50–100 nm. Electrical and optical characterization of the PbTe films shows thermally activated *p*-type conduction with a mobility of 53 $cm^2/Vs$, a room temperature carrier concentration of 2.1 x $10^{17}$ $cm^{-3}$, and an optical band gap of 0.386 eV. The ease of fabrication combined with low carrier concentration (i.e., high resistivity) and small band gap makes polycrystalline PbTe our material of choice for mid-IR photodetection in this thesis.

## 1.6 Lab-on-a-chip

Figure 1.3 shows a generic schematic illustration of a mid-IR lab-on-a-chip sensor system we envision. The sensor consists of the following basic components: a light source,

multiple sensor elements (with or without functionalization layers for specificity), photodetectors, and read-out circuitry on a silicon platform. By integrating all the necessary components for IR sensing on a silicon platform, this lab-on-a-chip design enables low cost and high sensitivity detection in a small footprint that can lead to its use in remotely deployable arrays of integrated mid-IR sensor devices. In this thesis, we will focus on the progress we have made on three key individual on-chip components: passive waveguides and optical resonators as the sensing element, surface functionalization layers, and photodetectors. We will also present our work towards integrating them on a monolithic silicon platform.

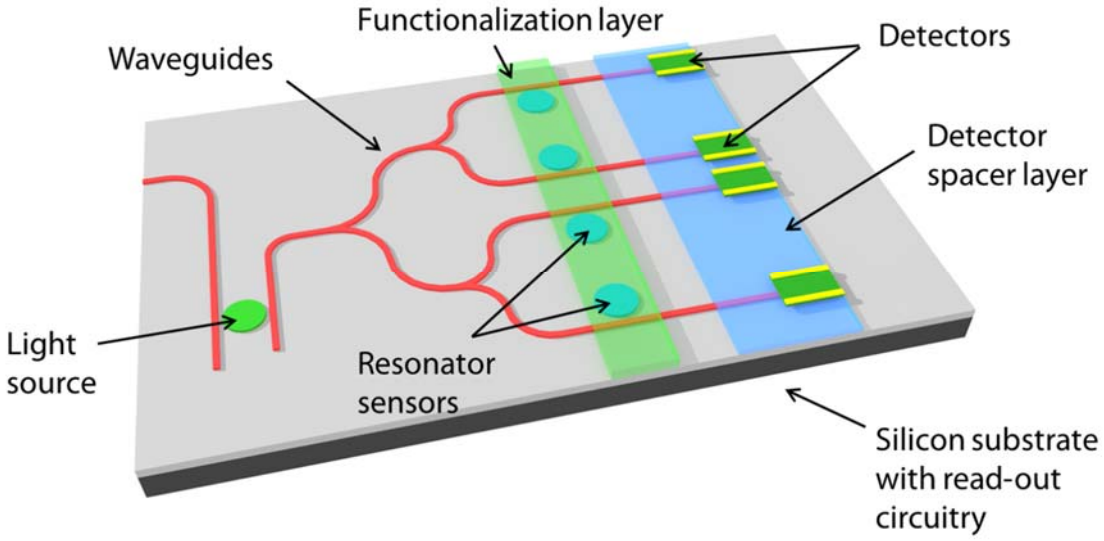


**Figure 1.3:** Schematic of a mid-IR lab-on-a-chip sensor system that combines a light source, sensing elements, a detector, and read-out circuitry on a monolithic silicon platform. The functionalization layer adds specificity to the sensor response for greater accuracy in analyte recognition[57].

## 1.7 Summary

We envision that this project will enable a Si-CMOS-compatible mid-IR microphotonics platform for applications such as integrated sensors for chemical and biological species using chalcogenide glasses (ChGs) for sensing and lead telluride for detection. In Chapter 2, we

investigate the materials behavior of ChGs to understand how their optical and structural properties can be tailored for applications such as sensing, nonlinear optical devices, and radiation detection. We attempt to understand the robustness of the structure and properties of chalcogenide thin films and devices against thin film processing and radiation. Chapter 3 describes relevant operating principles of waveguide and resonator devices that were fabricated and tested in this research. In Chapter 4, we develop process details for reproducible fabrication of chalcogenide glass waveguides and resonators on silicon. Chapters 5 and 6 address the characterization of the fabricated near-IR and mid-IR devices respectively to evaluate their performance. In Chapter 7, we develop novel designs for waveguide-integrated lead telluride photodetectors for on-chip sensing applications. Lastly, Chapter 8 summarizes key findings from this thesis project and presents ideas for directions that this work may lead to in the future.

# Chapter 2: Chalcogenide Glass Materials

## 2.1 Infrared Transparency

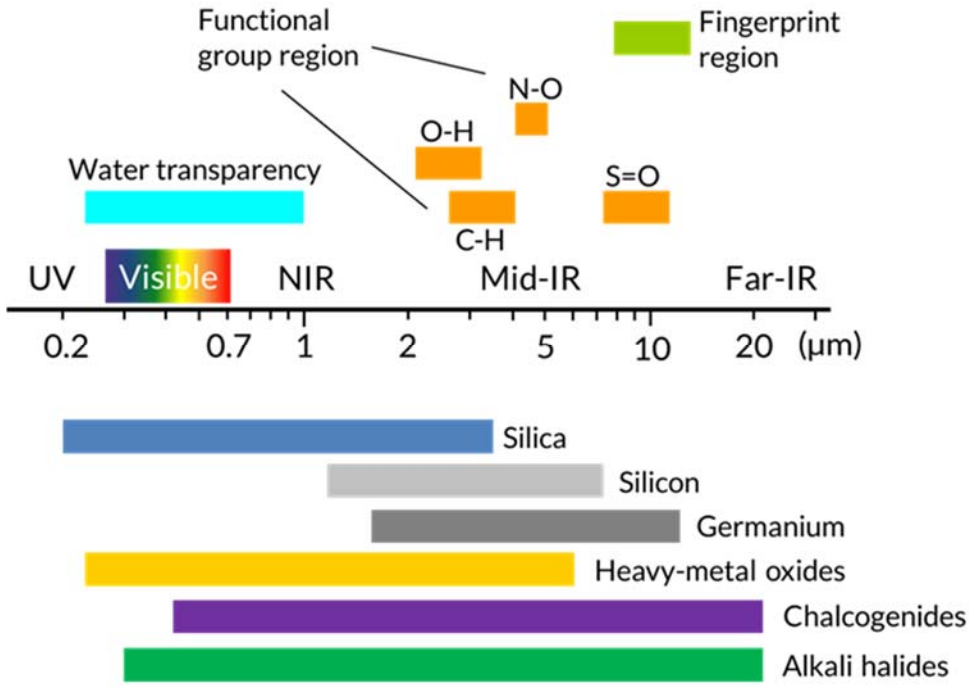


**Figure 2.1:** Approximate transparency windows for selected materials systems[58].

To build devices for infrared applications, the primary criterion that has to be satisfied is transparency of the selected materials to infrared radiation in the desired wavelength regime. A secondary concern is the refractive index of the materials; to build small footprint devices on chip, the refractive index has to be relatively high with the exact value at a given wavelength determining the eventual device dimensions. Optical transparency of materials is generally constrained by the presence of impurities with specific absorption bands and characteristic phonon vibration frequencies. Figure 2.1 summarizes approximate transparency ranges for selected materials systems along with a few characteristic bond vibrations. From Figure 2.1 it is clear that chalcogenide glasses and alkali halides offer the widest possible transparency windows stretching from the visible to the far-infrared regime

of the electromagnetic spectrum. However, compared to the halides, chalcogenide glasses have significantly higher refractive indices (n ~ 2-3 depending on composition) making them an excellent choice for near- and mid-IR applications. In this chapter, we will discuss the properties of chalcogenide glasses that make them amenable to microphotonics applications.

## 2.2 Chalcogenide Glasses

Chalcogenide glasses (ChGs) are amorphous compounds that contain one or more chalcogen elements (sulfur, selenium, and/or tellurium) covalently bonded to elements such as arsenic, germanium, antimony, gallium, lanthanum, etc. In this thesis, we will make extensive use of the following ChGs: arsenic sulfide ($As_2S_3$), arsenic selenide ($As_2Se_3$), and germanium antimony sulfide ($Ge_{23}Sb_7S_{70}$). This selection provides a broad range of refractive indices for microphotonic device design and allows us to examine differences between binary and ternary chalcogenides.

On an atomic scale, ChGs have a continuous random network structure. Binary ChGs such as $As_2S_3$ and $As_2Se_3$ ($As_2Ch_3$ in general) exhibit a locally two-dimensional network with weak van der Waals bonding (and a minor covalent component) between the layers[59, 60]. As a result, inter-layer distances tend to be much larger than first-neighbor distances within a layer. $As_2Ch_3$ structures are described in terms of pyramidal arrangements of $AsCh_3$ units. In $As_2S_3$, a ring is formed by the interlinking between six pyramids with a sulfur atom. The arsenic atom is on top and the sulfur atoms, linking pairs of arsenic neighbors, form the base of a pyramid with a bond angle of 99°. $As_2Se_3$ exhibits two kinds of pyramids with different nearest-neighbor distances and different valences on the arsenic atoms.

When fourfold-coordinated atoms such as germanium are added, the glass network becomes three-dimensional as bonds are created between layers, leading to higher network rigidity, glas transition temperature ($T_g$), strength, and hardness[59]. Due to the presence of many structural units and various types of homopolar and heteropolar bonds, structure and

bonding arrangements in ternary systems tend to be complicated and vary with composition. For $Ge_{23}Sb_7S_{70}$, investigation of IR and Raman spectra has shown that the glass structure is made up of $GeS_4$ tetrahedra and $SbS_3$ pyramids interlinked either with individual bridging sulfur atoms, or with two atom –S–S bridging groups[61].

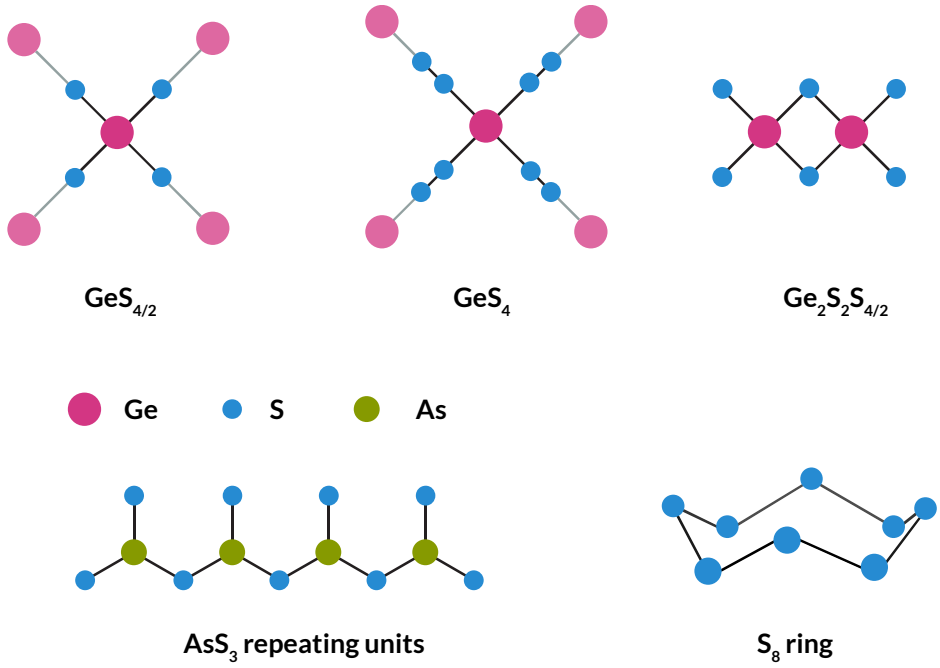


**Figure 2.2:** Schematic illustrations showing some of the key structural units making up ternary (above) and binary (below) chalcogenide glasses.

## 2.3 Optical Properties of ChGs

The optical band gap of ChGs lies in the visible or near-IR regions as the inter-atomic bonds are typically weaker than in oxide glasses. ChGs are composed of heavier atoms when compared to oxide glasses and exhibit low bond vibration energies and low phonon energies. This enables excellent transparency in the infrared wavelength regime that covers the characteristic absorption peaks of several chemical and biological species. However, ChGs still exhibit impurity and electronic absorption, which will be discussed in section 2.4. Although the weak bonding and heavy constituents make them excellent for mid- and far-

IR applications, other physical properties such as glass transition temperature ($T_g$), hardness, strength, and overall robustness tend to be lower than oxide glasses. Their relatively high densities and high polarizability endow ChGs with high linear refractive indices ($n$ = 2–3 depending on composition).

In addition to their excellent IR transparency, ChGs have also attracted attention due to their high Kerr (3rd order) nonlinearity that can be up to three orders of magnitude higher than that of silica[62, 63] and derives from electronic processes with an ultra-short time scale of $< 50$ fs[64] rather than free electrons with lifetimes on the order of nanoseconds. A nuclear contribution to the nonlinearity on the order of 12–13% has also been demonstrated[65]. Nonlinear absorption processes such as multi-photon absorption (multiple photons are absorbed to create an electron-hole pair) also occur in ChGs. Two-photon absorption (TPA) can lead to optical losses as the optical attenuation is now defined as $dI/dz = -\alpha I - \alpha_2 I^2$ where $\alpha_2$ is the TPA coefficient. ChGs tend to exhibit low TPA[66] which makes them excellent candidates for nonlinear applications as the figure-of-merit (FOM) for comparing nonlinear materials is defined as the ratio of the Kerr nonlinearity and the TPA coefficient[62, 63].

ChGs exhibit several photo-induced phenomena due to their structural flexibility and their high-lying lone-pair $p$ states in their valence bands[63]. A photo-induced change in the refractive index connected to an optical band edge shift leading to an absorption change is observed when light of energy close to the band gap is incident on ChGs[67-70]. The refractive index change can be either positive or negative depending on the dominant mechanism: photodarkening leads to an increase in the index while photo-volume expansion leads to a decrease in the index. Photodarkening is a process in which the optical band gap of the ChG material decreases upon illumination due to a red shift in the absorption edge and it can occur together with photo-volume expansion. Many models have been proposed in

literature to explain this phenomenon, but they can generally be categorized into one of the following structural changes[71-78]:

- bond-breaking and rearrangement
- changes in interlayer distances due to a weakening of van der Waals forces (can lead to photo-volume expansion)
- photo-induced polymerization processes

Although photosensitivity effects are most prominent under near-band gap illumination, they have been observed at longer wavelengths (e.g., 1550 nm) by using resonators for cavity enhancement in $As_2S_3$ glass[79]. Since the energy is below band gap, sub-gap defect absorption (Urbach band tail, mid-gap states, etc.) is believed to be responsible for photosensitivity at longer wavelengths. Photosensitivity of ChGs has been exploited for a number of applications including direct writing of device features[80-82] and changing the response of microring resonators to ease fabrication tolerances[83]. The latter technique enables the correction of the response of devices to match required specifications more closely (see Chapter 5). It is possible to reverse light-induced effects by annealing near the glass transition temperature.

## 2.4 Loss mechanisms in ChGs

Chalcogenide glasses are composed of heavier atoms when compared to oxide glasses and exhibit low bond vibration energies and low phonon energies. This enables excellent transparency in the infrared wavelength regime, which covers the characteristic absorption peaks of several chemical and biological species. To fully analyze the optical transparency of ChGs, we need to investigate their loss mechanisms. Optical loss reduction is a device performance necessity for the systems used as sensors since it enables a longer optical path inside resonant cavities (higher $Q$-factor). This allows the light to interact over a longer

time with the molecular species of interest, thus improving detection sensitivity. Quantitative analysis has revealed that low overall optical loss (~0.1 dB/cm) is the key to high detection sensitivity up to a point where temperature fluctuation noise starts to take over[12, 14, 84].

There are typically three main optical loss mechanisms in planar ChG devices: radiative loss, roughness scattering, and material attenuation. Radiative loss refers to optical loss due to coupling into radiative or substrate modes caused by waveguide bending or quantum tunneling through a finite cladding thickness. This loss mechanism can be significantly reduced by an appropriate choice of device geometry. Scattering loss arises from roughness at the sidewalls of fabricated devices when the optical mode traveling through the device overlaps with the sidewall. Material attenuation can be further categorized into extrinsic loss due to impurity absorption and intrinsic loss which includes electronic absorption by band tail or mid-gap states (nonlinear absorption neglected at low power), Rayleigh scattering caused by statistical density fluctuations, and phonon absorption. In the mid- and far-IR regimes, Rayleigh scattering is negligible as the wavelength is much larger than the length scale of density fluctuations. Phonon absorption depends on characteristic bond vibration frequencies and can be avoided by appropriate selection of ChG composition. This leaves electronic absorption and impurity absorption as the major contributors.

Impurity loss has been relatively well examined in ChG optical fibers[85-87], but similar investigations with thin films have been scarce. Despite the high purity of the starting materials used, impurities contributing to absorption are still present unless specific purification procedures are carried out on raw materials (e.g., pyrolysis of sulfur) or during the melting process by including gettering materials such as magnesium for oxygen removal and metal chlorides for hydrogen removal[88]. If gettering is carried out solely to remove oxygen, the hydrogen from O-H bonds tends to redistribute to other hydride bonds,

increasing their peak strengths as shown. In Chapter 5, we will see that the contribution of impurity absorption loss is typically smaller than roughness scattering. However, removing these impurities may be crucial in few situations such as for sensing applications, where impurity absorption peaks may overlap with absorption peaks from chemical species of interest and contribute false signals. In addition, impurity absorption peaks can increase total loss over specific wavelength ranges making it difficult to achieve low device propagation losses.

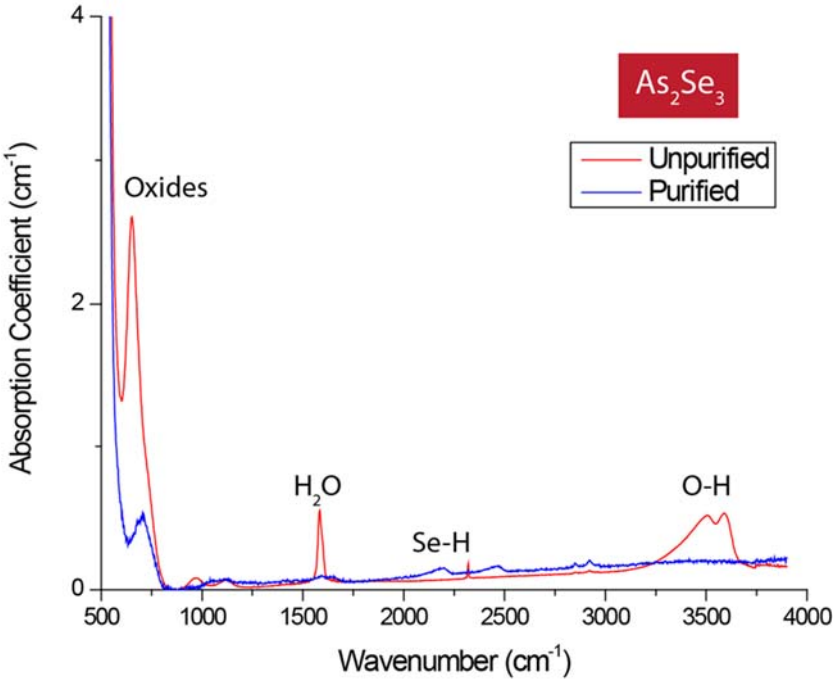


**Figure 2.3:** FTIR absorption spectra showing the effect of purification techniques on bulk $As_2Se_3$ glass. By gettering the hydrogen and oxygen impurities, absorption features attributed to $H_2O$ and O-H vibrations are significantly reduced[89].

Based on literature data showing oxygen, carbon, and hydrogen as the main impurities in bulk ChGs[43, 87, 88, 90], we carried out preliminary studies to assess the impact of thin film processing on impurity incorporation. Figure 2.4 shows oxygen, carbon, and hydrogen impurity concentrations in thermally evaporated thin films (~500 nm) and bulk samples taken from the same batch of $Ge_{23}Sb_7S_{70}$ and $As_2S_3$ glasses, measured using Secondary Ion

Mass Spectroscopy (SIMS). It is clear that while carbon and hydrogen concentrations are quite similar in film and bulk, oxygen concentration in the $Ge_{23}Sb_7S_{70}$ film is higher by almost 7-fold as compared to bulk, suggesting that residual oxygen in the high-vacuum chamber may have been incorporated into the film during deposition. The higher oxygen concentration can lead to higher mid-IR device losses, as the optical loss from the O-H absorption band (centered at 2.9 µm) is correspondingly higher. It is possible to reduce the oxygen present in the evaporation chamber by use of a gettering pump[91] or by distilling the glass during bulk synthesis; as few additional C and H impurities are introduced into the film, simply starting with purified raw materials can reduce their concentrations[92, 93].

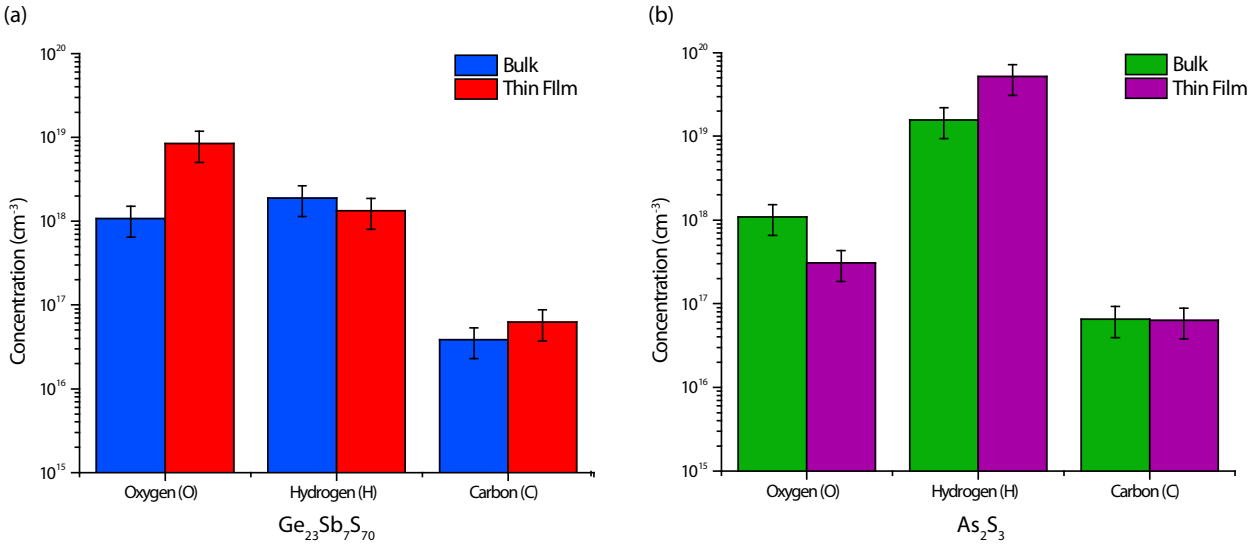


**Figure 2.4:** Secondary Ion Mass Spectroscopy (SIMS) data collected on bulk glass and thin films showing concentrations of common impurities such as oxygen, hydrogen, and carbon prior to any purification techniques.

Electronic absorption in amorphous materials such as ChGs is caused by mid-gap states arising from dangling bonds and band tailing of the density of states due to fluctuations in structural order[94, 95]. Their density may be controlled either by selective addition of chemical modifiers that reduce the Urbach tail[96, 97] or by modification of the chemical composition to increase the band gap. However, such modifications might lead to changes in the thermal

and optical properties of these glasses and have to be taken into account when designing planar microphotonic devices.

## 2.5 Chalcogenide glass processing

### 2.5.1 Bulk glass synthesis

Bulk ChG preparation involves a traditional melt-quench technique[66, 98] starting with high purity (99.999%) elemental constituents batched according to the composition required. The batched materials are vacuum-sealed inside a clean quartz ampoule free of larger impurities and moisture. The sealed ampoules are then heated at a temperature of several hundred degrees Celsius (dependent on specific composition) for several hours in a rocking furnace until the melt has homogenized. The ampoule is quenched in air to room temperature and returned to the furnace for annealing at sub-$T_g$ temperatures to prevent fracture of the ampoule and the bulk glass inside it.

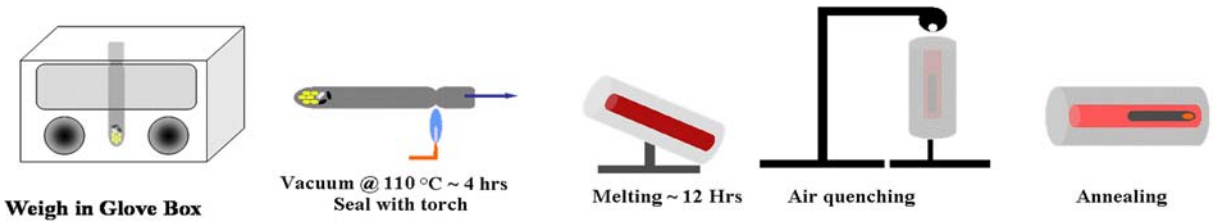


**Figure 2.5:** The process of synthesizing bulk chalcogenide glass using a traditional melt-quench technique.

### 2.5.2 Thin film processing and characterization

A number of deposition techniques have been used to fabricate thin films of ChGs including RF magnetron sputtering[99], pulsed laser deposition (PLD)[61, 100], chemical vapor deposition (CVD)[101], and spin coating of crushed glass dissolved in organic solvents such as propylamine[30, 102]. In this project, the bulk ChG materials synthesized by our collaborators at the University of Central Florida (formerly at Clemson University) are deposited on

silicon substrates by single-source thermal evaporation from resistively heated tantalum boats under high vacuum (~$10^{-6}$ – $10^{-7}$ Torr) as shown in Figure 2.6. Raw glass materials are prepared for evaporation by manually crushing them into small pieces ~1 mm in size using a mortar and pestle. Our planar device fabrication utilizes an ultraviolet photolithography process with a negative photoresist followed by thermal evaporation and photoresist lift-off in acetone (under sonication) to form patterned structures[14] (see Chapter 4). The photosensitivity of ChGs has also been exploited for fabrication by using femtosecond laser pulses to write patterns directly[80, 103] into ChG films.

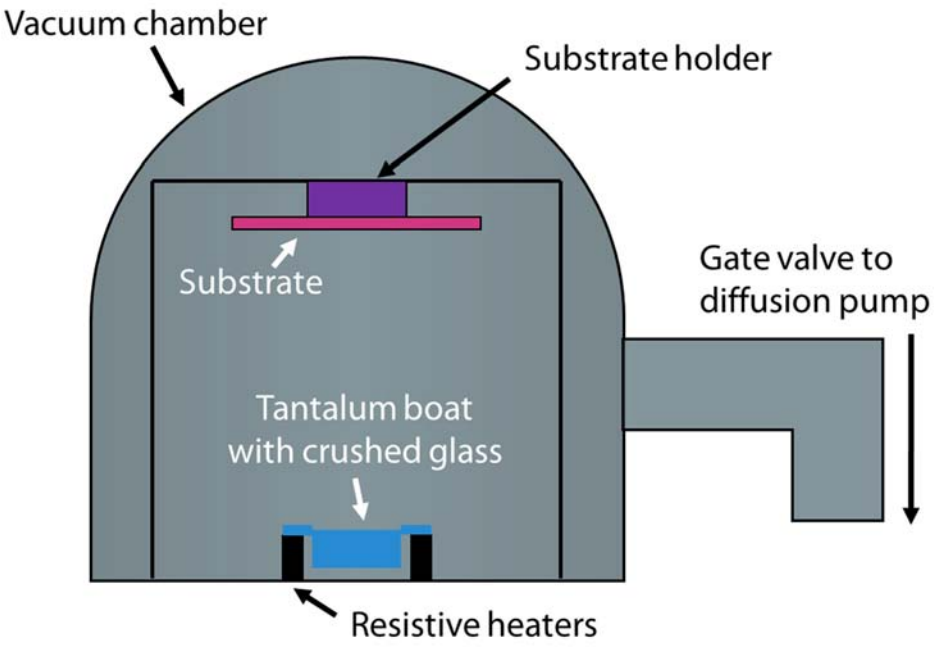


**Figure 2.6:** Schematic illustration of the thermal evaporator setup used for deposition of chalcogenide glass and PbTe films.

We analyze the deposited thin films by first evaluating their composition using Wavelength Dispersive Spectroscopy (WDS). This technique has demonstrated good agreement with bulk stoichiometry for our thin films (~500 nm) but cross-sectional measurements on thicker films of ternary glasses exhibit deviation from bulk stoichiometry

with increasing thickness. Thick films show a closer match to bulk stoichiometry at the bottom of the film than at the surface. We can attribute this to the different vapor pressures of the elements in ternary systems that lead to different rates of evaporation and a gradual change in the stoichiometry of glass material left in the evaporation boat. One way to address this issue is by starting out with a different composition such that the film composition is more closely matched to the target stoichiometry. Our measurements on binary chalcogenides such as $As_2S_3$ and $As_2Se_3$ showed more uniform stoichiometry across varying thicknesses[46].

**Table 2.1:** Wavelength Dispersive Spectroscopy (WDS) measurements on evaporated $Ge_{23}Sb_7S_{70}$ films demonstrate that thicker films tend to deviate further from the bulk composition when measured at the top surface.

| **Thickness** | **Average Atomic %** | | |
|---|---|---|---|
| | **Ge** | **Sb** | **S** |
| **0.4 µm** | 22.7 | 9.0 | 68.3 |
| **1.3 µm** | 18.9 | 11.0 | 70.1 |
| **3.7 µm** | 13.8 | 7.7 | 78.5 |
| **4.2 µm** | 14.7 | 7.7 | 77.6 |
| **Bulk** | 23 | 7 | 70 |

We have also evaluated $Ge_{23}Sb_7S_{70}$ thin films deposited by spin-coating and compared their stoichiometry to those deposited by thermal evaporation. Chalcogenide glasses are soluble in select organic solvents such as ethanoldiamine (EDA) and the solution can then be spin-coated on a substrate to create thin films. The residual solvent in the film is driven out through a baking process in a vacuum oven to obtain uniform films of ChG materials[102]. Table 2.2 shows a summary of our WDS results on spin-coated films.

**Table 2.2:** WDS composition data for spin coated $Ge_{23}Sb_7S_{70}$ films showing large deviation from bulk stoichiometry. We note an excess of germanium and a sulfur deficiency, even when compared to evaporated thin films.

| Thickness | Average Atomic % | | |
|---|---|---|---|
| | **Ge** | **Sb** | **S** |
| **321 nm** | 36.24 | 10.41 | 53.35 |
| **264 nm** | 33.57 | 9.8 | 56.63 |
| **201 nm** | 29.64 | 8.5 | 61.85 |
| **177 nm** | 29.81 | 8.62 | 61.57 |

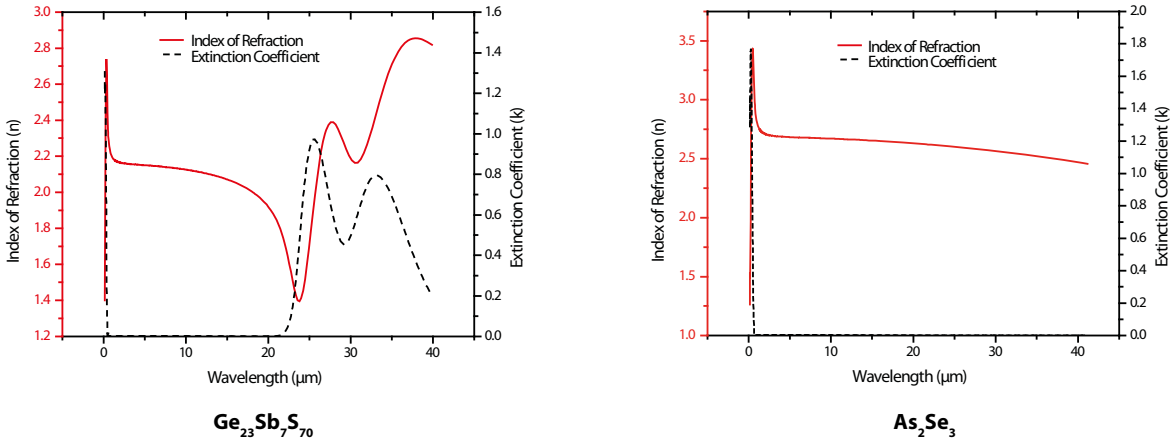


**Figure 2.7:** Ellipsometry data (n, k) collected from thin films of $Ge_{23}Sb_7S_{70}$ (Left) and $As_2Se_3$ (Right) deposited on 1 cm diameter $CaF_2$ substrates.

We measured the complex refractive index of thin films made from two of our glass compositions via a variable angle spectroscopic ellipsometry technique (performed at J. A. Woollam, Inc.). The real and imaginary parts of the refractive index were measured over a broad wavelength range and the results are plotted in Figure 2.7. The data shows that $Ge_{23}Sb_7S_{70}$ has a refractive index of about 2.15 in the near- and mid-IR wavelength ranges with low absorption coefficient. $As_2Se_3$ is a higher index material and its refractive index is about 2.75 over the range of interest. These values are slightly lower than their bulk

counterparts[61, 104, 105] indicating a different structural arrangement in the films and a reduced density.

## 2.6 Effects of radiation on ChG materials

Part of this thesis work was dedicated to understanding the radiation hardness of chalcogenide glass materials as we anticipate remote chemical sensors may be deployed in harsh environments such as those near nuclear facilities. Past literature on this subject has studied various ChG compositions in bulk form and found that relatively high radiation doses (a few MGy of gamma) are required before any measurable changes occur[106]. Further, many radiation-induced defects tend to be transient in nature and do not survive long-term[107]. The amorphous nature of our glass materials makes it harder to characterize defects introduced by radiation when compared with their crystalline counterparts. However, we can categorize defects in these materials into the following types[107-112]:

- structural defects such as dangling bonds and abnormal bonding configurations.
- deviation from stoichiometry
- presence of impurities that disrupt the glass network and interact with glass constituents (oxidation, hydrogenation, carbonization, etc.)

All of these defects are more likely to be present in thin films as the overall structure of films tends to deviate from the bulk based on how a given glass melts and evaporates. For instance, $As_2S_3$ glass tends to evaporate primarily as molecular units of $As_4S_4$ and consequently the film has a much different structure than the bulk, which is made up of repeating units of As-$S_3$ with one of the sulfur atoms bridging adjacent units. The defects can affect the thermal, optical, and microstructural properties of chalcogenide glasses and when present in sufficient numbers can be measured using common techniques such as

Raman spectroscopy, differential scanning calorimetry, and UV-Vis spectroscopy[107, 112]. Exposure to radiation can create more of these defects through bond breakage and bond-switching reactions, as illustrated schematically in Figure 2.8a and Figure 2.8b respectively for $As_2Se_3$.

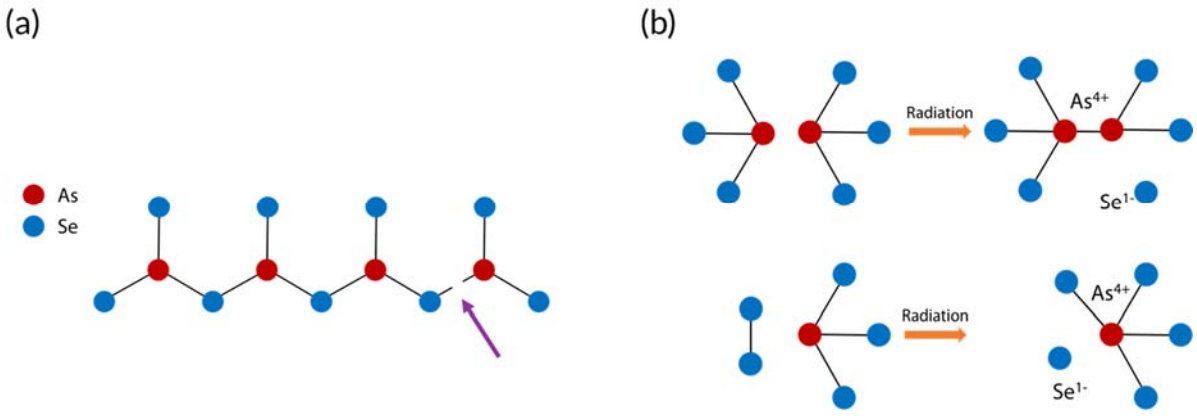


**Figure 2.8:** (a) Bond breakage leading to non-bridging anions; (b) coordination topological defects from bond-switching reactions upon irradiation.

We have measured the UV-Vis spectra of $Ge_{23}Sb_7S_{70}$ and $As_2Se_3$ bulk and thin films before and after irradiation with a dose of $5\times10^{15}$ $cm^{-2}$ alpha particles with 3 MeV energy at a grazing angle incidence (implanted at the Pacific Northwest National Laboratory). First, we observe that the $Ge_{23}Sb_7S_{70}$ bulk sample does not exhibit any appreciable change in the absorbance or the wavelength of the absorption edge post-irradiation. The $As_2Se_3$ bulk sample does show a slightly higher absorbance but it returns to the pre-irradiation level when the sample is measured again after one month. With the thermally evaporated thin films, $Ge_{23}Sb_7S_{70}$ once again does not exhibit much difference after irradiation, possibly indicating a relatively high degree of radiation hardness. The $As_2Se_3$ film appears to have two absorption edges with a plateau in between them after irradiation. This could be indicative of the formation of a secondary phase with a different bandgap or voids in the films. As we used soda-lime glass slides as our thin film substrates, it is conceivable that

the absorption edge at the lower wavelength is from the substrate due to through-thickness voids in the film. The spectrum also appears to be returning to the pre-irradiation state after a month, demonstrating that many of the defects created by irradiation are transient in nature. Since there is a time delay of a few days between irradiation of the samples and their measurement due to shipping, it may be possible to observe a larger change in irradiated samples if data is collected soon after radiation exposure.

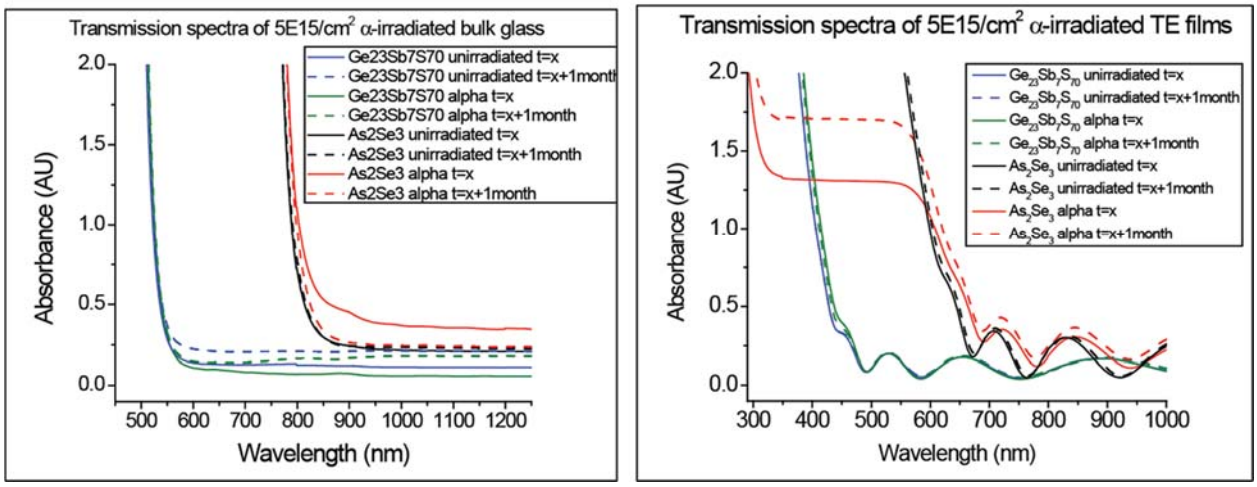


**Figure 2.9:** UV-Vis transmission spectra of $Ge_{23}Sb_7S_{70}$ and $As_2Se_3$ bulk glass (Left) and thermally evaporated thin films (Right) before and after alpha irradiation. In both cases, $As_2Se_3$ shows higher sensitivity to the radiation damage, including a possible second phase or voids formation for the thin film. In all cases, measurements done after a month show relaxation towards original state, indicating the transient nature of radiation-induced defects.

In Figure 2.10, we observe that the $As_2Se_3$ films do indeed exhibit the formation of voids/air holes after alpha irradiation, which may explain the plateau in the UV/Vis spectra. By comparison, our measurements on $Ge_{23}Sb_7S_{70}$ films show a much lower degree of void formation and hence their UV/Vis spectra remain unchanged post-irradiation. This data shows us that the $As_2Se_3$ films are more sensitive to radiation damage than the $Ge_{23}Sb_7S_{70}$ films.

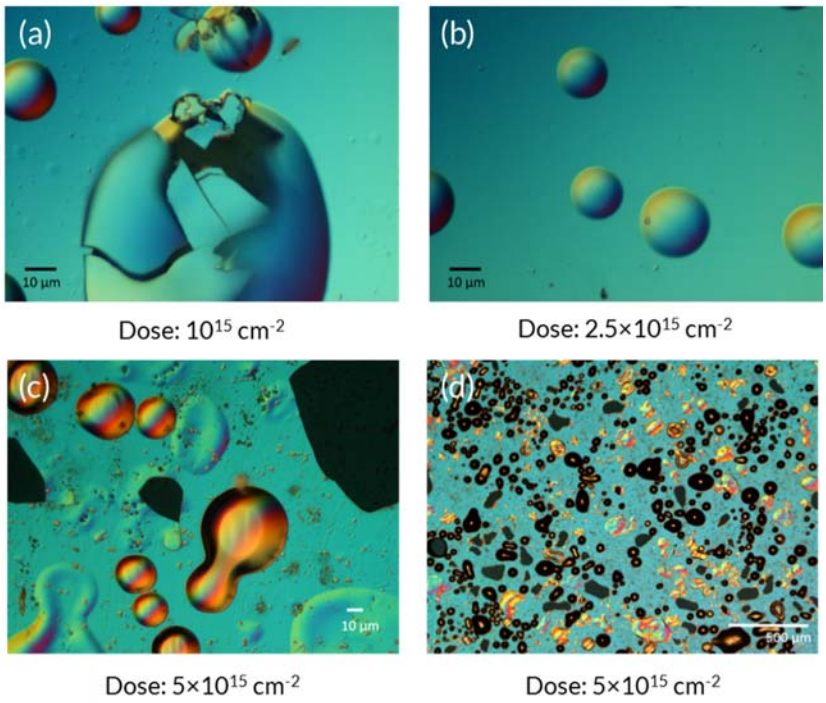


**Figure 2.10:** Optical microscope images showing holes and delamination in alpha-irradiated $As_2Se_3$ films. These defects could be responsible for the plateau seen in the UV-Vis sepctra.

### 2.6.1 Position annihilation lifetime spectroscopy

Positron annihilation lifetime spectroscopy (PALS) is a nondestructive technique to probe defects in materials on an atomic scale. A beam of positrons is implanted into the material under test and the time elapsed until their annihilation through interaction with electrons is measured by detecting the radiation emitted upon annihilation. When defects such as vacancies are present in a material, positrons are trapped in them and their lifetime increases. By comparing annihilation lifetimes of irradiated and non-irradiated samples, it should be possible to begin gaining an understanding of the nature of defects induced by radiation. One caveat is that the amorphous materials we will test already have defects and so the change after irradiation could be very small and hard to measure.

Our first set of measurements were carried out at Opole University in Poland on non-irradiated films to determine whether PALS would yield meaningful data for bulk and thin

film samples of $As_2Se_3$. From our UV/Vis data, we noted that this glass composition was more sensitive to alpha irradiation and we chose it for PALS measurements as well. Due to a low fraction of positrons annihilating in the film compare to the Si substrate we are not able to unambiguously decompose the various contributions from the films. Hence, we analyze them as an average contribution from all possible defects within the two-state positron-trapping model. Figure 2.11 shows a schematic of the two-state positron-trapping model. A positron entering the sample can either (i) annihilate by combining with an electron in the defect-free bulk to emit radiation with rate $\lambda_b$, or (ii) move from a delocalized state in defect-free bulk to a defect-trap state with a defect trapping rate of $\kappa_d$ and then annihilate at a later time with rate $\lambda_d$. For both spin-coated and thermally evaporated thin films, the fraction of positrons annihilated within the film was less than 3%.

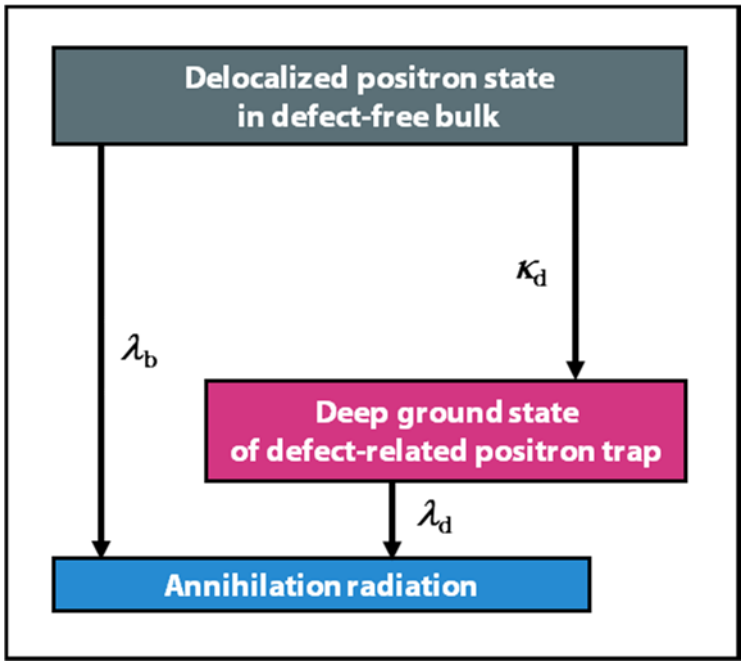


**Figure 2.11:** A two-state positron-trapping model used to analyze PALS data.

**Table 2.3:** PALS parameters for spin-coated films

| Sample | $\tau_{av}$ (ns) | $\kappa_d$ |
|---|---|---|
| **$As_2Se_3$ bulk** | 0.262 | 0.71 |
| **2.8 µm film** | 0.314 | 1.41 |
| **0.88 µm film** | 0.384 | 2.03 |
| **0.46 µm film** | 0.460 | 2.45 |

**Table 2.4:** PALS parameters for thermally evaporated films

| Sample | $\tau_{av}$ (ns) | $\kappa_d$ |
|---|---|---|
| **$As_2Se_3$ bulk** | 0.262 | 0.71 |
| **1.98 µm film** | 0.300 | 1.28 |
| **0.77 µm film** | 0.352 | 1.78 |
| **0.43 µm film** | 0.425 | 2.29 |

Based on the initial PALS measurement results, we can make a few preliminary conclusions.

- The average positron lifetime ($\tau_{av}$) decreases as thickness increases towards the bulk sample, which corresponds to a general trend in free volume (density) of these samples.
- A higher defect-trapping rate ($\kappa_d$) is observed as the thickness of the films goes down.
- The greater the thickness, the closer the PALS parameters are to the bulk sample.
- Spin-coated films possibly have more defects capable of trapping positrons than thermally evaporated ones do.

- If radiation-induced effects are large enough, we can detect them through changes in $\kappa_d$ or in the parameters of second channel of annihilation.

We have fabricated more bulk glass and thermally evaporated thin films of $As_2Se_3$ and exposed them to gamma radiation doses of about 220 Mrad (2.2 MGy) using a $^{60}Co$ source while placed inside vacuum-sealed quartz ampoules to reduce ozone formation. The samples were sent to Opole University for measurement immediately after removal from the irradiator to ensure that we can observe the effects of transient defects before they decay.

## 2.7 Other mid-IR transparent materials

Group IV elemental compounds silicon and germanium are excellent mid-IR candidates due to their high refractive indices and the ability to use single-crystal layers to fabricate microphotonic devices. Silicon-on-insulator (SOI) technology has been widely used in the telecom wavelength range and many research efforts have focused on doing the same for the mid-IR[17, 19, 113]. Germanium grown on silicon substrates has also been demonstrated as a mid-IR platform[114-116]. Our own work on silicon-based materials systems has yielded multiple successful mid-IR technologies:

- Silicon devices on silicon dioxide pedestals[117]: the oxide is isotropically etched to form an undercut pedestal. This structure reduces mode overlap with the oxide undercladding and enables transmission at wavelengths where the oxide would begin to show absorption.
- Silicon devices on silicon pedestals[118]: the silicon beneath the waveguide layer is etched once more and this type of structure can be built directly on a silicon wafer, reducing complexity and eliminating any potential issues with other materials.

- Silicon nitride devices on oxide[38]: thick, silicon-rich nitride films were grown using CVD and then etched to create mid-IR waveguides.

## 2.8 Summary

In this chapter, we have looked at chalcogenide glass materials and their suitability for infrared photonics applications due to their wide transparency window. Chalcogenide glasses are easy to fabricate (bulk and thin film) and their compositional flexibility allows tuning of optical properties such as refractive index. Further, material attenuation in ChG materials arises due to the presence of impurities in the raw materials and defects in the glass network. We have also performed UV/Vis and PALS measurements to gain a preliminary understanding of the defects induced by alpha radiation in ChG bulk and thin film samples. The $As_2Se_3$ samples show higher sensitivity to radiation damage but defects in ChG materials tend to be transient and further measurements are required. We discuss waveguides, resonators, and designs for near- and mid-IR devices in the next chapter.

# Chapter 3: Waveguides and Resonators

At the component level, passive waveguides and optical resonators constitute the key microphotonic elements for a number of on-chip applications such as telecommunications, optical interconnects, and most importantly, mid-IR sensing and spectroscopy. Waveguide sensors can transmit a wider wavelength range and hence are useful for fingerprinting across the entire mid-IR regime. Resonator sensors with a large quality ($Q$) factor can offer very high sensitivity to changes in the complex refractive index[12, 13, 15, 16]. The long optical path length in a resonant cavity leads to higher sensitivity from enhanced photon-matter interactions due to spatial light confinement over a longer period of time. In addition, it is feasible to fabricate resonator arrays that can be used for parallelized detection of multiple species while maintaining a small footprint. A good bio/chemical sensor must meet the criteria of (i) optical transparency in the mid-infrared wavelength range, (ii) high sensitivity, and (iii) high specificity all on an integrated silicon platform. In this chapter, we focus on the operating principles and design of dielectric waveguides and microresonators as the photonic elements of choice for this thesis work.

## 3.1 Dielectric waveguides

Waveguides are optical devices comprised of a higher refractive index core surrounded by a cladding material of lower index and light propagates through them via total internal reflection. Optical fibers, widely used in telecommunications applications, are an example of waveguides on a macroscopic scale. In this thesis, however, our focus is on waveguides fabricated on silicon substrates for microphotonics applications. When the waveguides comprise a higher index thin film on a lower index substrate, they are called slab waveguides and light is only confined along a single direction. Strip waveguides, as the name implies,

contain a narrow strip of the higher index material on a lower index substrate and confine light in both directions perpendicular to the propagation direction. A ridge waveguide combines the two types by placing a strip of the higher index material on a slab of the same material. Light is confined in two directions and the larger size confines light towards the center, which helps reduce scattering losses from the waveguide sidewalls. Figure 3.1 shows a schematic of the three main types of waveguides. Our emphasis this thesis is on strip waveguides.


**Figure 3.1:** Schematic showing the three main types of waveguides. The waveguide core is comprised of a higher index material than the undercladding to confine the mode spatially. The work presented in this thesis uses strip (or channel) waveguides.

A time-invariant, stable electromagnetic field pattern that is an eigensolution to Maxwell's equations is referred to as an optical mode. A guided mode (in a waveguide) is a stable amplitude and polarization profile in which the wave propagates at a given wavelength. The field profile of a given mode is determined entirely by the geometry and the refractive indices of the materials comprising the waveguide at the wavelength of interest. The geometry and indices also describe the effective refractive index ($n_{eff}$) of the propagating mode that is defined by the ratio of the velocity of light in vacuum and the phase velocity in the waveguide. The effective index is always less than the index of the waveguide core and greater than the index of the cladding. It is also related to the propagation constant, $\beta$, by the equation $n_{eff} = \beta\lambda/2\pi$ where $\lambda$ is the free-space wavelength.

While the effective index defines the mode index (higher $n_{eff}$ = lower mode order), the polarization of the mode determines which direction the electric and magnetic fields are oriented with respect to the direction of propagation. In a transverse electric (TE) mode, the electric field oscillates parallel to the substrate and perpendicular to the direction of propagation. Similarly, a transverse magnetic (TM) is defined by a magnetic field oscillating parallel to the substrate and perpendicular to the propagation (see Figure 3.2).

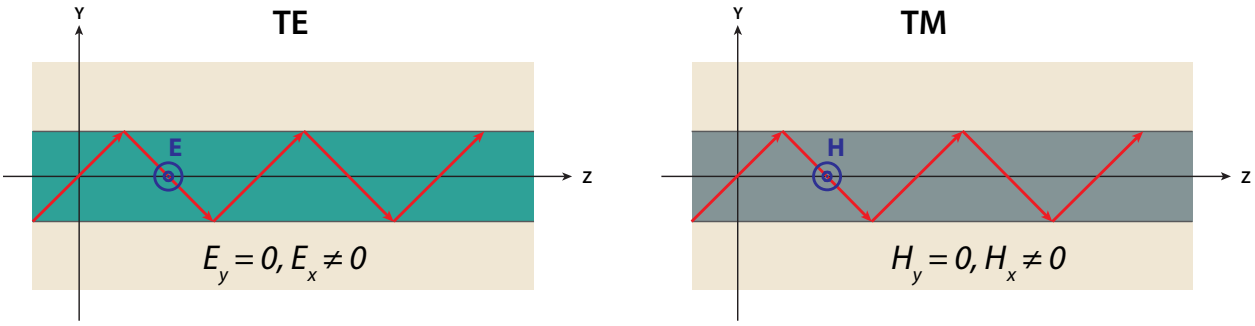


**Figure 3.2:** TE (Left) and TM (Right) propagation modes in a slab waveguide. The electric field in the TE mode and the magnetic field in the TM mode are oscillating along the X-axis as the mode travels in the Z direction[1].

Finally, the power confinement factor ($\Gamma$) is the ratio of the power confined within the waveguide core to the total power propagating through the structure[119]. The power is calculated as the integral of the Poynting vector as shown in Eqn (2). When the refractive index contrast between the core and cladding is high, the power confined within the core is correspondingly high. For sensing applications, we desire a small fraction of the mode to be present outside the waveguide as it leads to greater overlap with any chemical species that encounter the device.

$$\Gamma_{\text{core}} = \frac{\int^{core} P_z(s).\,ds}{\int^{\infty} P_z(s).\,ds} \tag{2}$$

## 3.2 Dielectric microresonators

Optical resonators, or resonant cavities, are devices in which light can interfere constructively and be confined at resonant frequencies that are defined by the resonance condition defined as $\lambda_r N = n_{eff} L$ where $\lambda_r$ is the resonant wavelength, $n_{eff}$ is the effective refractive index, $L$ is the cavity length, and $N$ is an integer referred to as the mode order. When the light meets the resonant condition of a resonator, there is an enhancement in the optical power when the light is confined, completing a higher number of round trips than it would at other frequencies. Due to their frequency selectivity, resonators have found widespread use in applications ranging from optical filtering, laser cavities, nonlinear optics, optical switching, and chem-bio sensing[120].

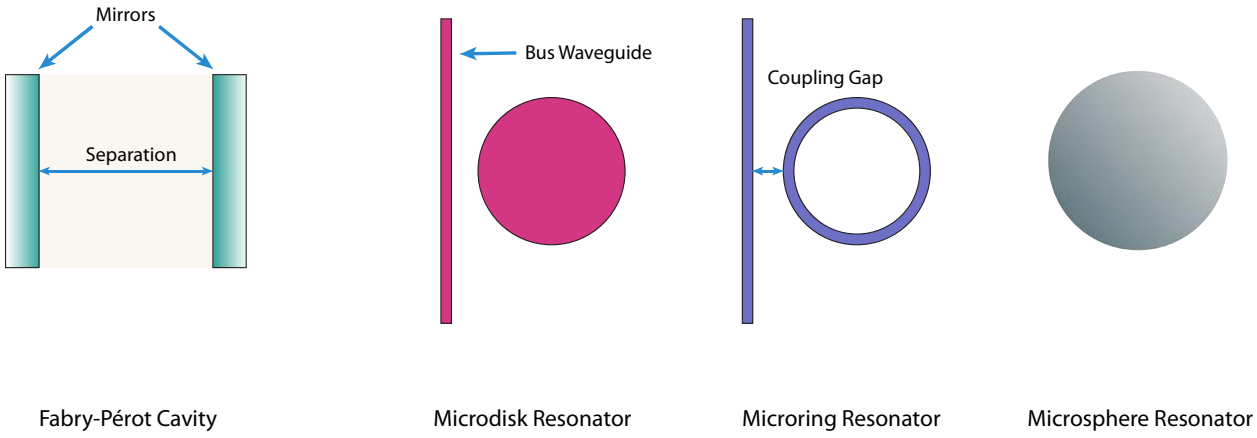


**Figure 3.3:** A few common types of resonator structures. The Fabry-Pérot cavity consists of two highly reflective mirrors between which light can travel and is the simplest resonator structure. The microdisk, microring, and microsphere resonators all require a bus waveguide to couple light into them. Fibers are typically used for microspheres.

A multitude of resonator configurations is in active use in research and commercial applications, as illustrated schematically in Figure 3.3. The simplest resonator device is a Fabry-Pérot structure that uses two parallel planar mirrors to form a low-loss cavity in which light is repeatedly reflected back and forth. Our research relies on dielectric

resonators, particularly microdisk and microring resonators that utilize total internal reflection at the boundary between the resonator and its surrounding medium. Propagation of light occurs at near-grazing incidence via whispering-gallery modes[1, 121].

The extinction ratio defines the height of a resonant peak while the quality factor ($Q = \lambda_r/\Delta\lambda$ where $\Delta\lambda$ is the full-width at half maximum of the resonant peak) is equivalent to the effective optical path length inside a resonator, and is correlated to the optical loss. Thus, a high $Q$-factor (sharp resonant peak) corresponds to a low loss and indicates that light is confined in the resonator for a longer period of time. For sensing applications, a high $Q$-factor and low loss are essential because they imply long photon-matter interaction time and hence high sensitivity. Our ChG-based resonators have achieved $Q$ values as high as $6\times10^5$ with loss as low as 0.6 dB/cm at telecom wavelengths.

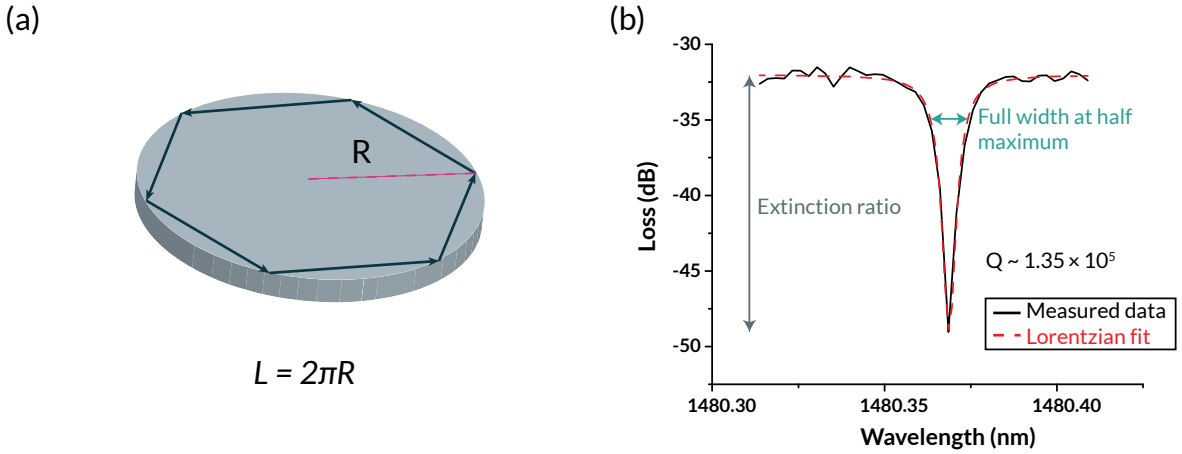


**Figure 3.4:** (a) Schematic illustration of microdisk resonator showing light propagation[1]. (b) Typical resonant peak measured with ChG resonators in the near-IR with Q factor of $1.35\times10^5$ (obtained from Lorentzian fit to data).

The cavity Q factor is related to the optical loss in the cavity, $\alpha_r$, by the equation $Q = 2\pi\nu_0/c\alpha_r$ where $\nu_0$ is the resonant frequency. The free spectral range (FSR) of a resonator is the separation (in frequency or wavelength) between adjacent peaks belonging to the

same resonant mode and is related to the group index and length of the resonant cavity with the following equations:

$$FSR\ (frequency) = \frac{c}{2n_g L} \tag{3}$$

$$FSR\ (wavelength) = \frac{\lambda^2}{n_g L} \tag{4}$$

where $c$ is the velocity of light in vacuum, $n_g$ is the group index, $L$ is the resonator circumference, and $\lambda$ is the free-space wavelength. The group index is the ratio of the velocity of light in vacuum and the group velocity in the medium and is related to the effective refractive index through the following equation:

$$n_g = n_{eff} - \lambda \frac{\partial n_{eff}}{\partial \lambda} \tag{5}$$

The $Q$-factor of a resonator can be divided into an intrinsic component ($Q_{in}$) and an extrinsic component ($Q_{ex}$). The intrinsic $Q$-factor can be sub-divided further into contributions arising from loss within the resonant cavity itself such as material attenuation, scattering losses, and radiative losses[122]. The extrinsic Q represents loss out of the resonator due to coupling out of the resonator into the environment. Based on the magnitudes of the intrinsic and extrinsic Q factors, we can define three coupling regimes for resonators: (i) critically coupled ($Q_{in} = Q_{ex}$), (ii) under coupled ($Q_{in} > Q_{ex}$), and (iii) over coupled ($Q_{in} < Q_{ex}$). When a resonator is critically coupled, the internal loss is equal to the external loss and hence, the transmission goes to zero. Figure 3.5: A transmission plot versus wavelength demonstrating the three resonator coupling regimes calculated for a resonator with effective index of 2.5 and radius of 100 µm shows a transmission versus wavelength plot demonstrating these three coupling regimes.

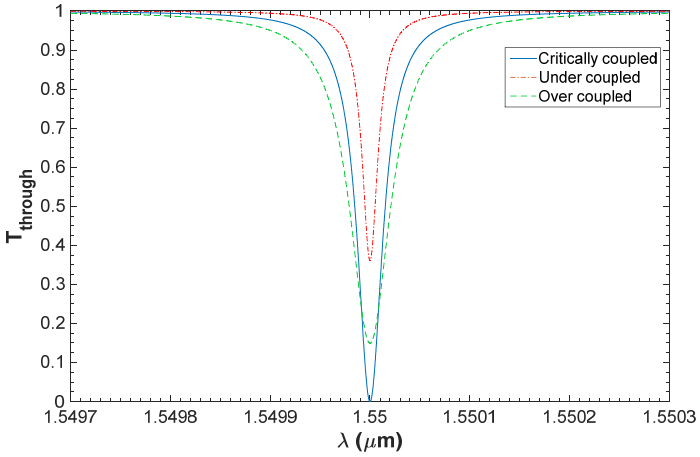


**Figure 3.5:** A transmission plot versus wavelength demonstrating the three resonator coupling regimes calculated for a resonator with effective index of 2.5 and radius of 100 µm at a resonance wavelength of 1.55 µm.

To perform sensing with microresonators, one of two approaches is used. In the first method, a change in the effective refractive index of the resonator caused by introduction of analyte species is measured as a change in the resonant peak position (wavelength). The second approach exploits the change in resonant peak height because of an absorbing analyte to sense its presence. The index shift method is able to sense very small changes (low analyte concentrations) but is susceptible to temperature fluctuations that can lead to larger shifts than those from analytes. Unlike absorption sensing, index sensing does not rely on the specific probe wavelength and hence specificity is limited without the use of functionalizing layers.

## 3.3 Near-IR device design

We first establish a waveguide geometry for chalcogenide glass devices operating at telecom wavelengths (~1550 nm). We select silicon as our substrate of choice for all near-IR applications for the following reasons: (i) it is easy to obtain due to its widespread use in the electronics industry, (ii) CMOS compatibility (back-end), and (iii) it is relatively cheap, even for high quality wafers. To design devices for the near-IR, we use silicon wafers with

a layer of silicon dioxide to act as a buffer. Silicon has a much higher refractive index than our chalcogenide materials and if we fabricated the waveguides directly on top of silicon, input light from a fiber would prefer to travel through the silicon substrate rather than our waveguides. A thermally grown oxide layer of 3 µm helps prevent leakage of light to the substrate due to the higher index contrast between the chalcogenide glass the silicon dioxide ($n = 1.45$).

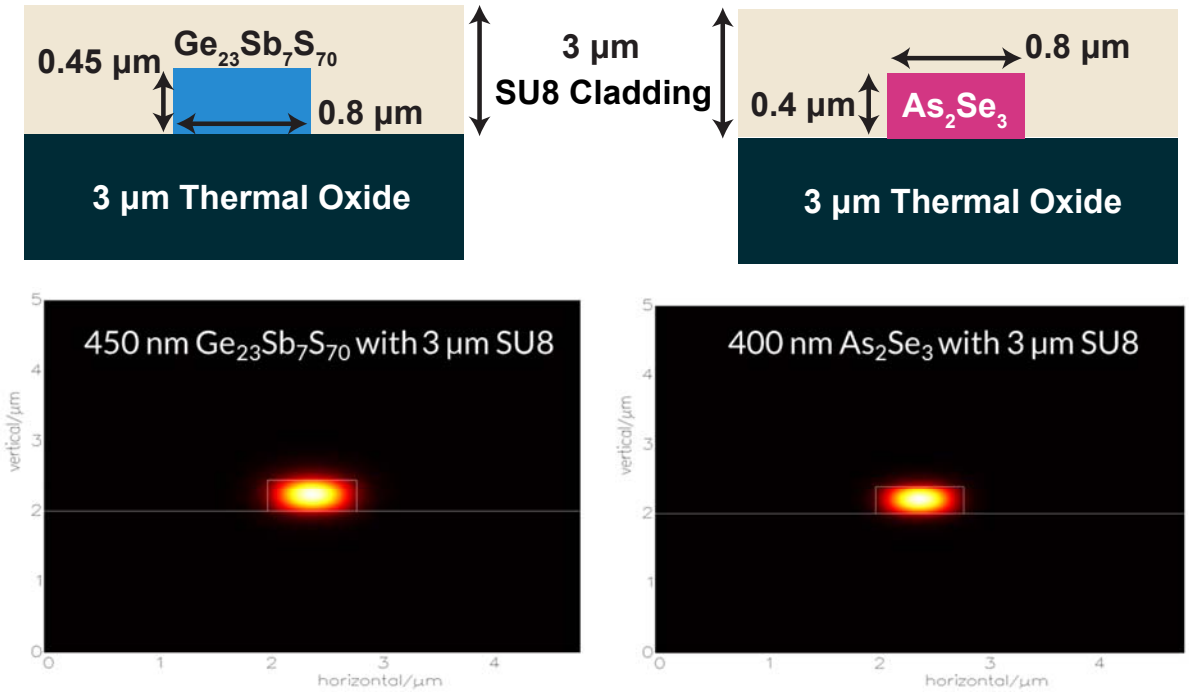


**Figure 3.6:** Schematic designs for near-IR devices and calculated fundamental TE modes for (Left) $Ge_{23}Sb_7S_{70}$ and (Right) $As_2Se_3$.

We design our waveguides for single-mode operation to prevent loss from higher order modes. Additionally, microdisk resonators are inherently multimoded even with a single input mode; adding multimode waveguides would lead to the possibility of more resonator modes being coupled, thus making it harder to isolate the resonant peaks of interest. However, as we will see in Chapter 6, multimode waveguides are still useful as the larger geometries allow easier coupling of light from a laser. Figure 3.6 shows mode profiles for two chalcogenide glass compositions. Typical thicknesses for our near-IR devices are

between 400-500 nm with the width fixed at 800 nm for single-mode operation, depending on the composition of chalcogenide glass that is used. Lower index materials require larger sizes to confine the mode better.

We use Photon Design's FIMMWAVE mode simulation tool for all our mode calculations during device design. The software allows us to define a cross-section similar to that presented in Figure 3.6 and then calculate a user-defined number of modes using a film mode matching (FMM) technique. We can obtain mode parameters such as the effective index, confinement factor, propagation constant, electric and magnetic field distributions, and loss through this mode simulation. More details on the simulation tool can be found in the Appendix.

The SU8 layer is spin-coated at the end to protect the fabricated devices from environmental effects and to add mechanical robustness. Further, the SU8 layer can be patterned if necessary using UV lithography since it is a negative photoresist material. For example, in sensing applications, we can open "windows" in the SU8 coating above resonators to ensure their exposure to analytes while still covering the rest of the sample. This would also allow the placement of a chamber on top of the devices with analyte delivery in liquid or vapor form through a closed loop that maintains saturation and reduces environmental interference.

## 3.4 Mid-IR device design

A variety of materials systems prove to be suitable for mid-IR devices, depending on the wavelengths in consideration. Silicon is an excellent candidate but it is only transparent until 7 µm and unless grown on sapphire, it is also limited by a lack of silicon dioxide transparency beyond 3.8 µm[58]. Although there have been successful demonstrations of mid- and far-IR transmission and sensing with III-V (GaAs/AlGaAs)[26] and silver halide

(AgBr/AgCl)[29] waveguides, they remain low-index contrast systems with high cost (III-V systems grown using MOCVD/MBE) or feature high sidewall roughness (silver halide) in single-mode designs. For near-IR applications, high-index contrast ChG waveguides (400–500 nm tall, 800 nm wide) fabricated on silicon with thermal $SiO_2$ and clad with SU-8 have already been demonstrated with low loss[14, 47].

For the mid-IR regime, two ChG-based device designs will be used: (i) $Ge_{23}Sb_7S_{70}$/$Ge_{28}Sb_{12}Se_{60}$ devices on silicon with 3 µm of thermal oxide and (ii) $As_2Se_3$ core devices with a thick undercladding of $Ge_{23}Sb_7S_{70}$ and a thin, protective overcladding of $Ge_{23}Sb_7S_{70}$ on silicon with 3 µm of thermal $SiO_2$. Although the first design is limited by absorption in $SiO_2$ beyond 3.8 µm, it is easier to fabricate as it only involves a single evaporation step and lithography on a standard silicon wafer. The second design introduces a ChG undercladding to prevent losses due to absorption in the $SiO_2$ and the higher refractive index of $As_2Se_3$ ($n = 2.75$) provides good index contrast with the $Ge_{23}Sb_7S_{70}$. The thin (100-200 nm) overcladding is added to protect the $As_2Se_3$ core from exposure to oxygen. Although this design presents some fabrication challenges due to multiple depositions and lithography on a ChG layer, an $As_2Se_3$ core/$Ge_{23}Sb_7S_{70}$ undercladding is our proposed design for longer wavelengths where silicon dioxide and even sapphire exhibit strong absorption[123, 124]. We can extend its range of operation by adjusting the dimensions of the ChG layers appropriately for longer wavelengths. For wavelengths up until 3.8 µm, the $Ge_{23}Sb_7S_{70}$/$Ge_{28}Sb_{12}Se_{60}$ on oxide design should prove to be a viable option.

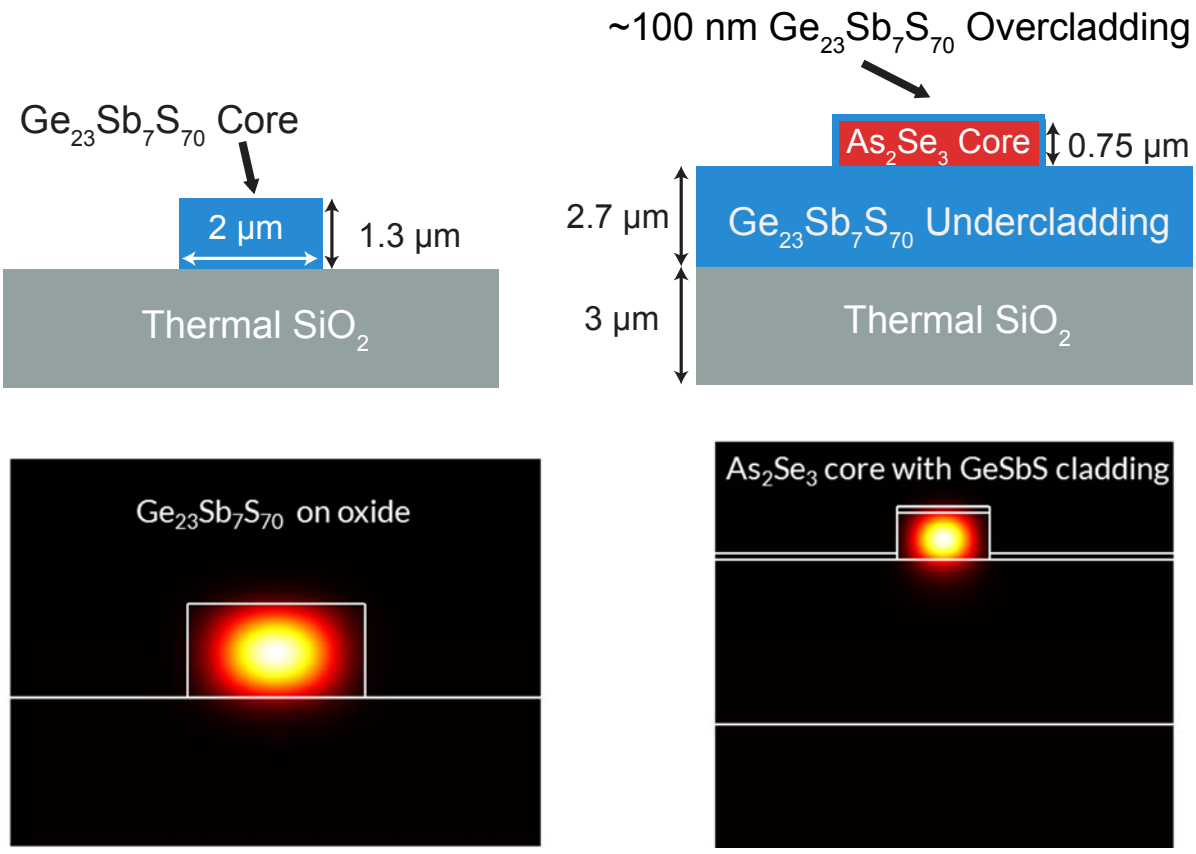


**Figure 3.7:** Schematic of mid-infrared waveguide designs and fundamental TE propagation mode profiles suitable for single mode operation at $\lambda = 3.2$ μm.

To design single-mode structures for mid-infrared operation, we carried out waveguide mode simulations that would determine the minimum waveguide width at which mid-IR radiation of a desired wavelength would exhibit a cut-off for the second order mode. The purpose of single mode operation of the waveguide is to ensure that results from sensing measurements are not affected by power coupling into higher order modes. The undercladding is $Ge_{23}Sb_7S_{70}$ for two reasons: first, since silicon dioxide has high absorption beyond 3.8 μm in the mid-infrared, a thick cladding of mid-IR transparent material is necessary; second, it helps minimize mode leakage into the silicon substrate. We also use a thin overcladding of GeSbS to simulate a real device where this layer prevents exposure of the $As_2Se_3$ waveguide to the environment. Arsenic-based devices tend to form $AsO_x$ crystallites when they interact with oxygen in the air[46].

In Figure 3.8, we can see the refractive index plotted as a function of waveguide width for the first two TE and TM polarizations. Based on the constant $n = 2.15$ line (approximate index for $Ge_{23}Sb_7S_{70}$), both the 2nd order modes are cut-off only for the 2 µm waveguide. At this width, the fundamental TE and TM modes are the only ones that can be supported by the waveguide, and hence, we select this width as ideal for single-mode mid-IR devices. Wider waveguides are also employed, as they are easier to align to and can provide useful information on the quality of the fabricated devices. Using the 2 µm wide waveguide, we estimate the size of the first order TE mode to be approximately 1.65 µm in height and 2 µm in width.

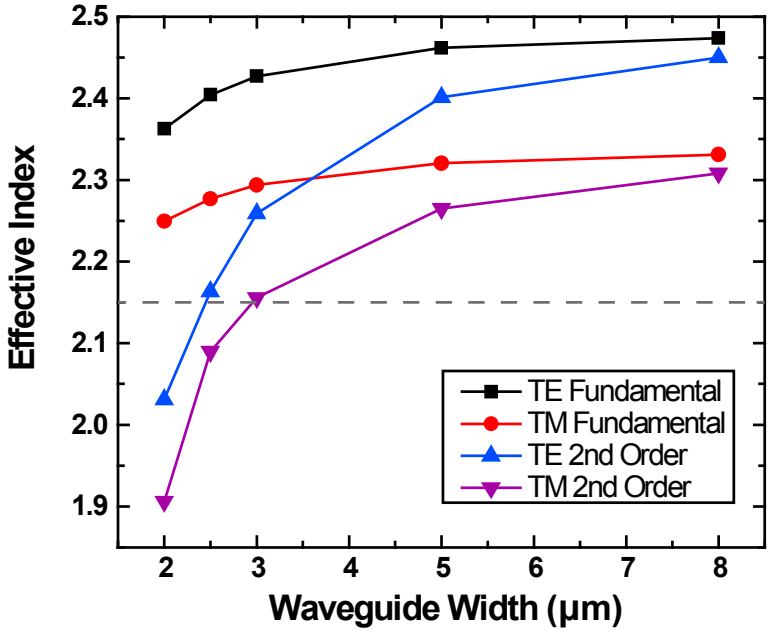


**Figure 3.8:** Graph showing the second order modes cutting off when the width is 2 µm.

## 3.5 Microresonators as a platform for studying materials behavior

Due to their sensitivity to refractive index and absorption changes, microresonators prove to be a versatile platform for studying various materials phenomena such as the effects of modifying the properties of chalcogenide glass after device fabrication. For example, we can

exploit the photosensitivity of chalcogenide glasses to alter photonic device performance post-fabrication in a process called "phototrimming." By coating resonators with a photosensitive glass such as $As_2S_3$, we gain the ability to tune the response of fabricated devices to better match theory and design expectations, thus bypassing geometric non-uniformities associated with fabrication tolerances. Exposure to above-bandgap radiation will change the index of the $As_2S_3$ layer, which in turn alters the effective index of the light propagating through the devices underneath. In the case of resonators, this shifts the position of the resonant peak to higher wavelengths controlled by the duration of exposure.

Further, we have complemented the materials study of radiation effects on chalcogenide glasses with transmission measurements performed on irradiate resonators. We have used chalcogenide glass resonators exposed to alpha radiation and silicon resonators exposed to gamma radiation to demonstrate radiation-induced changes even at low exposure doses. Chapter 5 goes into further detail on both of these applications.

## 3.6 Summary

In this chapter, we have discussed the background and theory on waveguides and microresonators that will be relevant to understanding the results presented in later chapters. Resonators are versatile devices that have found application in many areas, including sensing. In the next chapter, we develop fabrication schemes for the waveguide and resonator structures described in this chapter.

# Chapter 4: Fabrication of Waveguides and Resonators

An important part of this thesis work is the development and optimization of thin-film and device fabrication processes for chalcogenide glasses as well as for lead telluride. In this chapter, we discuss the various approaches utilized to fabricate the device structures described in Chapters 3. The process work described here was performed at the Microsystems Technology Laboratory (MTL) and Kimerling group labs at MIT as well as the Harvard Center for Nanoscale Systems.

## 4.1 Photolithography

Photolithography is the process of creating a pattern on a substrate coated with a light-sensitive polymer, called a photoresist, through a patterned photomask. In general, the photomask is a square slab of quartz that contains the desired pattern etched into chrome. When ultraviolet (UV) light of a specific wavelength is incident upon the polymer, it induces a chemical reaction in the photoresist in regions not covered by the chrome pattern. Photoresists can have a negative tone or a positive tone. For negative photoresists, regions exposed to light cross-link and become insoluble in developer solution. Conversely, UV light breaks crosslinks in positive tone resists, enhancing dissolution in developer. The photomask pattern is generated using computer aided design (CAD) software and then sent to specialized manufacturers who transfer the pattern to a photomask.

Two types of photolithography processes are typically used in microfabrication: projection lithography and contact lithography. UV light is usually generated by a mercury arc lamp although the output power may differ. The center wavelength is used to define

the type of UV light: i-line (365 nm), h-line (405 nm), and g-line (435 nm). Smaller wavelengths enable definition of finer features on the wafer and commercial fabrication facilities have turned to excimer lasers to produce smaller wavelength UV radiation[125]. Tools employing both types of lithography have been used in this thesis work using MTL's cleanroom facilities.

### 4.1.1 Projection lithography

In projection lithography, the pattern is written at a magnified size on the photomask (e.g., 4X, 5X, 10X) and then focused down to the desired size through UV optics. This approach allows the use of a high-throughput, automated stepper tools that can expose the same region of the photomask multiple times across a wafer, essentially creating many copies (called dies) of the same design. As the pattern needs to be reduced to the right size, the wafer and photomask never come into physical contact, which increases the usable life span of the photomask. The software can control the exact position of the dies as well as the exposure dose (provided in milliseconds) and the focus position.

At MTL, a Nikon NSR2005i9 projection lithography tool (i-line wafer stepper) is available and can be programmed to process up to 25 6" wafers. A single 6" wafer in this case yields more than a dozen samples with identical features. The tool can expose a maximum area of 22 mm x 22 mm on the photomask (6" x 6") with a 5X reduction on the wafer. The resolution of a projection lithography system is proportional to the wavelength of light and inversely proportional to the numerical aperture of the lens used. The theoretical minimum feature size possible with the Nikon tool is approximately 500 nm, making it ideal for fabrication of near-IR ChG devices.

### 4.1.2 Contact lithography

In contact lithography, the entire photomask area is exposed and hence cannot be stepped across a wafer sample. The pattern on the photomask is written at exactly the same size

as required on the wafer. The process derives its name from the photomask being in physical contact with the wafer during exposure. The UV exposure dose is once again controlled by time.

We used the Karl Suss MA-4 contact aligner in MTL for our contact lithography work. This tool can handle wafers up to 4" in diameter and has a minimum feature size of about 2 µm. Since our mid-IR devices are larger than our near-IR devices to accommodate the longer wavelengths, the contact aligner is appropriate for such devices. Further, when we fabricate devices that need an undercladding of ChG prior to lithography, this is our only available option due to CMOS-compatibility concerns in the area of MTL housing the stepper. Unlike the stepper, this tool offers some flexibility in the size of the chrome photomask accommodating 2", 4", and 5" sizes in addition to transparency masks.

## 4.2 Thin film deposition

We described our thermal evaporation process for chalcogenide glasses in Chapter 2. For lead telluride, we used thermal evaporation in the same deposition system using a secondary evaporation source. To avoid mixing PbTe with ChG materials, we used separate boats, quartz crystal monitors and deposition controllers for PbTe but the deposition process was otherwise identical. The PbTe raw material was sourced from Alfa Aesar (99.999% purity) in the form of small pieces. Since PbTe has a much higher melting point[126] of 1197K than our ChG materials, it required higher input powers for evaporation to begin and the deposition rates were also typically lower at ~5-7 Å/s (compared with up to 20 Å/s for ChG materials).

## 4.3 Lift-off process for ChG device fabrication

Chalcogenide glass waveguides and resonators presented in this thesis are fabricated using a negative resist lift-off photolithography technique. The process starts with spin-coating NR9-1000PY (Futurrex, Inc.) negative lift-off photoresist on a silicon wafer with 3 µm of thermally grown silicon dioxide. The thickness of the resist is controlled by the spin speed with higher speeds yielding thinner resists. This resist is chosen as it can be coated up to 2 µm thick with a single spin cycle and produces angled sidewalls (undercut) which prevent coating of the sidewalls, making lift-off easier. The resist is baked on a hotplate at 150°C for about 1 minute. and allowed to cool and before exposure to ultraviolet light (365 nm) through a chrome-on-glass photomask. A post-exposure bake (PEB) is carried out at 100°C for about 1 minute. Finally, the wafer is immersed in a developer solution (RD6, also by Futurrex, Inc.) containing tetramethyl ammonium hydroxide (TMAH) for a few seconds before being rinsed with deionized water and dried. The exposure dose and developer time control the eventual resolution achieved for a given sample as well as the degree of undercut in the resist.

Following lithography, the wafer sample is loaded into the thermal evaporator along with crushed raw material (placed in a tantalum boat) and the chamber is pumped to high vacuum before deposition. Once the film has been deposited, the wafer is removed from the chamber to perform resist lift-off. The NR9 series of resists lift-off easily when immersed in acetone. An ultrasonic bath can prove useful as the resist can be removed faster and more thoroughly but even gentle agitation for 30-60 seconds is sufficient to remove the resist in most cases. Once all the excess resist has been lifted-off, the wafer is placed in an isopropanol bath as a cleaning step before drying with nitrogen. A cross-section scanning electron microscopy (SEM) image of the patterned photoresist is shown in Figure 4.1 with a clear

undercut profile. Figure 4.2 summarizes the lift-off procedure descrived for chalcogenide device fabrication.

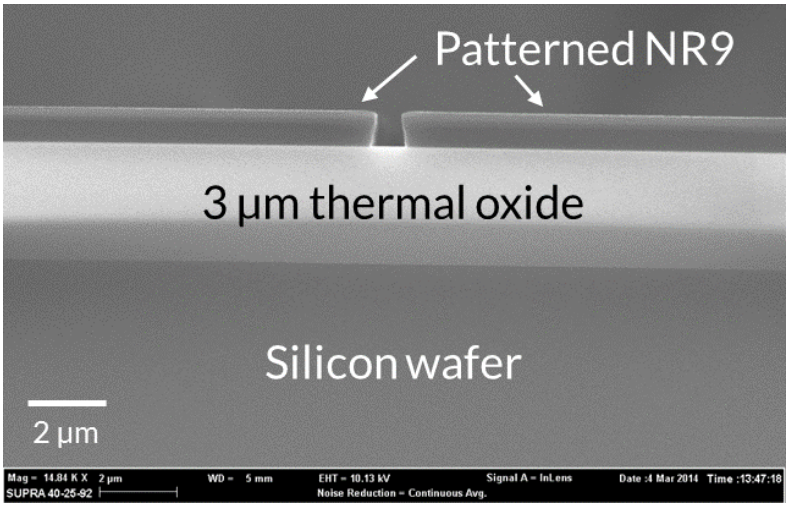


**Figure 4.1:** Cross-section SEM image of patterned NR9-1000PY photoresist demonstrating the undercut profile.

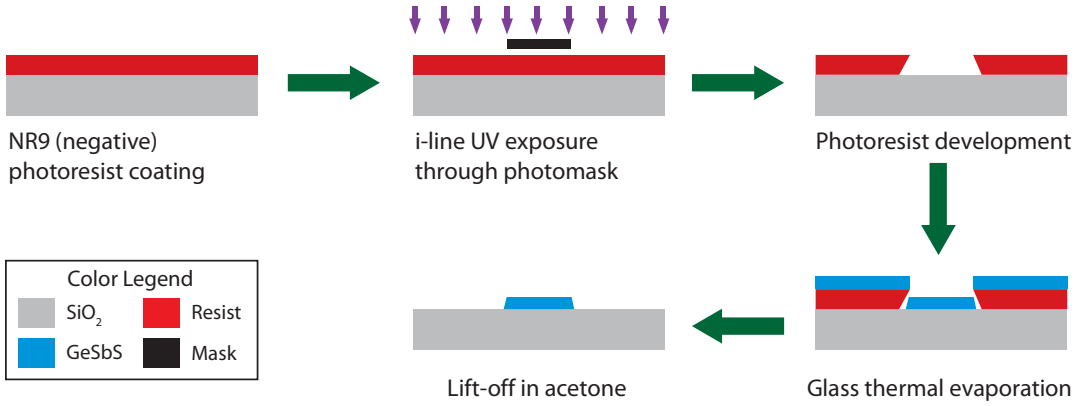


**Figure 4.2:** Lift-off process for ChG device fabrication. Resist exposure and development produces the inverse of the image on the photomask but following evaporation and lift-off, the chrome pattern is reproduced with the glass.

For mid-IR devices, the same lift-off process is used with a few modifications. First, the spin coating speed is reduced to get thicker photoresist (~1.9 µm vs. ~1 µm) as the deposited ChG films are also thicker. To fabricate the $As_2Se_3$ core waveguide devices, two extra deposition steps are required. Prior to lithography, a thick layer of $Ge_{23}Sb_7S_{70}$ is evaporated to serve as the undercladding. This is also necessitates a modification of the

resist exposure dose and baking temperatures as silicon dioxide has a different refractive index and thermal conductivity compared to $Ge_{23}Sb_7S_{70}$. During lift-off for $As_2Se_3$ core on $Ge_{23}Sb_7S_{70}$ devices, we avoid ultrasonication as we have found adhesion between the two ChG to be relatively weak. This typically leads to delamination of the $As_2Se_3$ features; hence, we only use gentle agitation of the acetone. Finally, after the WG core deposition and lift-off, a thin layer of $Ge_{23}Sb_7S_{70}$ is evaporated as the top cladding to protect the core from environmental exposure. This process is schematically illustrated in Figure 4.3 below.

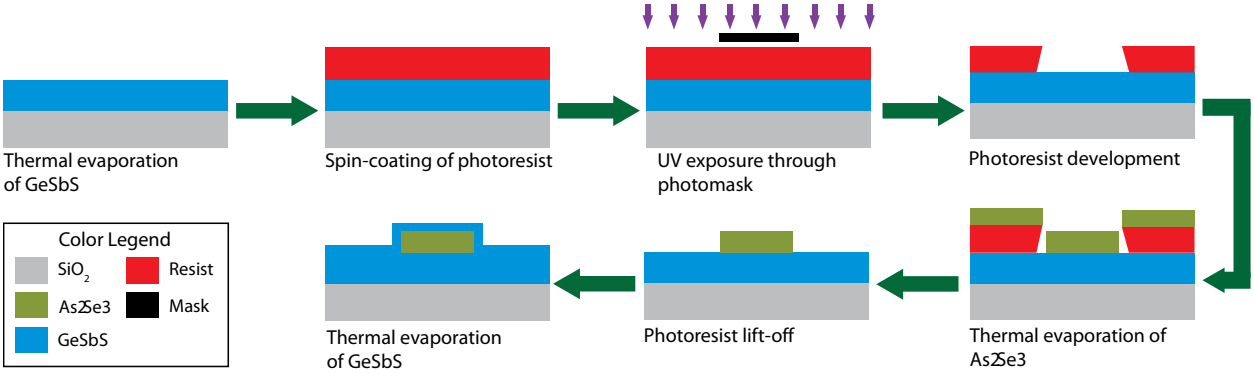


**Figure 4.3:** Modified process flow for the fabrication of $As_2Se_3$ core waveguides and resonators. These devices require two additional evaporation steps to deposit the GeSbS undercladding and overcladding.

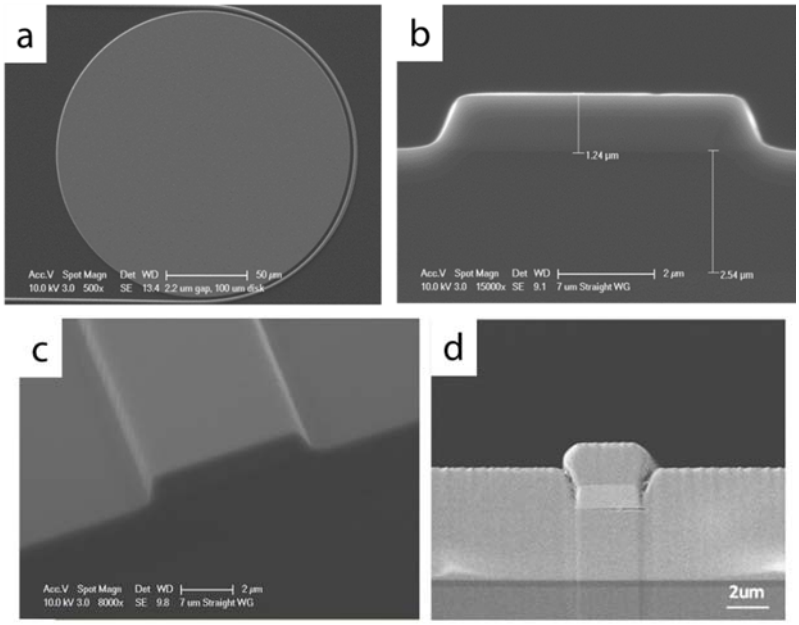


**Figure 4.4:** Scanning Electron Microscopy (SEM) images showing various fabricated ChG devices. (a) GeSbS microdisk resonator; (b), (c) GeSbS waveguides; (d) $As_2Se_3$ waveguide with GeSbS cladding for 5.2 µm operation[57, 127].

## 4.4 Process development for thick ChG waveguides

Although the waveguide designs present thus far use 1.3 µm or lower waveguide core thickness for our near- and mid-IR devices, we also explored fabrication process options for much thicker waveguides (up to ~4 µm) to better accommodate input light from a large fiber or a laser facet. This large waveguide thickness necessitates a much thicker lift-off resist film, in turn requiring a process modification. To obtain thicker waveguides we developed a new process using NR9-6000PY (Futurrex, Inc.) resist that is capable of producing film thicknesses of up to 12 µm. Our standard process has been optimized to include a spin-on step of about 7 µm of resist followed by the evaporation of 4 µm of GeSbS into the trenches produced after lithography to form our thick waveguides. Due to the larger amount of glass material required for the thicker film, we had to incorporate a new evaporation boat that is deeper than our standard boats, to prevent any adverse effects (such as spitting) that may be induced due to overflowing material. Figure 4.6 shows

fabricated thick waveguides after lift-off. The deeper boat design also improved our deposition process for the GeSbS undercladding for mid-IR devices. Initially, we used a two-step deposition process to reach the ~2.6 µm thickness necessary but the newer boats reduced that to a single step, thus reducing fabrication time and costs.

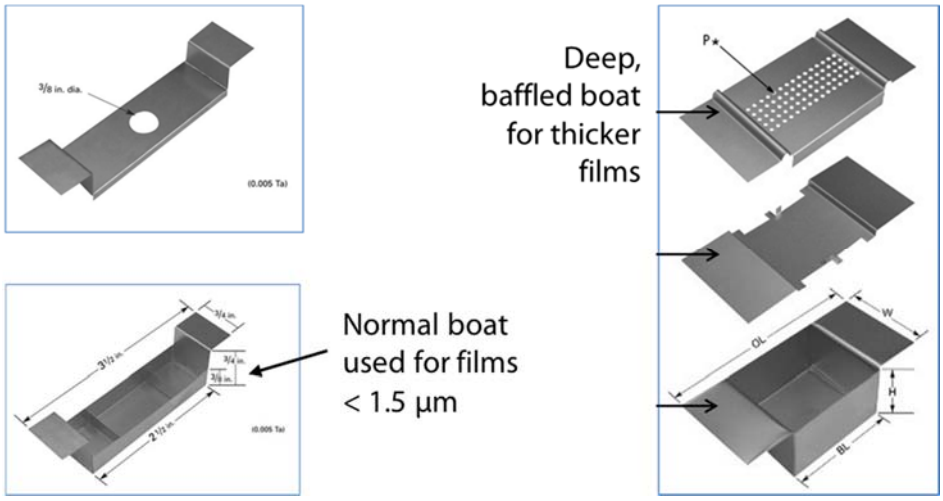


**Figure 4.5:** Comparison of tantalum boat designs for thinner films (Left) and thicker films (Right). The deep boat can hold more material and the baffle piece prevents the melt from flowing out.

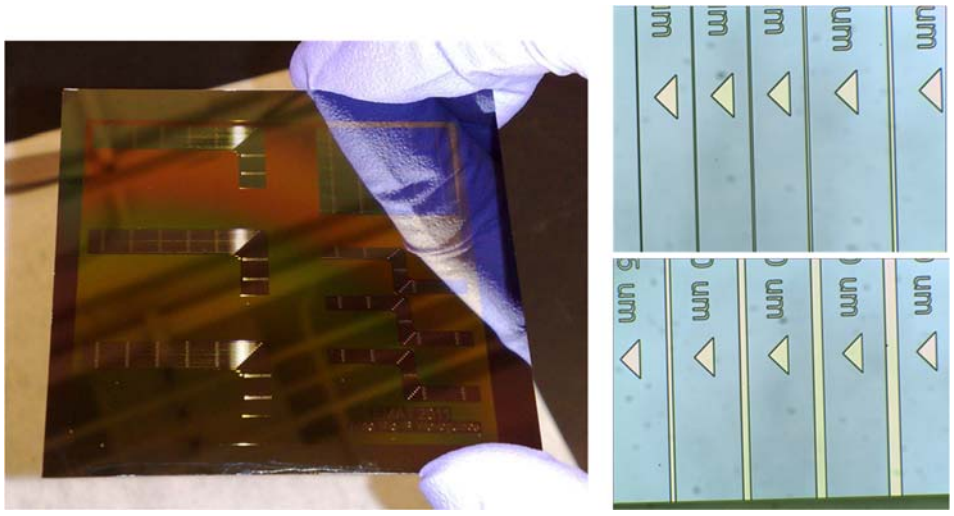

**Figure 4.6:** (Left) Image of thick waveguide chip after fabrication was complete; (right) optical micrographs showing some of the fabricated devices.

## 4.5 Other fabrication approaches

Thus far, we have presented fabrication techniques that involve photolithography and lift-off fabrication of our microphotonic devices. These approaches comprised the bulk of the work performed in this thesis work but newer techniques were also developed through collaborative work. These methods can be utilized in the future for device designs that may be limited by current methods (e.g., due to resolution constraints).

### 4.5.1 Electron beam lithography

Electron beam (e-beam) lithography, as the name implies, relies on writing device patterns in resist with a beam of electrons. This process provides two significant benefits over photolithography: (i) smaller features are possible due to the narrow width of the electron beam writing the pattern and (ii) greater freedom to evaluate new device designs as it only requires patterns created by CAD and no photomasks. However, e-beam lithography is a slower process as the exposure window is much smaller (~600 µm x 600 µm) and can only write on one sample at a time, losing the parallelism afforded by UV lithography.

We have developed fabrication processes using e-beam lithography for both lift-off and reactive-ion etching (next section). Poly(methyl methacrylate) or PMMA is a commonly used positive tone resist for e-beam lithography. The process flow is very similar to that for lift-off photolithography with the UV exposure step replaced by electron beam exposure (dose: 2200 µC/cm$^2$). We have fabricated ChG devices (see Figure 4.7) as well as PbTe structures using e-beam-patterned PMMA followed by lift-off in acetone to demonstrate viability of this process for future device work. The SEM images show that the waveguide cross-section is not uniform; this can occur due to a shadowing effect from the thick PMMA resist. To solve this asymmetry, we can either reduce the thickness of the PMMA layer or spin the substrate during deposition.

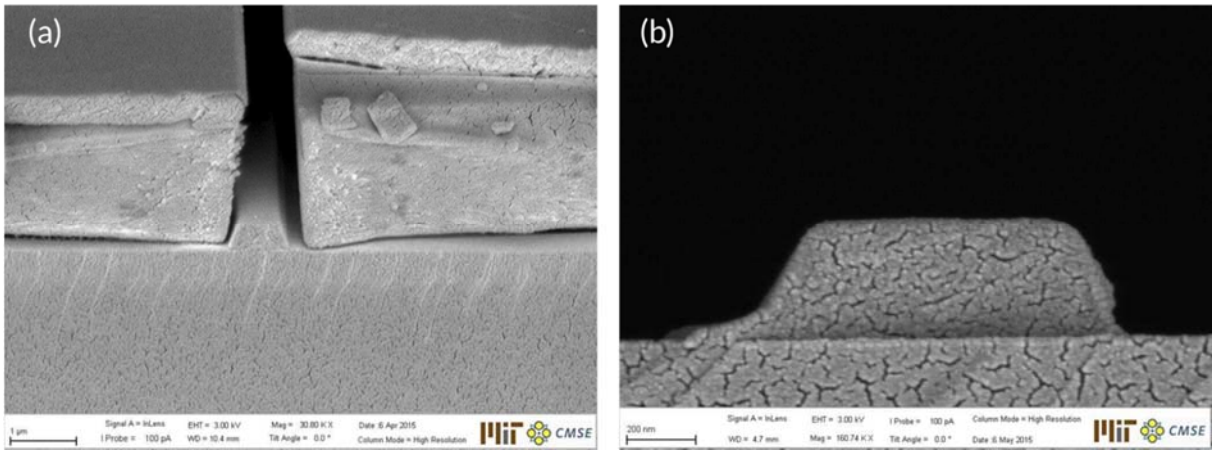


**Figure 4.7:** (a) ChG waveguide with PMMA pattern before lift-off; (b) Final waveguide after PMMA lift-off. The waveguide cross-section exhibits asymmetry due to shadowing from one photoresist sidewall during evaporation. This can be reduced by using a thinner resist layer or by rotating the substrate during deposition.

### 4.5.2 Reactive-ion Etching of ChG materials

Although this thesis work heavily favors lift-off processing for the simpler fabrication process, reactive-ion etching (RIE) can also be employed with the appropriate etching recipe to create structures using positive photoresists such as the Megaposit SPR700 series that are more commonly used in cleanrooms, particularly at MTL. However, this does require that the ChG film be deposited before lithography, which presents two challenges: (i) Certain cleanroom areas do not allow bringing in ChG films for processing (e.g., the stepper in MTL) and (ii) solvents such as tetramethyl ammonium hydroxide (TMAH) attack ChG materials if exposed for long so re-patterning the same wafer will retain an etched profile of the previous patterning. As a result, some of the flexibility gained by being able to use positive resists is lost. Work has shown that a mixture of $CF_4$ and $CHF_3$ gases or $Cl_2$ gas by itself can be used to effectively etch $Ge_{23}Sb_7S_{70}$ films patterned with SPR700 photoresist and ZEP e-beam resist.

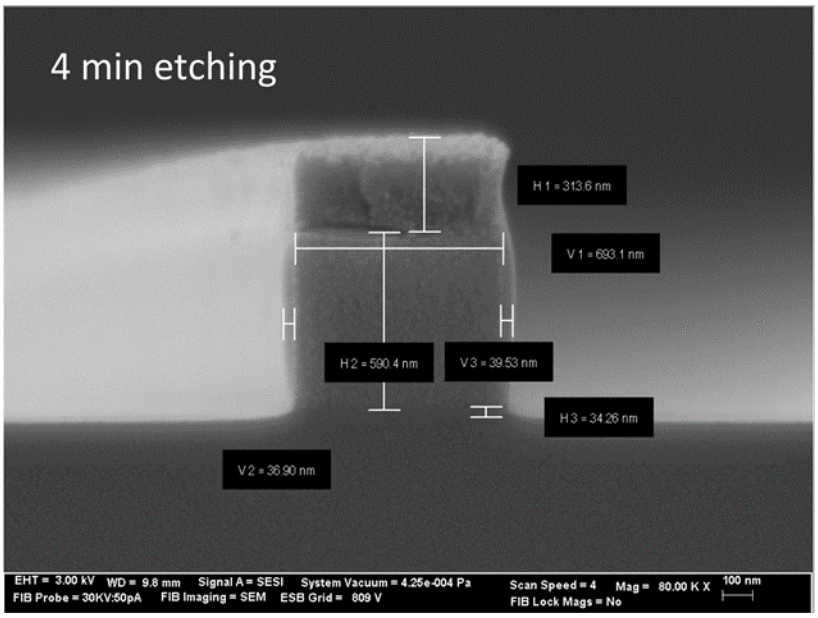


**Figure 4.8:** Cross-sectional SEM image showing an example of successful etching of a near-IR GeSbS waveguide achieved with a $CHF_3/CF_4$ plasma and an etching time of 4 minutes. Sidewalls appear to be smooth, which should lead to lower scattering losses.

## 4.6 Summary

In this chapter, we have established photolithography-based process flows that enable fabrication of chalcogenide glass and PbTe structures of various sizes to accommodate near- and mid-IR wavelength ranges. We have developed recipes for projection and contact lithography tools using negative lift-off photoresists (NR9 series) and a fabrication plan for our monolithically integrated detectors. Process development is an important part of this thesis work as it helps us translate the device structures designed by simulations into actual devices that we can test on our laser systems. The next chapter goes over the characterization of waveguides and resonators at telecom wavelengths.

# Chapter 5: Near-Infrared Device Characterization

In this chapter, we describe the characterization of waveguides and resonators fabricated for near-IR applications. Chalcogenide glass resonators are used to separate the contribution of various loss mechanisms in these materials and for sensing experiments with polymer coatings on them. Then we discuss the use of photosensitive $As_2S_3$ glass as a coating for building tunable photonic devices. Lastly, we use resonators as a test platform for studying the effects of radiation on silicon and chalcogenide materials systems.

## 5.1 Near-IR measurement setup and procedures

Our near-IR device measurement setup consists of a LUNA Optical Vector Analyzer (OVA) with a built-in tunable laser covering the C and L bands (1525 – 1610 nm) and a detector. Light from the OVA is coupled to a single-mode SMF-28 silica fiber with FC/PC connectors and then on to a tapered lens-tip fiber (Nanonics Imaging Ltd.) that assists in coupling to the on-chip devices due to a smaller mode size focused a few microns in front of the fiber tip. Light coming out of the devices is coupled to another lens-tip fiber that is connected to the detector input of the OVA with another SMF-28 fiber. Both lens-tip fibers are placed on software-controlled precision motion stages capable of movements as small as 50 nm in the ±X, ±Y, and ±Z directions. An optical fiber switch allows us to switch the output between a Newport power meter for fiber alignment and the OVA for measurement.

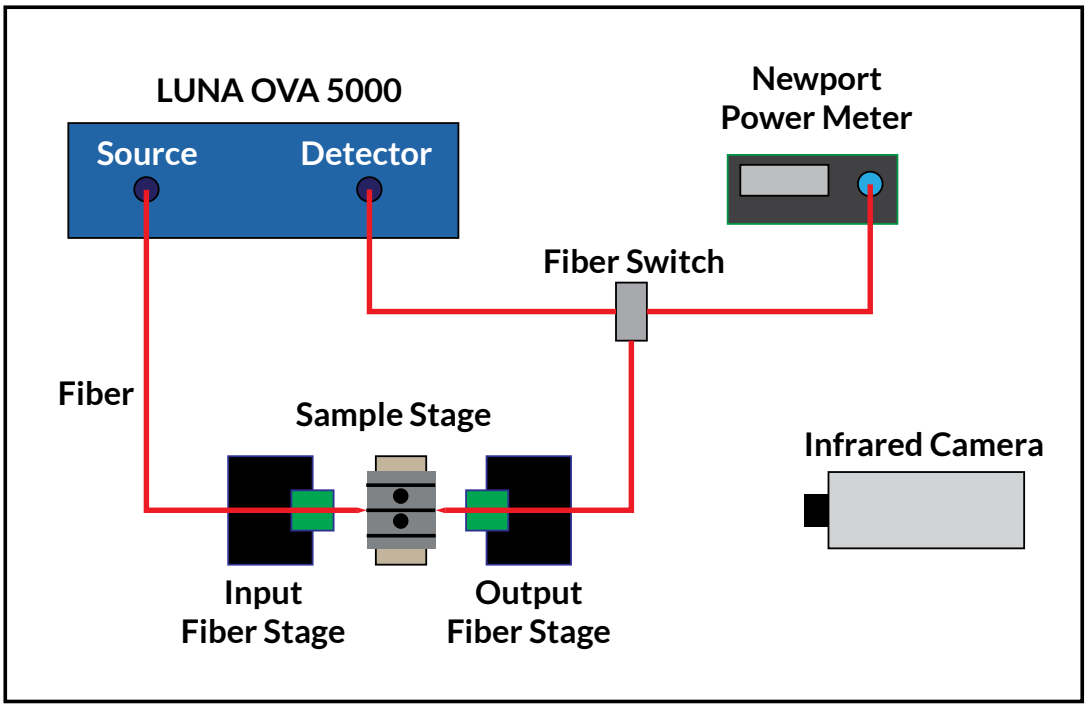


**Figure 5.1:** A schematic illustration of the near-IR LUNA OVA measurement setup showing the lens-tip fiber input coupled to a stationary sample and the output coupled to a power meter and the OVA through a fiber switch. An infrared camera is used during input fiber alignment to find the waveguide mode.

Optical fiber alignment to the sample is accomplished by first coupling the input fiber to the input facet of the device under measurement. An infrared camera images the output light and fiber alignment to a waveguide mode is indicated by a small, bright spot on the camera. The brightness of the waveguide mode image depends on the quality of the alignment as well as the loss in the device under test. Once the input fiber is coupled, the output fiber is then aligned using the Newport power meter, which measures the absolute power coupled in to the output fiber in µW. Optimal manual alignment is achieved when the power output is maximized. At this point, an automatic alignment program is executed which refines alignment further by moving the stages in small steps and recording the positions where power output is highest. After automatic alignment, the optical switch is moved to the OVA position and a wavelength scan is recorded with the tunable laser.

The OVA software measures the Jones Matrix of the device under test and calculates various parameters such as insertion loss, group delay, chromatic dispersion, and polarization-dependent loss simultaneously. The Jones Matrix is a method of representing the polarization state of light with a 2x2 matrix[128]. The Jones Matrix for a two-input, two-output optical system can be represented as:

$$\boldsymbol{J}(\omega) = \begin{bmatrix} a(\omega) & b(\omega) \\ c(\omega) & d(\omega) \end{bmatrix} \tag{6}$$

where the quantities $a$, $b$, $c$, and $d$ are four scalar transfer functions and $\boldsymbol{\omega}$ is the frequency. As light passes through the device, the matrix describes the evolution of the polarization of light and the output electric field is related to the input field by the following equation:

$$\tilde{\boldsymbol{E}}_{out}(\omega) = \boldsymbol{J}(\omega)\tilde{\boldsymbol{E}}_{in}(\omega) \tag{7}$$

When an optical element is placed in the path of a source-to-detector system, it introduces a frequency-dependent insertion loss, which can be calculated from the Jones Matrix parameters:

$$Insertion\ Loss = 10log\left(\frac{|a|^2 + |b|^2 + |c|^2 + |d|^2}{2}\right) \tag{8}$$

The LUNA instrument is also able to determine the minimum and maximum transmission states for the device being tested from the eigenvalues of the matrix $\mathbf{J}^{\dagger}\mathbf{J}$. The difference between the two states represents the polarization-dependent loss for the device under test.

From the spectrum measured by the software, we are able to measure propagation losses in our devices and obtain resonant peak locations and widths for resonators. For refractive index sensing applications, the OVA software also records shifts in resonant peak positions after exposure to chemical analytes. Cavity $Q$-factors for resonators can be

calculated by fitting a Lorentizian curve to the measured resonant peaks and dividing the resonant wavelength by the full width at half maximum (FWHM).

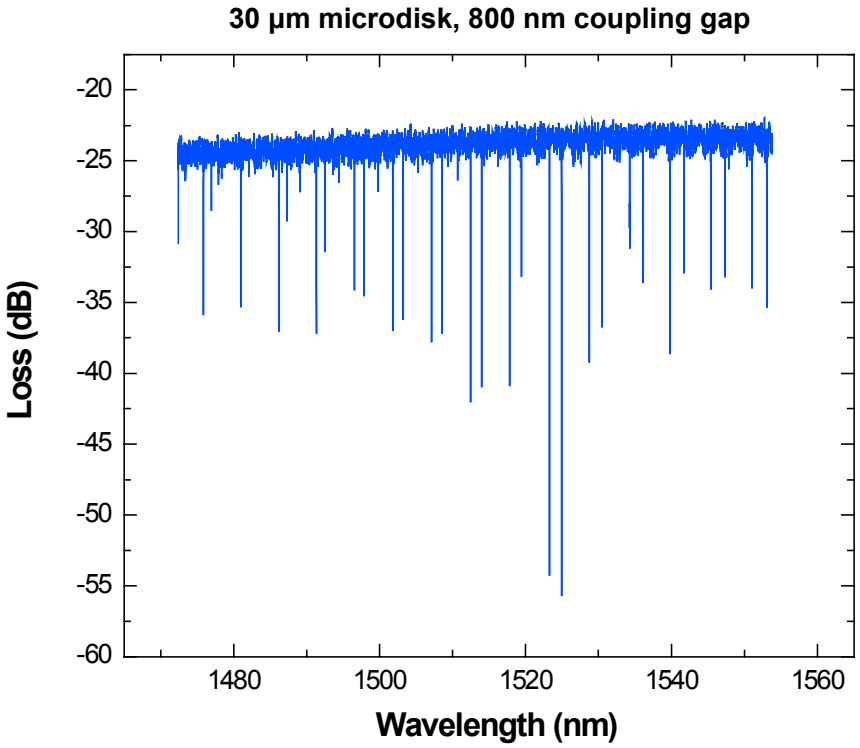


**Figure 5.2:** A sample transmission spectrum measured with the LUNA from a 30 μm radius GeSbS resonator with a waveguide coupling gap of 800 nm.

## 5.2 Separating loss mechanisms in chalcogenide glass resonators

In Chapter 2, we discussed sources of potential material attenuation in chalcogenide glasses and methods to minimize their contribution to the overall loss of microphotonic devices. One further loss mechanism arises in fabricated devices due to roughness on sidewalls imparted by roughness in the chrome pattern on the photomasks used for UV lithography[14].

Scattering loss arising from roughness on device surfaces is particularly severe in high-index contrast (HIC) devices, since the scattering loss scales with refractive index difference[129]. Due to the additive nature of our deposition processes, our devices exhibit low RMS roughness on their top surfaces. However, Atomic Force Microscopy (AFM)

measurements confirm the presence of significant roughness on the sidewalls (RMS amplitude ~10 nm), implying that the main scattering loss contribution comes from sidewall roughness. Roughness present in the chrome pattern on the photomask is transferred to the devices during fabrication making sidewall roughness difficult to avoid. However, it is possible to reduce the sidewall roughness after fabrication by a thermal reflow process[48] as shown in Figure 5.3. By heating the samples for a short time at $T > T_g$, the action of surface tension can cause viscous flow of material from the top of the waveguide toward the substrate. Although this reduces sidewall roughness, the waveguide geometry is altered. However, this alteration can be compensated by appropriate modifications to initial device geometry. Crystallization may also be a concern with the reflow process, particularly due to the large surface-area-to-volume ratio of microphotonic devices, but can be circumvented if the reflow timescale is short enough[48]. The thermal reflow technique for sidewall roughness smoothing is highly advantageous for ChGs due to (i) their lower $T_g$ (~500-600K) values compared to silica (~1600K) and (ii) the ability to choose different ChG compositions with different $T_g$ values.

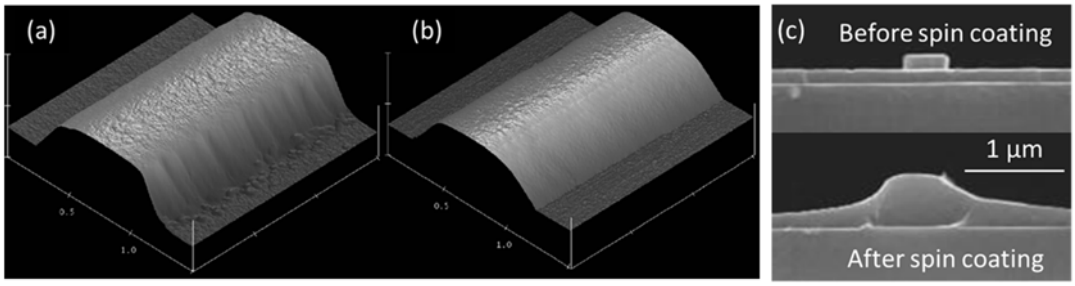


**Figure 5.3:** (a) As-fabricated $As_2S_3$ waveguide; (b) Waveguide after thermal reflow for 15 seconds[48]; (c) Cross-sectional SEM images showing the effect of spin coating a GeSbS film on top of an evaporated GeSbS waveguide[40].

For ChG systems less suitable to thermal reflow due to surface crystallization[130], spin-coating an overcladding of the same composition provides an alternative approach to reduce sidewall roughness. ChGs are soluble in organic solvents[30, 40, 102] and thus amenable to solution processing. Coating ChG waveguides with a solution-derived film of the same

composition exhibits a reduction of sidewall roughness (from 19±1 nm to 1.4±0.1 nm) and a corresponding decrease in propagation loss[40]. This process also leads to a change in geometry (Figure 5.3c) and has to be accommodated by changing the initial device dimensions.

### 5.2.1 Experiment design

Experimentally measured waveguide loss values represent the sum of the various sources of material attenuation and roughness scattering loss, and thus identification of their individual contributions requires special techniques[131-134]. One approach is to compare measured losses in HIC strip waveguides and ridge waveguides as the latter are less sensitive to sidewall roughness (mode is in the center)[133]. Very low loss values (~0.5 dB/cm) have been measured in larger Ge-Sb-S ridge waveguides while smaller strip waveguides exhibit losses almost one order of magnitude higher[14].

Quantitative information about the contributions of the different loss mechanisms can also be gleaned from microdisk resonators. Prior work with silicon microdisks has shown that while scattering loss depends on the radius of the microdisk, material loss is essentially independent of the radius[122] due to the electric field distribution in microdisk resonators of different sizes. As the radius increases, a smaller fraction of the resonator mode is confined at the sidewall (see Appendix), decreasing total loss, providing a way to decouple material and scattering loss contributions. $Ge_{23}Sb_7S_{70}$ resonator devices coated with SU8-2002 (for environmental protection) were fabricated and tested for this purpose. The material loss includes contributions from the glass (impurity absorption, electronic defects) and the SU8 overcladding. The breakdown of the various loss contributions is shown in the following equations:

$$\alpha_{total} \approx \alpha_{material} + \alpha_{scattering} \tag{9}$$

$$\alpha_{material} \approx \alpha_{glass} + \alpha_{cladding} \tag{10}$$

$$\alpha_{glass} \approx \alpha_{impurity} + \alpha_{electronic\ defects} \tag{11}$$

### 5.2.2 Separating material attenuation from scattering loss

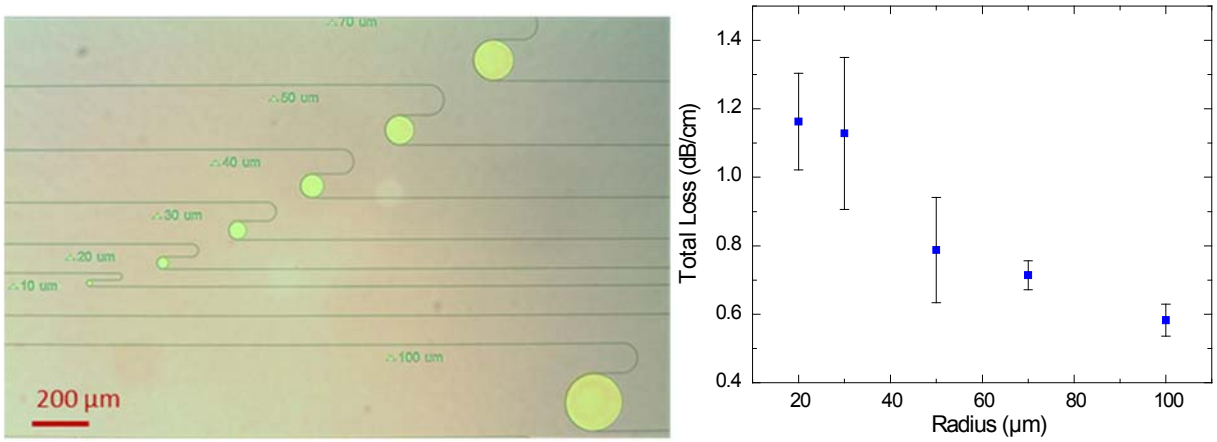


**Figure 5.4:** (a) Array of fabricated near-IR microdisk resonators of different radii; (b) Plot showing lower loss for larger microdisks due to a reduction in sidewall scattering as the whispering gallery mode is pulled inward. If scattering losses could be reduced to 0.1 dB/cm or lower, then material absorption would play a much larger role, as is the case for chalcogenide glass optical fibers.

To estimate the contributions from material absorption and scattering, we first start by measuring total propagation loss in our resonator devices. We measured the total loss in resonators with radii between 20 µm to 100 µm using the LUNA OVA setup. An optical image of the fabricated resonators and the measured loss is shown in Figure 5.4. We observe a trend of decreasing loss as the disk radius is increased; the 100 µm disk exhibits net loss that is nearly half the value for the 20 µm disk. Further, we can estimate the loss contribution from the SU8 cladding by first calculating the mode confinement factor in the SU8. Literature shows that propagation loss in SU8 is typically on the order of 2 dB/cm[135] and roughly 12% of the mode is in the SU8, hence it would contribute a maximum of ~0.24 dB/cm to total loss. We can also simulate the approximate fraction of the mode present at

the resonator sidewall (see Appendix) and use the measured loss values to estimate the material loss as ~0.39 dB/cm. Removing the SU8 contribution then leads us to the contribution from the glass itself as being ~0.15 dB/cm. Based on an absorbance value of about 9.6 $cm^{-1}$ of the O-H bond at the 1550 nm wavelength[136], we can estimate the impurity loss to be about 0.011 dB/cm, indicating that material losses are dominated by other mechanisms such as electronic defects that have yet to be investigated in detail. We can also confirm that sidewall roughness is the main source of optical loss in our HIC devices[137, 138].

## 5.3 Sensing experiments with polymer-functionalized resonators

### 5.3.1 Sensor functionalization using polymer coatings

A resonator can be extremely sensitive to refractive index variations of its surroundings brought about by the presence of very small quantities (ppb) of an analyte of interest. However, to be a good sensor it must also be specific, i.e., it must be able to differentiate between analytes. One way to increase specificity is to coat the top surface of the resonator with a functionalizing layer. Such a layer allows only the species of interest to bind to the surface and cause a shift in the refractive index. When designing resonators for absorption sensing, it is crucial that the species of interest absorbs in a region of wavelength where the resonator has a resonant peak. To enhance sensitivity of our sensor devices we have developed a procedure in collaboration with Prof. Luzinov's group at Clemson University to modify their surfaces with enrichment polymer layers (EPLs) grafted to their surface[139-146]. EPLs are thin polymer films (≤ 5 μm) deposited onto a surface intended to extend the qualitative or quantitative limit of detection by attracting organic compounds via chemical and/or physical interactions. The incorporation of such films into chemical sensors has been heavily researched since the late 1980s[147, 148]. EPLs have been demonstrated as efficient and

highly sensitive coatings for diverse evanescent waveguide-based optical monitoring systems[149-155]. On exposure to specific analytes, the polymeric coatings will change their internal structure *reversibly* or *irreversibly* at the nanolevel by swelling with an analyte.

Many different polymer materials have been compared to determine the most effective enrichment layer for specific analytes[149, 156, 157]. Optical properties of polymer film swelling versus film thickness have also been studied[158]. Large offsets of non-absorbing wavelengths observed in optical chemical sensors are due to the refractive index changes of the absorbing compound. This indicates that the waveguide is evanescently coupled to the sensing medium even if there is no absorption. To reduce the refractive index changes that result from the incorporation of analyte, it has been suggested that a thin polymer film ($< 0.5$ µm) is sufficient to avoid interferences from swelling.

One type of enrichment coating developed for optical resonators is an example of the EPL working in a dynamic (reversible) mode. It absorbs the vapors of interest during an exposure event and after the exposure, deswelling occurs and the layer returns to its initial state with no post-exposure signature left in the layer. By tailoring the composition of the film (or using multilayer films), swelling in response to the analyte of interest can be maximized and suppressed for other analytes[139]. A layer of poly(glycidyl methacrylate) or PGMA (active in various chemical reactions with carboxyl, hydroxyl, amino, epoxy, thiol, and anhydride functional groups) can serve as an anchoring layer for grafting polymers with affinity for targeted analytes.

However, for certain applications (e.g., monitoring without power being supplied to a device), it is important to be able to conduct post-exposure interrogation of the resonators. To this end, we have developed a class of irreversible EPLs for optical resonators that is capable of retaining the memory of a specific exposure event. This type of EPL is a

polymeric nanofoam coating that possesses the behavior of a shape memory material[159, 160] exhibiting mechanical action under external stimulus. On exposure to specific analytes, the nanofoam polymeric coatings change their internal structure irreversibly at the nano level leading to significant changes in the thickness and density. This in turn affects the optical properties of the film such as refractive index and optical absorption.

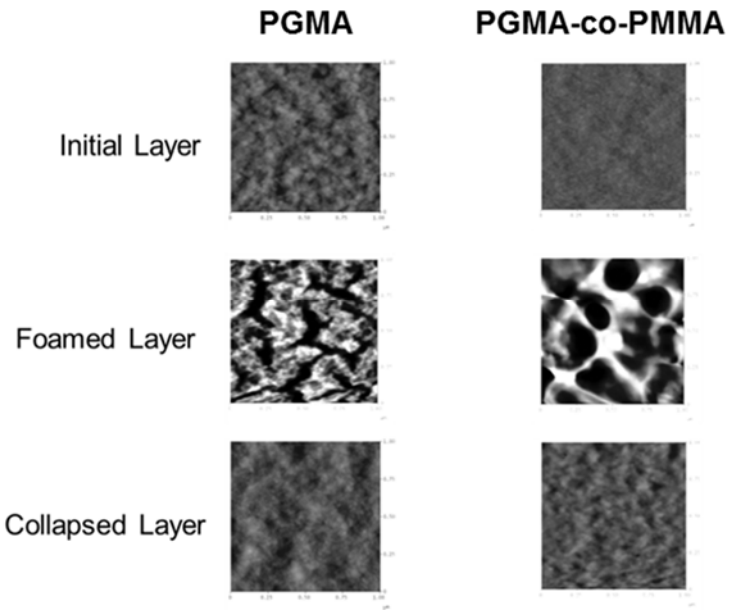


**Figure 5.5:** AFM topographical images of: initial PGMA layer and PMMA-PGMA layers; change in the layers morphology upon the foaming; and collapsed layers morphology upon exposure to chloroform vapor. Image size: 1x1 µm, vertical scale: 30 nm.

The nanofoam coatings are synthesized by first depositing a film of PGMA or poly(methyl methacrylate-co-glycidyl methacrylate) [PMMA-co-PGMA] random copolymer on the surface of a silicon substrate or micro-resonator via a dip coating technique[140]. The films are then cross-linked upon reaction between the PGMA epoxy groups to create a non-soluble, but swellable coating. The extent of the cross-linking is controlled to ensure that only a fraction of the epoxy groups is reacted to allow for further functionalization of the film. Finally, the films are swollen in a solvent such as chloroform and freeze-dried under reduced pressure to form a nanofoam anchored to the surface. Prior to foaming, the films

can be treated with polymers possessing carboxy groups that have the ability to react with the remaining epoxy group of the PGMA. To prove this concept we grafted carboxy-terminated polystyrene (PS) to the PGMA and PMMA-co-PGMA films before freeze-drying to obtain the nanofoam coating.

We used ellipsometry and reflectometry to monitor the extent of foaming via thickness measurements. For a 58 ± 3 nm PGMA film the average foaming was found to be 19 ± 1%. The PMMA-co-PGMA films with a thickness of 42 ± 3 nm foamed on average 23 ± 1%. Figure 5.5 shows the change in morphology of the coatings upon foaming and the formation of porous foamed structures can be clearly observed. The nanofoam was found to partially collapse when exposed to various solvents. For example, AFM images of the film exposed to chloroform vapor demonstrate a dramatic change in the nanofoam film morphology after exposure to the solvent (Figure 5.6).

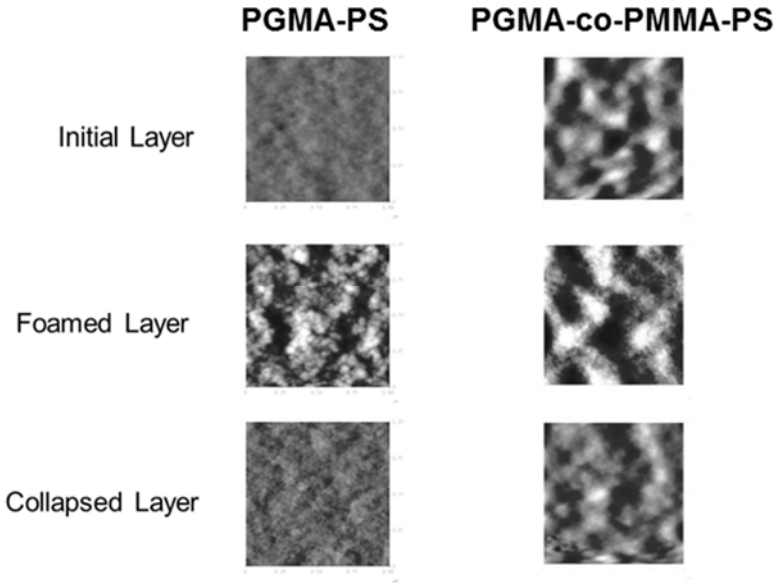


**Figure 5.6:** AFM topographical images of: initial PGMA-PS layer and PMMA-PGMA-PS layers; change in the layers morphology upon the foaming; and collapsed layers morphology upon exposure to chloroform vapor. Image size: 1x1 µm, vertical scale: 30 nm.

In our next experiment a 105.5 ± 10 nm film of PS was grafted to PGMA films, 32.7 ± 5.3 nm of PS was grafted to the copolymer film and the PGMA-PS film was foamed 44 ± 8%. PMMA-co-PGMA-PS film demonstrated a larger extent of foaming (50 ± 3%). Figure 5.6 reveals the AFM morphology of the PS functionalized layers before and after foaming. The imaging confirms formation of the porous structure that collapsed upon exposure to solvents.

### 5.3.2 Polymer thin-film-coated resonators

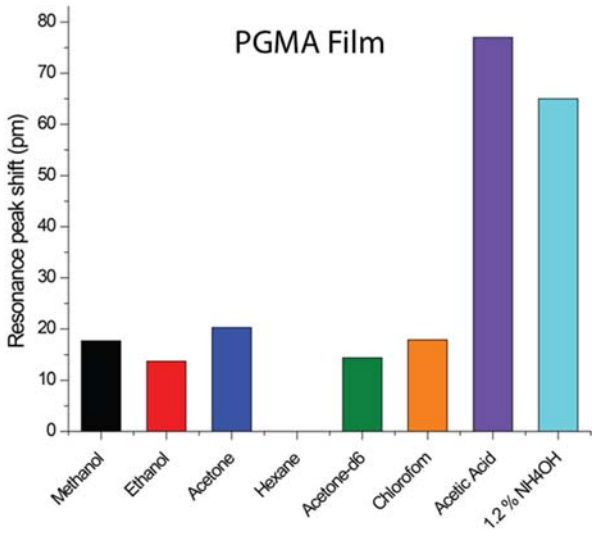


**Figure 5.7:** Measured resonant peak shifts for chalcogenide resonators coated with a PGMA film, which swells in response to analytes. We can enhance the response of such films to specific analytes by creating multilayer stacks with other polymers such as polyacrylic acid (PAA).

Peak shift data collected from a near-IR ChG resonator sample coated with a single layer of PGMA is summarized in Figure 5.7. We exposed the sample to vapors of several analytes by placing a small holder with the liquid next to the sample and covered the setup with a glass slide chamber. Measurements were taken at regular intervals over a period of ~30 minutes to monitor the peak shifts and the data shown in Figure 5.7 is from the final peak shift measurement. The samples were allowed to dry out (and de-swell) for an hour in between each analyte. Acetone and chloroform exhibit high swelling fractions with PGMA,

which results in the higher peak shift compared to methanol and ethanol. Hexane has the lowest swelling fraction with PGMA and hence we observe a negligible shift. The abnormally high peak shift for ammonium hydroxide ($NH_4OH$) can be explained by an exchange chemical reaction taking place with the OH groups in the polymer film. We performed an additional test with some amorphous silicon racetrack resonators by measuring their response to acetone before and after coating them with six layers of PGMA and polyacrylic acid (PAA). As we can see in Figure 5.8, the resonant peak barely moves without a polymer layer but has a large shift of nearly 50 pm once the six layers are coated. Thus, we have enhanced the sensitivity of these resonators by adding the polymer layers that can swell in response to analyte vapors and cause a larger index shift than would otherwise be possible.

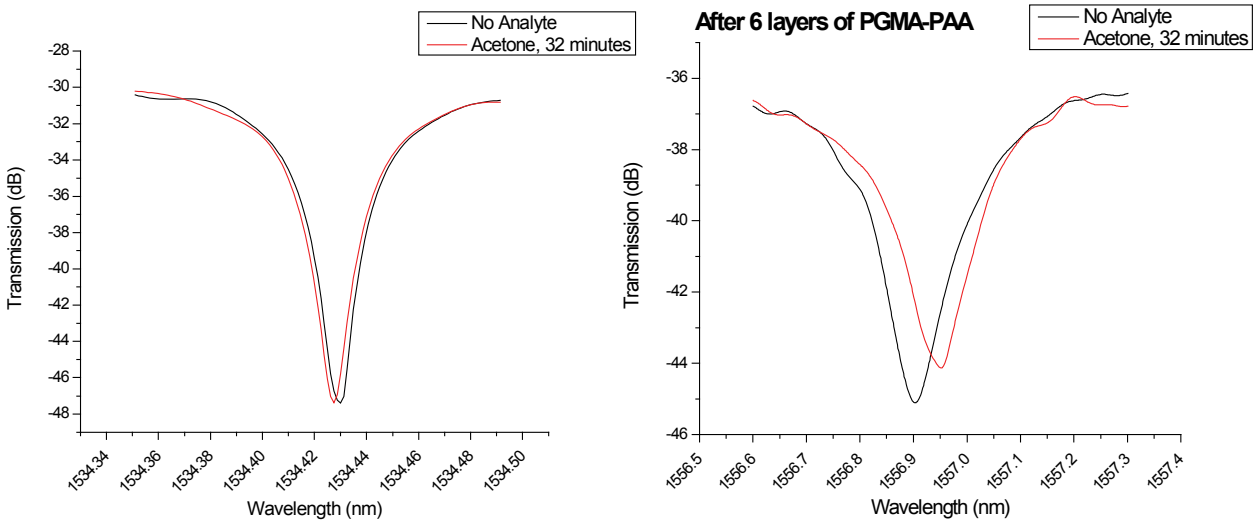


**Figure 5.8:** (Left) Truncated transmission spectra from a-Si showing a small, ~2.5 pm shift in the resonant peak. (Right) Analyte exposure after six layers of PGMA-PAA causes much larger resonant peak shift of 50 pm.

### 5.3.3 Polymer nanofoam-coated resonators

The response of polymer nanofoam-coated chalcogenide glass resonators was measured in the near-infrared regime with our LUNA setup. Resonator devices were first fabricated using the standard lift-off lithography procedure described in Chapter 4. A few samples were

tested to evaluate resonator performance and quality across the patterned wafer. Our Clemson collaborators then coated uncleaved samples with nanofoams of various compositions based around PGMA. The foamed samples were cleaved and measured with the LUNA system. The first measurement was performed on the "as-foamed" samples to act as a reference data point and each sample was subsequently exposed to a series of organic solvent vapors for approximately forty minutes. The samples were allowed to dry out for about two hours post-exposure before the next measurement was performed.

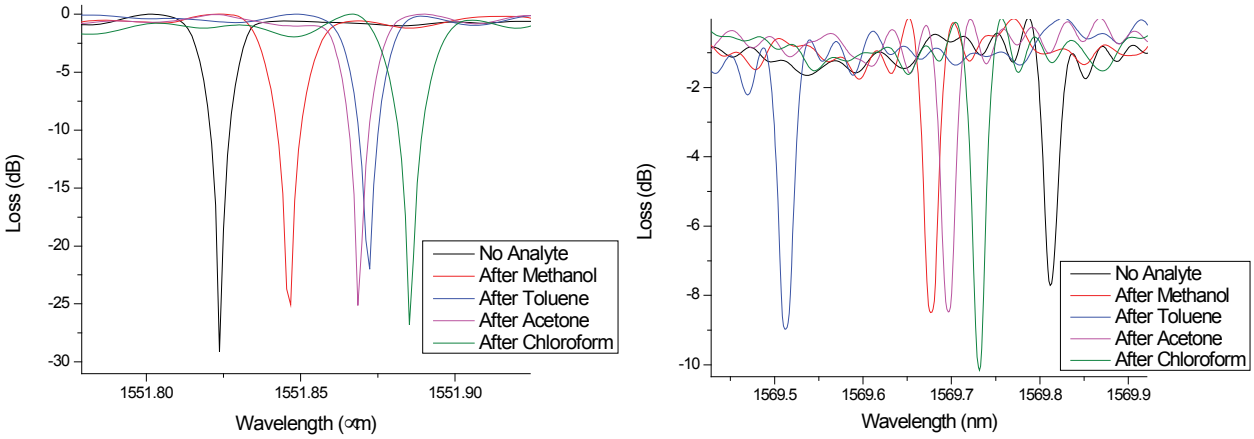


**Figure 5.9:** (Left) PGMA-only nanofoam; (Right) PGMA with 1% PS foam. The peak shifts for the PS-containing foam are larger and we observe a change in direction of the peak shifts.

In Figure 5.9, we compare the shifts from a PGMA-only nanofoam and a PGMA nanofoam with 1% polystyrene (PS) added to it. We can observe distinct peak shifts for the four tested analytes, and the magnitude and direction of shifts changes with the addition of PS. Similar behavior is observed for a copolymer-based nanofoam with PGMA and PMMA in a 70:30 ratio (see Figure 5.10). In particular, the first analyte, methanol, causes a red shift in the absence of PS but produces a blue shift when PS is added to the foam composition. Further, the copolymer foams exhibit a large difference in the magnitude of the induced peak shifts when PS is added to the mixture. Without PS, the peak shifts are about 0.1 nm but when PS is involved, the shifts can be as large as a few nm. Addition of

polystyrene also appears to increase foam sensitivity to toluene in particular. This indicates that the structure of the foams with PS is modified to a much higher degree in response to toluene when compared to the other analytes. We believe this change in behavior with PS addition arises due to the formation of a segregated PS-rich phase in the nanofoam, which reacts differently to analyte exposure when compared to the original foam. This represents a good first step towards making sensors that are specific to targeted analytes. For example, the copolymer with PS foam could serve as a specific coating for detection of toluene in a mixture of organic solvents as it induces a much larger change than other solvents.

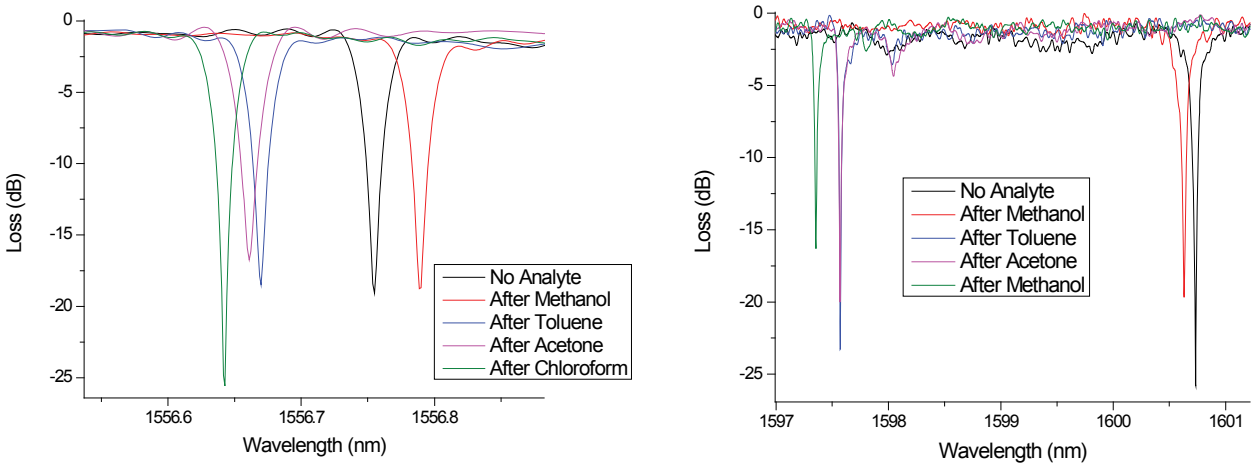


**Figure 5.10:** (Left) PGMA-co-PMMA nanofoam; (Right) PGMA-co-PMMA with 1% PS nanofoam. The PS-containing foam exhibits a much larger shift in resonant peak position with toluene, indicating high selectivity.

A further observation to be made from the data is that the resonant peak position does not return to the original location (before analyte exposure). This is expected as each analyte exposure causes irreversible change in the structure of the nanofoam layer, leading to a non-recoverable change in the refractive index. Irreversible changes are necessary for tamper-proofing applications to prevent evidence of tampering from being hidden. Future work would involve developing and testing more such foams that can target select chemical species and build a library of foam compositions that are effective against specific analytes.

## 5.4 Exploiting photosensitivity to alter photonic device response

### 5.4.1 Post-fabrication trimming of silicon-on-insulator resonators[161]

The high-index contrast and sub-micron waveguide dimensions for silicon-on-insulator (SOI) devices lead to a strong sensitivity to fabrication tolerances. In a typical single-mode waveguide, a width deviation of 1 nm causes an effective index variation of $2\times10^{-3}$, producing a frequency shift of about 100 GHz in the spectral response of any interferometric device[162, 163]. This poses a huge technological challenge even for advanced fabrication process and imposes severe design constraints. Post-fabrication treatments that can finely tailor the local properties of SOI devices are therefore mandatory to compensate for unavoidable fabrication inaccuracies in order to recover the desired specifications and functionalities. Moreover, they also open the way to reconfigurable photonic circuits. Active tuning techniques, such as local heating through thermo-optic actuators[164] or carrier injection through p-i-n junctions[165], are commonly used but require complex additional fabrication steps and, being based on "always-on" mechanisms, are inherently power-hungry and not very efficient when continuous and fast reconfiguration is not required.

Permanent trimming techniques, where the induced refractive index change does not disappear when the applied trimming source is switched off, have recently attracted great interest. The trimming of SOI microring resonators has been demonstrated by exploiting the oxide compaction induced by electron beam exposure[166] or the silicon oxidation induced by the tip of an atomic force microscope[167]. Although large (up to $1.3\times10^{-2}$) effective index variations can be achieved, these techniques require sophisticated, expensive, and power-consuming equipment that is not in line with low-cost manufacturing and makes real-time monitoring of the process difficult. A more flexible solution, successfully applied to both SOI photonic crystal cavities[168] and microring resonators[169], is the use of a highly localized

laser beam to selectively induce oxidation, amorphization or nanomilling of the silicon surface. However, it requires very high power density (about $10^{15}$ mW/cm$^2$) and is affected by transient thermo-optic and surface chemistry effects. Alternative techniques, used on different high index contrast technological platforms, employ UV sensitive polymer films as waveguide cladding[170, 171], whose refractive index is tailored by local UV exposure. Besides requiring a UV-source for the trimming, most polymers suffer from poor temporal stability and optical degradation at relatively low temperatures.

We have proposed an innovative approach to realize trimmable silicon devices. Chalcogenide-assisted silicon waveguides are made by depositing $As_2S_3$ glass as an upper cladding in an otherwise standard SOI process. The photosensitivity of chalcogenide glass (ChGs) materials is then exploited to selectively tailor the local optical properties of the waveguides, by using nothing more than a low-intensity visible-light source. We have investigated in detail its performance by trimming the resonance frequency of a silicon micro-ring resonator.

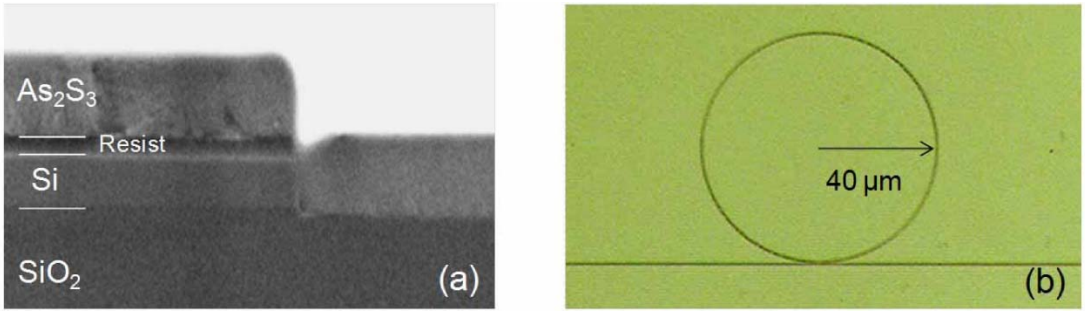


**Figure 5.11:** (Left) Cross-sectional SEM image of fabricated devices. (Right) Plan view optical image of ring resonator[161].

To modify the resonator response, we locally and selectively trim the $n_{eff}$ of the waveguide forming the ring, with a visible-light source (halogen lamp) coupled to a multimode optical fiber with a 30 µm mode field diameter positioned above the chip. The

spectral emission of the lamp ranges from 450 nm to 650 nm and the light intensity at the fiber output can be varied from 0.3 mW/cm$^2$ to 10 mW/cm$^2$.

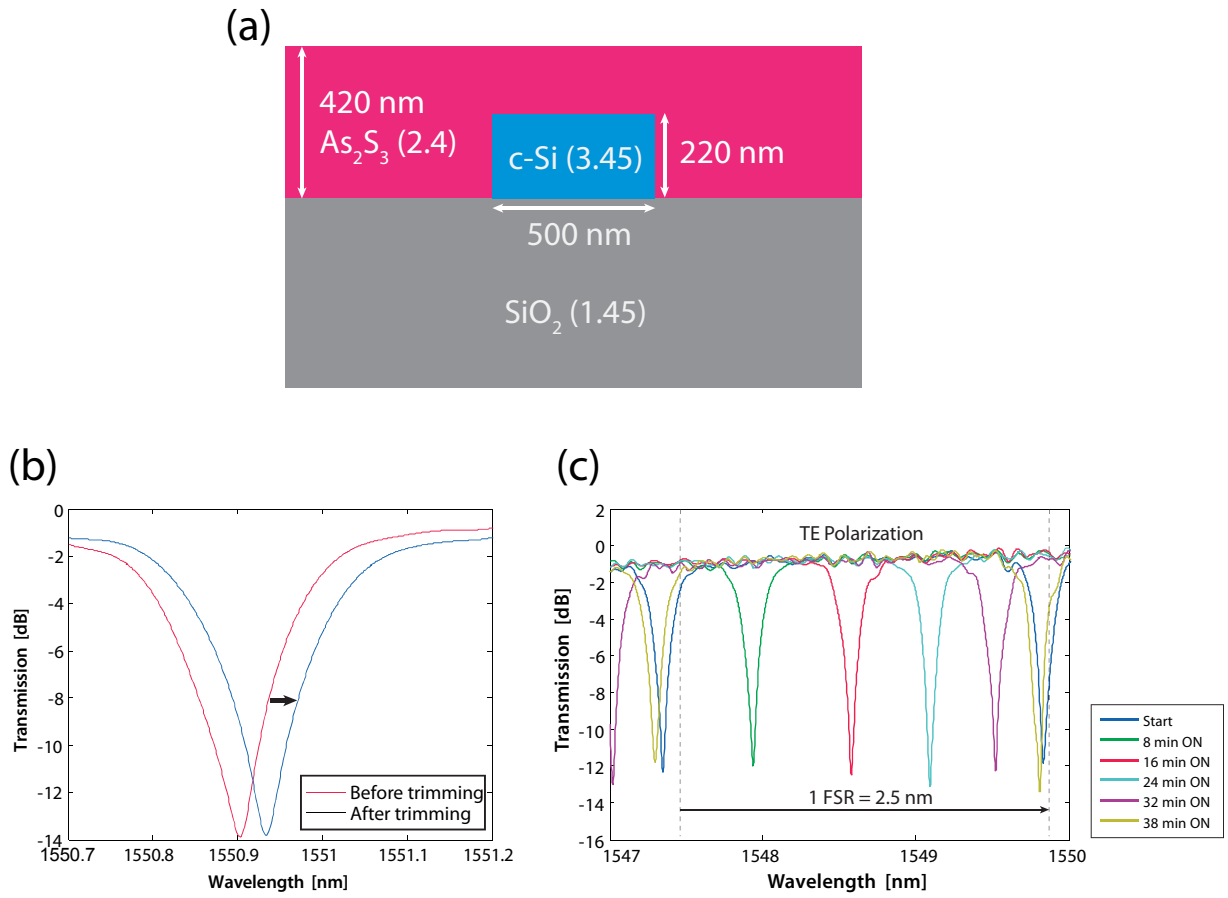


**Figure 5.12:** Exploiting the photosensitivity of $As_2S_3$ glass to trim the resonance of SOI resonators. Upon exposure to above band gap visible light, $As_2S_3$ undergoes a refractive index change, which shifts the position of the resonant peak. It is possible to shift the peak over an entire free spectral range (FSR) with this method[161].

The experimental results reported in Figure 5.12 show that the light exposure is responsible for a progressive red shift of the frequency response of the ring over an entire free spectral range (FSR). In this case, the entire waveguide forming the ring is uniformly exposed, except the coupling region to avoid coupling coefficient variations. The wavelength shift is rigid, with neither appreciable changes in the depth nor in the width of the resonant peak. This demonstrates that our trimming process does not induce additional losses and prevents exposure of the coupling region.

These achievements therefore demonstrate the twofold appeal of ChG-assisted SOI waveguides: (i) enabling easy counteraction of the fabrication tolerances of SOI platform and restoration of the desired response of the devices, and (ii) opening the way to the realization of photonic circuits that can be reconfigured after fabrication.

### 5.4.2 Phototrimming of athermal amorphous silicon devices

Athermal waveguides represent an important part of silicon photonic integrated circuits because they mitigate the strong dependence of silicon on temperature. Due to the large thermo-optic (TO) coefficient of Si ($1.8\times10^{-4}$ $K^{-1}$, about 20 times greater than silica[172]), even small temperature gradients or fluctuations across the chip may result in large wavelength shifts and severe distortions in the response of interferometric devices. For instance, in a traditional single-mode silicon channel waveguide[173], a temperature drift of 1°C shifts the overall transfer function of any device by about 70 and 50 pm for transverse-electric (TE) and transverse-magnetic (TM) polarizations respectively. Typically, in integrated optics, this is counteracted by utilizing active heaters on top of the waveguide[174] and thermo-electric chip coolers; however, this approach consumes power, and the thermal management of the chip becomes prohibitive when dealing with large-scale integrated photonic circuits[175].

Temperature drifts in photonic circuits may be passively neutralized by covering the waveguide core with a polymer top cladding with a negative TO coefficient, opposite to that of the core, thus achieving the desired thermal compensation. This approach was first proposed and demonstrated on glass slab[176] and channel waveguides[177], and then extended to standard Si waveguides[178], observing no appreciable wavelength shift with temperature variations[179]. Figure 5.13 shows the mode profile of an athermal amorphous silicon waveguide with a large fraction of the TM mode extending into the polymer cladding.

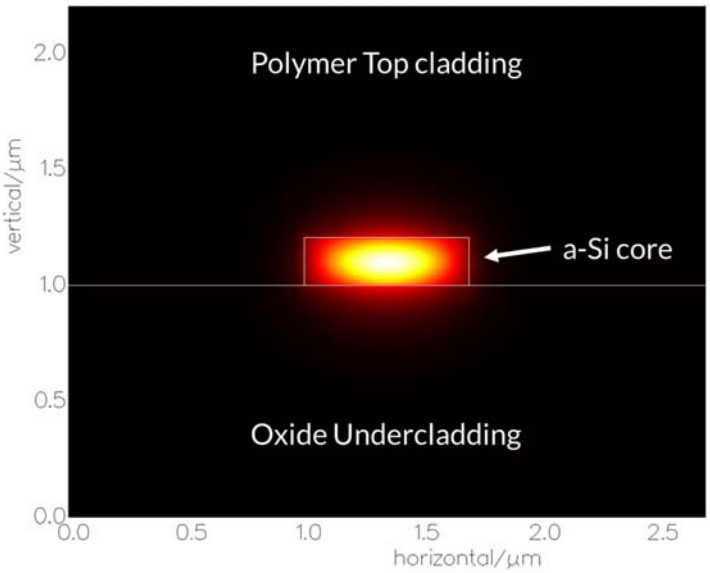


**Figure 5.13:** Example of athermal waveguide with nearly 30% of the mode power confined in the polymer cladding and only about 38% in the WG core.

However, as with SOI waveguides, athermal devices are also sensitive to fabrication tolerances and as the polymer cladding is being used for athermal operation, we cannot use the TO effect to compensate for fabrication variations. Instead, we use a thin film of $As_2S_3$ to coat the a-Si waveguide before polymer deposition and then use the phototrimming technique discussed in the previous section. Racetrack ring resonators in an all-pass filter configuration were fabricated to demonstrate the effectiveness of the athermal and trimmable waveguide technology. The rings have a length of 326 μm [free-spectral range, FSR = 256 GHz] and a bending radius of 20 μm, with a coupling length of 100 μm and a gap of 600 nm between the bus waveguide and the resonator.

The sensitivity of the ring resonance to temperature variation $\Delta\lambda/\Delta T$ was measured before and after trimming of its resonant wavelength, in the temperature range of 20–40°C, as shown in Figure 5.14. The temperature sensitivity of the as-fabricated device (blue circle markers) is more than one order of magnitude below that typical of Si waveguides (50 and 70 pm/°C, respectively, on TM and TE polarization) across a wavelength range of almost

50 nm. No appreciable wavelength shift with temperature is observed around 1569 nm, hereinafter named "athermal wavelength," with variations in wavelength that arise from waveguide dispersion. After a 10 nm trimming of the ring resonance, corresponding to about five FSRs, the athermal performance rigidly blue-shifts by about the same quantity (red square markers), with no appreciable change in the slope of the temperature sensitivity curve. It is worth noting that the athermal wavelength is continuously trimmed across the same 10 nm bandwidth, resulting in a value of around 1559 nm after exposure.

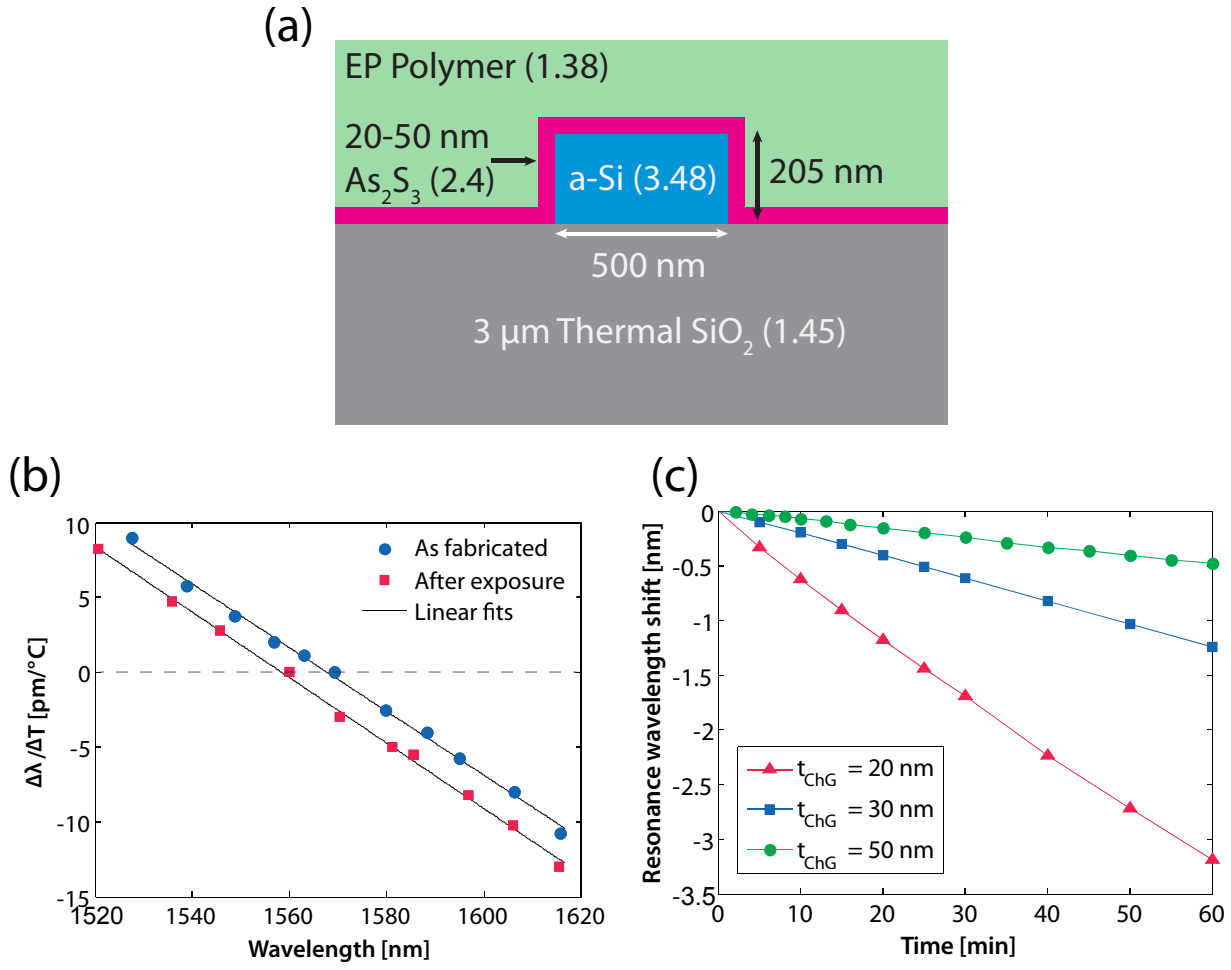


**Figure 5.14:** Extending the phototrimming process to athermal ($d\lambda/dT = 0$) amorphous silicon resonators. The devices retain athermal behavior and resonant peak shifts are observed with deposited $As_2S_3$ layers as thin as 20 nm[180].

Athermal and trimmable ring resonators with different thicknesses of the $As_2S_3$ chalcogenide layer, $t_{ChG}$, were fabricated in order to investigate the speed and time response of the trimming process, and the effect occurring in $As_2S_3$ under near-bandgap illumination. Figure 5.14 shows the resonant wavelength shift of three identical rings, but with different $t_{ChG}$ of 20, 30, and 50 nm. The exposure was performed with the same light intensity of 10 mW/cm$^2$ for 60 min for all the resonators. Visible light illumination linearly blue-shifts the resonances of the filters, with higher speed for samples with thinner $As_2S_3$ layer: 53, 21, and 8 pm/min, respectively, for $t_{ChG}$ = 20, 30, and 50 nm. The observed wavelength blue-shift, which corresponds to a decrease of the refractive index of the $As_2S_3$ glass, as well as the measured trimming rate, which increases with decreasing $As_2S_3$ thickness, suggests that the dominant effect occurring in these thin $As_2S_3$ films when exposed to visible light is volume expansion[71, 76].

## 5.5 Studying the effects of radiation on photonic materials with resonators

### 5.5.1 Amorphous silicon and SOI resonators

We investigated the effects of gamma (γ) radiation on Si-based devices to understand the degree of radiation hardness that can be expected from the materials system. We focused on two platforms: silicon-on-insulator (SOI) and polymer-assisted athermal silicon technologies (presented in previous section).

A schematic of the cross sections of the Si devices utilized in this work is shown in Figure 5.15. SOI waveguides, patterned via electron-beam lithography, have a 480 nm wide and 220 nm thick Si core ensuring single mode propagation for TE polarization (see Figure 5.15a). The waveguide core is placed on a 2 μm thick oxide buffer layer and then covered by a 1 μm thick layer of $SiO_2$ grown by plasma enhanced chemical vapor deposition

(PECVD). Figure 5.15b shows the cross section of the athermal Si waveguides, which were fabricated according to the design and procedure described elsewhere[179]. A 205 nm thick amorphous silicon (a-Si) layer was deposited by PECVD on a Si wafer with a 3 µm thick thermal $SiO_2$ layer. Channel waveguides with a width of w = 600 nm to ensure single mode propagation for TM polarization, were patterned via photolithography. Finally, a 3 µm thick layer of a proprietary hyperlinked fluoropolymer manufactured by Enablence Inc., hereinafter named EP, was spin coated and exposed to ultraviolet illumination before being baked in vacuum at 150°C for 4 hours to stabilize the polymer properties. The design of the waveguide cross section was optimized in order to make the fundamental TM mode expand from the a-Si core into the polymer cladding in such a way that the effective index behavior of the device is properly weighted over the indices of a-Si ($n$ = 3.48), EP polymer ($n$ = 1.38), and $SiO_2$ ($n$ = 1.45). Consequently, the effective thermo-optic (TO) behavior of the waveguide is determined by the amount of optical mode contained in each layer: a-Si (TO coefficient: $2.3\times10^{-4}$, confinement factor: 0.35), EP polymer (TO coefficient: $-2.65\times10^{-4}$, confinement factor: 0.27), and $SiO_2$ (TO coefficient: $1\times10^{-5}$, confinement factor: 0.38).

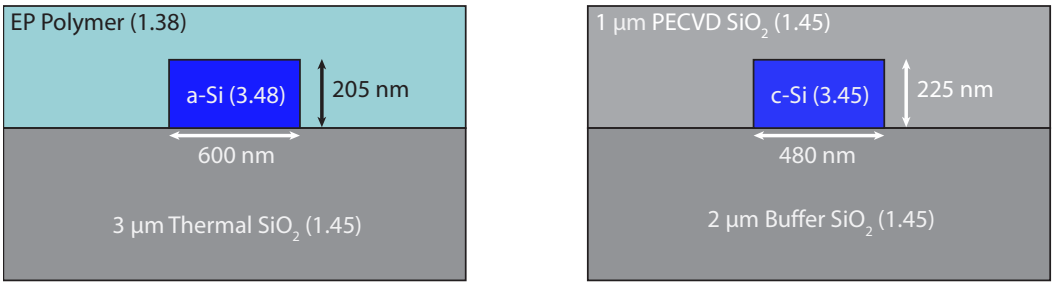


**Figure 5.15:** Schematic view of the cross sections of (Left) the polymer-assisted amorphous silicon waveguide exposed to gamma radiation and (Right) the SOI waveguide.

We investigated the effects of γ-radiation on these two technologies by an extensive experimental characterization of ring resonators, whose optical response was measured before and after irradiation to determine refractive index and optical loss variations. The samples were uniformly exposed within an irradiator cell containing cobalt-60 ($^{60}Co$) sources

emitting two cascade gamma rays with energies of 1.17 MeV and 1.33 MeV. We use the LUNA OVA system once again and control the chip temperature (above room temperate ~30°C) via a thermocouple-based temperature controller.

Table 5.1 shows the results of  -irradiation of an SOI ring resonator with a 20 μm radius (length $L$ = 157.903 μm, $FSR$ = 450 GHz), and quality factor of about $10^4$. The table reports the waveguide group index $n_g$ for the non-irradiated resonator and for two different absorbed doses, 2 and 35.6 Mrad, at different wavelengths across a bandwidth of about 15 nm. The group index is directly derived from the measured $FSR$ as $n_g = c/(FSR \cdot L)$, with $c$ being the velocity of light in vacuum. The measured group index changes are on the order of $10^{-3}$, corresponding to small refractive index changes of Si on the order of $10^{-5}$. Due to this very small observed change of refractive index, we can suggest that SOI technology exhibits excellent resistance to gamma radiation.

**Table 5.1:** Measured group index $n_g$ of the un-irradiated SOI waveguides, and after gamma ray exposures with doses of 2 Mrad and 35.6 Mrad; measurements are performed across a bandwidth of 15 nm from 1559 nm to 1575 nm.

| **Wavelength [nm]** | **$n_g$ (No Irradiation)** | **$n_g$ ($\gamma$ = 2 Mrad)** | **$n_g$ ($\gamma$ = 35.6 Mrad)** |
|---|---|---|---|
| 1559.949 | 4.257 | 4.258 | 4.258 |
| 1563.580 | 4.254 | 4.255 | 4.257 |
| 1567.207 | 4.279 | 4.277 | 4.278 |
| 1570.866 | 4.261 | 4.260 | 4.257 |
| 1574.541 | 4.262 | 4.265 | 4.265 |

Racetrack ring resonators formed with the athermal design were measured to investigate the effect of γ-radiation on athermal Si waveguides. The resonators have a ring length of 426 μm ($FSR$ = 1.62 nm) with a coupling length of 150 μm and a gap of 500 nm

between the ring and the bus waveguide. The TO sensitivity $\Delta\lambda/\Delta T$ of the resonators, which is shown in Figure 5.1a, was measured across a bandwidth of 50 nm around 1550 nm and in the temperature range from 30°C to 50°C. The black line represents the TO curve of the non-irradiated resonator, which is well below that of standard SOI waveguides[180] and shows no appreciable wavelength shift with temperature at the wavelength of 1529.285 nm with wavelength dependent variations arising from waveguide dispersion. The TO measurement is then repeated after γ-irradiation of the chip with absorbed doses of 1 Mrad, 3 Mrad, 7 Mrad, and 10 Mrad. The measurements show an overall blue-shift of the TO curve which increases in magnitude when increasing the γ-irradiation dose and reaches a value of 4.123 nm with a 10 Mrad dose at the athermal wavelength (0 pm/K, wavelength 1529.285 nm).

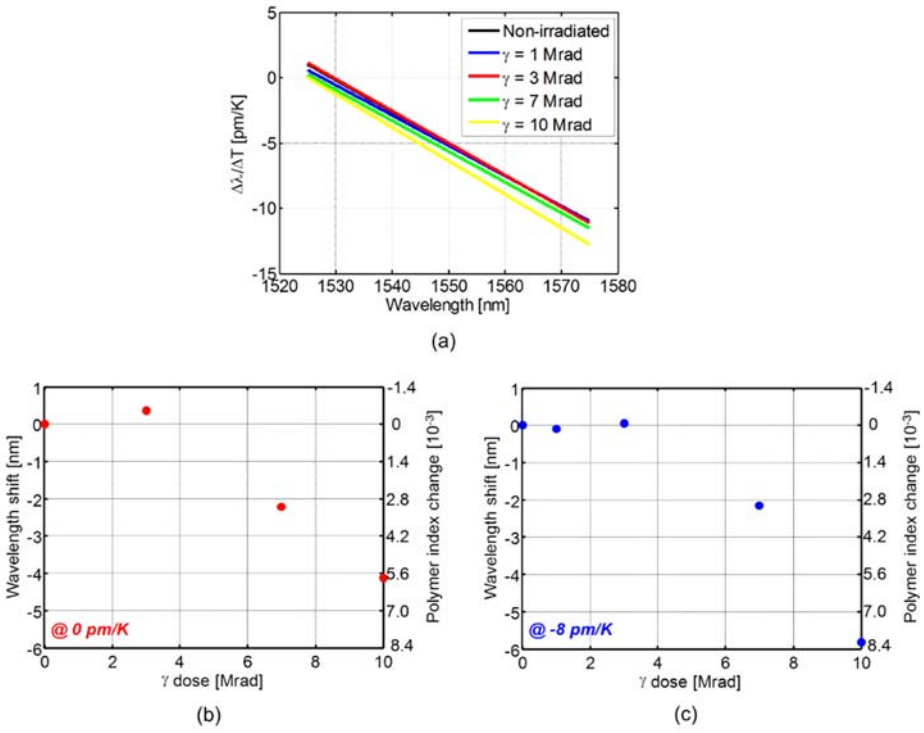


**Figure 5.16:** (a) Measured TO sensitivity curve of the athermal ring resonator, as a function of the wavelength, after exposure to gamma radiation from 1 to 7 Mrad, in the temperature range 30-50 °C. Wavelength shift of the TO sensitivity curve and polymer refractive index change, at

$\Delta\lambda/\Delta T$ = 0 pm/K (c) and at $\Delta\lambda/\Delta T$ = -8 pm/K, achieved after exposure to γ-radiation with increasing doses from 1 to 10 Mrad.

Since the athermal design requires a significant portion of the propagating light mode to be in the polymer cladding instead of being well confined within the waveguide core, γ-irradiation can induce changes in the polymer layer as well as in the amorphous silicon waveguide. However, the wavelength shift of the TO sensitivity is essentially induced by a variation of the refractive index of the top cladding polymer because we do not observe any significant radiation-induced effects in the a-Si core up to a dose of 10 Mrad. Moreover, polymers exhibit changes in structure without requiring high radiation doses. Crosslinking is promoted in non-crosslinked polymers but radiation will cause degradation of molecular weight (due to chain scission and free radical formation) in crosslinked polymers. Increasing the number of broken bonds will also increase the polarizability of the polymer, potentially leading to a refractive index increase. Since we use a heavily crosslinked fluoropolymer, the increase in effective index observed is likely caused either by an increase in the amount of crosslinking or due to the radiation breaking chemical bonds in the polymers.

Furthermore, we quantitatively correlate the measured wavelength shift of the TO sensitivity curve to variation in the polymer refractive index by means of electromagnetic simulations. As shown in Figure 5.16b and Figure 5.16c, which report wavelength shifts and polymer index changes at the athermal wavelength ($\Delta\lambda/\Delta T = 0$ pm/K) and at $\Delta\lambda/\Delta T =$ -8 pm/K, an overall index change larger than $8\times10^{-3}$ is obtained at a γ-dose as high as 10 Mrad with wavelength dependent variations due to changes in the waveguide confinement. We expect that at a certain radiation dose level, the rise in the refractive index will saturate and further irradiation will lead to a decrease in index due to degradation of the polymer film[181].

### 5.5.2 Chalcogenide glass resonators

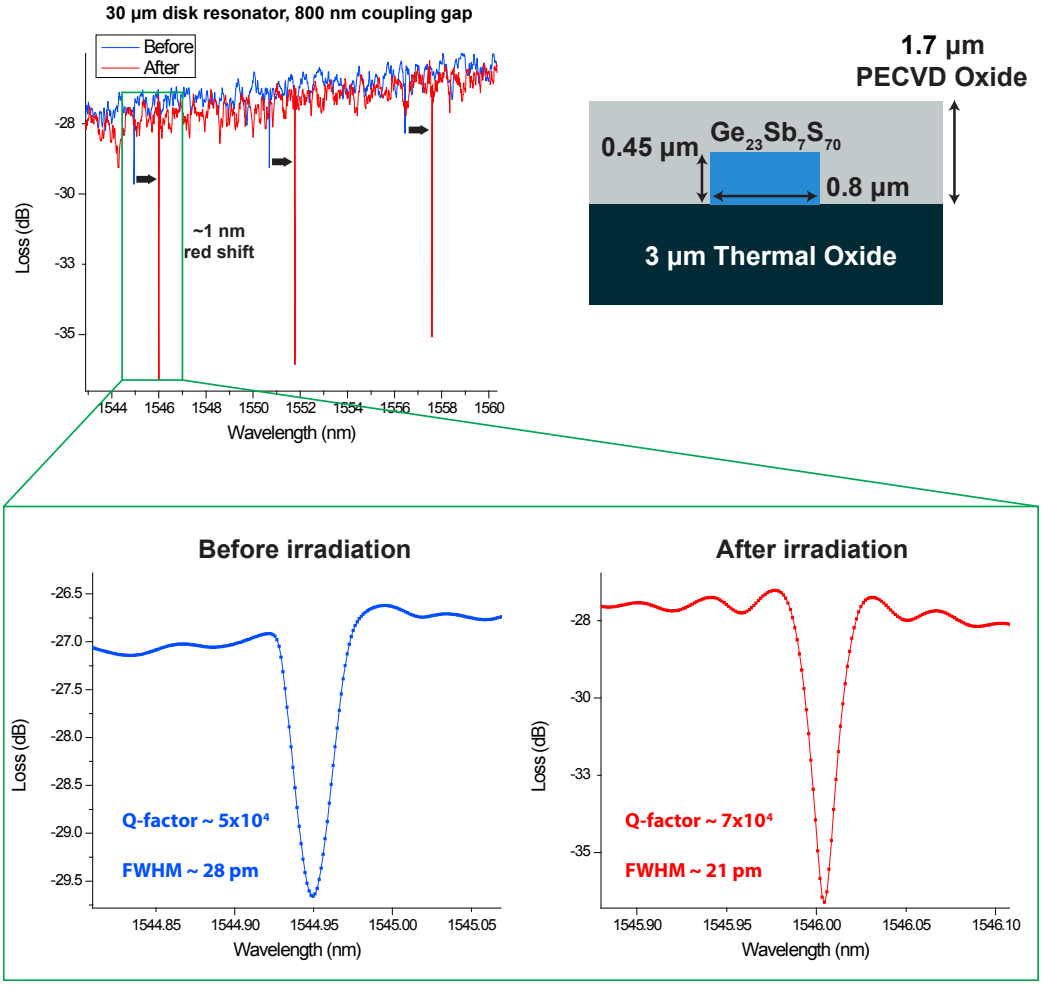


**Figure 5.17:** (Top) Transmission spectra for a 30 µm radius chalcogenide glass microdisk resonator before and after alpha irradiation (0.5 MeV energy, $10^{15}$ cm$^{-2}$ dose) showing a peak shift ~1 nm. (Bottom) Focusing on individual peaks before and after irradiation shows a decrease in the full width half maximum and an increase in the cavity Q factor after irradiation.

In addition to evaluating chalcogenide glass thin films and bulk samples (Chapter 2), we have also characterized near-IR microdisk resonators made from $Ge_{23}Sb_7S_{70}$ glass before and after alpha radiation. The devices were fabricated using the process described in Chapter 4 and then coated with 1.7 µm of PECVD $SiO_2$ to ensure that the peak of the radiation damage would be located inside the waveguide core. The samples were irradiated with a dose of $10^{15}$ cm$^{-2}$ at an energy of 0.5 MeV and normal incidence. Optical characterization of

the resonators was carried out the LUNA system. The sample stage was kept at a constant temperature of 27°C to prevent peak shifts from temperature fluctuations.

Figure 5.17 shows the structure and results from a 30 µm radius microdisk with an 800 nm coupling gap to the bus waveguide. We observe that post-irradiation, the resonant peaks show a red shift of about 1 nm and an increase in the Q-factor and extinction ratio. We also present a magnified view of individual resonant peaks before and after irradiation demonstrating an increase in the Q-factor from $5\times10^4$ to $7\times10^4$ resulting from a decrease in the full-width half-maximum (FWHM) of the peak from 28 pm to 21 pm.

We hypothesize that the red shift in the resonant peaks could be due to an increase in the refractive index of the chalcogenide glass material due to disruption of the glass network through broken bonds and atomic displacements that can increase the polarizability of the glass. This would lead to better light confinement within the waveguides and resonators, leading to an increase in the effective refractive index of the propagating light that manifests as a red shift in the resonant peak position. A change in the refractive index can also affect the coupling from the bus waveguide to the resonator that may explain the observed change in extinction ratio and FWHM[182, 183]. It is likely that the index of the PECVD oxide layer changed along with the waveguide layer, which makes it difficult to isolate the effects of ChG modification. Grazing angle incidence irradiation may eliminate the need for the oxide layer, but further measurements with more resonator samples at different doses and energies are required to understand these results better.

## 5.6 Summary

Over the course of this chapter, we have described our device efforts in the telecom wavelength range. We used chalcogenide glass resonators to separate the contribution of various loss mechanisms in these materials and learned that scattering losses dominate in

microphotonic devices. In comparison, material attenuation from impurities is low but can play a significant role when scattering loss is low (i.e., in fibers or large waveguides). We also exploited the photosensitivity of $As_2S_3$ glass to build trimmable photonic devices with SOI and amorphous silicon that offer post-fabrication tuning to optimize performance. Finally, we used resonators as a test platform for studying the effects of radiation on silicon and chalcogenide materials systems. Exposing resonators to alpha and gamma radiation caused changes in the refractive indices of our materials that could be measured using our LUNA system by examining the resonant peak shifts. In the next chapter, we discuss our mid-IR devices and highlight differences between the telecom and mid-IR wavelength regimes.

# Chapter 6: Mid-Infrared Device Characterization

In this chapter, we describe our device characterization efforts in the mid-infrared wavelength regime. We will discuss in detail the experimental setups used to measured mid-IR devices and how they differ from our near-IR experimental work. Challenges of working with mid-IR sources and devices along with potential solutions are also addressed.

## 6.1 Mid-IR measurement setup and procedures

Three different mid-infrared measurement setups were used in this work, each operating in a different wavelength range to gain broad coverage of the mid-IR spectrum. Although the laser sources are different, all three systems feature liquid-nitrogen-cooled InSb focal-plane array (FPA) cameras as the detection elements. Our primary measurement system is based around a broadly tunable ($\lambda$ = 2.4-3.8 µm) Firefly laser (MSquared Lasers Ltd) coupled to a zirconium fluoride ($ZrF_4$) mid-IR fiber as shown in Figure 6.1. The laser output is coupled into the fiber through a reflective collimator and the bare end of the fiber is then used to couple the light to the devices under test. Light exiting the output facet of the device under test is captured and focused by a mid-IR $CaF_2$ (25 mm focal length) lens into the InSb camera for imaging (256 x 256 pixel resolution). The bare fiber end, the sample, and the $CaF_2$ coupling lens are all placed on positioning stages with micrometers for precision manual control. We note here that alignment is considerably harder with a manual setup such as this one when compared with the software-controlled alignment on our LUNA system. The lack of lens-tip fibers in the mid-IR also poses a challenge as the core diameter of our fiber is 9 µm (cladding diameter 125 µm) and despite the larger size of mid-IR devices,

their single-mode dimensions are still smaller than the fiber core. As a result, even with the fiber coupled into a waveguide mode, a substantial amount of mid-IR light makes its way to the camera from the free space above the waveguide and the substrate underneath it. A solution to this problem is presented in the next section.

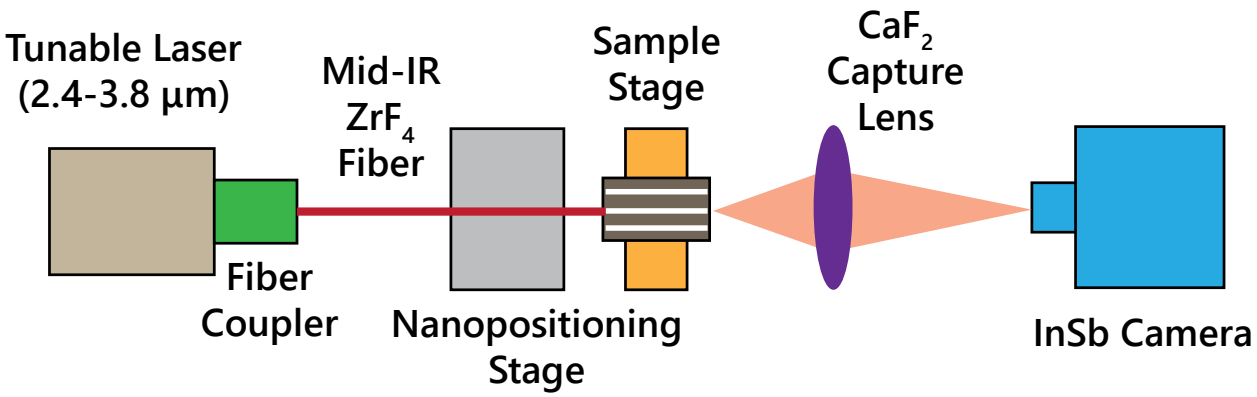


**Figure 6.1:** Schematic showing the Firefly laser setup. Light output from the laser is coupled to a fluoride mid-IR fiber placed on a nanopositioning stage. The sample is placed on a separate stage and the output from the sample is captured by a cooled InSb camera after passing through a collection lens.

We use a similar setup with a tunable 5.2 µm laser by Daylight Solutions to test resonators at the longer wavelengths in Prof. J. Hu's lab at MIT/University of Delaware. One key difference is the type of fiber used – an $InF_3$ multimode fiber with a core diameter of 40 µm and a cladding diameter of 160 µm.

The third system is based around an interband cascade laser (ICL) produced by NRL and operating at a central wavelength of 3.8 µm (see Figure 6.2). A small amount of wavelength tuning can be achieved by changing the laser current and temperature. Laser output from the ICL is coupled into the devices using a free-space telescopic lens arrangement. Although the sample is placed on a precision, piezo-controlled motion stage alignment is even more challenging in this case due to a lack of visual guidance from a fiber.

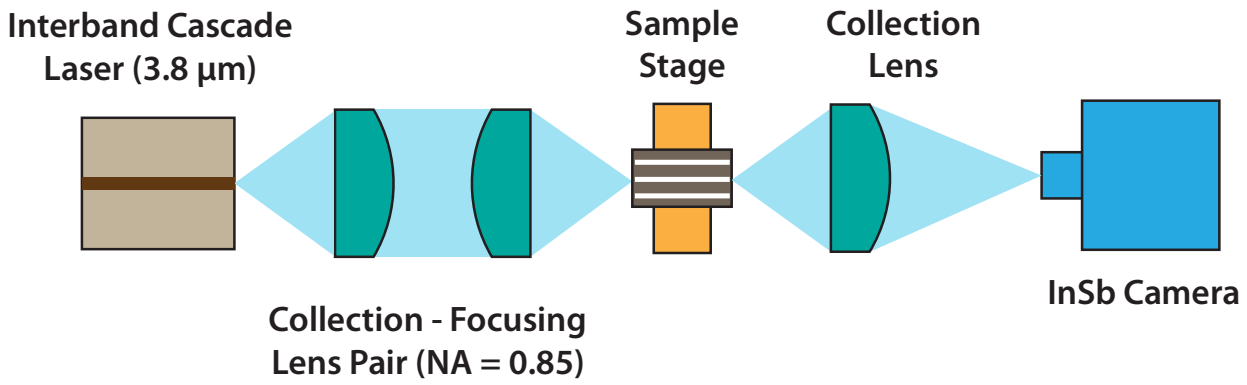


**Figure 6.2:** Free-space lens coupling setup at PSI with interband cascade laser. The output from the laser facet is coupled to the sample using a free-space collection-focusing lens pair.

## 6.2 Demonstration of mid-IR transparent ChG waveguides

### 6.2.1 Design solutions to meet mid-IR challenges

Working with mid-IR sources and fibers presents a unique set of challenges that have largely been solved for near-IR (telecom) wavelengths. Availability of tunable light sources with sufficient power in the 3-4 µm band is still limited, as is the fiber selection for these wavelengths (which also leads to higher system costs). Our fabrication limitations impose further constraints on device design that must be overcome before we can successfully couple light into a mid-IR waveguide.

The first coupling issue we must address is one of stray light overwhelming the propagating mode on the InSb camera. As discussed previously, this is caused by the physical size (and the mode size) of the fiber being larger (~10 µm) than our waveguides (~2 µm). Our solution is to offset the input and output facet of the waveguide such that there is a physical separation between the stray light that continues to propagate in a straight line and the mode, which goes around two (or four) 90° bends. Figure 6.3 below shows a schematic of an offset waveguide coupled to a resonator. Although the offset increases the length and footprint of individual devices, we can still pack a number of them close together to reduce wasted space on the chip.

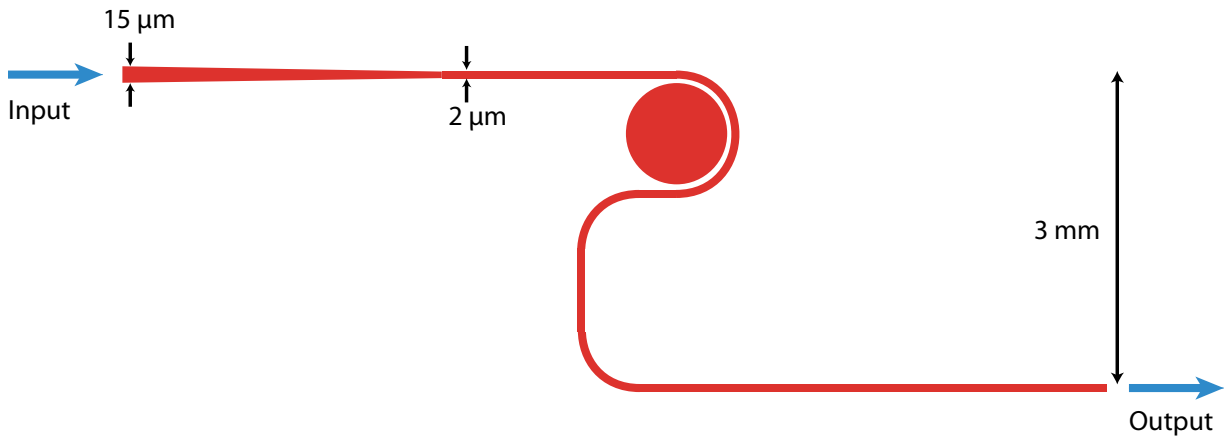


**Figure 6.3:** Illustration of an offset device with an input taper. The waveguide is tapered down from a 15 micron width at the facet (to help match the input fiber), down to a single mode dimension of 2 µm width.

The second issue we wish to solve is that of the mode overlap between the fiber and the waveguide core. For the near-IR, we work with lens-tip fibers that reduce mode field size significantly to improve waveguide coupling. Silicon microphotonics for telecom has also made extensive use of inverse tapers[184] that make the waveguide narrower at the input facet to enlarge the mode diameter such that it overlaps well with the input fiber. The input is then adiabatically tapered to the normal single-mode dimensions. As we are limited to ~2 µm resolution for our contact lithography process (Chapter 4), inverse tapers are not a feasible option (unless we switch to e-beam lithography). Hence, we fabricate a normal taper where the waveguide is wider at the input to match the physical size of the mid-IR fiber. Once again, the waveguide is adiabatically tapered to the single-mode width by making the taper long enough (~1 mm). As shown in Figure 6.3, we chose 15 µm as the input size for our devices, although we have also coupled to narrower input sizes and we present those results in the next section.

The third and final coupling issue is one of getting the laser output into a fiber. To our knowledge, there are no fiber-coupled 3-4 µm mid-IR light sources available commercially. Hence, we couple the free-space laser output from our Firefly laser into a mid-IR fiber using

a reflective collimator (Thor Labs). The collimator uses a 90° off-axis parabolic metallic mirror to focus the laser beam into a fiber coupler. The mirror maintains a constant focal length and high reflectivity (>96%) over a broad wavelength range, making it an excellent choice for our tunable Firefly laser.

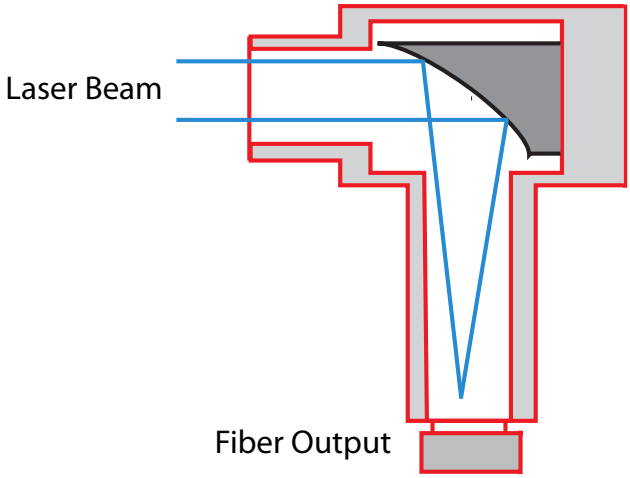


**Figure 6.4:** Schematic showing how the reflective fiber collimator functions. This component allows reasonably efficient coupling from a free-space laser into a fiber. The advantage with obtaining light out of a fiber is the relative ease with which one can then couple this light into an on-chip waveguide.

### 6.2.2 Coupling to mid-IR sources

We fabricated mid-IR devices using (i) $Ge_{23}Sb_7S_{70}$ and (ii) $Ge_{28}Sb_{12}S_{60}$ as the core material on a 4" silicon wafer with 3 µm of thermally grown silicon dioxide. An optical image showing one of our $Ge_{23}Sb_7S_{70}$ chips is shown in Figure 6.5; we can observe the offset devices as well as the non-offset devices comprising the device set. The 40 µm wide waveguides in this layout are used for alignment reasons – it is easier to couple to a large waveguide first (as a reference) and then move on to narrower ones. We have also fabricated samples with straight and offset waveguides (resonators) of various widths.

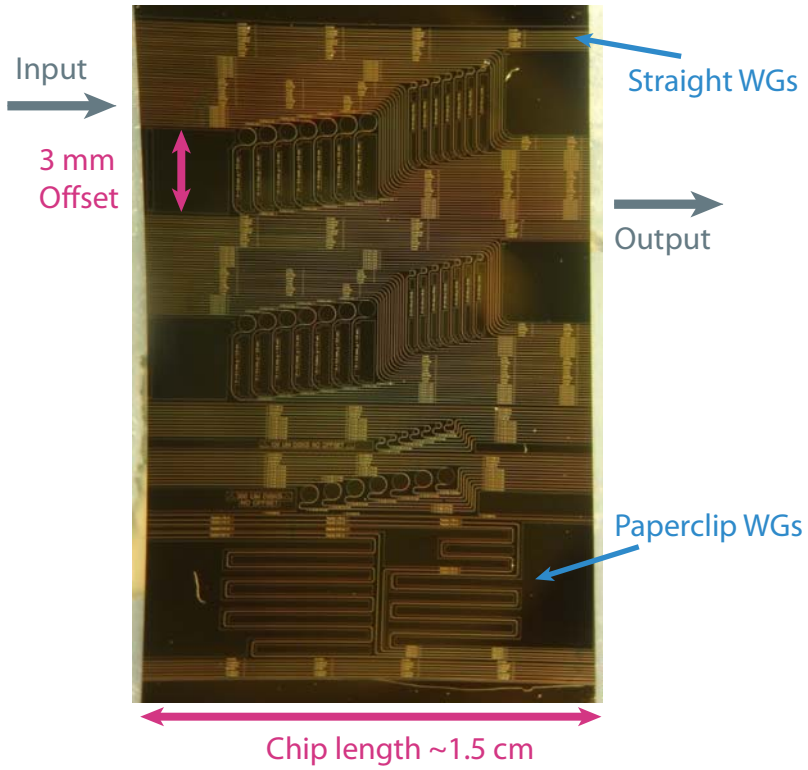


**Figure 6.5:** Image of fabricated GeSbS-on-oxide chip showing the offset structures and paper-clip like waveguides that offer variable lengths for measurement of transmission loss from a single chip.

Figure 6.6a and b show the first order mode captured by our InSb camera for a 40 µm wide $Ge_{23}Sb_7S_{70}$ straight waveguide at 3.3 µm and 3.6 µm. Although we can see the mode in these images, the fiber and substrate background is strong and makes finding the mode more difficult. We are also able to couple into the second-order mode for this waveguide by moving the fiber laterally along the width of the waveguide as seen in Figure 6.6c. Next, we look at a 40 µm $Ge_{23}Sb_7S_{70}$ waveguide with a 3 mm offset (Figure 6.7). The effect of adding an offset is evident: we are able to eliminate stray/background radiation from the optical fiber and the substrate and obtain a very clear image of the waveguide mode when compared to the non-offset case. Light guided through the waveguides is able to travel around the bends while light traveling through the substrate and the free space above the waveguides continues to travel in a straight line. The offset allows us to find waveguide modes more readily when measuring mid-IR devices as it is no longer buried within

background light. Figure 6.8 shows light coupled to a single-mode waveguide with a 15 µm input taper at 3.6 and 3.67 µm wavelengths. The mode is weaker, likely due to higher propagation losses, but still visible. Our collaborators at Physical Sciences, Inc. (PSI) performed independent measurements and have corroborated our results. Mode images from their system are shown in Figure 6.9.

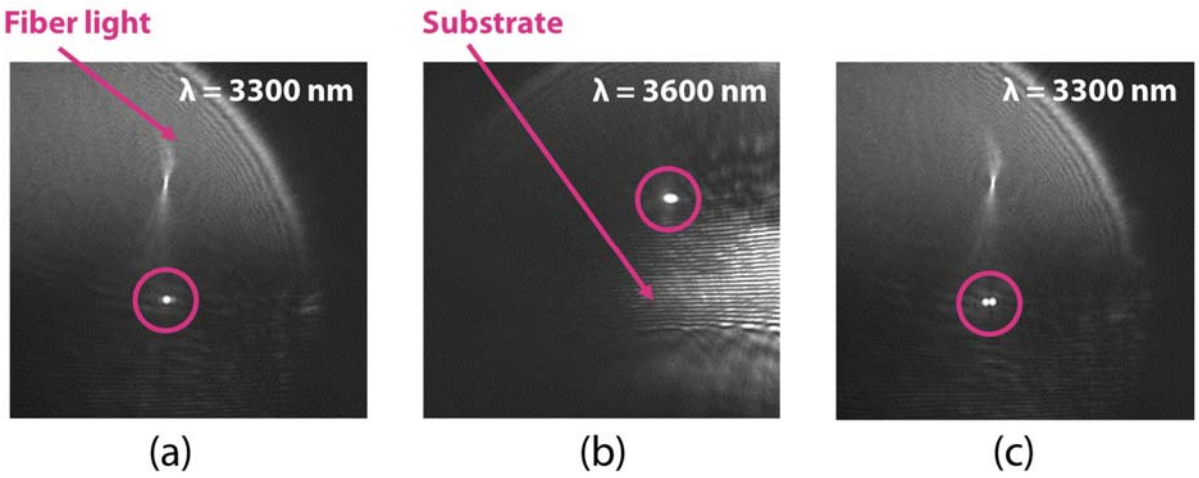


**Figure 6.6:** Mode images from 40 µm waveguides. (a) and (c) show first and second order modes from a straight waveguide at 3.3 µm while (b) shows the first order mode from a straight waveguide at 3.6 µm.

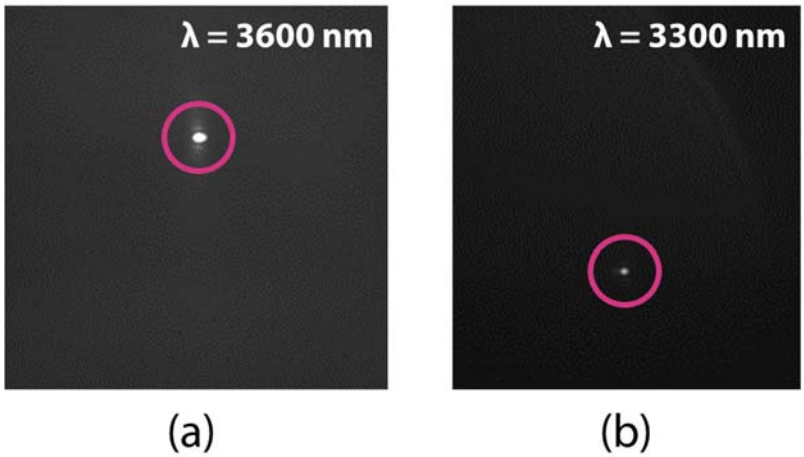


**Figure 6.7:** Mode images from an offset 40 µm waveguide at (a) 3.6 µm and (b) 3.3 µm showing a reduction in background radiation.

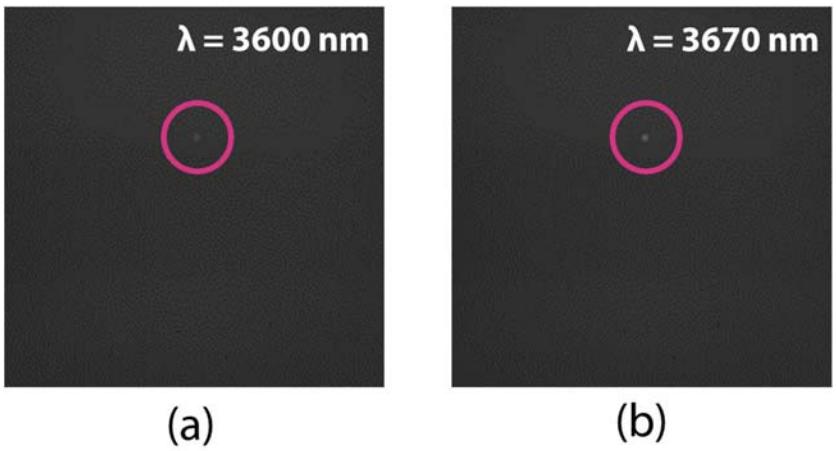


**Figure 6.8:** Mode images from a single-mode 2 µm waveguide with a 15 µm input taper at (a) 3.6 µm and (b) 3.67 µm.

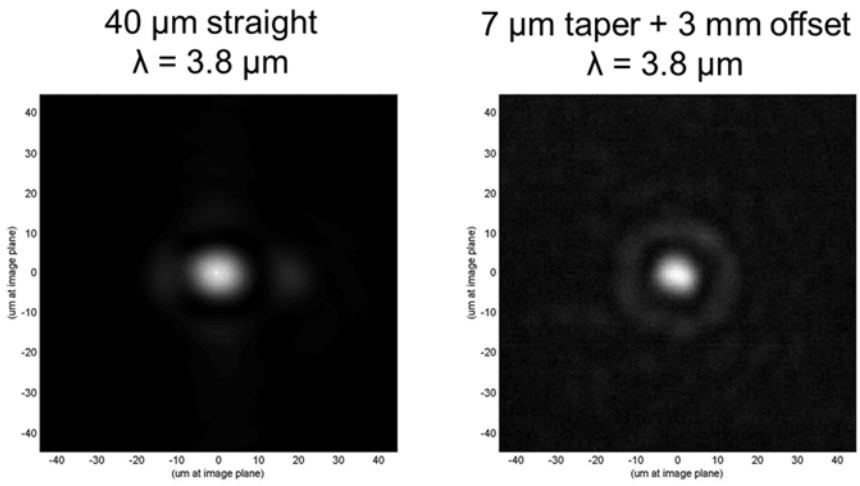


**Figure 6.9:** Mode images from ICL-coupled waveguides showing coupling to a 40 µm straight waveguide and a waveguide with a 7 µm input taper and 3 mm offset. Both measurements were performed at 3.8 µm.

We characterized our mid-IR waveguides by measuring propagation loss at various wavelengths. Loss numbers were obtained by first recording the mode intensity profiles for waveguides of different lengths. We observed that the strong light emission from our Firefly laser (60 mW average) saturated the camera so we used a neutral density (ND) filter between the fiber output and the camera. The ND filter reduces the light reaching the camera by three orders of magnitude and prevents camera saturation. By measuring the

laser intensity, we were able to obtain a dB value for transmission for each waveguide. We employ the cutback method for $Ge_{28}Sb_{12}Se_{60}$ waveguides and use the paperclip structures of different lengths for $Ge_{23}Sb_7S_{70}$ waveguides. Plotting the transmission in dB versus waveguide length gives dB/cm loss values from the slope of the linear fit. Figure 6.10 shows a loss versus length plot for the $Ge_{23}Sb_7S_{70}$ waveguides. Similar measurements on single-mode $Ge_{23}Sb_7S_{70}$ waveguides with 15 µm input tapers yielded a loss of 5.34 dB/cm. The precision of our measurements can be improved in the future by: (i) recording data from several waveguides with the same length and cross-section and (ii) starting with longer waveguides to get more waveguide lengths during cutback.

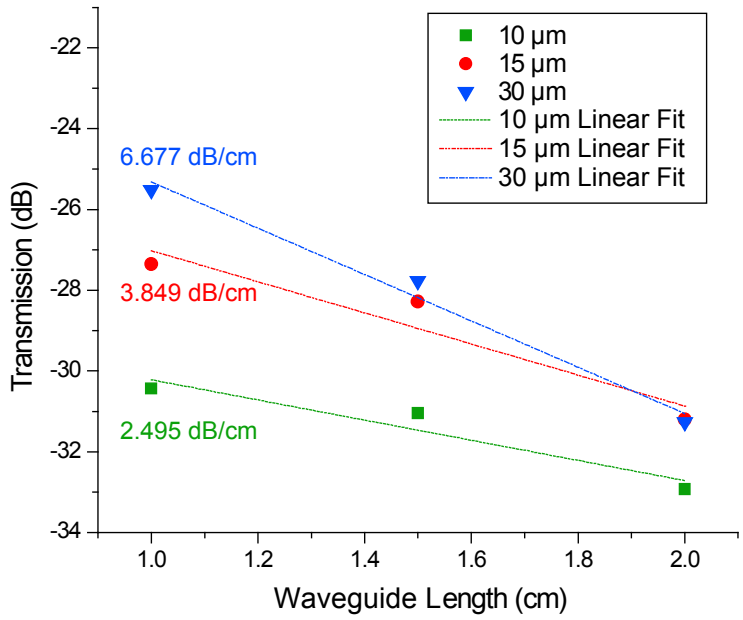


**Figure 6.10:** Transmission loss measurements from multimode $Ge_{28}Sb_{12}Se_{60}$ waveguides. The 10 µm wide waveguide yields the lowest loss of the ones tested at just under 2.5 dB/cm although the high insertion loss indicates that the coupling loss from the fiber is much higher. We can attribute the increase in loss with larger waveguides to a greater degree of multimode behavior.

For the longer-wavelength devices at 5.2 µm, we were able to calculate the propagation loss by characterizing measured resonant peaks in a similar manner to the near-IR resonator

measurements shown in Chapter 5. Our measurements reveal a loss of 0.7 dB/cm in $As_2Se_3$ core waveguides with $Ge_{23}Sb_7S_{70}$ as the cladding material[127].

## 6.3 Chemical sensing with uncoated ChG devices

Since various chemical and biological species exhibit absorption features in the 3-5 µm waveband, we can perform basic absorption sensing experiments using our mid-IR devices without any functionalization coatings. In this section, we present sensing results from waveguide-based devices at 3.6 µm using hexane as the chemical species and resonator-based devices at 5.2 µm using ethanol.

We select hexane as the absorbing species due to its strong absorption over the 3.4–3.6 µm wavelength range. Our wide $Ge_{23}Sb_7S_{70}$ waveguides demonstrated strong transmission at $\lambda = 3.6$ µm hence we would expect to see measurable changes in intensity upon addition of hexane liquid to the top of the waveguides. Preliminary testing reveals this assumption to hold true as shown in Figure 6.11. The integrated intensity incident on the InSb camera was monitored over a period of several minutes. Once we add hexane to the sample, the integrated intensity immediately drops by a significant amount. Given hexane's high vapor pressure[185], it evaporates rapidly and the intensity recovers within a few seconds. The intensity then remains constant until the end of the measurement.

During such a measurement, we observe that the change in intensity is not solely due to absorption in the analyte. Since most organic solvents have refractive indices around 1.3-1.4[185], the effective index of the waveguide being tested changes after the analyte is added. For multimode waveguides, this leads to a change in the order of the mode coupled into the waveguide. As this perturbs the fiber-waveguide coupling from its ideal position, the recorded intensity also drops. We tested for this behavior by exposing waveguides to carbon tetrachloride ($CCl_4$) which does not exhibit any absorption in this wavelength range. In

Figure 6.12, we show the reduction in intensity upon addition of $CCl_4$ and the presence of two peaks indicating a shift in the coupled mode from first order to second order.

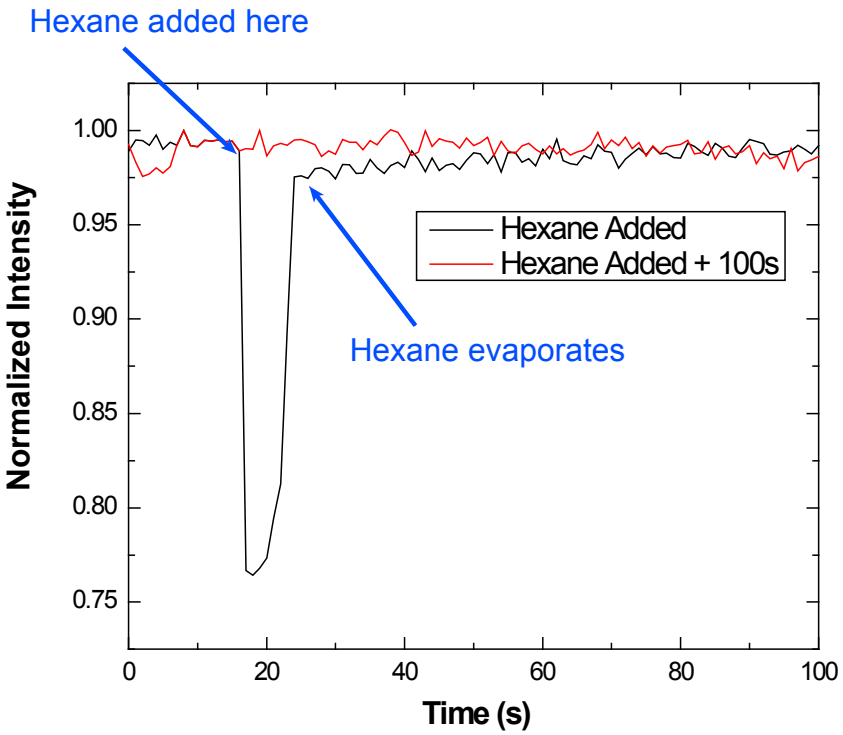


**Figure 6.11:** Average intensity plot showing the effects of adding hexane to our waveguides. We note that our InSb camera can only record data in 100-second intervals so the black data is for the first 100 seconds (includes the hexane addition) and the red data is for the following 100 seconds. The drop in intensity measured at a wavelength of 3.6 microns can occur due to (i) absorption and/or (ii) a change in effective index due to analyte addition, and hence a shift in the coupled mode from first order to second order. Better results may be obtained by using single-mode waveguides where the effective index change cannot cause a shift in mode order.

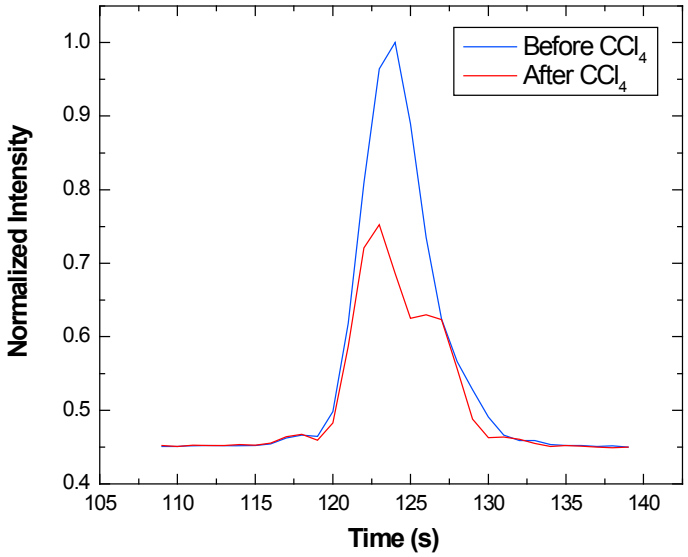


**Figure 6.12:** Normalized intensity profiles demonstrating a change in the mode order after $CCl_4$ is added to the waveguide. The reduction in intensity upon addition of $CCl_4$ and the presence of two peaks indicates a shift in the coupled mode from first order to second order.

At 5.2 µm, we have performed sensing measurements using ethanol to induce a change in the absorption as well as a shift in the refractive index of ChG resonators. Similar to the analyte index-induced change in effective index for waveguides, we can measure a shift in the resonant peak when an analyte is added to the resonator devices. Figure 6.13 shows an example of the change in resonant peaks as ethanol of various concentrations is added. We observe that the resonant peak position changes as in the case with nanofoams in Chapter 5 but there is also an associated change in the resonant peak height due to absorption from the O-H group in ethanol.

The organic chemicals used in the sensing tests, cyclohexane and ethanol ($> 99.5\%$), were purchased from Sigma-Aldrich. Cyclohexane shows low optical absorption around 5.2 µm and was used as the blank solvent. Ethanol has a weak absorption peak ($\sim 200$ dB/cm) at 5.19 µm and was used as the solute to analyze the performance characteristics of our resonator sensor. Their mixtures were prepared based on volume ratios. During the test, the entire surface area of the mid-IR resonators sensor was covered by drop-casted solutions.

Replacing air with cyclohexane led to increased coupling strength between the bus waveguide and resonator and a higher extinction ratio, suggesting that the device operates in an under coupling regime in air. At the same time, FSR of the resonator changed from 8.23 nm to 7.81 nm, which corresponded to a group index change from 2.12 to 2.20. The resonator *Q*-factor, however, remains almost constant, indicating relatively good optical transparency of cyclohexane at this wavelength range. Each transmission spectrum was obtained by averaging over five wavelength-sweeping scans. The temperature was stabilized at 20$^{o}$C throughout the tests.

Figure 6.13a shows the transmission spectra of the mid-IR $Ge_{23}Sb_7S_{70}$ resonator in cyclohexane solutions of ethanol of different concentrations (given in volume fractions). From the spectra we can see that the extinction ratio decreased with the increasing ethanol concentration, a clear indication of the resonator's transition into the under coupling regime. The wavelength blue shift of resonance peaks in solutions of different concentrations were attributed to the reduced refractive index of ethanol compared to cyclohexane, from which we estimate a confinement factor of about 10% in the solution. Figure 6.13b plots the optical absorption induced by ethanol solutions extracted from the spectra in Figure 6.13a. While this proof-of-concept experiment demonstrated the feasibility of on-chip cavity-enhanced sensing using chalcogenide glass micro-resonators, detection limit of the resonator device in terms of absorption coefficient is estimated to be only ~ 0.02 $cm^{-1}$, corresponding to a tens of parts-per-million (ppm) level limit of detection when applied to chemical sensing. Sensitivity of the device is primarily limited by the relatively high propagation loss in the resonator (~1 dB/cm), and can be possibly improved by implementing post-fabrication loss reduction treatment[48], or resorting to new detection mechanisms that circumvents the intrinsic sensitivity limit of direct cavity-enhanced spectroscopy[186, 187].

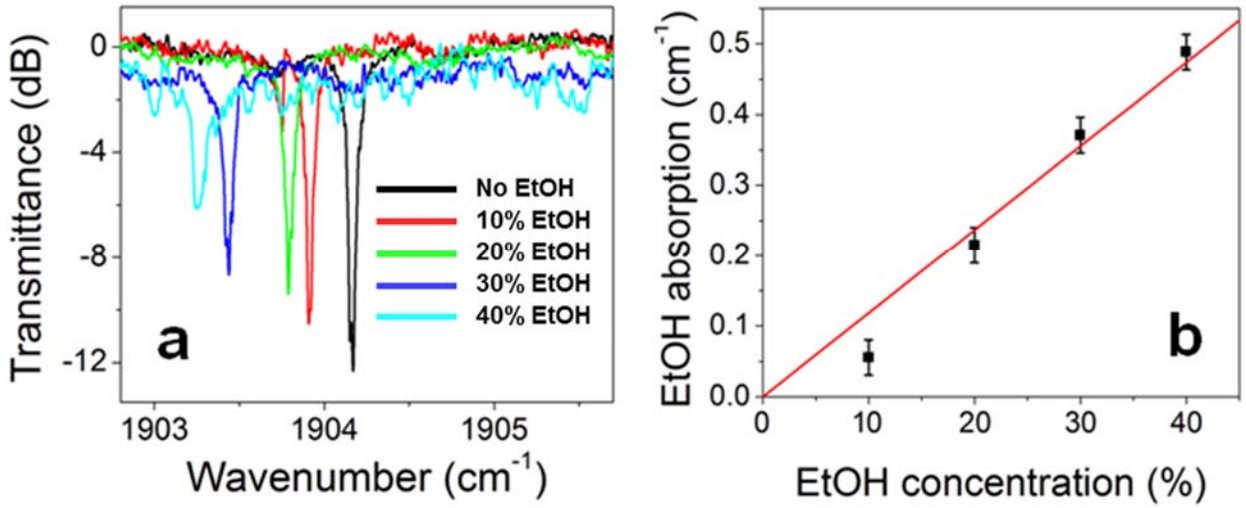


**Figure 6.13:** (a) Effect of adding progressively higher concentrations of ethanol in cyclohexane to ChG resonators. The peaks show a red shift and increase in extinction ratio with higher ethanol concentrations. (b) Plot of measured absorption caused by ethanol versus its concentration[57].

## 6.4 Silicon-based mid-IR waveguide systems

In addition to ChG-based mid-IR devices, we have also demonstrated mid-IR waveguide sensors operating at wavelengths from 2.5 µm to 3.7 µm using pedestal waveguides fabricated from crystalline silicon (shown in Figure 6.14a)[188] that can circumvent the $SiO_2$ absorption in the mid-IR (> 4.0 µm). Figure 6.14c demonstrates the in-situ sensing effect (with analyte addition) captured by an InSb camera placed near the output facet of a silicon pedestal waveguide. Prior to analyte addition, the camera image shows a single spot of light from the guided waveguide mode along with some scattered light. Following the chronological sequence as depicted by the thick red arrows in the figure, we see that the scattered light slowly disappears while the guided light intensity is attenuated by the absorption of analyte. The diminished scattered light intensity and the attenuated guided mode gradually recover over time as the analyte starts to evaporate and finally return to their original intensity when the analyte has completely evaporated. We have also developed

a similar structure on SOI with the pedestal being etched from the silicon dioxide undercladding. This Silicon on Oxide Undercladding Pedestal (SOUP) waveguide is shown in Figure 6.14b[117]. The large refractive index contrast and oxide undercut ensure minimal overlap of the waveguide mode with the silicon dioxide undercladding and we observe propagation of mid-IR light at wavelengths up to 3.7 µm.

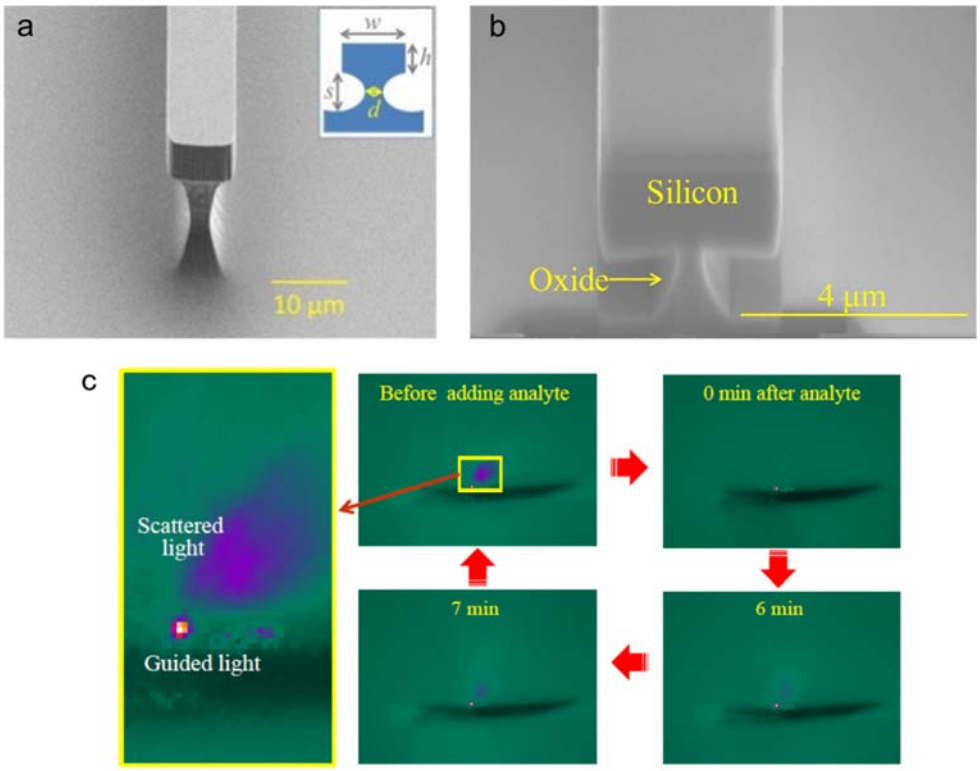


**Figure 6.14:** (a) SEM image of a silicon pedestal waveguide[188]; (b) SEM image of a SOUP waveguide[117]; (c) Mid-IR camera images showing in-situ attenuation and recovery of waveguide mode as an absorbing analyte is introduced and then allowed to evaporate.

The propagation loss in our air-clad pedestal Si structures is measured to be 2.7 ± 0.15 dB/cm using paper clip structures[118]. Since the devices and the substrate come from the same crystalline silicon wafer, our devices exhibit good mechanical stability and no defects are found during the cleaving process. From the mode characterization, the waveguides show a fundamental mode dominated profile at 3.7 µm. The large dimensions of the

waveguide increase the available interaction volume between the probe light and analytes, which increases the sensitivity despite a small evanescent field.

To demonstrate quantitative chemical sensing, air-clad Si pedestal waveguides are used to evaluate organic mixtures with different concentrations of target analytes. Figure 6.15 shows a plot of toluene (diluted with carbon tetrachloride) concentration versus waveguide mode intensity. As the weight ratio of toluene (in $CCl_4$) is gradually increased from 0 to 1, the guided mode light intensity measured at the output end of the waveguide consistently decreases. Since toluene has a strong absorption from the aromatic C-H stretch at $\lambda = 3.3$ µm, this is the selected wavelength. Carbon tetrachloride is chosen as the diluent, since it has no C-H bonds, hence its absorption will not interfere with that from toluene.

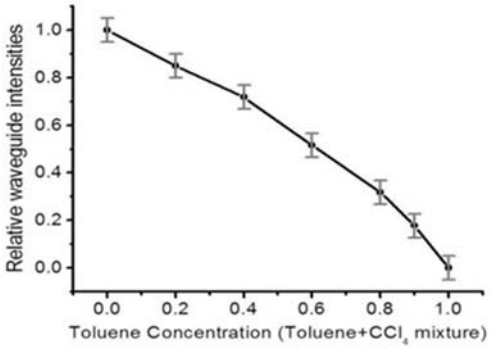


**Figure 6.15:** The waveguide mode intensities at different toluene/$CCl_4$ concentrations. The intensities decrease as the toluene ratio increases because of Mid-IR absorption from the aromatic C-H stretch in toluene at the selected wavelength $\lambda = 3.3$ µm[188].

Additionally, we can use the pedestal silicon waveguides to identify the chemical make-up of an unknown solution by appropriate selection of probe wavelengths that overlap with known characteristic absorption features. Silicon's mid-IR transparency window of up to 7 µm allows broadband laser scanning for multi-spectral and diverse chemical analyses. For instance, hexane has distinguishably higher absorbance at $\lambda = 3.55$ µm whilst compounds containing an amine functional group show an absorption feature between $\lambda = 2.85$ µm and

3.22 µm arising from N-H stretching. Figure 6.16 shows the measured absorbance for each chosen chemical analyte and compares it with prior literature results[188].

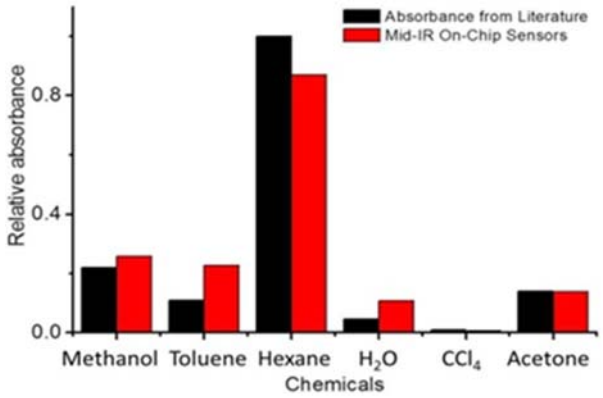


**Figure 6.16:** Chemical sensing using our fabricated on-chip mid-IR pedestal silicon waveguide sensor. Tested analytes show different absorbance at $\lambda = 3.55$ µm. Results from our measurements (red bars) are compared with that from literature (black bars)[188].

Amorphous low-stress silicon nitride ($SiN_x$) is an excellent material of choice for mid-IR microphotonic sensing devices since it is transparent up to a wavelength of 8.5 µm. Directional coupler devices allow on-chip light manipulation, a desirable feature in differential sensing. To demonstrate such a component for the mid-IR regime, we designed and fabricated $SiN_x$ directional couplers operating over the wavelength range 2.45 µm and 2.65 µm[189]. The spectral response of the fabricated devices, as captured by our mid-IR camera, is shown in Figure 6.17a. At an input wavelength of $\lambda = 2.45$ µm, a strong guided mode appears in the left waveguide (channel 1) but only a dim signal is observed in the right waveguide (channel 2). As the wavelength increases, the intensity of the left guided mode gradually decreases whereas the light from the right output increases. At $\lambda = 2.55$ µm the power transmitted through both channels is equal (50-50 power splitter). At $\lambda = 2.65$ µm, the guided light has completely transitioned into the right arm of our directional coupler.

Intensity profiles as a function of wavelength are shown in Figure 6.17b to quantitatively analyze the spectral dependence of coupling. We note that the guided modes from both channels retain sharp Gaussian profiles over the entire spectrum, confirming that the fundamental modes are well preserved during coupling. This preservation of the fundamental mode is critical for many applications, including mid-IR sensing and nonlinear light generation, because a higher order mode is associated with a different effective refractive index leading to undesired dispersion that can (i) lead to a false positive sensor signal during mid-IR detection and (ii) lower the efficiency of light generation. In addition, the total power from two channels remains constant during coupling yielding a high switching/splitting efficiency with minimal optical loss, thus enabling our $SiN_x$ mid-IR platform to be used for real-time on-site toxin monitoring and multi-chemical tracing.

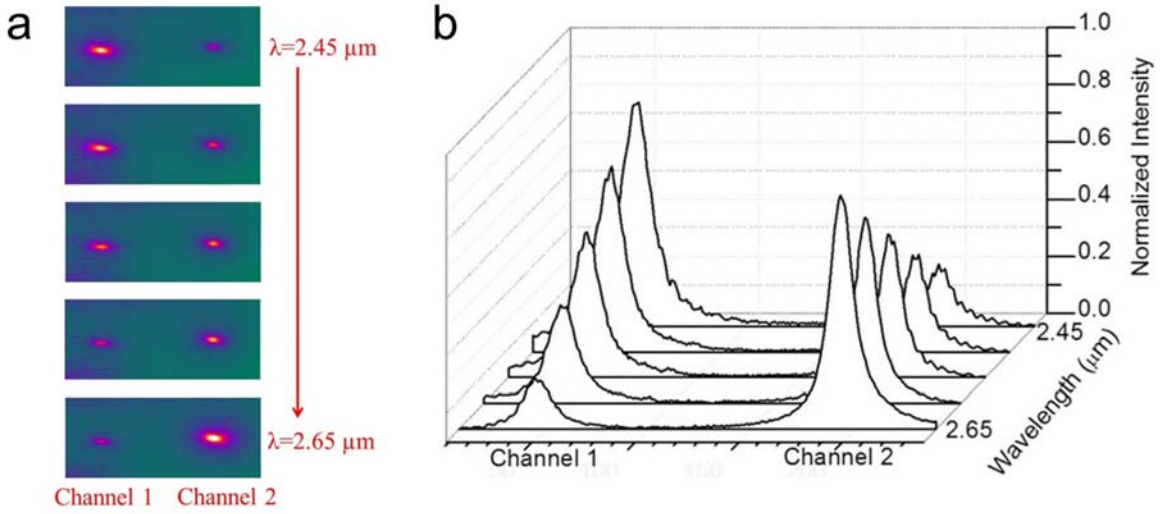


**Figure 6.17:** (a) Captured mid-IR images and (b) Intensity profiles of $SiN_x$ directional coupler as a function of wavelength. At $\lambda = 2.45$ μm channel 1 has maximum output, whereas maximum of channel 2 appears at $\lambda = 2.65$ μm. Guided waves remain fundamental modes in both channels[189].

## 6.5 Summary

In this chapter we have discussed (i) our recent device characterization efforts in the mid-infrared wavelength regime and (ii) the challenges associated with measuring mid-IR devices

and solutions to address them. We employ input-to-output offsets, standard tapered waveguides, and a fiber collimator to improve mid-IR measurements. We have also evaluated chemical sensing in the mid-IR using ChG waveguides and a tunable light source and observed that multimode waveguides are not ideal for sensing. In the next chapter, we consider lead telluride as a photodetector material and develop mid-IR waveguide-integrated detector structures for on-chip sensing applications.

# Chapter 7: Lead Telluride for On-chip Photodetection

## 7.1 Infrared detection

Photodetection of infrared radiation is key to many technical applications across the IR spectrum. In the near-IR regime, the development of low-loss silica fibers[1] has enabled high-speed telecommunications at 1310 and 1550 nm wavelengths and detectors based on germanium[190] and III-V materials[191] have gained widespread use. Moving to longer wavelengths, IR detection can play a key role in various fields such as spectroscopy, bio/chemical sensing, thermal imaging, environmental monitoring, and forensic analyses. Hence, there exists a significant body of work researching various materials systems and device designs for IR photodetection. A number of different device structures exist for photodetection in general and IR detectors in particular. Broadly, we can divide the types of detectors into two categories[1, 49]:

(i) Thermal detectors that rely on a change in the temperature induced by absorption of photons. The change in temperature is then responsible for a change in a material property such as resistance. Bolometers and pyroelectric detectors fall into this category.

(ii) Photon detectors that rely on the generation of carriers in the material when light with the appropriate photon energy is incident on them. The change in the carrier concentration can then be related to a photovoltage or photocurrent output. Photoconductors, photodiodes, Schottky diodes, and quantum well photodetectors fall into this category.

Thermal detectors tend to have simpler structures and lower production costs[49] when compared to photon detectors that often need multiple layers and single-crystal growth techniques, which inherently increase fabrication costs. However, thermal detectors have slower response times and typically lower responsivities as well. No matter the type of detector used, smaller bandgaps ($< 0.4$ eV) of mid-IR materials increase the possibility of noise at room temperature where the thermal energy of electrons ($kT \sim 25$ meV) becomes significant. Hence, to avoid the associated dark current noise and achieve the highest possible responsivity, most mid- and long-wave-IR detectors are operated at low temperatures such as 213K (thermoelectric coolers) and 77K (liquid nitrogen).

In this chapter, we will explore using thermally evaporated lead telluride (PbTe) based photoconductive detectors for monolithic integration with our chalcogenide glass devices. The basic operating principle of a photoconductor involves applying a voltage or current bias to the detector between two metal electrodes that form ohmic contacts[1]. When the detector is illuminated by above-bandgap radiation, electrons and holes are generated in the material and swept to the contacts due to the electric field created by the applied bias. When a constant current bias is applied, the photo-induced change in voltage across the metal contacts can be measured; similarly, the photocurrent can be measured when the applied bias is a constant voltage.

## 7.2 Materials systems for IR detection

The choice of materials for infrared photodetection depends on the wavelength range demanded by the given application. Mercury cadmium telluride (HgCdTe or MCT) remains the most commonly used photodetector material for the mid-IR as its bandgap can be tuned for response covering a wide range of wavelengths (3–30 µm)[49, 192]. Commercial detectors based on MCT are widely available, including ones operating at room temperatures[193]. Many

III-V materials are also suitable candidates for mid-IR photodetection. Indium antimonide (InSb) has been used for imaging applications[194, 195] such as the mid-IR camera discussed in Chapter 6. However, these semiconductor materials are limited to lattice-matched substrates using expensive growth techniques such as molecular beam epitaxy (MBE) and metal organic vapor phase deposition (MOCVD). Often, integrating electronics with these detectors requires flip-chip bonding[49]. Consequently, integration with other structures such as waveguides for on-chip applications presents a significant challenge.

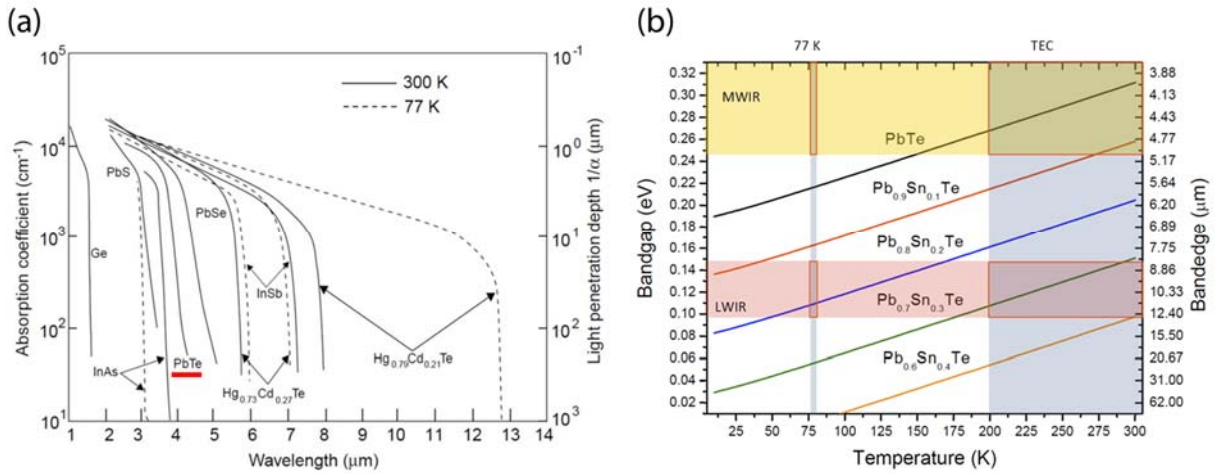


**Figure 7.1:** (a) Absorption spectra of various commonly used mid-IR detector materials[49]. (b) Bandgap variation of PbTe-SnTe alloys[196].

Lead chalcogenides (PbTe, PbSe, PbS) are II-VI semiconductor compounds with small band gaps suitable for mid-IR applications in the 3–5 µm wavelength range and have been extensively studied[49, 51, 54, 197]. PbTe has a rock salt crystal structure with a lattice parameter of 6.46 Å[198]. Single-crystal films of PbTe have been grown using liquid-phase epitaxy and molecular beam epitaxy[199, 200] on lattice-matched substrates such as $BaF_2$. However, for monolithic integration applications, growing epitaxial films presents significant challenges due to thermal restrictions and limited choice of substrate materials. To this end, we have proposed using polycrystalline PbTe as an alternative. With no lattice-matching constraints,

we can grow PbTe films on any substrate using simple thermal evaporation techniques from a single source of PbTe at room temperature.

PbTe offers another key advantage: the ability to alloy with SnTe ($E_g \sim 0.19$ eV) to form a $Pb_xSn_{1-x}Te$ alloy with a smaller bandgap[196, 201] as shown in Figure 7.1b. This allows the possibility of longer wavelength detection in the 6–12 µm wavelength range for coverage of a large fraction of the mid-IR spectrum where all the chemical vibrational absorption features reside.

## 7.3 Characterization of PbTe thin films

Prior work in our research group has studied the responsivity of thermally evaporated polycrystalline PbTe thin films of varying thicknesses at room temperature and at thermoelectrically-cooled temperatures (-60°C or 214 K). A 100 nm thick PbTe detector layer was found to exhibit high photoresponsivity (25 V/W) in the 3-4 µm wavelength range under a bias current of 0.1 mA at -60°C[52, 55, 56].

Before working on integrated detector structures, it was vital to ensure that the PbTe films being deposited for this work had similar or better performance figures compared to past films. We characterized the newly deposited PbTe films using X-Ray Diffraction (crystalline structure), Atomic Force Microscopy (surface roughness), Transmission Electron Microscopy (grain size and shape), Hall Effect (electrical properties), and photoconductivity (responsivity) measurements. Thin films of PbTe with a thickness of 250 nm were prepared using thermal evaporation techniques described in Chapter 2.

X-Ray Diffraction (XRD) measurements (Figure 7.2) of the 250 nm film demonstrate a polycrystalline film with a preferred (200) orientation. In comparison with the standard reference spectrum, our evaporated film shows good agreement but the ratio of intensities

of the (200) peak to the (220) peak is higher in our films at 4 versus the reference at 1.45, indicating a degree of preferred texturing in our films.

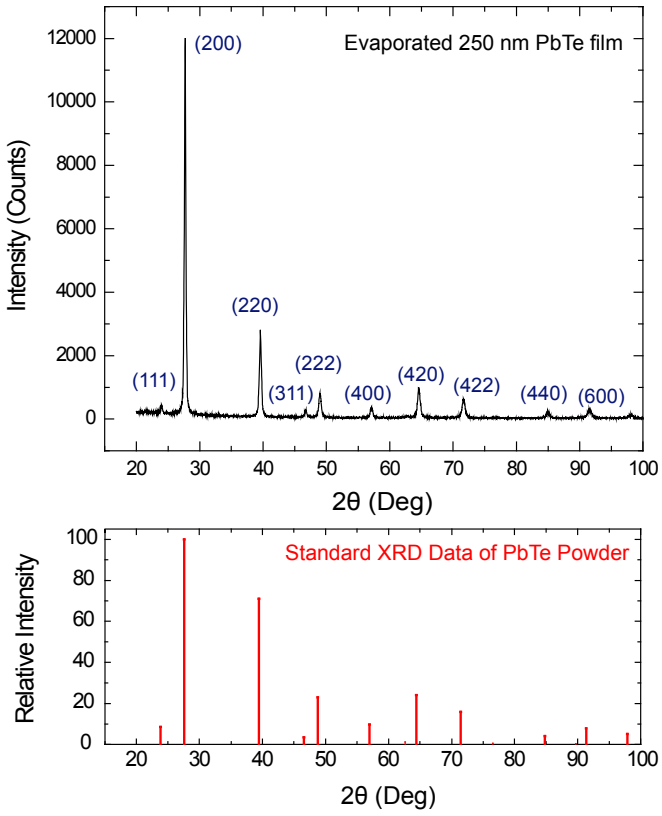


**Figure 7.2:** X-Ray Diffraction (XRD) data measured from the evaporated 250 nm film. We observe that the film matches the reference pattern very closely but the ratio of the intensities of the (200) and (220) peaks is higher, indicating that the (200) direction is favored by the film.

We also characterized the structure of the films using cross-sectional transmission electron microscopy measured grain sizes of about 50-100 nm in the PbTe films. Atomic force microscopy measurements of the surface of the deposited films exhibit a low RMS roughness value of 2.8 nm for the 250 nm thick film. Both results are shown in Figure 7.3.

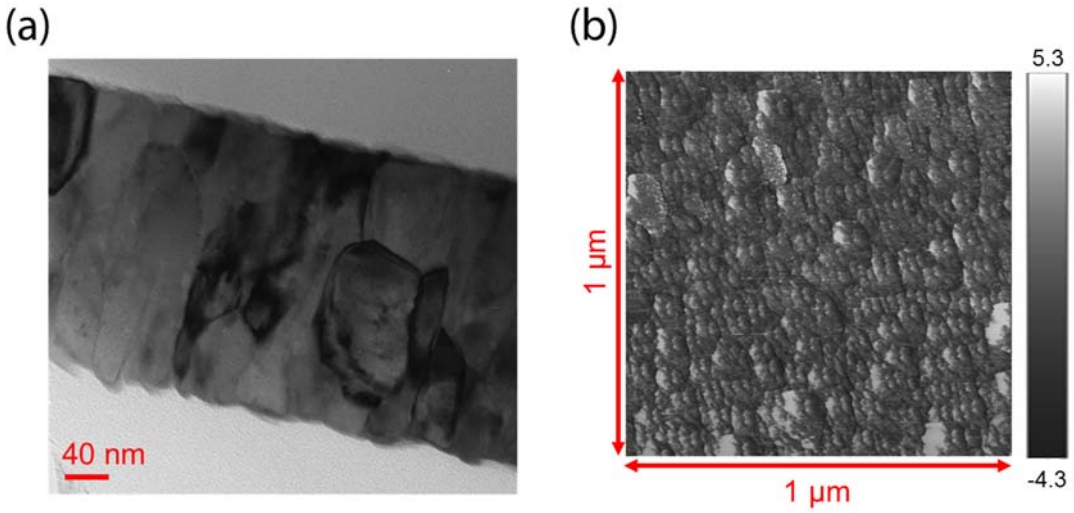


**Figure 7.3:** (a) Cross-sectional TEM image taken from a 250 nm thick film showing grain sizes of ~50-100 nm; (b) AFM phase image of the same film. The RMS roughness calculated from the AFM measurement is approximately 2.8 nm.

Electrical characterization of the deposited films was performed using Hall Effect measurements at room temperature. Table 7.1 summarizes the measured data and compares it to prior collected data. We see that the new films exhibit *p*-type conduction and relatively low carrier concentration.

**Table 7.1:** A comparison of current and previous PbTe films shows good agreement in electrical properties, although the new films exhibit somewhat higher resistivity and lower mobility, which could lead to higher responsivity values.

| | **Current Film** | **Wang et al.[52]** |
|---|---|---|
| **Carrier concentration ($cm^{-3}$)** | $1.49\times10^{17}$ | $2.1\times10^{17}$ |
| **Carrier type** | p-type | p-type |
| **Resistivity (Ω-cm)** | 1.99 | 0.56 |
| **Mobility ($cm^2/V \cdot s$)** | 20.81 | 53 |

In addition to this data, we also measured the resistance of the thin film over a range of temperatures, demonstrating that the electrical conductivity mechanism is thermally activated hopping conduction with an activation energy of 0.137 eV. A plot of the resistance (log) versus inverse temperature with a linear fit is shown in Figure 7.4.

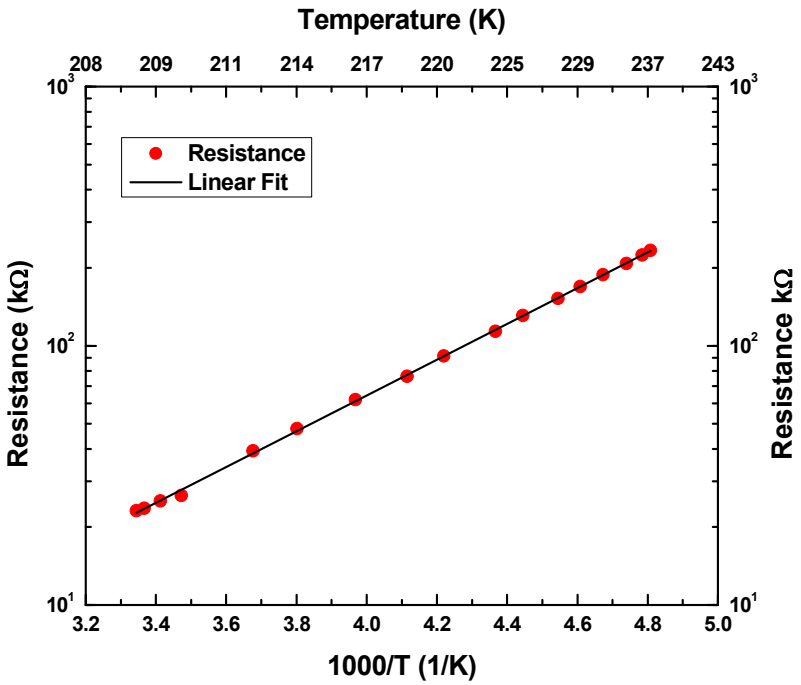


**Figure 7.4:** Resistance of a 2 mm x 1 mm film of PbTe across a range of temperatures controlled by a thermoelectric cooler (TEC) demonstrating that the electrical conductivity mechanism is thermally activated hopping conduction.

Finally, we measured the photoresponse of the evaporated films using a monochromator setup illustrated in Figure 7.5 over a wavelength range of 1–5 µm. First, a reference measurement is taken with a thermocouple-based detector with known active area (1 mm$^2$) and responsivity (0.3 V/W). Next, the PbTe structure is measured over the same wavelength range. Knowing the area of the PbTe film (2 mm$^2$), we can calculate the responsivity of the PbTe film with the following equation:

$$\Re_{PbTe} = \Re_{Ref} \frac{V_{PbTe}}{V_{Ref}} \frac{A_{Ref}}{A_{PbTe}} \tag{12}$$

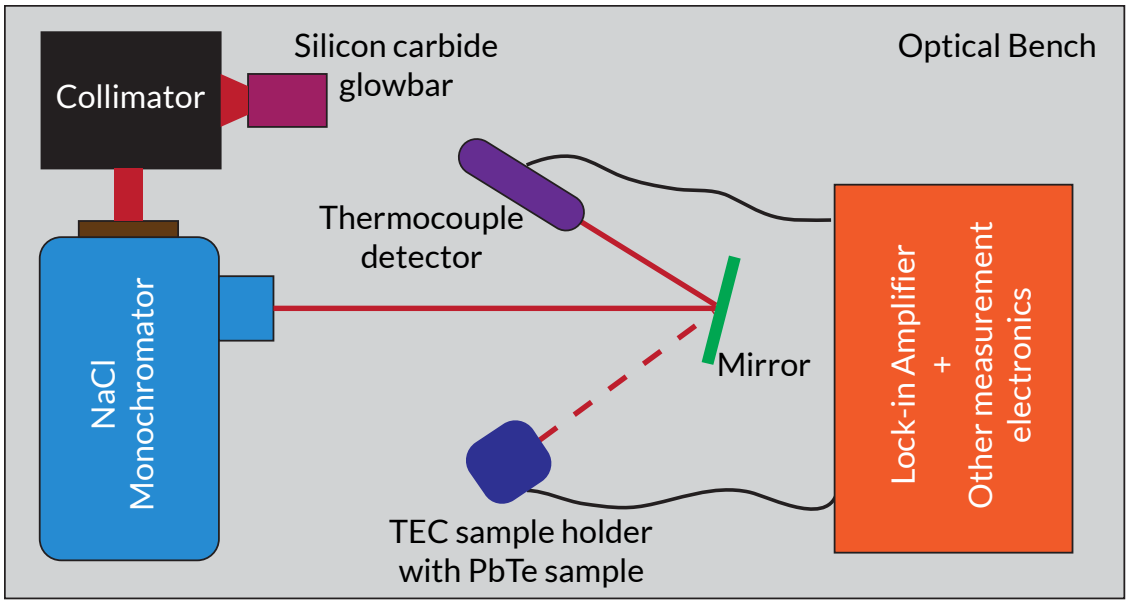


**Figure 7.5:** A schematic of our photoconductivity measurement setup. The light source is a silicon carbide glowbar that acts as a blackbody source, which passes through a NaCl prism-based monochromator. The output light is reflected from a metal mirror into a thermocouple reference detector first and then into the PbTe sample holder (with TEC).

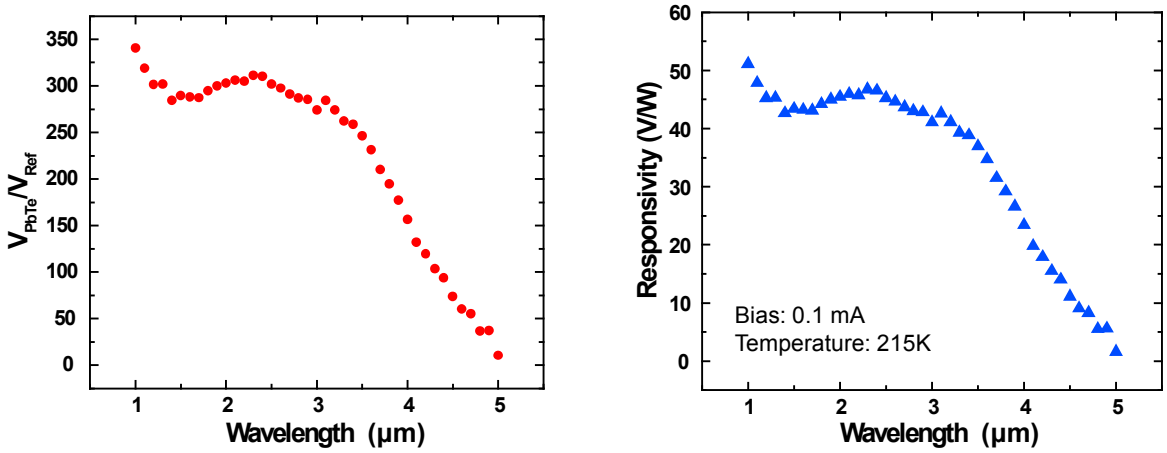


**Figure 7.6:** (Left) Ratio of the measured voltages of the PbTe film and the reference thermocouple detector. (Right) Responsivity of the PbTe film under a 0.1 mA bias and a temperature of 215K. Peak responsivity in the 1-4 μm wavelength range is approximately 45 V/W, which is higher than our previous efforts[55].

The measured films show good responsivity peaking at about 45 V/W, which is higher than the numbers achieved in prior research. We also note that the responsivity drops off

after 4 μm indicating that the incident photon energy is not high enough to induce electronic transitions from the valence band to the conduction band.

## 7.4 Oxygen sensitization of PbTe

From a materials perspective, further improving the responsivity of polycrystalline PbTe films for mid-IR detection may be possible by increasing carrier lifetime or by reducing carrier concentration. One way to enhance the photoresponsivity of polycrystalline PbTe films is to incorporate some oxygen into the films during either the deposition or post-deposition through diffusion from the ambient. For example, incorporation of oxygen in lead chalcogenide films can enhance carrier lifetimes due to spatial separation of photo-generated electrons and holes by minority carrier traps ($PbO^+$)[202-205]. Since as-deposited PbTe films tend to be Te-deficient[206], they start out as *n*-type with relatively high carrier concentrations. Upon oxygen exposure, the $PbO^+$ traps capture the electrons and the conduction switches over to *p*-type with a carrier concentration defined by the amount of oxygen incorporated. Typically, there will be an ideal amount of oxygen that compensates the *n*-type carriers such that the carrier concentration of the film is close to intrinsic levels[204, 206, 207]. Further addition of oxygen beyond this level increases the hole concentration and reduces resistivity, proving detrimental to the photoresponsivity of the films.

Oxygen sensitization is typically achieved using high temperature ($> 450°C$) anneals in an oxidizing atmosphere[208, 209]. For the monolithically integrated structure that we are proposing, such anneals will have detrimental effects on the ChG materials underneath the PbTe layer. However, we have demonstrated that room temperature oxygen sensitization of PbTe is possible and leads to improved responsivity[55, 56]. Sufficient oxygen can be added to films by exposure to ambient or through oxygen gas leaked into the deposition chamber during PbTe growth.

## 7.5 Optimization of key parameters for high signal-to-noise ratio

Detector optimization requires that we examine the physics underpinning the signal to noise ratio (SNR). The key parameters controlling the SNR can then be used to design our integrated detector structures to ensure the highest possible absorption in the PbTe layer. We start by looking at the changes induced in the photoconductor upon illumination with above-bandgap radiation. The change in voltage in the illuminated portion of the photoconductor with an applied current bias is given by:

$$\Delta V = I \times \Delta R = I \times \left[\frac{1}{\sigma + \Delta\sigma} - \frac{1}{\sigma}\right] \frac{l}{wt} \approx I \frac{l}{wt} \times \frac{-\Delta\sigma}{\sigma^2}, \Delta\sigma \ll \sigma \tag{13}$$

where $w$ and $t$ are the width and the thickness of the photoconductor, $l$ is the length parallel to the bias current $I$, $\Delta R$ is the change in resistance, $\boldsymbol{\sigma}$ is the conductivity, and we assume that PbTe exhibits long carrier lifetimes. The change in conductivity ($\boldsymbol{\Delta\sigma}$) is related to changes in carrier concentration and to changes in mobility[210]:

$$\sigma = ne\mu_n + pe\mu_p \rightarrow \Delta\sigma = (\Delta ne\mu_n + \Delta pe\mu_p) + (ne\Delta\mu_n + pe\Delta\mu_p) \tag{14}$$

where $n$ and $p$ are the electron and hole concentrations, $e$ is the elementary charge, and $\mu_n$ and $\mu_p$ are the electron and hole mobilities. The change in conductivity can thus be written as the sum of the changes due to carrier concentration (first term) and the mobility (second term):

$$\Delta\sigma = (\Delta\sigma)_{cc} + (\Delta\sigma)_{\mu} \tag{15}$$

Our PbTe photoconductive films show no change in mobility with illumination therefore the barrier modulation contribution[211] linked to the change in mobility may be ignored and we adopt number modulation theory[212], which has produced results consistent with experimental measurements on our previous photodetector devices[56]. As the lifetimes

of electrons and holes in our materials are nearly equal, we can equate $\Delta n$ and $\Delta p$, to express the change in the number of carriers as:

$$\Delta n = \Delta p = \frac{\tau}{\frac{hc}{\lambda} ltw^2} \int_0^w P(w)dw \rightarrow \frac{\eta\tau P_{opt}}{\frac{hc}{\lambda} ltw} \tag{16}$$

where $P_{opt}$ is total optical power sent down the waveguide (integrated over the width $w$), $\lambda$ is the wavelength of illumination, $\tau$ is the photo-generated carrier lifetime, $\eta$ is the quantum efficiency, $h$ is Planck's constant and $c$ is the velocity of light. We can assume that incident optical power is distributed evenly along the propagation direction of the waveguide, and thus we can combine Eqn. (14) and Eqn. (16):

$$\Delta\sigma = \frac{e\eta\lambda\tau(\mu_n + \mu_p)P_{opt}}{hc \times lwt} \tag{17}$$

Defining the responsivity $\mathfrak{R}$ as the change in voltage over the incident light power (V/W) and setting $\sigma = pe\mu_p$ for a $p$-type system we can combine Eqn. (13) and Eqn. (17) to get

$$\mathfrak{R} = \frac{I\eta\lambda\tau(1+b)}{hce \times w^2t^2p^2\mu_p} \rightarrow \mathfrak{R} \propto \frac{\eta}{(wt)^2} \tag{18}$$

where $b$ is the electron-hole mobility ratio and $w$ and $t$ are the width and the thickness of photoconductor. To optimize the design we focus on the dimensions of the photoconductor, thus simplifying the equation. For photoconductive detectors, shot noise is non-existent and at reasonably high chopping frequencies, Johnson noise, defined as $V_J = [4kTR_d\Delta f]^{1/2}$, is the dominant noise contributor in our detectors[56, 213] where $R_d$ is the dark space resistance of the entire detector and $\Delta f$ is the bandwidth. We use a noise voltage because we hold current constant and measure a change in the voltage. If we assume that $\Delta\sigma << \sigma$, the signal-to-noise ratio (SNR) becomes:

$$SNR \propto \sqrt{\frac{\eta^2}{w^3 t^3 l}} \tag{19}$$

From Eqn. (19) we see that thinner and shorter detectors maximize the SNR, but our simulations show that the quantum efficiency is also linked to detector dimensions.

## 7.6 Waveguide-integrated PbTe detector design and simulations

### 7.6.1 Design overview

Our integrated detector design uses vertical evanescent coupling from ChG waveguides into mid-IR PbTe detectors. An inherent challenge with such a design is the large index difference at $\lambda$ = 3.2–3.8 μm between our ChG materials ($n$ = 2-3) and PbTe ($n$ = 5.2). Placing the detector layer in direct contact with the waveguide layer will give rise to modal mismatch and Fresnel reflection, leading to inefficient absorption. Evanescently coupled detectors using hybrid integration of III-V detectors for 2.2–2.3 μm detection[214] and monolithically integrated Ge detectors for telecom wavelengths have been demonstrated[190]. However, we present design and simulation results for a new and important wavelength range useful in chem-bio sensing. We demonstrate a mid-IR waveguide-detector integration scheme using a ChG waveguide monolithically integrated with a mid-IR PbTe photoconductive detector. Unlike their bulky off-chip counterparts, mid-IR microsensor arrays integrated with PbTe detectors can enable the low-cost, small footprint, remote detection of multiple chemical/biological species on a single silicon platform.

Figure 7.7a shows the layout of our ideal evanescently coupled detector and Figure 7.7b shows a cross section of the detector waveguide system. The $As_2Se_3$ waveguide in this case is designed for single mode operation at 3.2 μm and the $Ge_{23}Sb_7S_{70}$ glass ($n$ = 2.15) undercladding prevents leakage into the silicon substrate. The spacer (nominally $n$ = 1.5) in Figure 7.7 covers the entire sample and can function as a planarizing layer, with the

PbTe extending laterally beyond the waveguide. In the next section, we will focus on improving waveguide-detector coupling performance by optimizing the geometry of the PbTe detector layer for a high signal-to-noise ratio.

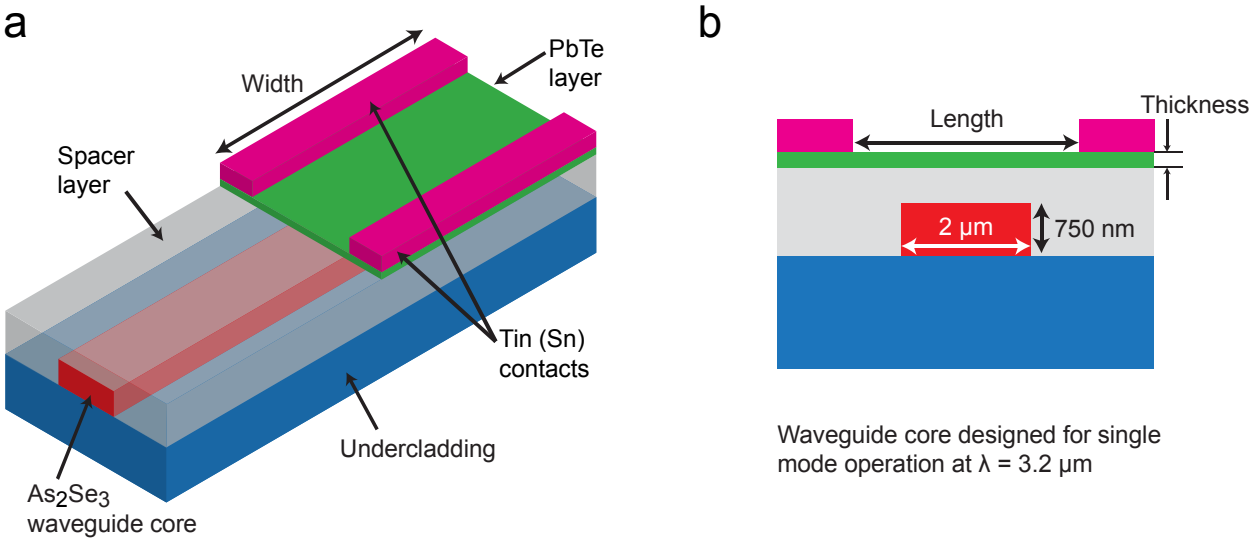


**Figure 7.7:** (a) Integrated structure with a single mode ($\lambda$ = 3.2 µm) $As_2Se_3$ waveguide, GeSbS glass undercladding to prevent leakage of mode into Si substrate, low index spacer to minimize modal mismatch and Fresnel reflection, and the photoconductive PbTe layer. (b) Cross section of the device with dimensions used for design and simulation[215].

### 7.6.2 Electromagnetic simulations

For the structure shown in Figure 7.7, the modes were first calculated using the commercially available mode solver FIMMWAVE and then injected into FIMMPROP (both by Photon Design) to study the field distribution during propagation. In addition to simulating mode behavior in the integrated structure, detailed 3D finite-difference time-domain (FDTD) simulations were also carried out with Lumerical's FDTD Solutions package to find optimal values of the detector dimensions that lead to the highest quantum efficiency. A conformal mesh size setting of 6 was used for the entire structure with a finer mesh (10 nm) chosen for the PbTe layer due to the lower thickness. The light source in Lumerical was a single wavelength mode source at $\lambda$ = 3.2 µm. Note that we will refer to

the internal quantum efficiency of the detector as the quantum efficiency for this analysis and assume that lifetimes and current applied are held constant as we change dimensions. More details on the simulation tools used can be found in the Appendix.

Figure 7.8 illustrates the role of the spacer layer; Figure 7.8a shows the field distribution with the PbTe placed directly on top of the waveguide while Figure 7.8b demonstrates the effect of adding the spacer layer shown in Figure 7.7. Without a spacer layer, the incident power is concentrated in the first 10 µm and such a design is undesirable due to high Fresnel reflection arising from the large refractive index contrast between the waveguide and detector. The addition of the spacer layer helps to extend the distance over which the field is distributed as it modifies the effective index such that the waveguide-detector mode survives longer and the field distribution is more uniform. Figure 7.8c shows the cross-sectional profile of the waveguide-detector mode.

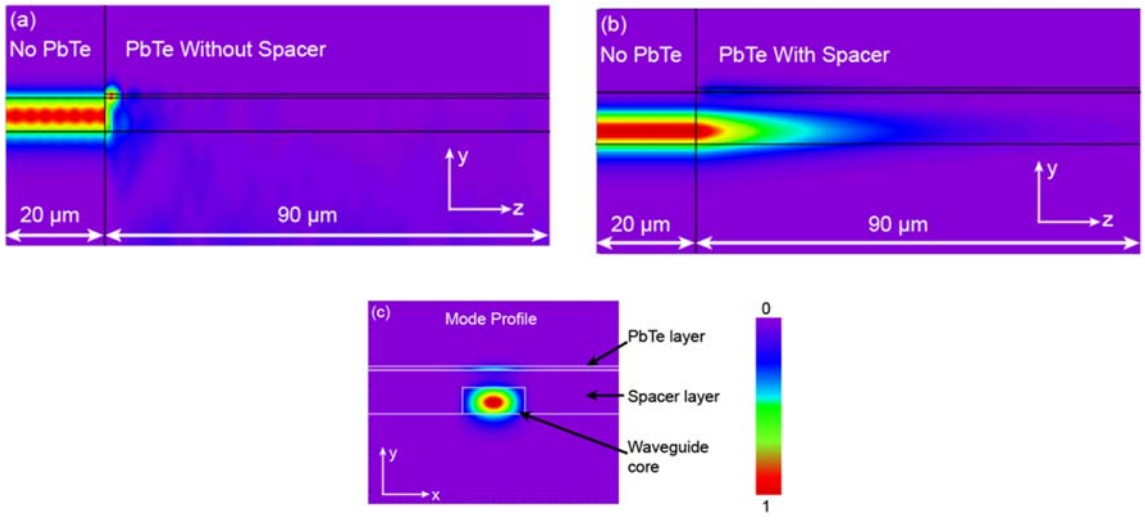


**Figure 7.8:** (a) Cross section of field profile of detector without spacer layer showing non-uniform mode absorption in the first 5-10 µm of the material; (b) Field profile with a spacer layer shows a less abrupt transition to the detector over 50 to 100 µm allowing for lower current densities. (c) Profile of the waveguide-detector mode with the field in both the waveguide and the PbTe layer[215]. The larger detector size also assists the fabrication process as alignment tolerances and resolution requirements can be lowered.

Figure 7.9 shows the effect of varying the width and thickness of the detector on the quantum efficiency. As the width of the photoconductor is increased, more IR radiation couples into the system increasing the quantum efficiency. However, the thickness of the detector sets the maximum quantum efficiency of the system, which is clearly seen in Figure 7.9b where the quantum efficiency increases as the thickness of the detector increases up to 90-100 nm of thickness. A thicker film contains more of the evanescently coupled mode, thus increasing the likelihood of absorption. As films grow thicker than 100 nm the quantum efficiency decreases due to higher reflection resulting from the larger refractive index of PbTe. If the detector layer is too thin, an insufficient amount of light is absorbed which leads to lower quantum efficiency.

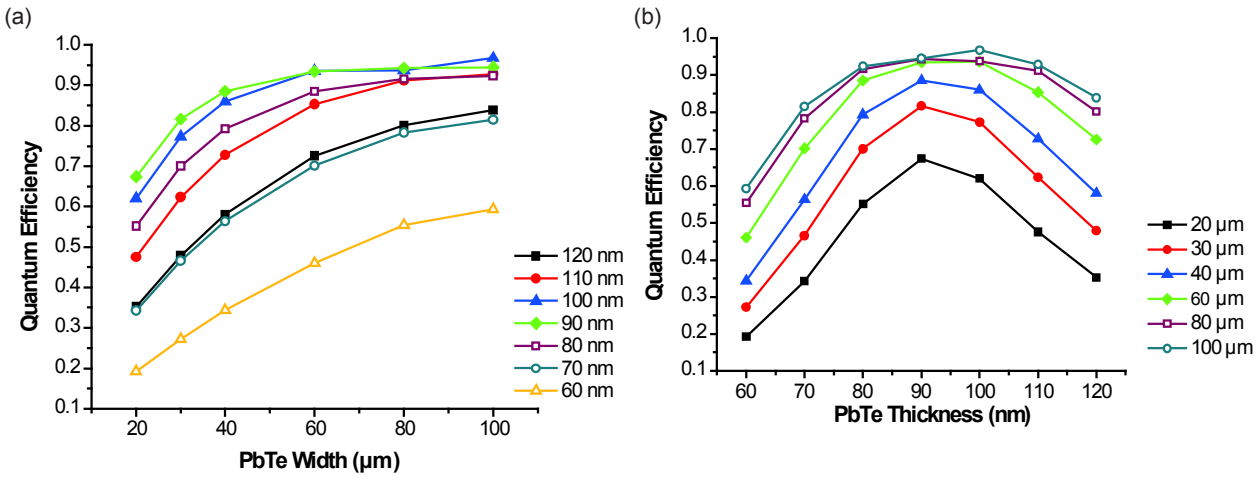


**Figure 7.9:** (a) Relation between quantum (or absorption) efficiency and the detector width at various detector thicknesses shows higher efficiency with increasing detector width as more light couples into the system. (b) Relation between quantum efficiency and the detector thickness at various detector widths shows that increasing the detector thickness increases the efficiency as more of the propagating mode is contained in the detector. Increasing the thickness beyond 90-100 nm alters the effective index to an extent that negatively impacts performance[215].

These results can be inserted into Eqn. (19) to evaluate the impact of the width and thickness on the device's SNR. Figure 7.10a shows the normalized figure-of-merit (FoM) for the SNR of the detector – smaller widths are preferable even though the quantum efficiency is reduced due to the relatively small effect of detector width on quantum efficiency and the

$w^{-3/2}$ dependence of SNR on width. In Figure 7.10b we see that the intensity of the incident light is not constant, however, if we assume that charge carriers have sufficient mobility to drift towards areas of lower concentration and that even in the highest intensity areas the $\Delta\sigma << \sigma$ assumption still holds true, we do not have to alter the SNR FoM.

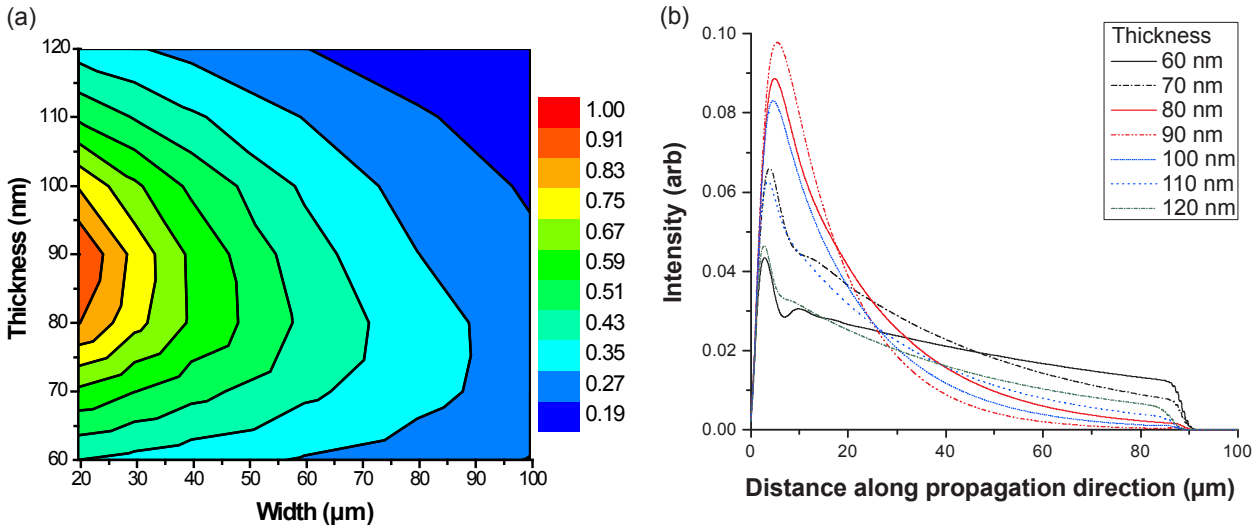


**Figure 7.10:** (a) The effect of the width and thickness of the detector on the SNR figure-of-merit represented in a contour plot. (b) Intensity of the coupled light along the width of the detector. In all cases, a good portion of the light is absorbed within the first 20-30 μm, and then falls off gradually with distance.

The length of the detector (distance between electrical contacts) also affects the SNR. Eqn. (19) states that a shorter detector will improve the SNR but parasitic absorption losses from metal contacts can negatively impact the quantum efficiency. From FDTD simulations we have found that a minimum separation of 750 nm between the waveguide edges and the metal contacts is required to limit the change in quantum efficiency to less than 5%. Given the geometry shown in Figure 7.7 this pins the minimum length of our devices to about 4 μm.

### 7.6.3 Spacer layer materials

The spacer layer is an important part of our waveguide-integrated detector design and the choice of an appropriate spacer layer material is contingent on it meeting the primary requirements of transparency in the wavelength range of interest and relatively low refractive index (1.4 – 1.6 is ideal). Ease of deposition should also be a consideration so that integrity of the lower waveguide layer remains intact. With these considerations in mind, polymer materials that can be spin-coated may prove to be good choices in some wavelength ranges. However, most polymers have a backbone comprised of C-H bonds and might contain N-H and O-H bonds which all exhibit characteristic absorption peaks in the 3-3.5 μm wavelength range.

**Table 7.2:** Comparison of some spacer layer material candidates.

| | **Transparency** | **Index** | **Fabrication** |
|---|---|---|---|
| **Polymers** | O-H absorption around 2.9 μm, C-H vibration around 3.4 μm | 1.2-1.6 | Spin-coating/CVD |
| **Alkali halides** | Up to 7 μm ($CaF_2$), 22 μm (KBr) | 1.3-1.6 | Sputtering/evaporation |
| **Silica** | Up to 3.8 μm | 1.41 | Sputtering/evaporation/CVD |
| **Alumina** | Up to 5 μm | 1.7 | Sputtering/evaporation |
| **Fluorinated, deuterated polymers** | Up to 7 μm (Teflon) | 1.3 | Spin-coating/CVD |

Relatively few materials meet all of these requirements but we have identified some inorganic compounds that are suitable at certain mid-IR wavelength ranges. Silicon dioxide ($SiO_2$) can be used for wavelengths below 3.8 μm where the loss is lower than 0.5 dB/cm (for silica glass)[32]. It can be deposited using a variety of thin film deposition techniques such as sputtering and chemical vapor deposition. For wavelengths up to about 5 μm[58], we believe

that $Al_2O_3$ (deposited via electron beam evaporation or sputtering) is a viable option. Finally, extending the use our design at still longer wavelengths to take advantage of the wide transparency window of ChGs will likely require alkali halides such as $CaF_2$ or KBr.

To evaluate the effect of using different spacer layers on our design parameters, we conducted further 3-D FDTD simulations. Figure 7.11 shows how the waveguide-integrated detector design is able to accommodate different materials with different refractive indices (1.43 for $SiO_2$ and 1.65 for $Al_2O_3$) by a simple modification of the spacer layer thickness. The thickness and width of the PbTe layer remain available as further variables that can be optimized to achieve the maximum possible absorption efficiency with any choice of spacer material that fits the criteria described above.

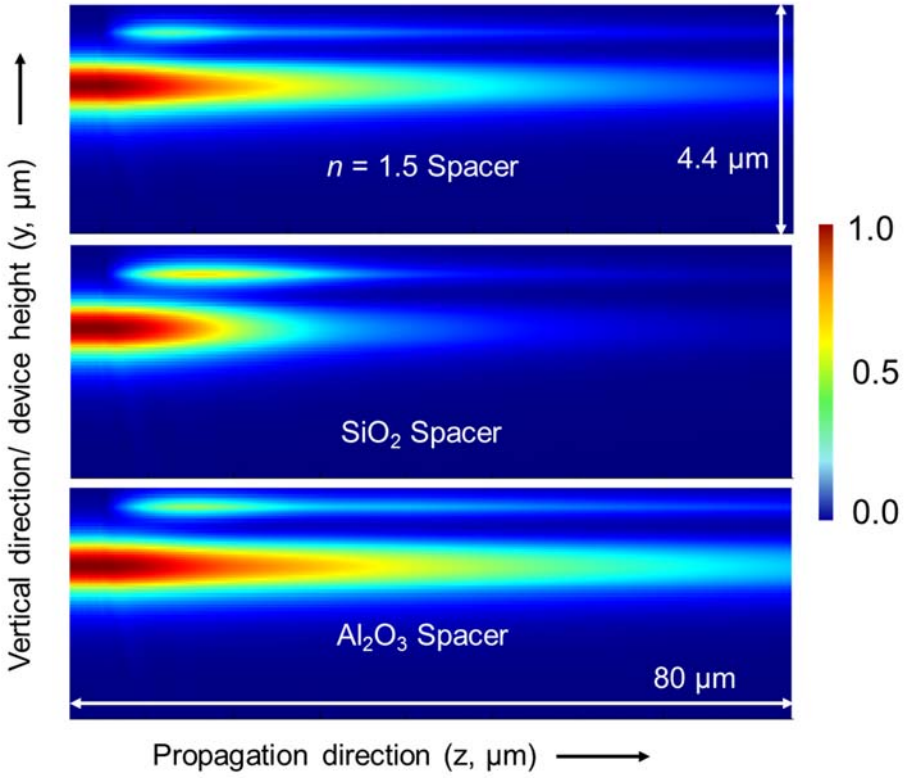


**Figure 7.11:** 3-D FDTD simulations of integrated device at $\lambda = 3.2$ μm for a 100 nm thick PbTe layer. The side (YZ) cross-section views presented for three different spacer layers exhibit the flexibility of the proposed design: all three materials allow for a gradual absorption of light in the PbTe layer with minimal reflections[117].

## 7.7 Integrated detector fabrication development

Fabrication of the integrated detector structure with a spacer layer builds upon the demonstrated processing expertise in fabricating ChG-based waveguide and resonator structures as well as PbTe-based detectors. As shown in Figure 7.12, the process flow for the detector structure begins with a waveguide/resonator structure already fabricated. The spacer layer is then deposited (spin-coating or evaporation/sputtering) on the devices followed by deposition and patterning of negative photoresist. After evaporation of the detector material and lift-off, the process is repeated to get the metal contacts in place using e-beam evaporation and lift-off photolithography.

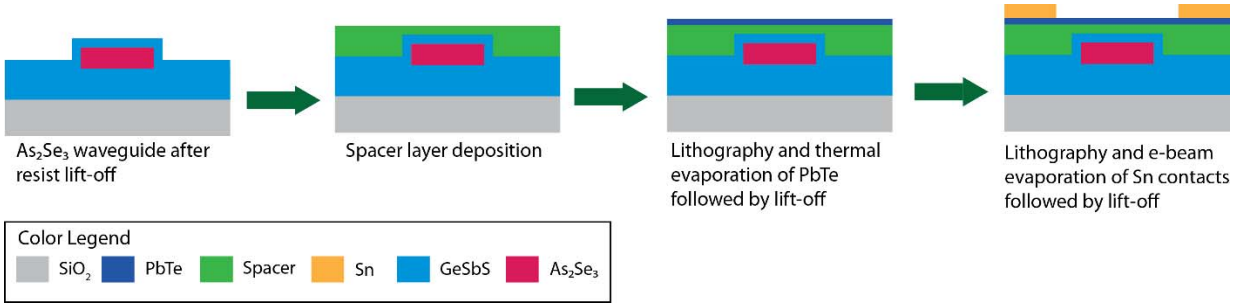


**Figure 7.12:** Process layout for fabricating an integrated PbTe detector on top of a ChG waveguide. We start with a fabricated waveguide structure and then deposit the spacer layer before performing separate lithography and evaporation steps for PbTe and metal contacts.

The waveguide-integrated detector designs we have proposed incorporate disparate materials that need to be integrated together in a monolithic fashion with each successive layer aligned to, and process-compatible with the previous layer. Starting with mid-IR waveguides and resonators fabricated according to details presented in Chapter 4, we have developed waveguide-integrated detector processing plans that have allowed us to fabricate our first prototype devices designed for 3.2-3.8 µm wavelength operation. For these mid-IR wavelengths below our 4 µm cut-off, we (i) selected $SiO_2$, deposited via plasma-enhanced chemical vapor deposition (PECVD) at a low substrate temperature of 130°C to prevent heating the ChG layers to their glass transition and to protect them from potentially

cracking due to a thermal expansion mismatch with the substrate; (ii) developed a suitable photolithography process with NR9-1000PY and a thermal evaporation process for PbTe followed by lift-off in acetone; (iii) incorporated a second lithography step to define the electrical contact patterns in resist on an electron beam evaporated tin (Sn) metal contact layer. Resist lift-off is once again performed in acetone accompanied by sonication[117].

Figure 7.13 shows optical images taken at different steps along the device fabrication process. The multimode interferometer (MMI) structure shown in Figure 7.13a was designed for a 50-50 split between the two arms with the aim of placing the detector structure on one arm and using the other arm to align the light source to the waveguide. The single-mode (2 µm wide) waveguides gradually taper out to a 5 µm width to improve the alignment tolerance between the PbTe layer and the waveguide. Figure 7.13b is an optical image of the device before metal deposition and the final device is shown in Figure 7.13c. We observe that the detector and metal layers are well aligned to each other as well as to the waveguide underneath the spacer layer (not visible, as $SiO_2$ is transparent).

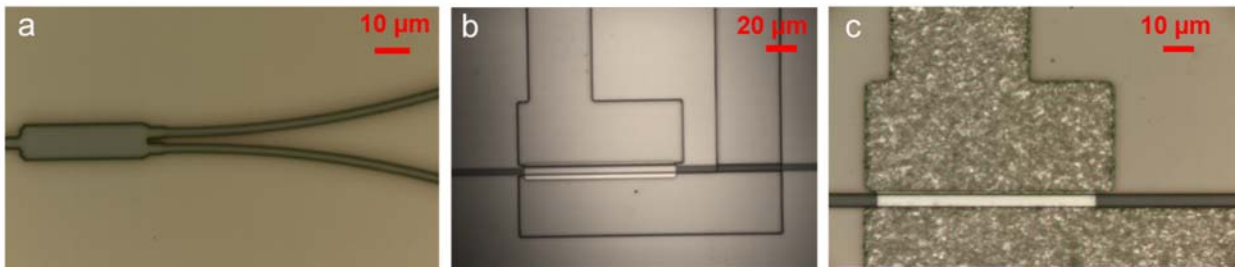


**Figure 7.13:** (a) MMI waveguide prior to spacer layer deposition; (b) Resist pattern for metal contacts aligned to PbTe layer; (c) Final device after metal deposition.

Figure 7.14 shows SEM images of the fabricated prototype devices including cross-sectional views. We can clearly see all the layers involved in the integrated detector structure and that the various structures are well-aligned to each other demonstrating that the processing approach proposed here is viable and produces devices that closely match the design parameters discussed in this chapter. However, we do note that the PECVD

oxide is a conformal coating and hence the PbTe layer is not planarized. An ideal choice of spacer layer material would allow for a flatter PbTe layer so that the discontinuities in the film do not effect electrical performance.

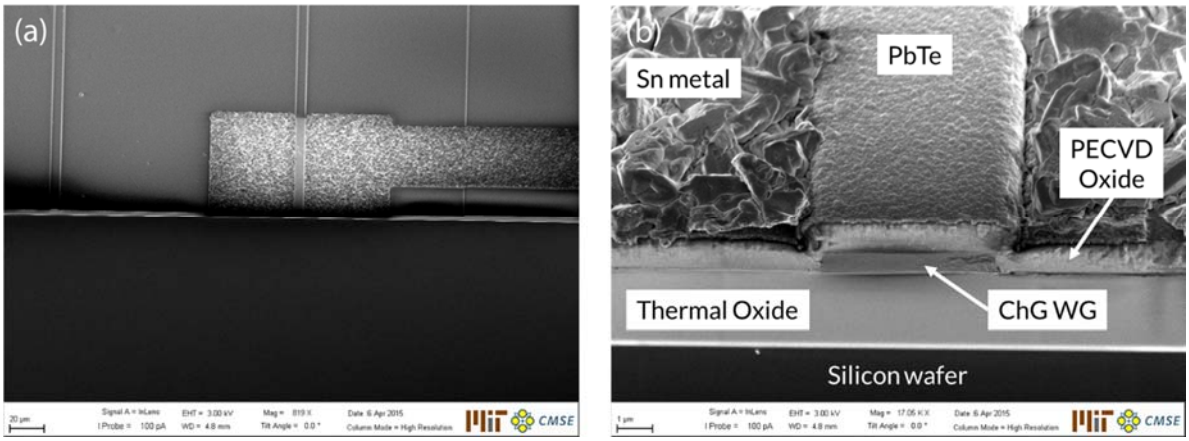


**Figure 7.14:** (a) Plan view SEM image of the integrated detector structure; (b) 45° tilted view. The $As_2Se_3$ waveguide is on a silicon wafer with 3 µm thermal oxide. A layer of PECVD $SiO_2$ is on top of the waveguide followed by PbTe and Sn layers.

For initial testing purposes, we also fabricated two further structures with multimode waveguides similar to those tested in Chapter 6. The first is comprised of a $Ge_{23}Sb_7S_{70}$ core and a silicon dioxide spacer layer deposited via PECVD with PbTe on top. The second design places the PbTe layer first, ensuring planarity, and uses $Ge_{23}Sb_7S_{70}$ as a thin spacer layer with a $Ge_{28}Sb_{12}Se_{60}$ core as the top layer. Cross-sectional SEM images of the two structures are shown in Figure 7.15 and we discuss experimental results in the next section. Our FDTD simulations for these structures show high absorption efficiency but the light is not absorbed uniformly as in the ideal case.

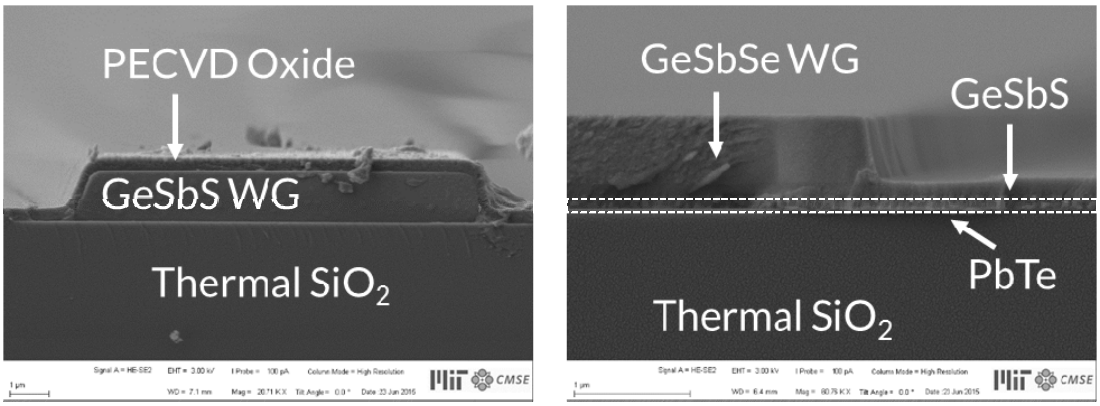


**Figure 7.15:** (Left) Integrated detector structure with PECVD oxide and PbTe on top; (Right) Detector structure with PbTe on the bottom and $Ge_{23}Sb_7S_{70}$ as a spacer.

## 7.8 Testing waveguide-integrated PbTe detector prototypes

We first tested the $Ge_{23}Sb_7S_{70}$ waveguides clad with PECVD oxide and observed no waveguide transmission at ~3.2-3.6 μm and weak modes at shorter wavelengths. To obtain any coupling at all, the oxide sample had to be cleaved to a very short (~4 mm) length after which we achieved good coupling at a shorter wavelength of 2.672 μm but not at 3.6 μm. Waveguides fabricated in the same batch but without an oxide layer performed similarly to those presented in Chapter 6. This indicates that the PECVD oxide is a source of significant loss at longer wavelengths, potentially due to the presence of impurities and defects causing absorption and scattering losses. We note that the thermally grown oxide used as the undercladding in our structures does not exhibit the same problem.

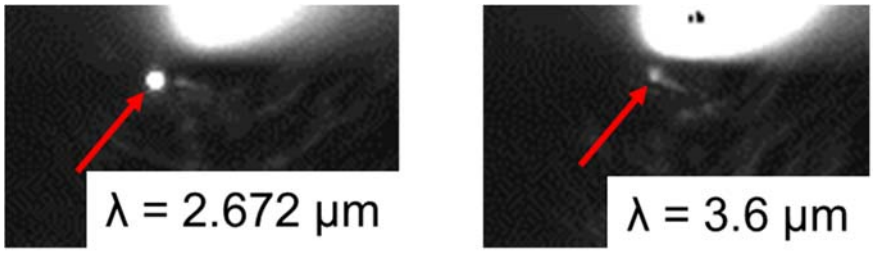


**Figure 7.16:** We observe an intense mode at the shorter wavelength of 2.672 μm (left) but it is much weaker at 3.6 μm. This shows that the PECVD oxide is affecting transmission at longer wavelengths, potentially due to defects and impurities.

As the quality of the oxide did not affect transmissivity of the waveguides at telecom wavelengths, we were able to perform integrated detector characterization at the shorter wavelengths. Ellipsometry measurements on our evaporated PbTe thin films show a large absorption coefficient at telecom wavelengths ($k \sim 0.73$). We measured the mid-IR waveguides before and after depositing a layer of PbTe on the LUNA system and compared loss values. If all of the light is attenuated due to the addition of a PbTe layer (absorption, reflection, and scattering), we should expect to see no output on our infrared camera. Our data shows that insertion loss increase by about 11 dB after a PbTe layer is deposited, indicating that not all of the light coupled into the waveguide is affected. We also measured similar uncoated waveguides after PbTe deposition on other parts of the sample and found the loss to only increase by about 1.4 dB, which can be accounted for by considering differences in coupling efficiency at the waveguide input.

**Table 7.3:** Insertion loss data at 1570 nm from $Ge_{23}Sb_7S_{70}$ waveguides designed for multimode operation in the mid-IR. The waveguides are measured before and after a PbTe deposition that only covers half of them. Our measurements on uncoated waveguides exhibit minor changes in transmission loss (~1.4 dB) indicative of typical measurement variation.

| Waveguide Width (μm) | Loss before PbTe deposition (dB) | Loss after PbTe deposition (dB) | Difference (dB) |
|---|---|---|---|
| **10** | 17.35 | 28.30 | 10.96 |
| **15** | 17.10 | 28.88 | 11.78 |

We then tested multimode $Ge_{28}Sb_{12}Se_{60}$ waveguides with and without a PbTe layer underneath. Unlike the PECVD oxide waveguides, the $Ge_{28}Sb_{12}Se_{60}$ waveguides without PbTe exhibit strong transmission at 3.6 μm as shown in Figure 7.19. When we try to couple light into waveguides with PbTe under them, we observe no guided mode, only stray light from the fiber and substrate. We tested multiple waveguides with and without PbTe and

obtained the same results, demonstrating that the PbTe layer is responsible for attenuation of the mid-IR radiation in these structures. With electrical measurements, we should be able to identify what fraction of the input light is being absorbed by the PbTe layer in this case.

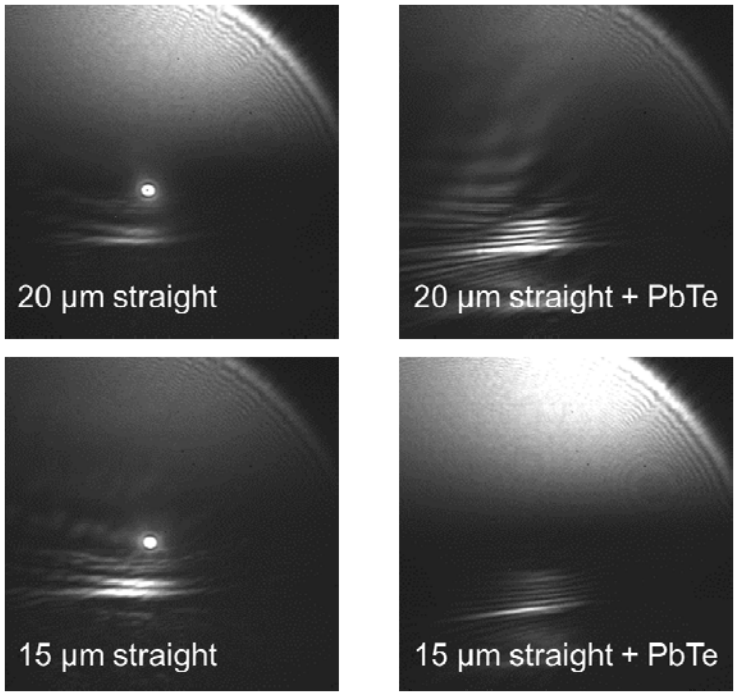


**Figure 7.17:** Transmission captured from multimode $Ge_{28}Sb_{12}Se_{60}$ waveguides fabricated on top of PbTe and a spacer layer of $Ge_{23}Sb_7S_{70}$. When we compare identical waveguides from the same sample, we observe that the waveguides with PbTe under them do not show any mode transmission whereas the waveguides with no PbTe show intense modes. This indicates that the addition of the PbTe layer has led to the waveguide light being absorbed as predicted by our simulations.

## 7.9 Summary

In summary, we have proposed a novel design that integrates PbTe detectors with ChG waveguides for on chip mid-IR detection. Our simulations show that the use of a spacer layer leads to a well-distributed field along the width of the detector, and that the quantum efficiency of the detector increases as the detector becomes wider. We see that thicker films lead to higher quantum efficiency up to a point but eventually changes in the

effective index reduce the quantum efficiency. We have also derived a FoM for the SNR of our evanescently coupled detectors and after factoring in the non-uniformity of the field, shown that narrower detectors yield a higher FoM. In addition, we demonstrated evanescent absorption on the waveguide-integrated PbTe detectors in the mid-IR with the $Ge_{28}Sb_{12}Se_{60}$ structures and in the near-IR with the $Ge_{23}Sb_{7}S_{70}$ devices. The next step will be to fabricate and test the $As_2Se_3$ structures as our ideal design. We believe that such an integrated sensor design will enable the creation and deployment of low-cost remote sensor arrays with small footprints.

# Chapter 8: Summary and Future Directions

## 8.1 Chalcogenide glass materials for infrared applications

For our evaluation of chalcogenide glass (ChG) thin films, we have conducted measurements to determine important optical properties such as the complex refractive index and the absorption peaks caused by vibrations of impurity bonds. Compositional analyses were also carried out to measure the concentrations of the elemental glass constituents in bulk and thin films as well as major impurities (carbon, oxygen, hydrogen). We learned that the composition of evaporated films of $Ge_{23}Sb_7S_{70}$ varies with thickness, with thicker films showing higher deviation from bulk stoichiometry. This may be important for device applications requiring very thick films as optical properties of ChG materials depend on the composition and structure. Our results also show that impurity levels in our glasses are currently not high enough to be the main source of loss and these impurities can be reduced by gettering and purification during synthesis of the bulk glass materials. Sidewall roughness in fabricated devices tends to dominate the propagation losses and two mitigating solutions have been offered.

Photosensitivity of chalcogenide glasses was exploited to trim the resonant peaks of silicon resonators post-fabrication. When exposed to above band gap visible light, $As_2S_3$ undergoes a change in refractive index, which shifts the resonant peaks proportionately. This can be used to tune the performance of optical devices to be in line with requirements thus increasing fabrication yields.

The robustness of ChG films in response to radiation is an important materials issue if our sensors are to be used in space or in hostile areas such as near nuclear reactors. The existing body of literature deals with bulk ChG materials and uses relatively high radiation doses before any measurable changes occur. Measured UV/Vis spectra for alpha-irradiated thin films of $Ge_{23}Sb_7S_{70}$ and $As_2Se_3$ show the latter to be more sensitive to radiation damage, with radiation-induced changes slowly decaying over time.

## 8.2 Infrared microphotonic device fabrication

Procedures for fabricating waveguides and resonators using ChG materials have been established for both near- and mid-IR applications using negative photoresist lift-off photolithography. We have also demonstrated a process flow to make monolithically integrated PbTe detectors on ChG waveguides for integrated sensing in the mid-IR that builds on our waveguide fabrication process.

## 8.3 Resonators as a platform for chemical sensing and more

The near-IR resonators developed during this thesis work have been deployed for a number of applications. We studied the contribution of material losses to the total loss in photonic devices and found that they are small in comparison to scattering losses arising from sidewall roughness. The use of polymer nanofoams on resonator sensors enables a high degree of selectivity to target analytes. We tested the response of near-IR microdisk resonators coated with these polymers by exposing them to analytes and observed different peak shifts corresponding to different analytes, showing methacrylate nanofoams with added polystyrene to be selective. Further work can focus on narrowing down ideal nanofoam compositions for specific analytes.

We have also exploited the sensitivity of microresonators to refractive index changes to tune the response of ChG-coated SOI devices post-fabrication over a large wavelength

range to ease fabrication tolerances and enable reconfigurable photonic circuits. Additionally, we exposed silicon-based and ChG resonators to alpha and gamma radiation to study their effects on the materials as well as device performance. We observed measurable changes induced by radiation in both material systems caused by refractive index modifications that altered light propagation behavior through the devices. Our work has demonstrated the value of resonators as a platform not just for sensing applications but also for the metrology of the materials used to fabricate them.

## 8.4 Pushing into the mid-IR

We have successfully moved the near-IR device design and fabrication expertise to the mid-IR (wavelengths of 3.2-3.8 µm and 5.2 µm). New solutions have been developed to enable characterization of mid-IR devices with wide input and offset waveguides. We demonstrated the first successful chalcogenide glass waveguides in the 3-4 µm wavelength range with losses as low as 2.5 dB/cm at 3.6 µm. Successful light coupling to mid-IR resonators has also been realized with high-$Q$ resonant peaks at 5.2 µm through collaborative work.

## 8.5 PbTe for low-cost monolithic detector integration

Electromagnetic simulations of our waveguide-integrated detector structure have demonstrated the feasibility of an evanescently coupled approach. We have identified several suitable spacer layer materials (depending on the wavelength of operation) and fabricated our first structures for testing. Our measurements show that low-temperature PECVD oxide introduces high degree of loss at longer wavelengths, potentially due to its defects and impurities. We tested a PbTe-first design with $Ge_{28}Sb_{12}Se_{60}$ waveguides that demonstrated evidence of absorption in the PbTe layer. The $Ge_{23}Sb_{7}S_{70}$ devices with oxide were tested at telecom wavelengths and we found that absorption was incomplete but the insertion loss did increase significantly for devices after the PbTe deposition.

## 8.6 Future directions

### 8.6.1 Resonator arrays with gradient nanofoams for sensing

Our collaborators in Prof. Luzinov's group at Clemson University have shown that it is possible to deposit nanofoams that a composition gradient in both lateral directions. If we place an array of resonators under this "gradient nanofoam" layer, we can probe the deformation of the nanofoam in a specific region with precision. Such an array can also be used for parallel detection of multiple analytes, as different compositions will be sensitive to different analytes.

### 8.6.2 Chalcogenide-on-sapphire as a mid-IR platform

Although thermally grown silicon dioxide proves to be a good choice of substrate material for the mid-IR up until 3.8 µm wavelength, our waveguide materials exhibit transparency that can scale up to 11 µm (longer with telluride glasses). One way to take full advantage of the wide transparency window of ChG materials is to deposit an undercladding of a lower-index ChG as discussed in Chapter 3 to bypass the substrate material entirely. The other option is to explore alternate substrate materials that are transparent at longer wavelengths. In addition to transparency at longer wavelengths, we also require that the substrate material have a lower refractive index than our glass materials to ensure good mode confinement within small waveguides structures. III-V materials such as GaAs are transparent at longer wavelengths but their relatively high refractive indices make them unsuitable for ChG-based waveguides (other III-V materials and Si/Ge are still good choices, however). Alkali halides present another option but they are often hygroscopic in nature[216] and substrates tend to be expensive and fragile. This brings us to sapphire, which is transparent until ~5 µm[58] and despite being more expensive than silicon, is available as wafer-sized substrates. We have conducted investigations into using sapphire as a substrate

for longer wavelength operation, particularly in the 4–5 µm wavelength band. A modified version of our NR9 lithography process was developed to fabricate $Ge_{23}Sb_7S_{70}$ waveguides and resonators on sapphire substrates for operation at 4.4 µm.

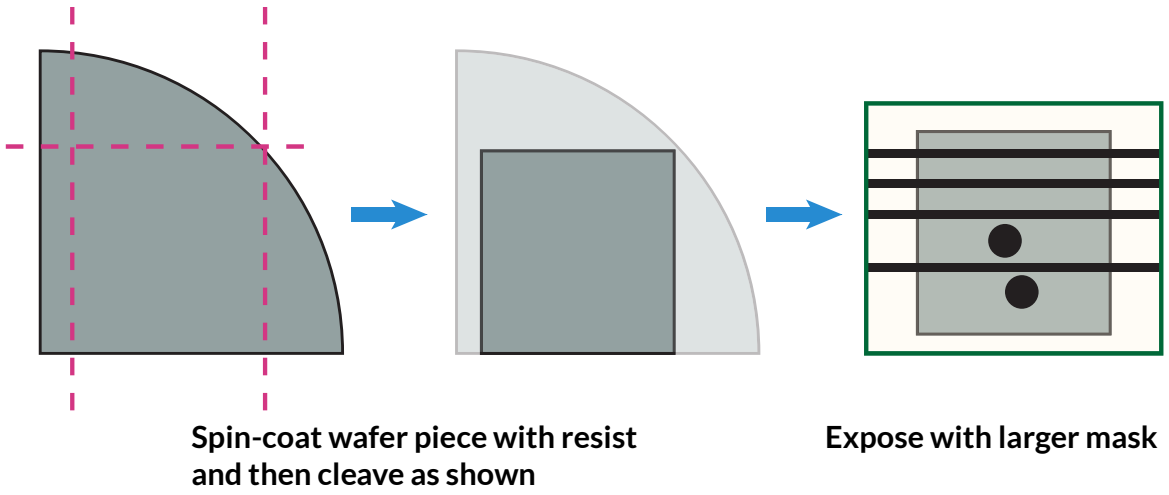


**Figure 8.1:** Schematic illustration showing how we can get around issues with sapphire cleaving by spin-coating the wafer before cleaving and then using a photomask that is wider than the sample so that the waveguide facets are exposed without having to re-cleave after deposition.

Switching to sapphire substrates is not without its challenges. Sapphire substrates are far more expensive and harder to cleave than silicon, often producing rough facets after cleaving. Effective cleaving requires scribing the back surface of the wafer multiple times with a diamond scriber and it is possible for the cleaved facet to deviate from the scribed line. When devices have been fabricated on the front of the wafer, it can be difficult to scribe the back without damaging them. We could cleave the wafer before any lithography but small samples tend to suffer non-uniform resist coatings as excess resist piles up near the edges (thus also affecting proper contact with photomask). Our solution is to first spin-coat a larger wafer piece and then cleave it right before UV exposure to the required size. By ensuring that the mask is wider than the sample, we can obtain good waveguide facets without having to cleave the sample again as illustrated in Figure 8.1. However, this process

is still more challenging than lithography on silicon wafers and needs further refinement before it can reproducibly yield high quality ChG-on-sapphire devices.

### 8.6.3 Chalcogenide glass devices with undercut oxide

Given the challenges associated with fabrication on sapphire, we can also attempt to extend the operation of ChG-on-oxide devices to wavelengths beyond 4 µm by reducing mode confinement in the oxide layer such that the loss due to absorption in the oxide is minimized. Similar to our silicon devices with undercut oxide in Chapter 6, we have performed preliminary work on ChG devices with undercut oxide. Hydrofluoric acid (HF) does not attack ChG materials but is a fast etchant for silicon dioxide. Buffered oxide etch or BOE is typically preferred to straight HF but it contains ammonium hydroxide, which attacks ChGs.

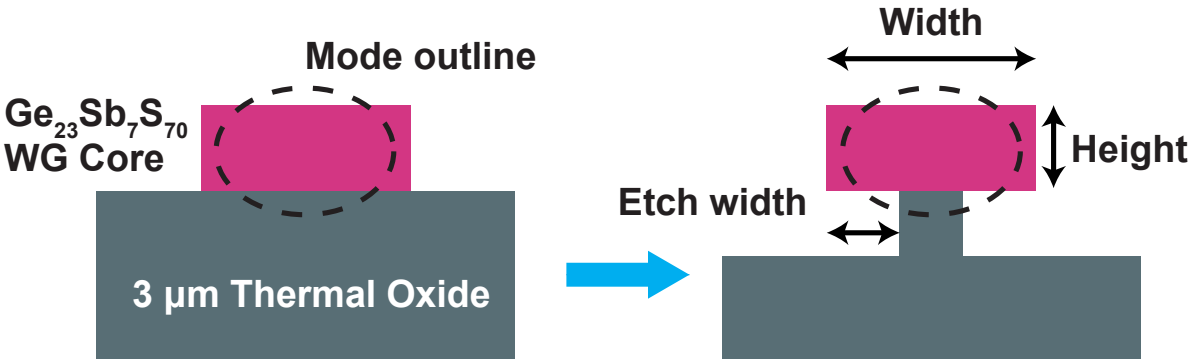


**Figure 8.2:** Schematic illustration showing the effect of undercutting the oxide layer.

We first simulated the effect of undercutting the oxide to estimate the reduction in optical loss at 4.4 µm. The schematic structure is shown in Figure 8.2; practically speaking, the etch would be more isotropic but this simplified structure allows us to get an estimate of the theoretical loss reduction. Assuming a loss of 40 dB/cm[32] in the oxide, Table 8.1 summarizes simulation the results. We observe that as the etch width is increased, the loss drops very quickly and at 0.8 µm, is only 0.24 dB/cm. This is due to the reduction in the mode confinement within the oxide layer by a factor of nearly ten. For a single-mode

waveguide at this wavelength, the width is ~2.5 µm so an etch width of 0.8 µm represents a total oxide undercut of 1.6 µm, which is more than 50% and could lead to the waveguides not being supported well enough.

**Table 8.1:** Effect of waveguide undercut width on confinement and propagation loss.

| **Etch width (µm)** | **Loss (dB/cm)** | $\Gamma_{oxide}$ | $\Gamma_{air}$ |
|---|---|---|---|
| 0.0 | 4.82 | 0.125 | 0.094 |
| 0.5 | 1.45 | 0.053 | 0.134 |
| 0.7 | 0.63 | 0.027 | 0.154 |
| 0.8 | 0.24 | 0.016 | 0.164 |

Experimentally, we tried etching the oxide using both liquid phase HF (diluted 10:1 solution in deionized water) and vapor phase HF (sample placed over beaker with pure HF). In most cases, we observed that the waveguides would either lift-off completely or exhibit "waviness" as shown in Figure 8.3a. To improve waveguide adhesion, we exposed samples to HMDS (hexamethyldisilazane) after lithography and cleaved one facet of the sample after fabrication was complete. Exposing such a sample to HF vapor showed positive results, as shown in Figure 8.3b where the devices have survived damage. In Figure 8.4, we see that there is a small amount of undercut but more work is necessary to establish an etching recipe that leaves devices unharmed but also etches a sufficient amount of oxide to cause a measurable loss reduction.

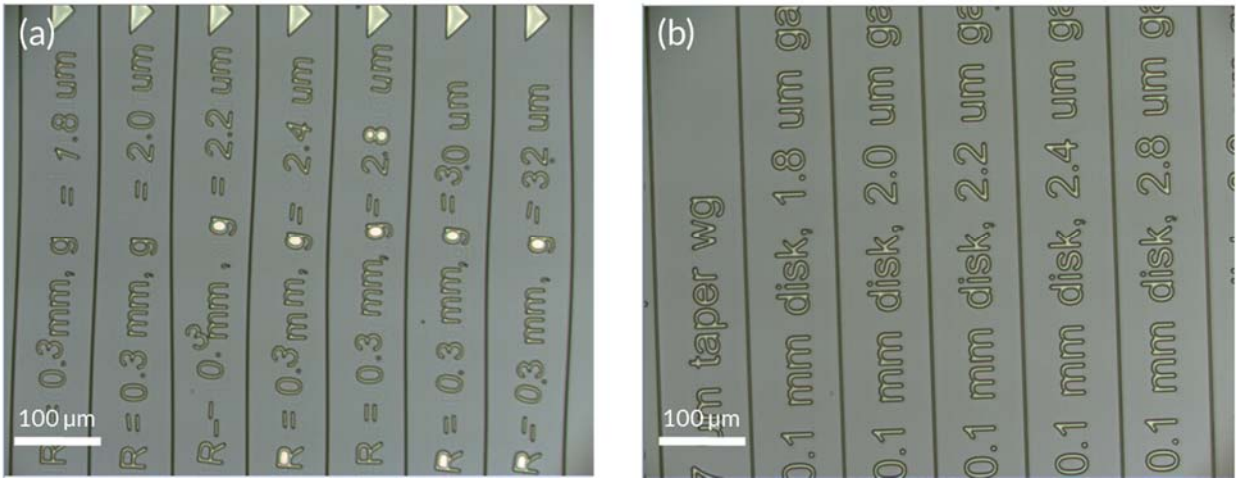


**Figure 8.3:** (a) Waveguides damaged during undercut etching; (b) Unharmed waveguides after one side was cleaved before etching.

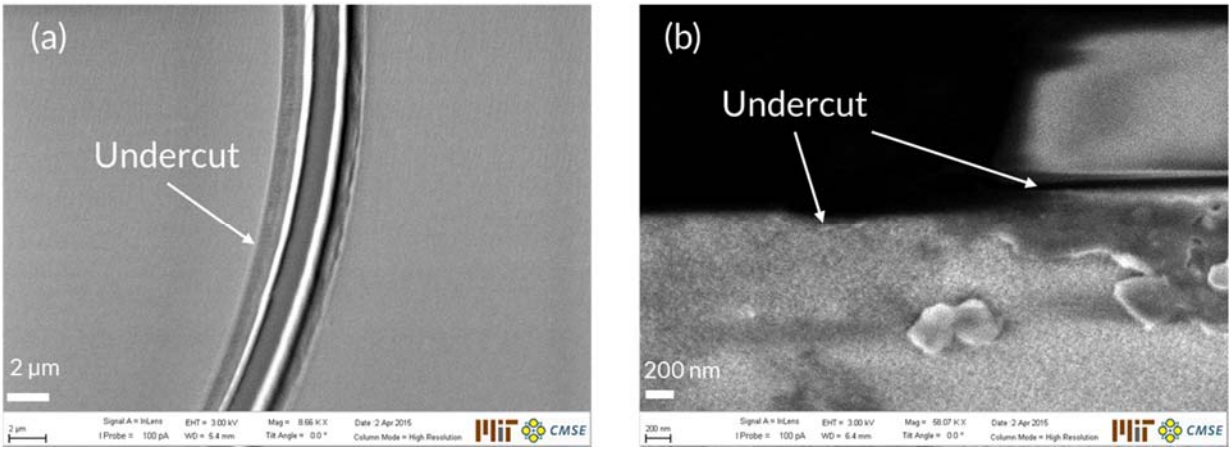


**Figure 8.4:** (a) Plan view SEM image showing possible undercut; (b) Cross-section view SEM image showing small amount of undercut.

### 8.6.4 Development of an integrated light source

On-chip mid-infrared (mid-IR) optical sources have a significant role to play in building a fully integrated lab-on-a-chip system. Instead of expensive, off-chip quantum cascade laser sources, we have explored practical designs of erbium-doped chalcogenide-based mid-IR lasers using a multimode microresonator. The cavity is carefully designed to have a high $Q$-factor at both pump and lasing wavelengths, which are separated by more than two octaves. This is achieved by operating the cavity as a microdisk at the pump wavelength and as a

microring at the lasing wavelength. Detailed numerical analysis shows that the high $Q$-factor of the cavity greatly reduces the lasing threshold to 7.6 µW, with a laser slope efficiency of 10%.

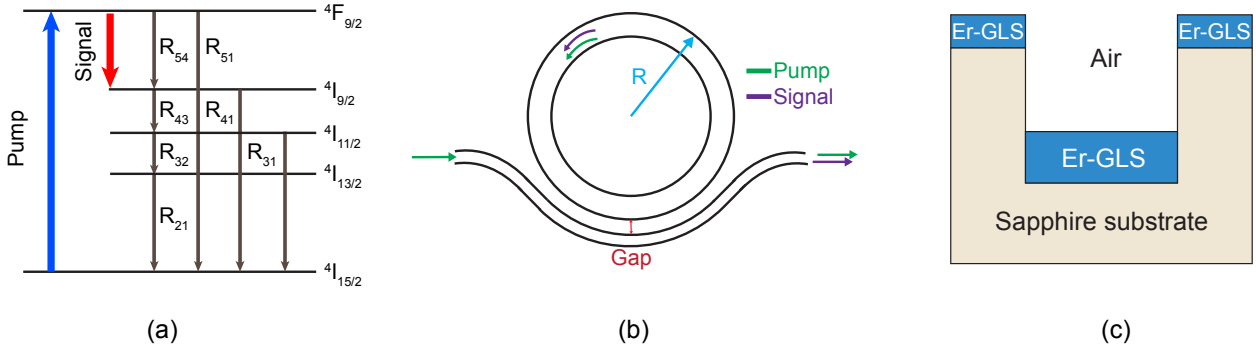


**Figure 8.5:** (a) Erbium (Er) energy levels and inter-level transition parameters with the first energy level at the bottom and the fifth level at the top. (b) Device configuration of a high-Q microresonator-based mid-IR laser, which consists of a multi-mode ring resonator with a curved bus waveguide. (c) Cross section of a chalcogenide waveguide that is in an $Al_2O_3$ trench.

We choose gallium lanthanum sulfide (GLS) as the host material for erbium as it exhibits no toxicity or hygroscopicity in addition to low phonon energy and low non-radiative decay rate. As shown in Figure 8.5, a 660 nm laser is used as pump, and we can get 3.6 µm light emission as output (signal). Due to the relatively low material gain (~4 dB/cm), a high $Q$-factor is needed to build a laser source.

The large difference between the pump and signal wavelength makes it challenging to find a design which provides high $Q$ for both wavelengths. The curved-waveguide structure shown in Figure 8.5b is chosen to increase the coupling at pump wavelength as well as decrease the coupling loss at signal wavelength. Besides, to get high quality, stoichiometry-maintaining thin films, sputtering is used, which makes lift-off of photoresist a challenging process. To solve this problem, a trench in a sapphire wafer is introduced and a waveguide is formed at the bottom of the trench automatically without lift-off of photoresist, as shown

in Figure 8.5c. Thus, the resonator exhibits a high cavity $Q$-factor greater than $10^5$ at both pump and signal wavelengths and the pump threshold can be reduced to below 0.01 mW.

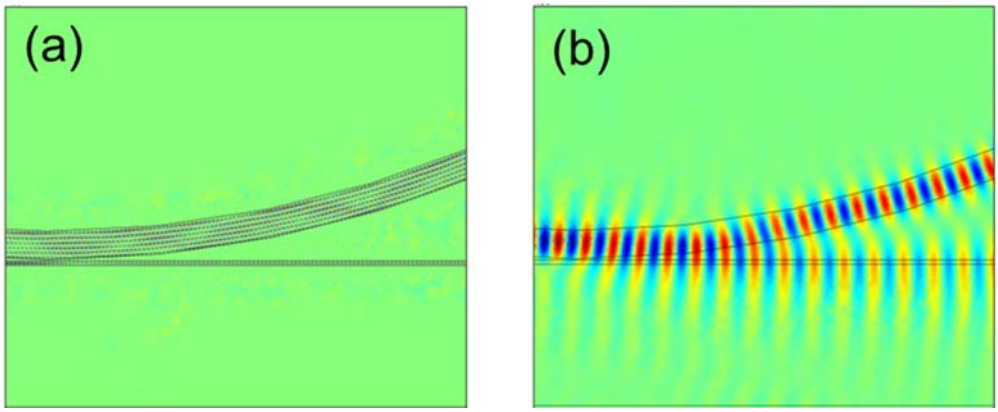


**Figure 8.6:** Mode field distributions inside the cavity for the TE modes at different wavelengths. (a) At 0.66 µm, the 6th-order mode is chosen, which has a well-isolated resonant peak away from other modes. (b) At 3.6 µm, the ring waveguide is single-mode, with mode distribution as shown - the bus waveguide at the right needs to be widened after the ring and bus waveguides are spatially separated further.

We show the mode field distributions inside the cavity in Figure 8.6 for the TE modes at different wavelengths. At 0.66 µm, the 6th-order mode is chosen as shown in Figure 8.6a, which has a well-isolated resonant peak away from other modes. The cavity is more like a disk resonator with higher-order modes excited, and these are preferred for pumping light, because of a better overlap with the fundamental mode at the signal wavelength, which spreads more widely than the fundamental mode at the pump wavelength. The microdisk waveguide is therefore more uniformly pumped by this higher-order mode, which can enable lasing. On the other hand, at 3.6 µm, the microring waveguide is single-mode, with mode distribution shown in Figure 8.6b.

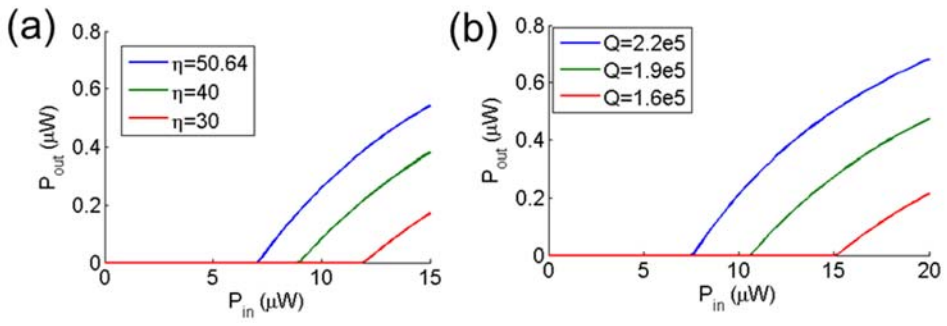


**Figure 8.7:** Lasing performance for *gap* = 100 nm and $L_C$ = 0.6 μm, and accordingly the power enhancement factor $\eta$ = 50.64 at the pump wavelength and cavity $Q = 2.2\times10^5$ at the signal wavelength. The influence of (a) the power enhancement factor and (b) the cavity Q-factor, on the lasing threshold. As the power enhancement factor and the Q-factor increase, the lasing threshold decreases.

By varying the gap and coupling distance $L_C$, we can modify the $Q$ factor of the signal wavelength as well as the power enhancement factor $\eta$ of the pump, which is defined as:

$$\eta = P_{ring}/P_{bus}$$

The optimized design parameter is at *gap* = 100 nm and $L_C$ = 0.6 μm, with $\eta$ = 50.64 and $Q = 2.2\times10^5$. Then, by solving the rate equation at equilibrium condition, we obtain the laser performance curves in Figure 8.7. The optimal threshold power is 7.6 μW, and slope efficiency is 10.26%. As expected, the higher the power enhancement factor, the lower the lasing threshold obtained, when we keep the $Q$ factor the same at 3.6 μm, as shown in Figure 8.7(a). Similarly, with an increased $Q$ factor and $\eta$ fixed at 50.64, less gain is needed to balance the loss, and threshold power drops too. As the 100 nm gap is quite small and could prove challenging to fabricate, we also investigated a gap of 200 nm. The optimized design parameter is now $L_C$ = 8 μm, and the lasing threshold scales with the power enhancement factor to around 60 μW.

### 8.6.5 Chalcogenide glasses for nonlinear photonics

As discussed previously, chalcogenide glasses exhibit high Kerr nonlinearity and hence we can explore device designs for on-chip, nonlinear applications such as light generation using frequency combs. In particular, octave-spanning frequency comb generation offers the opportunity to achieve extremely accurate timing and positioning, explore ultrafast electronic and photonic dynamics of the microscopic world, and provide ultra-broadband information acquisition and processing capability for a wide range of applications[217].

Resonance-enhanced optical nonlinearity in high-$Q$-factor micro-resonators[218] facilitates nonlinear spectral broadening of incoming light waves to generate broadband optical frequency combs (also called Kerr frequency combs)[219-222]. The high-$Q$ micro-resonators enable compact, lightweight, power-efficient and cost-effective (sub) systems for information acquisition and processing with high signal integrity[217]. Various types of micro-cavities based on different material platforms have been demonstrated as a Kerr frequency comb generator[223]. A few theoretical models have been developed to explain how the frequency combs are generated in high-$Q$ resonators[224, 225]. Nevertheless, some critical issues remain unsolved due to the lack of comprehensive understanding of the nonlinear dynamics underlying the on-chip frequency comb generation. Those include, but are not limited to, fundamental limiting factors of nonlinear efficiency and flatness of the generated combs, nonlinear dynamics, and mode competition in the Kerr comb generation, reduction of noise figure, and relationship between intensity and phase noises and their conversion.

Choosing a materials system based on chalcogenide glasses provides a great opportunity to obtain high nonlinearity and desirable integration capability. Optimization of waveguide and resonator structures composed of these materials will allow dispersion tailoring and the investigation of the nonlinear dynamics and physics underlying comb generation for different operating conditions.

### 8.6.6 Electrical PbTe measurements

To achieve a true lab-on-a-chip design for sensing, the integrated detector signal has to be read electrically in a quantitative fashion. This can be achieved by placing metal electrodes on the detector layers to bias the PbTe with constant current and measure the photo-generated voltage. To ease coupling of light to the waveguide, we propose using a Y-junction or a multimode interferometer (MMI) structure to split the input power into two equal halves and only cover one waveguide with a detector layer. This way, alignment to the input waveguide can be performed by observing the mode exiting the waveguide without PbTe and we can be certain that light is also traveling through the waveguide with PbTe for electrical measurements. A beam propagation simulation demonstrating the 50-50 split is shown in Figure 8.8 and a schematic of the planned structure is shown in Figure 8.9.

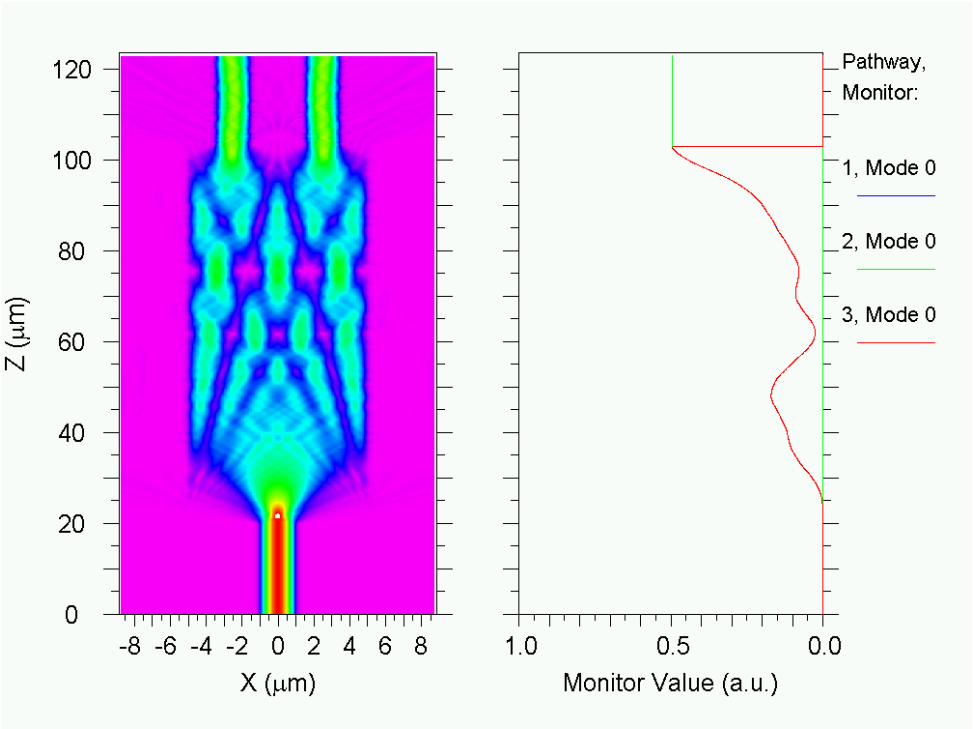


**Figure 8.8:** A beam propagation simulation showing an even 50-50 split of input light between the two arms.

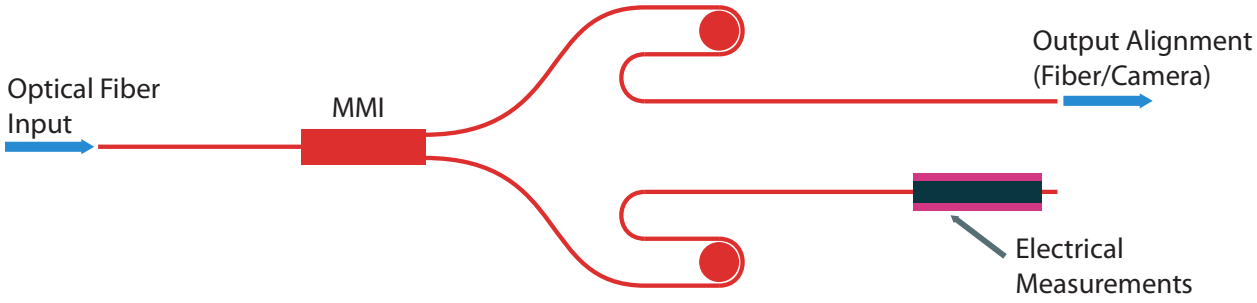


**Figure 8.9:** Schematic of MMI structure with PbTe detector on one arm. The MMI splits the light evenly and enables alignment of the input fiber to the waveguide through the mode image captured by the InSb camera on the arm with no PbTe.

### 8.6.7 Electrical/capacitive sensing measurement

The physical changes induced in a nanofoam layer by analyte exposure can also be electrically probed, as studied in detail in literature[226, 227], via a capacitance change through a set of interdigitated metal electrodes. The sensor area and electrode geometry will determine the maximum capacitive change due to the nanofoam collapse. The two main design considerations are:

(i) The electrode pitch should be of the same order of magnitude as the nanofoam layer thickness. In practice, this will depend on the maximum possible nanofoam thickness as well as the resolution limits of the lithography technique used. Further, the sensor area should not exceed 0.5 $in^2$, both for lithography and nanofoam deposition limitations.

(ii) The overall sensor capacitance should be at least comparable to the input readout channel capacitance (typically smaller than 5 pF), in order to maximize the readout single-to-noise ratio (SNR). The capacitance of the electrodes can be analytically estimated as explained in Igreja et al.[226]

Different topologies with permutations of the remaining undetermined geometric parameters (number of electrodes, electrode width and length) can then be implemented

and comparisons between them can provide information about the best configuration. The thickness of the electrodes is the last parameter to be determined: to get the best sensitivity it is desirable for the electrodes to match the foam thickness (a configuration similar to a parallel plate capacitor).

To improve the sensor readout and reduce thermal drift effects that could affect the measurement, a fully differential structure with a reference sensor can also be designed. The reference structure has the same capacitance and the same thermal fluctuations as the sensor and by applying an inverted signal, its value can be subtracted from the output, yielding a nominal, insensitive-to-temperature zero capacitance value at the output. The readout dynamic range is therefore reduced significantly and sensor capacitance change would be clearly seen as a change from the zero level. Additionally, any parasitic capacitance associated with the substrate should be compensated by the fully differential structure.

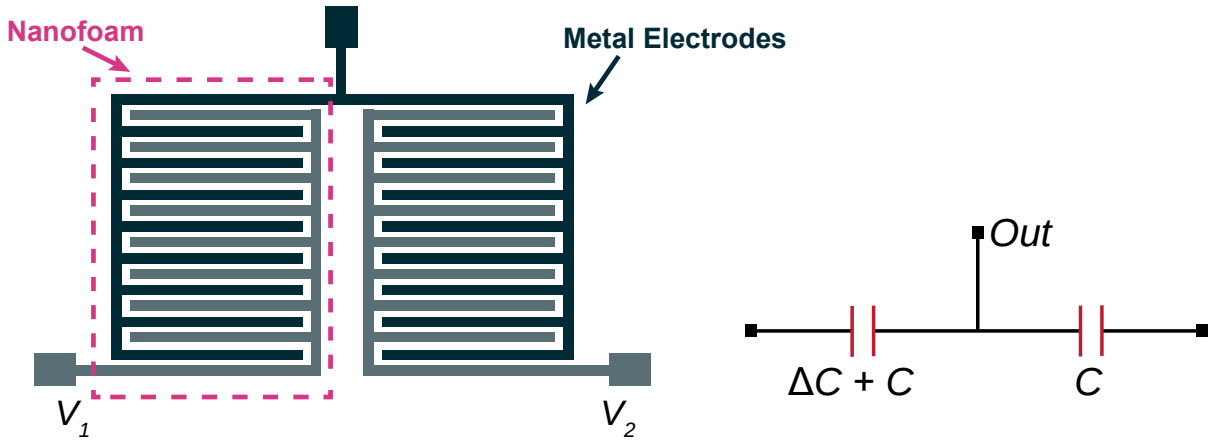


**Figure 8.10:** Interdigitated metal electrodes where one side is covered with a nanofoam that has a different capacitance.

The electrodes on our samples can be contacted through microprobes. However, the measured capacitance is sensitive to the microprobe positioning (due to input to output stray capacitance) and in order to avoid false capacitance changes, the contacts will need to be stationary during the solvent exposure. Thus the capacitance measurements (before

and after exposure) would be directly comparable and a real-time capacitance measurement can be performed. Such an electrical sensor could be integrated into our vision for a lab-on-a-chip device for a hybrid sensing platform that can operate in two detection modes simultaneously.

# Appendix A: Impurities in Chalcogenide Glasses

## A.1 Sources of impurities

Despite best practices, ChGs produced for this thesis work using 99.999% (or 5N) quality elemental starting materials still contain non-zero levels of extrinsic impurities. The most frequent impurities encountered are embedded elements (i.e. H, O, N), stable dissolved compounds (i.e. $H_2O$, COS, $CO_2$) and heterogeneous inclusions (i.e. C, $SiO_2$, $Al_2O_3$). Moreover, macroscopic structural defects such as striae and bubbles are produced during the glass melting due to non-uniformities in thermal convection and rocking of the melt. Together, these impurities are at the origin of scattering, refractive index inhomogeneity, and specific absorption bands, which interfere with light propagation through the material and/or thermo-mechanical stability.

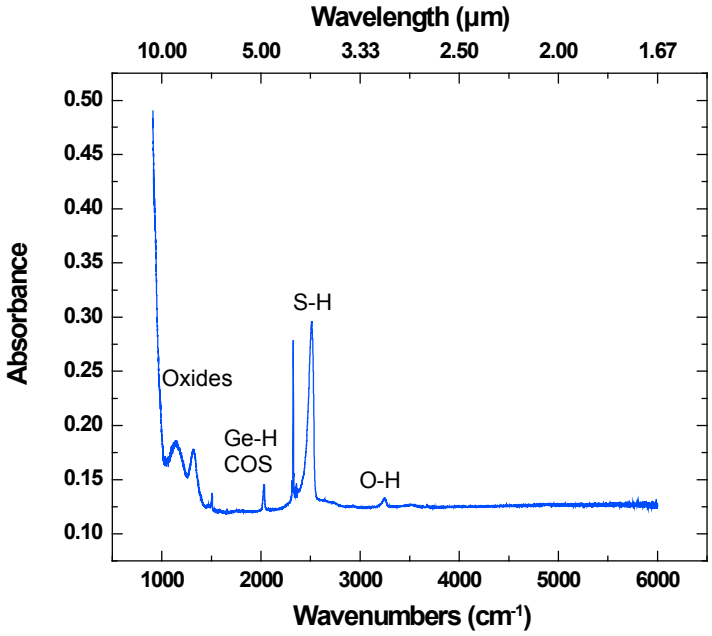


**Figure A.1:** FTIR spectrum from a polished disk of $Ge_{23}Sb_7S_{70}$.

## A.2 Purification techniques

At a basic level, purification can be achieved by baking the elemental components before they are sealed into ampoules. The quartz ampoules used for sealing the components can also be baked at a high temperature (800-900°C) to drive out adsorbed impurities and cleaned with hydrofluoric acid to obtain a "fresh" inner surface that reduces the possibility of inclusions from the ampoule itself. However, these techniques are not sufficient for high purity materials (particularly for fiber applications) and hence more advanced methods have been developed that can also target specific impurities.

### A.2.1 Chemical gettering and distillation

Impurities such as oxygen and hydrogen can be targeted specifically through gettering the distillation processes. For example, oxygen can be gettered by including a small quantity (~0.1 wt%) of magnesium, aluminum, or zirconium. The getter preferentially forms thermodynamically stable oxides with residual oxygen atoms left in the precursor materials, which are subsequently removed from the glass by static distillation. Chlorines such as $AlCl_3$ and $TeCl_4$ are useful for hydrogen removal as they react with hydrogen to form HCl gas, which can be pumped out to purify the material. Aluminum trichloride ($AlCl_3$) can remove both oxygen and hydrogen by forming $Al_2O_3$ (removed from melt by distillation) and HCl.

## A.3 Impurity measurement with SIMS

Impurity content in bulk samples may be estimated using Fourier Transform Infrared (FTIR) spectroscopy; we can compare the absorption strength of a specific peak belonging to a particular bond vibration with the expected vibrational strength for that bond. FTIR measurements of thin films can prove to be challenging due to the limited optical path length and require grazing angle techniques. To obtain accurate values for elemental impurity content, secondary ion mass spectroscopy (SIMS) can be employed. SIMS is a

destructive technique can detect low concentrations of impurities. First, the sample is etched by an ion beam (typically O or Cs) to sputter secondary ions. These ions are then collected and analyzed by a mass spectrometer that can detect concentrations down to parts per million levels. SIMS is also ideal for thin films as the ion beam will gradually etch through the thickness and provide a depth profile. We made use of SIMS measurements to estimate the concentrations of C, H, and O in our ChG films and compared them with bulk samples as described in Chapter 2. Figure A.2 below shows a typical SIMS measurement on a $Ge_{23}Sb_7S_{70}$ film.

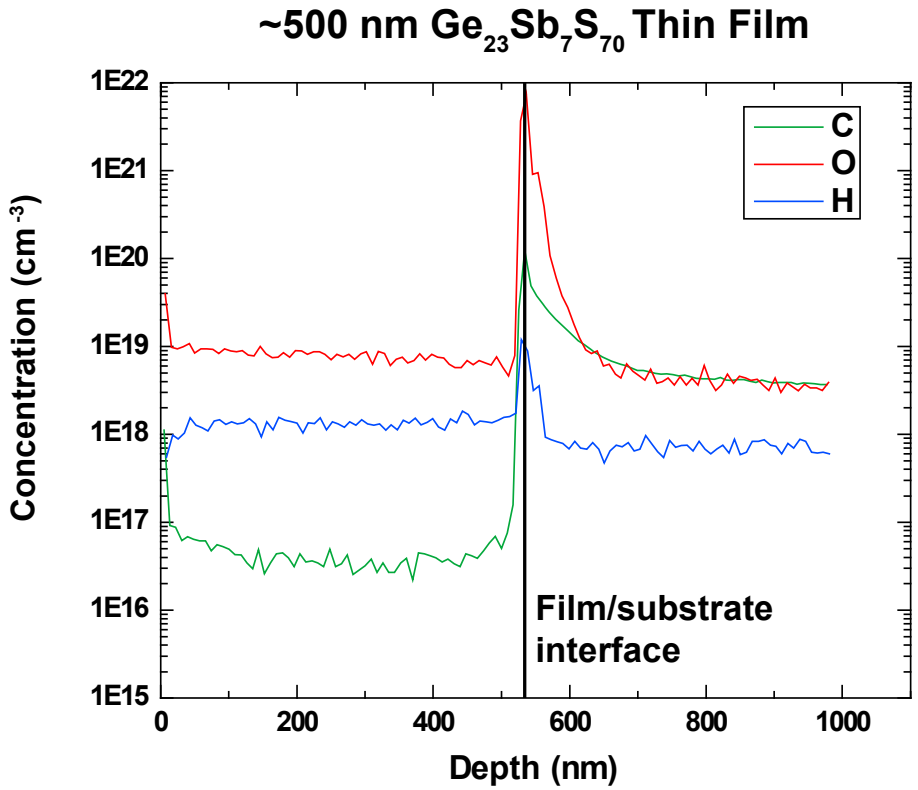


**Figure A.2:** SIMS data from a ~500 nm thin film of $Ge_{23}Sb_7S_{70}$ showing elemental impurity concentrations. The film-substrate interface is delineated by the sharp rise in impurity levels.

# Appendix B: Electromagnetic simulation tools

In this appendix, we briefly describe the simulation tools used in the design of our photonic devices and the theory behind their operation. The two main software tools employed in this thesis work are Photon Design's FIMMWAVE/FIMMPROP and Lumerical Solutions' FDTD Solutions. FIMMWAVE was primarily used to design the cross sectional geometry of our waveguides by solving for supported guided modes at a given wavelength and FIMMPROP was used to get a relatively fast estimate of the electric field profile as the mode propagates through a certain length (predominantly for integrated detector simulations). FDTD Solutions was used to perform more thorough propagation calculations when developing the integrated detector structure and estimate the fraction of the mode being absorbed in the detector layer.

## B.1 Film-mode matching (FMM) in FIMMWAVE

The mode solver in FIMMWAVE performs its calculations using a semi-analytic, fully vectorial method known as film-mode matching or FMM[228, 229]. This method models an arbitrary waveguide geometry by a set of vertical slices with uniform width. Each vertical slice is made up of a number of layers (defined by waveguide geometry) and the solver finds 2D mode solutions from the TE and TM 1D modes of each slice. Although the method is theoretically exact for an infinite number of 1D modes, in practice we limit the number to $< 200$. If the waveguide geometry uses relatively large features, the number of 1D modes can be reduced to about 100 to speed up calculations.

Figure B.1 demonstrates how the FMM solver discretizes a waveguide with arbitrary geometry. The solver collects modes with the same $z$-component of the modal wavevector ($k_z$) and matches the field distributions at the slice interfaces by adjusting the modal amplitudes in each film. Since this value of $k_z$ is also the propagation constant of the mode being solved for, we can only find a set of non-zero film mode amplitudes with matching distributions at the slice interfaces for specific values of $k_z$.

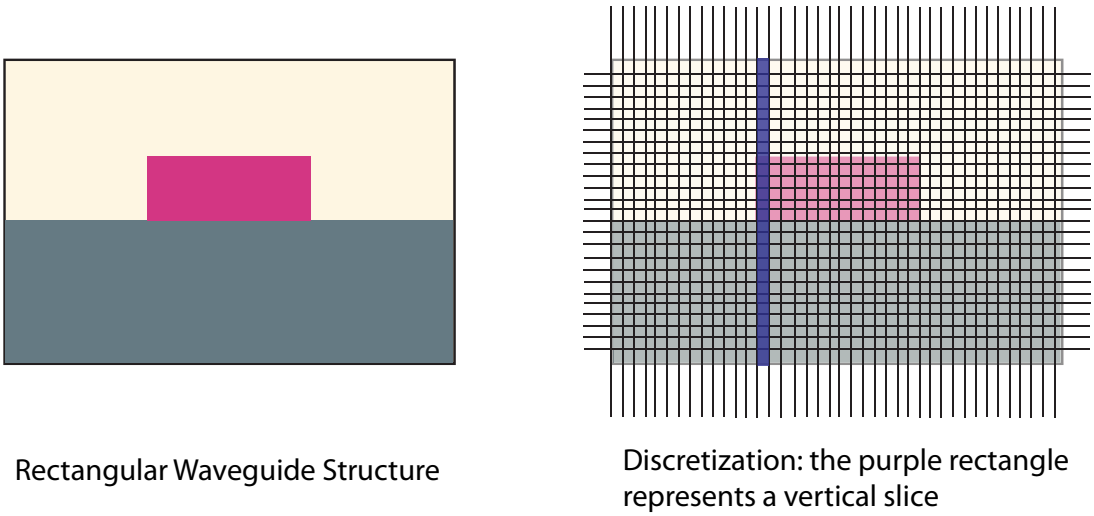


**Figure B.1:** Schematic illustration of FIMMWAVE's discretization. The purple stripe represents a "vertical slice" which is made up of several horizontal pieces.

Artificial boundaries or "walls" placed at the edges of the simulation window discretize the otherwise continuous mode spectrum. In our simulations, we typically use electric walls ($E$-field = 0) at the top and bottom of the structure and magnetic walls ($H$-field = 0) at the left and right. Photon Design's FIMMPROP tool is used to propagate the calculated modes through a certain length and shape to understand how the propagating light will behave. FIMMPROP uses an eigenmode expansion (EME) technique explained elsewhere[230]. When simulating the integrated structures, we used FIMMPROP to perform quick checks before using FDTD for more detailed calculations.

## B.2 3-D FDTD with Lumerical

Finite Difference Time Domain or FDTD in this thesis refers to a numerical method of solving time-dependent Maxwell's equations by discretizing them in space and time (using a central difference approximation) and calculating the electric and magnetic fields at each grid point[231]. It is a fully vectorial method – no approximations are made and electric and magnetic fields can oscillate in all planes. The accuracy of the method and the computation relies on how finely divided the simulation grid is and the volume of the simulation region.

When dealing with dielectric materials, we can reduce Maxwell's equations from four to the following two:

$$-\mu_0 \frac{\partial \boldsymbol{H}}{\partial t} = \nabla \times \boldsymbol{E} \tag{20}$$

$$\epsilon_0 \epsilon_r \frac{\partial \boldsymbol{E}}{\partial t} = \nabla \times \boldsymbol{H} \tag{21}$$

where **E** and **H** are the electric and magnetic fields respectively while $\mu_0$ is the vacuum permeability, $\epsilon_r$ is the dielectric constant, and $\epsilon_0$ is the vacuum permittivity. In a Cartesian coordinate system, the electric and magnetic fields are vectors with $x$, $y$, and $z$ components and we can expand Maxwell's equations into individual component equations:

$$-\mu_0 \frac{\partial H_x}{\partial t} = \frac{\partial E_z}{\partial y} - \frac{\partial E_y}{\partial z} \tag{22}$$

$$-\mu_0 \frac{\partial H_y}{\partial t} = \frac{\partial E_x}{\partial z} - \frac{\partial E_z}{\partial x} \tag{23}$$

$$-\mu_0 \frac{\partial H_z}{\partial t} = \frac{\partial E_y}{\partial x} - \frac{\partial E_x}{\partial y} \tag{24}$$

$$\epsilon_0 \epsilon_r \frac{\partial E_x}{\partial t} = \frac{\partial H_z}{\partial y} - \frac{\partial H_y}{\partial z} \tag{25}$$

$$\epsilon_0 \epsilon_r \frac{\partial E_y}{\partial t} = \frac{\partial H_x}{\partial z} - \frac{\partial H_z}{\partial x} \tag{26}$$

$$\epsilon_0 \epsilon_r \frac{\partial E_z}{\partial t} = \frac{\partial H_y}{\partial x} - \frac{\partial H_x}{\partial y} \tag{27}$$

Next, we set up the simulation grid, which will be used to discretize the structure we are trying to simulate. FDTD simulations start with some initial **E** and **H** field distribution that is injected into the structure. In our simulations, this could be a laser source or a mode inside a waveguide. To discretize, we use a construction known as the Yee Lattice shown in Figure B.2 after Kane Lee, who first proposed the FDTD method. In this cubic lattice, we place electric field values along the edges of the cube and the magnetic field components normal to the faces of the cube. This is arranged such that the **E** and **H** values are staggered in both time and space since we cannot calculate both at the same point.

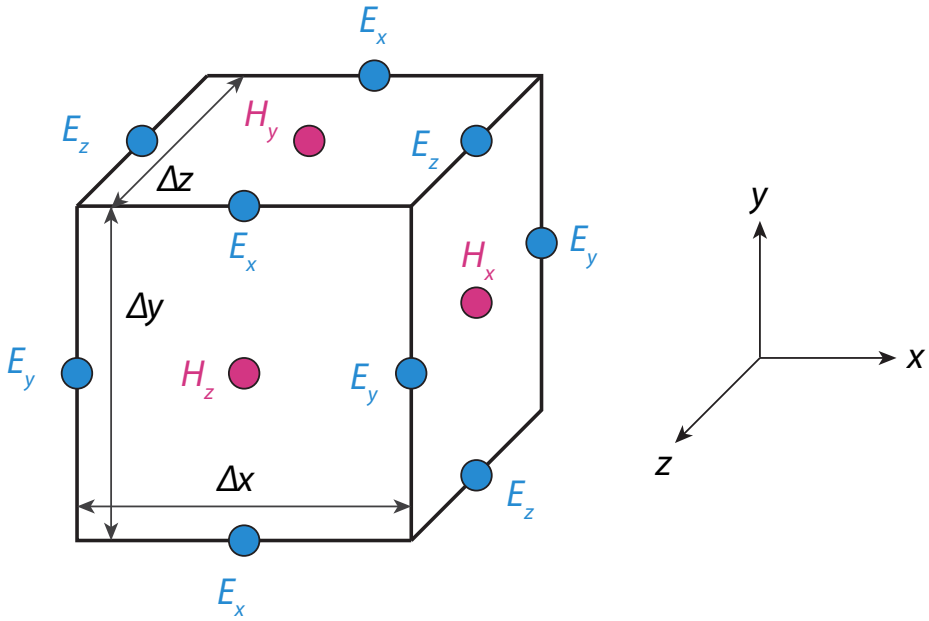


Figure B.2: The Yee Lattice representation.

At time $t = 0$, we start with the initial injected field. We then move forward by half a time step and calculate one of the components, say the E-field, using initial values. Next, we move by another half time step and calculate the H-field using the E-field values calculated in the previous step. Propagating forward by another half time step, we once again calculate the E-field, but now we use the H-field calculated in the prior step. The

calculation proceeds until all points in the simulation grid have been accounted for. We can now discretize the E and B field components:

$$H_x[i,j,k,l = H_x[i\Delta x,(j+0.5)\Delta y,(k+0.5)\Delta z,(l-0.5)\Delta t] \tag{28}$$

$$H_y[i,j,k,l = H_y[(i+0.5)\Delta x,j\Delta y,(k+0.5)\Delta z,(l-0.5)\Delta t] \tag{29}$$

$$H_z[i,j,k,l = H_z[(i+0.5)\Delta x,(j+0.5)\Delta y,k\Delta z,(l-0.5)\Delta t] \tag{30}$$

$$E_x[i,j,k,l = E_x[(i+0.5)\Delta x,j\Delta y,k\Delta z,l\Delta t] \tag{31}$$

$$E_y[i,j,k,l = E_y[i\Delta x,(j+0.5)\Delta y,k\Delta z,l\Delta t] \tag{32}$$

$$E_z[i,j,k,l = E_z[i\Delta x,j\Delta y,(k+0.5)\Delta z,l\Delta t] \tag{33}$$

where $i$, $j$, and $k$ describe the spatial position (running from 1 to the simulation bounds) while $l$ defines the time step. A changing magnetic field induces an electric field and a changing electric field induces a magnetic field. The component Maxwell equations are now of the form:

$$\begin{aligned} -\frac{\epsilon_0\epsilon_r[(i+0.5)\Delta x,q\Delta y,r\Delta z]}{\Delta t}&[E_x(j,i,k,l+1)-E_x(i,j,k,l)] \\ &= \frac{1}{\Delta y}\big(H_z(i,j,k,l)-H_z(i,j-1,k,l)\big) \\ &- \frac{1}{\Delta z}\big(H_y(i,j,k,l)-H_y(i,j,k-1,l)\big) \end{aligned} \tag{34}$$

$$\begin{aligned} &-\frac{\mu_0}{\Delta t}[H_x(i,j,k,l+1)-H_x(i,j,k,l) \\ &= \frac{1}{\Delta y}\big(E_z(i,j+1,k,l)-E_z(i,j,k,l)\big) \\ &+ \frac{1}{\Delta z}\big(E_y(i,j,k+1,l)-E_y(i,j,k,l)\big) \end{aligned} \tag{35}$$

The remaining four components can be written in a similar fashion. Since the wave cannot move faster than the speed of light, the time step, $\Delta t$, must be set accordingly:

$$\Delta t < \frac{1}{c_0 \sqrt{\frac{1}{(\Delta x)^2} + \frac{1}{(\Delta y)^2} + \frac{1}{(\Delta z)^2}}} \tag{36}$$

Lumerical's FDTD Solutions enables such a rigorous calculation for any structure that can be built using its CAD editor with an appropriate choice of input light and simulation mesh. Lumerical uses a conformal mesh to build the simulation grid whereby smaller feature sizes are assigned a finer mesh to ensure good accuracy. The software defines mesh size through a slider that goes from 1 to 8, with 8 being the finest mesh. It is also possible to define a custom mesh over a given region of the structure to override the conformal mesh. For our integrated detector simulations, we assigned a custom mesh over the PbTe region with a step size of 10 nm in the vertical direction (thickness). The data shown in Chapter 7 use a conformal mesh size setting of 6 after we determined that the simulation converged at this value, thus negating the need for finer meshes that would significantly increase simulation time. The absorption efficiency of the PbTe layers was determined by placing a power monitor in the PbTe layer that was programmed to calculate the fraction of the input power absorbed by PbTe. The simulation was initiated by injecting the first-order mode of the waveguide structure and letting it propagate through detector structures of various dimensions.

# Appendix C: Loss separation calculations

In this appendix, we describe the exact calculations used to obtain our loss contribution values in Chapter 5. We started by first measuring the various microdisk resonators and calculated the total propagation loss. If we know the resonator Q-factor, extinction ratio ($k$), free spectral range (FSR, in nm), length ($L$, in µm), and resonant wavelength ($\lambda$, in µm), the loss can be determined as follows[183]:

$$n_g = \frac{\lambda^2}{L \cdot FSR \cdot 10^{-3}} \tag{37}$$

$$A = \frac{\pi n_g L}{Q\lambda} \tag{38}$$

$$T_{min} = 10^{-\frac{k}{10}} \tag{39}$$

$$B = A\sqrt{T_{min}} \tag{40}$$

If the resonant peak is undercoupled:

$$\alpha = \frac{1}{2} \cdot \left(-B + \sqrt{B^2 - 4(A-1)}\right) \tag{41}$$

$$Loss = -\frac{2}{L} \cdot \log(\alpha) \cdot 10^4 \cdot 4.3429 \tag{42}$$

Conversely, if the resonant peak is overcoupled:

$$t = \frac{1}{2} \cdot \left(-B + \sqrt{B^2 - 4(A-1)}\right) \tag{43}$$

$$\alpha = \frac{1-A}{t} \tag{44}$$

$$Loss = -\frac{2}{L} \cdot \log(\alpha) \cdot 10^4 \cdot 4.3429 \tag{45}$$

Both loss values should be equal if the resonator is critically coupled. Once the resonator loss has been determined, we can separate the loss contributions. To estimate what fraction of light resides in the resonator sidewall and the SU8 cladding, we performed FIMMWAVE simulations to calculate confinement factors in each region. Figure C.1 shows the simulation

results. The glass and SU8 together account for roughly 95% of the power the remaining 5% is in the oxide cladding (not shown).

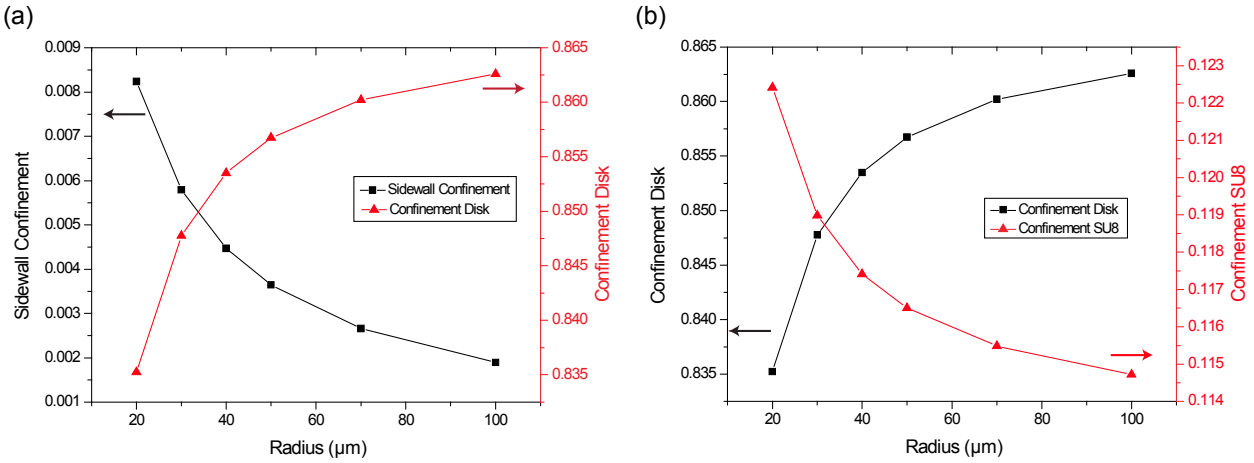


**Figure C.1:** (a) Sidewall and disk confinement values versus disk radius show a decrease in sidewall confinement as radius goes up; (b) Disk and SU8 confinement versus disk radius show disk confinement increasing with radius.

From this simulation data, we can verify that the disk mode is indeed pulled inward with an increase in radius leading to a smaller fraction being confined at the sidewall and reducing sidewall scattering losses. Since we know the total loss as well as the sidewall confinement factors, we can write the total loss as the sum of material attenuation and scattering loss times the confinement factor:

$$\alpha_{total} = \alpha_{material} + (\alpha_{scattering}\Gamma) \tag{46}$$

Now, if we select two of the measured resonators, say the 20 μm disk with a loss of 1.16 dB/cm and the 100 μm disk with a loss of 0.58 dB/cm, we can write the above equation for each one separately:

$$1.16 = \alpha_{material} + (\alpha_{scattering}\Gamma)_{20} \tag{47}$$

$$0.58 = \alpha_{material} + (\alpha_{scattering}\Gamma)_{100} \tag{48}$$

From Figure C.1, we see that the sidewall confinement factor for the 20 µm disk is four times higher than that for the 100 µm disk so we can assume that the scattering loss in the 20 µm resonator will be roughly four times higher. In contrast, the confinement factors in the disk and the SU8 only change by about 3% when going from the 20 µm resonator to the 100 µm one. We assume that the material attenuation is constant within a margin of 3%. This yields a linear system of two equations with two unknowns and we can calculate the material loss as approximately 0.39 dB/cm. With SU8 showing a loss of 2 dB/cm and confining 12% of the mode power, we can estimate the loss from SU8 to be just 0.24 dB/cm leaving 0.15 dB/cm for the total loss in the GeSbS loss. The scattering loss is .19 dB/cm in the 100 µm resonator and .77 dB/cm in the 20 µm resonator. Although the large resonator exhibits a low scattering loss, its size is not conducive for practical devices at telecom wavelengths as it has an extremely small FSR (~1.65 nm) that leads to dozens of peaks that have to be analyzed separately.

# Appendix D: The Importance of a Long Optical Path Length

## D.1 Waveguides versus resonators for sensing applications

We have mentioned during the course of this thesis that absorption spectroscopy relies on optical path length in the test sample; a longer optical path length leads to a high probability of interaction with analytes thus increasing measurement sensitivity. We can also consider the importance of optical path length for on-chip devices used for sensing applications. In particular, we can evaluate the path lengths necessary for a simple waveguide to be able to perform high sensitivity gas sensing and compare it with ways to extend the path length (e.g., serpentine waveguides and resonators).

Gas sensing proves to be a significant challenge due to the small absorption cross-sections of gas species leading to low absorption values. Further, gases in the atmosphere tend to be present in low concentrations so gas sensing requires very high sensitivity. One way to perform optical gas detection is by using high-power lasers aimed at a chamber containing the gas[232]. However, this can be a bulky and oftentimes expensive setup. If we wish to use on-chip devices for gas sensing we have to understand the limits of detection with the various design options available.

If we consider a strip waveguide with no overcladding above it, the evanescent tail of the waveguide mode sticking outside the core can interact with gas molecules for sensing. Hence, one way to enhance the sensitivity is by making waveguides where a large fraction of the guided mode leaks into the surrounding air, thereby increasing interaction with gas molecules. However, the maximum amount of mode sticking out into the air will be

determined by the choice of waveguide materials (i.e., refractive indices) and geometry that can be achieved with microfabrication. Increasing the mode fraction outside the waveguide core requires a smaller core geometry. As the core size is reduced, we eventually get to a point where the effective index is not high enough for the waveguide to support a guided mode at a given wavelength.

The sensitivity of detection also relies on the detector end of the equation. Even if the waveguide design enables high sensitivity, the detector needs to be able to measure the small changes in intensity induced by gas absorption. To this end, we carried out calculations to estimate the expected intensity change from evanescent absorption at different concentrations of methane gas as the mode fraction outside the core and the waveguide length are varied. The mode fraction numbers are independent of the waveguide geometry and the design considerations described above will determine what is feasible.

We choose methane as a representative gas as it exhibits an absorption pea at 3.25 µm. The absorption cross-section of methane is $\sigma = 1.5\times10^{-18}$ cm$^2$/molecule [ref] and can be used to approximate the absorption coefficient at room temperature and atmospheric pressure through the ideal gas law:

$$\frac{N}{V} = \frac{P}{kT} \rightarrow \frac{N}{V} = 2.68 \times 10^{19}\ molecules/cm^3 \tag{49}$$

$$\alpha = \frac{\sigma N}{V} \rightarrow \alpha = 40.2\ cm^{-1} \tag{50}$$

We multiply the concentration (e.g., 1 ppm) of methane by the absorption coefficient to obtain the effective absorption coefficient. The Beer-Lambert Law then yields the percentage change in the intensity.

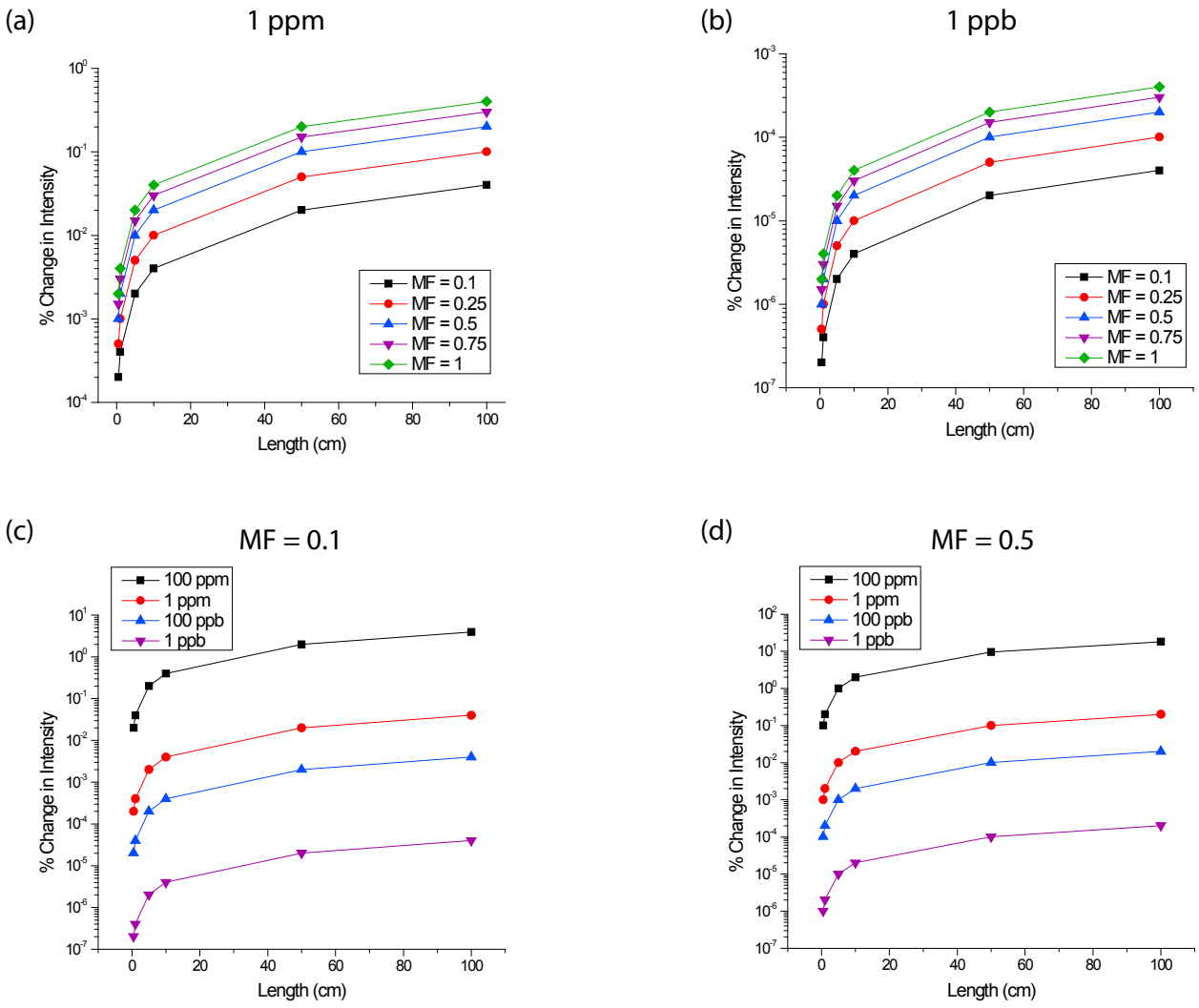


**Figure D.1:** (a) and (b) show the percentage change in intensity versus length due to absorption from 1 ppm and 1 ppb of methane respectively for various mode fraction values; (c) and (d) plot the percentage change in intensity versus length due to absorption from four different concentrations of methane at mode fraction values of 0.1 and 0.5 respectively. We observe that for waveguides shorter than 10 cm, the change in intensity is less than 0.1%. Based on the sensitivity of the detector used and the absolute power exiting the waveguide, this may be too small to detect above the noise level.

In Figure D.1, we plot the expected intensity change as a function of mode fraction and waveguide length. We observe that it requires very long waveguide lengths and high mode fractions to achieve even a 0.1% change in intensity. Since the absolute power leaving the waveguide that can be measured relies on the sensitivity of the detector, we may be left with a scenario where the small changes in intensity are difficult to detect over the noise

level. Typical power levels from our near-IR devices measured on the LUNA system vary between 300-1000 nW based on the loss in the devices being characterized. At a power output of 1000 nW, a 0.1% change in intensity is 1 nW, which is too low to stand out above the noise level of the detector. Of course, if we used a laser with higher output power or a detector with a higher sensitivity, we can increase the power level that corresponds to a 0.1% change. However, this example demonstrates that 0.1% can prove to be too small to measure on some measurement systems. Further, if we need waveguides that are several centimeters long, we run into other design issues. A straight waveguide becomes impractical due to the large, lateral footprint. We can instead use waveguides laid out in serpentine or spiral patterns in their structure that can increase path length in a much smaller footprint but bending loss can be a concern if the bends are too small or if there is a large number of bends.

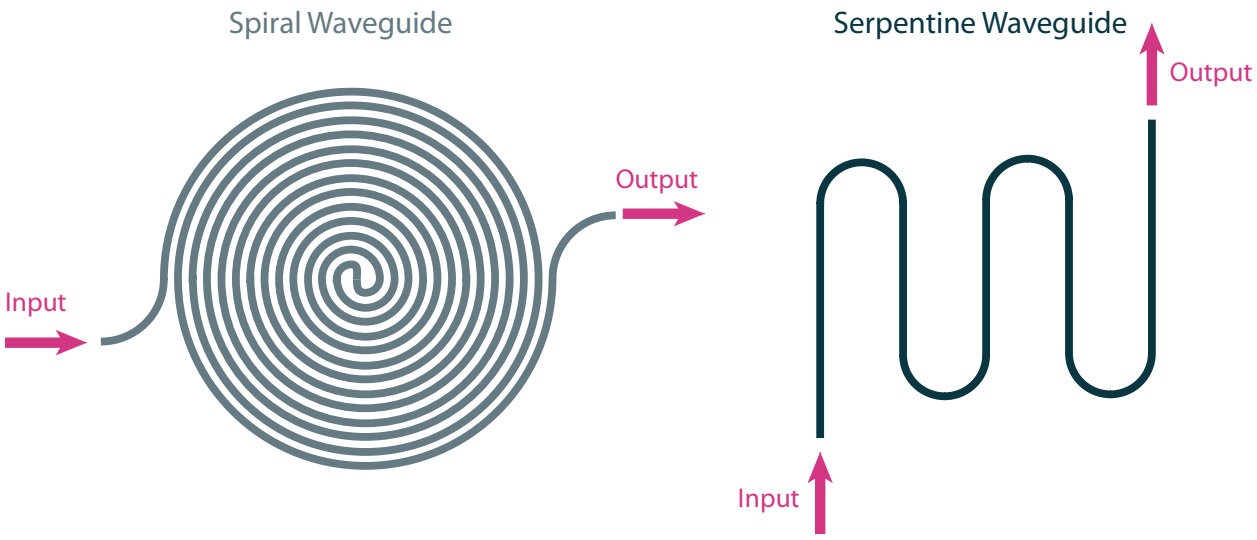


**Figure D.2:** Schematic illustrations of spiral and serpentine waveguides that can increase the path length without a significant increase in device footprint.

This is where resonators can prove to be extremely useful: long effective path lengths are possible using resonators with radii of ~50-100 µm and bus waveguides only need to be

a few mm long leading to small footprints. The resonator loss is inversely proportional to its intrinsic $Q$-factor and the photon lifetime ($\tau_p$) inside the cavity.

$$Q = \frac{2\pi n_g}{\lambda \alpha_r} \tag{51}$$

$$\tau_p = \frac{1}{c\alpha_r} \rightarrow L_{eff} = c\tau_p = \frac{1}{\alpha_r} = \frac{Q\lambda}{2\pi n_g} \tag{52}$$

Here, $n_g$ is the group index, c is the velocity of light, $L_{eff}$ is the effective path length, and $\alpha_r$ is the resonator loss. Hence, we see that the path length inside a resonator is inversely proportional to the loss. With a $Q$-factor of $5\times10^5$, the path length for a ChG resonator at telecom wavelengths is about 5.5 cm. If the $Q$-factor improves by an order of magnitude, the path length will also increase by an order of magnitude. High-$Q$ microtoroidal resonators[218] can achieve $Q$-factors as high as $10^9$ that can significantly increase sensitivity. Addition of an absorptive analyte will increase the resonator loss by the absorption coefficient (scaled by concentration) multiplied by mode confinement in the analyte. This is similar to the case for a simple waveguide.

$$\alpha_{r,new} = \alpha_r + \alpha_{analyte}\Gamma \tag{53}$$

The constraints on the resonator size are simple: it must be large enough to prevent radiative losses (and reduce sidewall scattering) but small enough such that the free spectral range is not too small. Depending on the materials used to build the resonator and desired wavelength of operation, radii in the 10-100 μm will satisfy both criteria. Our telecom work has demonstrated resonators with high $Q$-factors in the 30-100 μm range. However, waveguides still hold one advantage over resonators in that they can transmit over a broadband range of wavelengths and are not limited to wavelengths that meet the resonance condition.

# References


1. B. E. A. Saleh and M. C. Teich, *Fundamentals of Photonics*, Second ed. Hoboken, NJ: John Wiley & Songs, Inc. (2007).
2. P. A. Martin, "Near-infrared diode laser spectroscopy in chemical process and environmental air monitoring," *Chem. Soc. Rev.* **31**, 201-210 (2002).
3. S. Hocdé, O. Loréal, O. Sire, C. Boussard-Plédel, B. Bureau, B. Turlin, J. Keirsse, P. Leroyer, and J. Lucas, "Metabolic imaging of tissues by infrared fiber-optic spectroscopy: an efficient tool for medical diagnosis," *J. Biomed. Opt.* **9**, 404-407 (2004).
4. R. C. Schneider and K. A. Kovar, "Analysis of ecstasy tablets: comparison of reflectance and transmittance near infrared spectroscopy," *Forensic Sci. Int.* **134**, 187-195 (2003).
5. G. Reich, "Near-infrared spectroscopy and imaging: Basic principles and pharmaceutical applications," *Adv. Drug Delivery Rev.* **57**, 1109-1143 (2005).
6. T. McGarvey, A. Conjusteau, and H. Mabuchi, "Finesse and sensitivity gain in cavity-enhanced absorption spectroscopy of biomolecules in solution," *Opt. Express* **14**, 10441-10451 (2006).
7. R. E. Kunz and K. Cottier, "Optimizing integrated optical chips for label-free (bio-)chemical sensing," *Anal. Bioanal. Chem.* **384**, 180-190 (2006).
8. J. Homola, S. S. Yee, and G. Gauglitz, "Surface plasmon resonance sensors: review," *Sensor Actuat. B: Chem* **54**, 3-15 (1999).
9. L. Fadel, F. Lochon, I. Dufour, and O. Français, "Chemical sensing: millimeter size resonant microcantilever performance," *J. Micromech. Microeng.* **14**, S23-S30 (2004).
10. J. Verd, A. Uranga, G. Abadal, J. L. Teva, F. Torres, J. López, F. Pérez-Murano, J. Esteve, and N. Barniol, "Monolithic CMOS MEMS oscillator circuit for sensing in the attogram range," *IEEE Electron Device Lett.* **29**, 146-148 (2008).
11. A. G. Brolo, "Plasmonics for future biosensors," *Nature Photon* **6**, 709-713 (2012).
12. J. Hu, X. Sun, A. Agarwal, and L. Kimerling, "Design guidelines for optical resonator biochemical sensors," *J. Opt. Soc. Am. B: Opt. Phys.* **26**, 1032-1041 (2009).
13. Z. Yu and S. Fan, "Extraordinarily high spectral sensitivity in refractive index sensors using multiple optical modes," *Opt. Express* **19**, 10029-10040May (2011).

14. J. Hu, V. Tarasov, N. Carlie, N.-N. Feng, L. Petit, A. Agarwal, K. Richardson, and L. Kimerling, "Si-CMOS-compatible lift-off fabrication of low-loss planar chalcogenide waveguides," *Opt. Express* **15**, 11798-11807 (2007).
15. G. Farca, S. I. Shopova, and A. T. Rosenberger, "Cavity-enhanced laser absorption spectroscopy using microresonator whispering-gallery modes," *Opt. Express* **15**, 17443-17448 (2007).
16. N. M. Hanumegowda, C. J. Stica, B. C. Patel, I. White, and X. Fan, "Refractometric sensors based on microsphere resonators," *Appl. Phys. Lett.* **87**, 201107 (2005).
17. M. Muneeb, X. Chen, P. Verheyen, G. Lepage, S. Pathak, E. Ryckeboer, A. Malik, B. Kuyken, M. Nedeljkovic, J. Van Campenhout, G. Z. Mashanovich, and G. Roelkens, "Demonstration of Silicon-on-insulator mid-infrared spectrometers operating at 3.8 $\mu$ m," *Opt. Express* **21**, 11659-11669 (2013).
18. C. Reimer, M. Nedeljkovic, D. J. M. Stothard, M. O. S. Esnault, C. Reardon, L. O'Faolain, M. Dunn, G. Z. Mashanovich, and T. F. Krauss, "Mid-infrared photonic crystal waveguides in silicon," *Opt. Express* **20**, 29361-29368 (2012).
19. R. Shankar, R. Leijssen, I. Bulu, and M. Lončar, "Mid-infrared photonic crystal cavities in silicon," *Opt. Express* **19**, 5579-5586 (2011).
20. X. Liu, B. Kuyken, G. ROelkens, R. Baets, R. M. Osgood, and W. M. J. Green, "Bridging the mid-infrared-to-telecom gap with silicon nanophotonic spectral translation," *Nature Photon* **6**, 667-671 (2012).
21. Z. Cheng, X. Chen, C. Y. Wong, K. Xu, and H. K. Tsang, "Mid-infrared Suspended Membrane Waveguie and Ring Resontor on Silicon-on-Insulator," *IEEE Photon. J.* **4**, 1510-1519 (2012).
22. Z. Cheng, X. Chen, C. Y. Wong, K. Xu, C. K. Y. Fung, Y. M. Chen, and H. K. Tsang, "Focusing subwavelength grating coupler for mid-infrared suspended membrane waveguide," *Opt. Express* **37**, 1217-1219 (2012).
23. A. Spott, Y. Liu, T. Baehr-Jones, R. Ilic, and M. Hochberg, "Silicon waveguides and ring resonators at 5.5 μm," *Appl. Phys. Lett.* **97**, 213501 (2010).
24. T. Baehr-Jones, A. Spott, R. Ilic, A. Spott, B. Penkov, W. Asher, and M. Hochberg, "Silicon-on-sapphire integrated waveguides for the mid-infrared," *Opt. Express* **18**, 12127-12135 (2010).
25. R. Shankar, I. Bulu, and M. Lončar, "Integrated high-quality factor silicon-on-sapphire ring resonators for the mid-infrared," *Appl. Phys. Lett.* **102**, 051108 (2013).
26. C. Charlton, M. Giovannini, J. Faist, and B. Mizaikoff, "Fabrication and Characterization of Molecular Beam Epitaxy Grown Thin-Film GaAs Waveguides

for Mid-Infrared Evanescent Field Chemical Sensing," *Anal. Chem.* **78**, 4224-4227 (2006).

27. X. Wang, S.-S. Kim, R. Roßbach, M. Jetter, P. Michler, and B. Mizaikoff, "Ultra-sensitive mid-infrared evanescent field sensors combining thin-film strip waveguides with quantum cascade lasers," *Analyst* **137**, 2322-2327 (2012).
28. G. Z. Mashanovich, M. M. Milošević, M. Nedeljkovic, N. Owens, B. Xiong, E. J. Teo, and Y. Hu, "Low loss silicon waveguides for the mid-infrared," *Opt. Express* **19**, 7112-7119 (2011).
29. T. Lewi and A. Katzir, "Silver halide single-mode strip waveguides for the mid-infrared," *Opt. Lett.* **37**, 2733-2735 (2012).
30. C. Tsay, Y. Zha, and C. B. Arnold, "Solution-processed chalcogenide glass for integrated single-mode mid-infrared waveguides," *Opt. Express* **18**, 26744-26753 (2010).
31. Y. Zha, M. Waldmann, and C. B. Arnold, "A review on solution processing of chalcogenide glasses for optical components," *Opt. Mater. Express* **3**, 1259-1272 (2013).
32. R. Kitamura, L. Pilon, and M. Jonas, "Optical constants of silica glass from extreme ultraviolet to far infrared at near room temperature," *Applied Optics* **46**, 8118-8133 (2007).
33. T. Baehr-Jones, T. Pinguet, P. Lo Guo-Qiang, S. Danziger, D. Prather, and M. Hochberg, "Myths and rumours of silicon photonics," *Nature Photon* **6**, 206-208 (2012).
34. G. Roelkens, U. Dave, A. Gassenq, N. Hattasan, C. Hu, B. Kuyken, F. Leo, A. Malik, M. Muneeb, E. Ryckeboer, S. Uvin, Z. Hens, R. Baets, Y. Shimura, F. Gencarelli, B. Vincent, R. Loo, J. Van Campenhout, L. Cerutti, J. Rodriguez, E. Tournié, X. Chen, M. Nedeljkovic, G. Mashanovich, L. Shen, N. Healy, A. Peacock, X. Liu, R. Osgood, and W. Green, "Silicon-based heterogeneous photonic integrated circuits for the mid-infrared," *Opt. Mater. Express* **3**, 1523-1536 (2013).
35. Y. Yao, A. J. Hoffman, and C. F. Gmachl, "Mid-infrared quantum cascade lasers," *Nature Photon* **6**, 432-439 (2012).
36. I. Vurgaftman, W. W. Bewley, C. L. Canedy, C. S. Kim, M. Kim, J. R. Lindle, C. D. Merritt, J. Abell, and J. R. Meyer, "Mid-IR Type-II Interband Cascade Lasers," *IEEE J. Sel. Topics Quantum Electron* **17**, 1435-1444 (2011).
37. S. Khan, J. Chiles, J. Ma, and S. Fathpour, "Silicon-on-nitride waveguides for mid- and near-infrared integrated photonics," *Appl. Phys. Lett.* **102**, 121104-121104 (2013).
38. P. T. Lin, V. Singh, L. Kimerling, and A. M. Agarwal, "Planar silicon nitride mid-infrared devices," *Appl. Phys. Lett.* **102**, 251121-251121 (2013).

39. N. Duan, H. Lin, L. Li, J. Hu, L. Bi, H. Lu, X. Weng, J. Xie, and L. Deng, "$ZrO_2$-$TiO_2$ thin films: a new material system for mid-infrared integrated photonics," *Opt. Mater. Express* **3**, 1537-1545 (2013).
40. N. Carlie, J. D. Musgraves, B. Zdyrko, I. Luzinov, J. Hu, V. Singh, A. Agarwal, L. Kimerling, A. Canciamilla, F. Morichetti, A. Melloni, and K. Richardson, "Integrated chalcogenide waveguide resonators for mid-IR sensing: leveraging material properties to meet fabrication challenges," *Opt. Express* **18**, 26728-26743 (2010).
41. Z. Yang and P. Lucas, "Tellurium-Based Far-Infrared Transmitting Glasses," *J. Am. Ceram. Soc.* **92**, 2920-2923 (2009).
42. S. Shibata, M. Horiguchi, K. Jinguji, S. Mitachi, T. Kanamori, and T. Manabe, "Prediction of Loss Minima in Infrared Optical Fibers," *Electron. Lett* **17**, 775-777 (1981).
43. M. F. Churbanov, "High-Purity Chalcogenide Glasses as Materials for Fiber Optics," *J. Non-Cryst. Solids* **184**, 25-29 (1995).
44. S. R. Ovshinksky, "Reversible electrical switching phenomena in disordered structures," *Phys. Rev. Lett.* **21**, 1450-1453 (1968).
45. J. Feinleib, J. deNeufville, S. C. Moss, and S. R. Ovshinksky, "Rapid reversible light-induced crystallization of amorphous semiconductors," *Appl. Phys. Lett.* **18**, 254-257 (1971).
46. J. Hu, "Planar Chalcogenide Glass Materials and Devices," Ph. D., Materials Science and Engineering, Massachusetts Institute of Technology, Cambridge, MA (2009).
47. J. Hu, N. Carlie, N.-N. Feng, L. Petit, A. Agarwal, K. Richardson, and L. Kimerling, "Planar waveguide-coupled, high-index-contrast, high-Q resonators in chalcogenide glass for sensing," *Opt. Lett.* **33**, 2500-2502 (2008).
48. J. Hu, N.-N. Feng, N. Carlie, L. Petit, A. Agarwal, K. Richardson, and L. Kimerling, "Optical loss reduction in high-index-contrast chalcogenide glass waveguides via thermal reflow," *Opt. Express* **18**, 1469-1478 (2010).
49. A. Rogalski, "Infrared detectors: status and trends," *Prog. Quant. Electron.* **27**, 59-210 (2003).
50. *Lead Selenide Detectors.*Available: http://www.judsontechnologies.com/lead_sel.html
51. D. E. Bode, *Lead salt detectors* vol. 3. New York: Academic Press (1966).
52. J. Wang, J. Hu, X. Sun, A. Agarwal, D. Lim, R. Synowicki, and L. Kimerling, "Structural, electrical and optical properties of thermally evaporated nanocrystalline PbTe films," *J. Appl. Phys.* **104**, 053707 (2008).

53. J. Wang, T. Zens, W., J. Hu, P. Becla, L. Kimerling, and A. M. Agarwal, "Monolithically integrated, resonant-cavity-enhanced dual-band mid-infrared photodetector on silicon," *Appl. Phys. Lett.* **100**, 211106 (2012).
54. M. Böberl, T. Fromherz, J. Roither, G. Pillwein, G. Springholz, and W. Heiss, "Room temperature operation of epitaxial lead-telluride detectors monolithically integrated on midinfrared filters," *Appl. Phys. Lett.* **88**, 041105 (2006).
55. J. Wang, J. Hu, P. Becla, A. M. Agarwal, and L. Kimerling, "Room-temperature oxygen sensitization in highly textured, nanocrystalline PbTe films: A mechanistic study," *J. Appl. Phys.* **110**, 083719 (2011).
56. J. Wang, "Resonant-cavity-enhanced Multispectral Infrared Photodetectors for Monolithic Integration on Silicon," Ph.D., Materials Science and Engineering, Massachusetts Institute of Technology, Cambridge, MA (2010).
57. V. Singh, P. T. Lin, N. Patel, H. Lin, L. Li, Y. Zou, F. Deng, C. Ni, J. Hu, J. Giammarco, A. P. Soliani, B. Zdyrko, I. Luzinov, S. Novak, J. Novak, P. Wachtel, S. Danto, J. D. Musgraves, K. Richardson, L. C. Kimerling, and A. M. Agarwal, "Mid-infrared materials and devices on a Si platform for optical sensing," *Science and Technology of Advanced Materials* **15**, 014603 (2014).
58. E. D. Palik, *Handbook of Optical Constants of Solids* vol. 1. London: Academic Press (1998).
59. B. J. Eggleton, B. Luther-Davies, and K. Richardson, "Chalcogenide photonics," *Nature Photon* **5**, 141-148 (2011).
60. M. A. Popescu, *Non-Crystalline Chalcogenides* vol. 8. Dordrecht, The Netherlands: Kluwer Academic Publishers (2000).
61. J. D. Musgraves, N. Carlie, J. Hu, L. Petit, A. Agarwal, L. Kimerling, and K. Richardson, "Comparison of the optical, thermal and structural properties of Ge–Sb–S thin films deposited using thermal evaporation and pulsed laser deposition techniques," *Acta Mater.* **59**, 5032-5039 (2011).
62. G. Lenz, J. Zimmermann, T. Katsufuji, M. E. Lines, H. Y. Hwang, S. Spälter, R. E. Slusher, S.-W. Cheong, J. S. Sanghera, and I. D. Aggarwal, "Large Kerr effect in bulk Se-based chalcogenide glasses," *Opt. Lett.* **25**, 254-256 (2000).
63. A. Zakery and S. R. Elliott, *Optical Nonlinearities in Chalcogenide Glasses and their Applications* vol. 135. New York: Springer (2007).
64. R. Slusher, G. Lenz, J. Hodelin, J. S. Sanghera, L. Shaw, and I. D. Aggarwal, "Large Raman gain and nonlinear phase shifts in high-purity $As_2Se_3$ chalcogenide fibers," *J. Opt. Soc. Am. B: Opt. Phys.* **21**, 1146-1155 (2004).
65. M. Yamane and Y. Asahara, *Glasses for photonics*. Cambridge: University Press (2000).

66. N. Carlie, L. Petit, and K. Richardson, "Engineering of glasses for advanced optical applications," *J. of Engineered Fibers and Films* **4**, 21-29 (2009).
67. C. Lopez, "Evaluation of the photo-induced structural mechanisms in chalcogenide glass," Ph.D., University of Central Florida, (2004).
68. A. v. Popta, R. DeCorby, C. Haugen, T. Robinson, J. McMullin, D. Tonchev, and S. Kasap, "Photoinduced refractive index change in $As_2Se_3$ by 633 nm illumination," *Opt. Express* **10**, 639-644 (2002).
69. G. Yang, H. Jain, A. Ganjoo, D. Zhao, Y. Xu, H. Zeng, and G. Chen, "A photo-stable chalcogenide glass," *Opt. Express* **16**, 10565-10571 (2008).
70. P. Lucas, "Energy landscape and photoinduced structural changes in chalcogenide glasses," *J. Phys.: Condens. Matter* **18**, 5629-5638 (2006).
71. K. Tanaka, "Photoexpansion in $As_2S_3$ glass," *Physical Review B* **57**, 5163-5167 (1998).
72. K. Shimakawa, N. Yoshida, A. Ganjoo, Y. Kuzukawa, and J. Singh, "A model for the photostructural changes in amorphous chalcogenides," *Philos. Mag. Lett.* **77**, 153-1581998/03/01 (1998).
73. H. Hisakuni and K. Tanaka, "Giant photoexpansion in $As_2S_3$ glass," *Appl. Phys. Lett.* **65**, 2925-2927 (1994).
74. B. Singh, S. Rajagopalan, P. K. Bhat, D. K. Pandya, and K. L. Chopra, "Giant photocontraction effect in amorphous chalogenide thin films," *J. Non-Cryst. Solids* **35–36, Part 2**, 1053-1059 (1980).
75. V. K. Tikhomirov, K. Asatryan, T. V. Galstian, R. Vallee, and A. B. Seddon, "Photoinduced volume changes related to photoinduced anisotropy in chalcogenide glasses," *Philos. Mag. Lett.* **83**, 117-1242003/01/01 (2003).
76. Y. Zhiyong, C. A. Norman, Jr., A. Q. Hong, and L. Pierre, "Simultaneous microscopic measurements of photodarkening and photoexpansion in chalcogenide films," *J. Phys. D: Appl. Phys.* **42**, 135412 (2009).
77. M. Bertolotti, F. Michelotti, V. Chumash, P. Cherbari, M. Popescu, and S. Zamfira, "The kinetics of the laser induced structural changes in As2S3 amorphous films," *J. Non-Cryst. Solids* **192–193**, 657-660 (1995).
78. A. Ganjoo and K. Shimakawa, "Dynamics of Photodarkening in Amorphous Chalcogenides," *J. Optoelectron. Adv. Mater.* **4**, 595-604 (2002).
79. J. Hu, M. Torregiani, F. Morichetti, N. Carlie, A. Agarwal, K. Richardson, L. Kimerling, and A. Melloni, "Resonant cavity-enhanced photosensitivity in $As_2S_3$ chalcogenide glass at 1550 nm telecommunication wavelength," *Opt. Lett.* **35**, 874-876 (2010).

80. N. Hô, M. Phillips, H. Qiao, P. Allen, K. Krishnaswami, B. Riley, T. Myers, and N. Anheier, "Single-mode low-loss chalcogenide glass waveguides for the mid-infrared," *Opt. Lett.* **31**, (2006).
81. A. Saliminia, A. Villeneuve, T. V. Galstian, S. LaRochelle, and K. Richardson, "First and second order Bragg gratings in single mode planar waveguides of chalcogenide glasses," *J. Lightwave Technol.* **17**, 837-842 (1999).
82. M. Lee, C. Grillet, C. Smith, D. Moss, B. J. Eggleton, D. Freeman, B. Luther-Davies, S. Madden, A. Rode, Y. Ruan, and Y. Lee, "Photosensitive post tuning of chalcogenide photonic crystal waveguides," *Opt. Express* **15**, 1277-1285 (2007).
83. A. Canciamilla, F. Morichetti, S. Grillanda, P. Velha, M. Sorel, V. Singh, A. Agarwal, L. Kimerling, and A. Melloni, "Photo-induced trimming of chalcogenide-assisted silicon waveguides," *Opt. Express* **20**, 15807-15817 (2012).
84. J. Hu, N. Carlie, L. Petit, A. Agarwal, K. Richardson, and L. Kimerling, "Cavity-enhanced infrared absorption in planar chalcogenide glass resonators: experiment & analysis," *J. Lightwave Technol.* **27**, 5240-5245 (2009).
85. C. Moynihan, P. Macedo, M. Maklad, R. Mohr, and R. Howard, "Intrinsic and Impurity Infrared Absorption in $As_2Se_3$ Glass," *J. Non-Cryst. Solids* **17**, 369-385 (1975).
86. J. S. Sanghera, V. Q. Nguyen, P. C. Pureza, F. H. Kung, R. Miklos, and I. D. Aggarwal, "Fabrication of Low-Loss IR Transmitting $Ge_{30}As_{10}Se_{30}Te_{30}$ Glass Fibers," *J. Lightwave Technol.* **12**, 737-741 (1994).
87. V. Shiryaev, S. Smetanin, D. Ovchinnikov, M. Churbanov, E. Kryukova, and V. Plotnichenko, "Effects of Oxygen and Carbon Impurities on Optical Transmission of $As_2Se_3$ Glass," *Inorg. Mater.* **41**, 308-314 (2005).
88. V. S. Shiryaev, J. Troles, P. Houizot, L. A. Ketkova, M. F. Churbanov, J.-L. Adam, and A. A. Sibirkin, "Preparation of optical fibers based on Ge-Sb-S glass system," *Opt. Mater.* **32**, 362-367 (2009).
89. S. Danto, B. Giroire, D. Thompson, P. Wachtel, J. D. Musgraves, and K. Richardson, "A comparative study of purification routes for As2Se3 chalcogenide glass," *Int. J. of Applied Glass Science* **4**, 31-41 (2013).
90. V. S. Shiryaev, L. A. Ketkova, M. F. Churbanov, A. M. Potapov, J. Troles, P. Houizot, J. L. Adam, and A. A. Sibirkin, "Heterophase inclusions and dissolved impurities in Ge25Sb10S65 glass," *J. Non-Cryst. Solids* **355**, 2640-2646 (2009).
91. R. K. Sharma, N. Mithal, Jagannath, K. G. Bhushan, D. Srivastava, H. R. Prabhakara, S. C. Gadkari, J. V. Yakhmi, and V. C. Sahni, "Ti–Zr–V Thin Films as Non-Evaporable Getters (NEG) to Produce Extreme High Vacuum," *J. Phys.: Conf. Ser.* **114**, 012050 (2008).

92. A. M. Reitter, A. N. Sreeram, A. K. Varshneya, and D. R. Swiler, "Modified preparation procedure for laboratory melting of multicomponent chalcogenide glasses," *J. Non-Cryst. Solids* **139**, 121-128 (1992).
93. W. A. King, A. G. Clare, and W. C. LaCourse, "Laboratory preparation of highly pure $As_2Se_3$ glass," *J. Non-Cryst. Solids* **181**, 231-237 (1995).
94. S. R. Elliott, *Physics of Amorphous Materials*. New York: Longman Inc. (1984).
95. N. F. Mott and E. A. Davis, *Electronic Processes in Non-Crystalline Materials*. Oxford: Clarendon Press (1971).
96. J. Hu, X. Sun, A. Agarwal, J.-F. Viens, L. Kimerling, L. Petit, N. Carlie, K. Richardson, T. Anderson, J. Choi, and M. Richardson, "Studies on Structural, Electrical and Optical Properties of Cu-doped As-Se-Te Chalcogenide Glasses," *J. Appl. Phys.* **101**, 063520 (2007).
97. E. Mytilineou, "Chalcogenide amorphous semiconductors chemical modification of doping?," *J. Optoelectron. Adv. Mater.* **4**, 705-710 (2002).
98. J.-F. Viens, C. Meneghini, A. Villeneuve, T. V. Galstian, and É. J. Knystautas, "Fabrication and Characterization of Integrated Optical Waveguides in Sulfide Chalcogenide Glasses," *J. Lightwave Technol.* **17**, 1184-1191 (1999).
99. V. Balan, C. Vigreux, and A. Pradel, "Chalcogenide thin films deposited by radio-frequency sputtering," *J. Optoelectron. Adv. Mater.* **6**, 875-882 (2004).
100. K. E. Youden, T. Grevatt, R. W. Eason, H. N. Rutt, R. S. Deol, and G. Wylangowski, "Pulsed laser deposition of Ga-La-S chalcogenide glass thin film optical waveguides," *Appl. Phys. Lett.* **63**, 1601-1603 (1993).
101. C. C. Huang, C. C. Wu, K. Knight, and D. W. Hewak, "Optical properties of CVD grown amorphous Ge-Sb-S thin films," *J. Non-Cryst. Solids* **356**, 281-285 (2010).
102. S. Song, N. Carlie, J. Boudies, L. Petit, K. Richardson, and C. B. Arnold, "Spin-coating of $Ge_{23}Sb_7S_{70}$ chalcogenide glass thin films," *J. Non-Cryst. Solids* **355**, 2272-2278 (2009).
103. A. Zoubir, M. Richardson, C. Rivero, A. Schulte, C. Lopez, K. Richardson, N. Hô, and R. Vallée, "Direct femtosecond laser writing of waveguides in $As_2S_3$ thin films," *Opt. Lett.* **29**, 748-750 (2004).
104. J. Hu, V. Tarasov, N. Carlie, L. Petit, A. Agarwal, K. Richardson, and L. Kimerling, "Exploration of waveguide fabrication from thermally evaporated Ge-Sb-S glass films," *Opt. Mater.* **30**, 1560-1566 (2008).
105. N. Carlie, N. C. J. Anheier, H. A. Qiao, B. Bernacki, M. C. Phillips, L. Petit, J. D. Musgraves, and K. Richardson, "Measurement of the refractive index dispersion of As2Se3 bulk glass and thin films prior to and after laser irradiation and annealing using prism coupling in the near- and mid-infrared spectral range," *Rev. Sci. Instrum.* **82**, 053103 (2011).

106. S. K. Sundaram, J. S. McCloy, B. J. Riley, M. K. Murphy, H. A. Qiao, C. F. Windisch Jr., E. D. Walter, J. V. Crum, R. Golovchak, and O. Shpotyuk, "Gamma Radiation Effects on Physical, Optical, and Structural Properties of Binary As–S Glasses," *J. Am. Ceram. Soc.* **95**, 1048-1055 (2011).
107. O. I. Shpotyuk, "Chapter 6 Radiation-induced effects in chalcogenide vitreous semiconductors," in *Semiconductors and Semimetals*. vol. Volume 78, F. Robert and U. Boris, Eds., ed: Elsevier, 2004, pp. 215-260.
108. O. I. Shpotyuk and A. O. Matkovskii, "Radiation-stimulated processes in vitreous arsenic trisulphide," *J. Non-Cryst. Solids* **176**, 45-50 (1994).
109. M. Shpotyuk, R. Golovchak, A. Kozdras, and O. Shpotyuk, "Radiation-induced physical ageing in network arsenic-sulfide/selenide glasses," *IOP Conference Series: Materials Science and Engineering* **15**, 012056 (2010).
110. O. I. Shpotyuk, N. M. Vakiv, A. P. Koval'skii, E. Skordeva, E. Vateva, D. Arsova, R. Y. Golovchak, and R. V. Lutsiv, "Radiation-induced effects in Ge-As-S chalcogenide glasses," *Glass Phys. Chem* **26**, 260-264May 2000 (2000).
111. O. I. Shpotyuk and A. P. Kovalskiy, "Compositional Trends in Radiation-Optical Properties of Chalcogenide Glasses," *J. Optoelectron. Adv. Mater.* **4**, 751-762 (2002).
112. O. Shpotyuk, A. Kovalskiy, R. Golovchak, A. Zurawska, and H. Jain, "Radiation-induced defects in chalcogenide glasses characterized by combined optical spectroscopy, XPS and PALS methods," *physica status solidi (c)* **4**, 1147-1150 (2007).
113. M. M. Milošević, M. Nedeljkovic, T. M. B. Massaud, E. Jaberansary, H. M. H. Chong, N. G. Emerson, G. T. Reed, and G. Z. Mashanovich, "Silicon waveguides and devices for the mid-infrared," *Appl. Phys. Lett.* **101**, 121105 (2012).
114. A. Malik, M. Muneeb, Y. Shimura, J. Van Campenhout, R. Loo, and G. Roelkens, "Germanium-on-silicon mid-infrared waveguides and Mach-Zehnder interferometers," in *Photonics Conference (IPC), 2013 IEEE*, 2013, pp. 104-105.
115. Y.-C. Chang, V. Paeder, L. Hvozdara, J.-M. Hartmann, and H. P. Herzig, "Low-loss germanium strip waveguides on silicon for the mid-infrared," *Opt. Lett.* **37**, 2883-28852012/07/15 (2012).
116. L. Shen, N. Healy, C. J. Mitchell, J. S. Penades, M. Nedeljkovic, G. Z. Mashanovich, and A. C. Peacock, "Mid-infrared all-optical modulation in low-loss germanium-on-silicon waveguides," *Opt. Lett.* **40**, 268-2712015/01/15 (2015).
117. P. T. Lin, V. Singh, J. Wang, H. Lin, J. Hu, K. Richardson, J. D. Musgraves, I. Luzinov, J. Hensley, L. C. Kimerling, and A. Agarwal, "Si-CMOS compatible materials and devices for mid-IR microphotonics," *Opt. Mater. Express* **3**, 1474-1487 (2013).

118. P. T. Lin, V. Singh, Y. Cai, L. C. Kimerling, and A. Agarwal, "Air-clad silicon pedestal structures for broadband mid-infrared microphotonics," *Opt. Lett.* **38**, 1031-1033 (2013).
119. T. D. Visser, B. Demeulenaere, J. Haes, D. Lenstra, R. Baets, and H. Blok, "Confinement and modal gain in dielectric waveguides," *Lightwave Technology, Journal of* **14**, 885-887 (1996).
120. A. B. Matsko and V. S. Ilchenko, "Optical Resonators With Whispering-Gallery Modes–Part II: Applications," *IEEE J. Sel. Topics Quantum Electron* **12**, 15-32 (2006).
121. A. B. Matsko and V. S. Ilchenko, "Optical Resonators With Whispering-Gallery Modes–Part I: Basics," *IEEE J. Sel. Topics Quantum Electron* **12**, 1-14 (2006).
122. M. Borselli, T. J. Johnson, and O. Painter, "Beyond the Rayleigh scattering limit in high-Q silicon microdisks: theory and experiment," *Opt. Express* **13**, 1515-1530 (2005).
123. H. Lin, Y. Zou, S. Danto, J. D. Musgraves, K. Richardson, P. T. Lin, V. Singh, A. Agarwal, L. Kimerling, and J. Hu, "Mid-infrared $As_2Se_3$ chalcogenide glass-on-silicon waveguides," in *IEEE 9th International Conference on Group IV Photonics (GFP)*, San Diego, CA, 2012, pp. 246-248.
124. V. Singh, J. Hu, J. Wilkinson, J. D. Musgraves, D. R. Scherer, J. M. Hensley, K. R. Parameswaran, B. D. F. Casse, J. Giammarco, I. Luzinov, A. Agarwal, K. Richardson, and L. Kimerling, "Thermally evaporated chalcogenide thin films for mid-infrared applications: materials analysis, device design, fabrication, and testing," presented at the Glass & Optical Materials Division Annual Meeting, St. Louis, MO (2012).
125. J. D. Plummer, M. D. Deal, and P. B. Griffin, *Silicon VLSI Technology: Fundamentals, Practice and Modeling*, First ed. Upper Saddle River, NJ: Prentice Hall (2001).
126. V. Fano, "Lead Telluride and Its Alloys," in *CRC Handbook of Thermoelectrics*, ed: CRC Press, 1995.
127. H. Lin, L. Li, Y. Zou, S. Danto, J. D. Musgraves, K. Richardson, S. Kozacik, M. Murakowski, D. Prather, P. T. Lin, V. Singh, A. Agarwal, L. C. Kimerling, and J. Hu, "Demonstration of high-Q mid-infrared chalcogenide glass-on-silicon resonators," *Opt. Lett.* **38**, 1470-1472 (2013).
128. R. C. Jones, "A New Calculus for the Treatment of Optical Systems," *J. Opt. Soc. Am.* **31**, 488-4931941/07/01 (1941).
129. T. Barwicz and H. Haus, "Three-dimensional analysis of scatteirng losses due to sidewall roughness in microphotonic waveguides," *J. Lightwave Technol.* **23**, 2719-2732 (2005).

130. We have experimentally observed second phase precipitates and optical loss increase in Ge-Sb-S glass waveguides and resonators reflowed at temperatures above 300°C., "Title," unpublished.
131. H. Liu, Y. Lin, and W. Hsu, "Sidewall roughness control in advanced silicon etch process," *Microsyst. Technol.* **10**, 29-34 (2003).
132. M. Borselli, T. J. Johnson, and O. Painter, "Accurate measurement of scattering and absorption loss in microphotonic devices," *Opt. Lett.* **32**, 2954-2956 (2007).
133. D. Sparacin, R. Sun, A. Agarwal, M. Beals, J. Michel, L. Kimerling, T. Conway, A. Pomerene, D. Carothers, M. Grove, D. Gill, M. Rasras, S. Patel, and A. White, "Low-Loss Amorphous Silicon Channel Waveguides for Integrated Photonics," in *Proceedings of the 3rd IEEE International Conference on Group IV Photonics*, Ottawa, 2006, pp. 255-257.
134. M. Webster, R. Pafchek, G. Sukumaran, and T. Koch, "Low-loss quasi-planar ridge waveguides formed on thin silicon-on-insulator," *Appl. Phys. Lett.* **87**, 231108 (2005).
135. B. Yang, L. Yang, R. Hu, Z. Sheng, D. Dai, Q. Liu, and S. He, "Fabrication and Characterization of Small Optical Ridge Waveguides Based on SU-8 Polymer," *J. Lightwave Technol.* **27**, 4091-4096 (2009).
136. K. F. Palmer and D. Williams, "Optical properties of water in the near infrared," *J. Opt. Soc. Am.* **64**, 1107-11101974/08/01 (1974).
137. D. Choi, S. Madden, A. Rode, R. Wang, and B. Luther-Davies, "Plasma etching of $As_2S_3$ films for optical waveguides," *J. Non-Cryst. Solids* **254**, 3179-3183 (2008).
138. Y. Ruan, W. Li, R. Jarvis, N. Madsen, A. Rode, and B. Luther-Davies, "Fabrication and characterization of low loss rib chalcogenide waveguides made by dry etching," *Opt. Express* **12**, 5140-5145 (2004).
139. J. Giammarco, B. Zdyrko, L. Petit, J. D. Musgraves, J. Hu, A. Agarwal, L. Kimerling, K. Richardson, and I. Luzinov, "Towards universal enrichment nanocoating for IR-ATR waveguides," *Chem. Commun.* **47**, 9104-9106 (2011).
140. A. P. Soliani, B. Zdyrko, and I. Luzinov, *Abstracts of Papers of the American Chemical Society* **242**, (2011).
141. J. Giammarco, B. Zdyrko, J. Hu, A. Agarwal, L. Kimerling, N. Carlie, L. Petit, K. Richardson, and I. Luzinov, *Abstracts of Papers of the American Chemical Society* **238**, (2009).
142. J. Giammarco, B. Zdyrko, L. Petit, J. D. Musgraves, J. Hu, A. Agarwal, L. Kimerling, K. Richardson, and I. Luzinov, *Abstracts of Papers of the American Chemical Society*

**242**, (2011).

143. J. Giammarco, B. Zdyrko, J. Hu, A. Agarwal, L. Kimerling, N. Carlie, L. Petit, K. Richardson, and I. Luzinov, "Design and application of multiple polymer layered systems to facilitate waveguide sensor detection," *Abstracts of Papers of the American Chemical Society* **240**, (2010).
144. J. Giammarco, J. Hu, A. Agarwal, L. Kimerling, N. Carlie, L. Petit, K. Richardson, and I. Luzinov, "Enrichment polymer layers for detection of volatile vapors by FT-IR," *Abstracts of Papers of the American Chemical Society* **241**, (2011).
145. B. Zdyrko, J. Hu, A. Agarwal, L. C. Kimerling, N. Carlie, L. Petit, K. Richardson, T. Anderson, M. Richardson, and I. Luzinov, "Polymer coatings as enrichment layers for evanescent wave sensors," *Abstracts of Papers of the American Chemical Society* **237**, (2009).
146. B. Zdyrko, J. Hu, A. Agarwal, L. Kimerling, N. Carlie, L. Petit, K. Richardson, and I. Luzinov, *Abstracts of Papers of the American Chemical Society* **238**, (2008).
147. S. Saeki, S. Tsubotani, H. Kominami, and M. Tsubokawa, "Phase Separation Temperatures in the Ternary System Polystyrene/Poly(methyl styrene)/Cyclopentane," *Polymer Science: Polymer Physics Edition* **24**, 325-335 (1986).
148. J. Janata and A. Bezegh, *Anal. Chem.* **60**, R62-R74 (1988).
149. G. T. Dobbs, B. Balu, C. Young, C. Kranz, D. W. Hess, and B. Mizaikoff, *Anal. Chem.* **79**, 9566 (2007).
150. P. McLoughlin, K. Flavin, P. Kirwan, B. Murphy, and K. Murphy, "Modelling of Fickian diffusion to enhance polymer-modified sensor performance," *Sens. Actuator B-Chem.* **107**, 170-177May (2005).
151. P. Heinrich, R. Wyzgol, B. Schrader, A. Hatzilazaru, and D. W. Lubbers, *Appl. Spectrosc.* **44**, 1641 (1990).
152. R. Gobel, R. Krska, R. Kellner, R. W. Seitz, and S. A. Tomellini, *Appl. Spectrosc.* **48**, (1994).
153. B. Murphy and P. McLoughlin, *Int. J. Environ. Anal. Chem.* **83**, (2003).
154. Y. Luzinova, B. Zdyrko, I. Luzinov, and B. Mizaikoff, "Detecting trace amounts of water in hydrocarbon matrices with infrared fiberoptic evanescent field sensors," *Analyst* **137**, 333-341 (2012).
155. Y. Luzinova, B. Zdyrko, I. Luzinov, and B. Mizaikoff, *Anal. Chem.* **84**, 1274 (2012).
156. M. P. Eastman, R. C. Hughes, G. Yelton, A. J. Ricco, S. V. Patel, and M. W. Jenkins, *J. Electrochem. Soc.* **146**, 3907 (1999).
157. S. V. Patel, *Sensor Actuat. B: Chem* **96**, 541 (2003).

158. W. P. Carey and M. D. DeGrandpre, *Anal. Chem.* **61**, 1674 (1989).
159. B. Yang, W. M. Huang, C. Li, and L. Li, "Effects of moisture on the thermomechanical properties of a polyurethane shape memory polymer," *Polymer* **47**, 1348-1356Feb (2006).
160. C. Liu, H. Qin, and P. T. Mather, "Review of progress in shape-memory polymers," *J. Mater. Chem.* **17**, 1543-1558 (2007).
161. A. Canciamilla, F. Morichetti, S. Grillanda, P. Velha, M. Sorel, V. Singh, A. Agarwal, L. C. Kimerling, and A. Melloni, "Photo-induced trimming of chalcogenide-assisted silicon waveguides," *Opt. Express* **20**, 15807-158172012/07/02 (2012).
162. A. Canciamilla, M. Torregiani, C. Ferrari, F. Morichetti, R. M. D. L. Rue, A. Samarelli, M. Sorel, and A. Melloni, "Silicon coupled-ring resonator structures for slow light applications: potential, impairments and ultimate limits," *Journal of Optics* **12**, 104008 (2010).
163. M. A. Popovic, T. Barwicz, E. P. Ippen, and F. X. Kartner, "Global design rules for silicon microphotonic waveguides: Sensitivity, polarization and resonance tunability," in *Lasers and Electro-Optics, 2006 and 2006 Quantum Electronics and Laser Science Conference. CLEO/QELS 2006. Conference on*, 2006, pp. 1-2.
164. A. Melloni, A. Canciamilla, C. Ferrari, F. Morichetti, L. O'Faolain, T. F. Krauss, R. De La Rue, A. Samarelli, and M. Sorel, "Tunable Delay Lines in Silicon Photonics: Coupled Resonators and Photonic Crystals, a Comparison," *Photonics Journal, IEEE* **2**, 181-194 (2010).
165. S. Ibrahim, N. K. Fontaine, S. S. Djordjevic, B. Guan, T. Su, S. Cheung, R. P. Scott, A. T. Pomerene, L. L. Seaford, C. M. Hill, S. Danziger, Z. Ding, K. Okamoto, and S. J. B. Yoo, "Demonstration of a fast-reconfigurable silicon CMOS optical lattice filter," *Opt. Express* **19**, 13245-132562011/07/04 (2011).
166. J. Schrauwen, D. Van Thourhout, and R. Baets, "Trimming of silicon ring resonator by electron beam induced compaction and strain," *Opt. Express* **16**, 3738-37432008/03/17 (2008).
167. Y. Shen, I. B. Divliansky, D. N. Basov, and S. Mookherjea, "Electric-field-driven nano-oxidation trimming of silicon microrings and interferometers," *Opt. Lett.* **36**, 2668-26702011/07/15 (2011).
168. C. J. Chen, J. Zheng, T. Gu, J. F. McMillan, M. Yu, G.-Q. Lo, D.-L. Kwong, and C. W. Wong, "Selective tuning of high-Q silicon photonic crystal nanocavities via laser-assisted local oxidation," *Opt. Express* **19**, 12480-124892011/06/20 (2011).
169. D. Bachman, Z. Chen, A. M. Prabhu, R. Fedosejevs, Y. Y. Tsui, and V. Van, "Femtosecond laser tuning of silicon microring resonators," *Opt. Lett.* **36**, 4695-46972011/12/01 (2011).

170. S. T. Chu, W. Pan, S. Sato, T. Kaneko, B. E. Little, and Y. Kokubun, "Wavelength trimming of a microring resonator filter by means of a UV sensitive polymer overlay," *Photonics Technology Letters, IEEE* **11**, 688-690 (1999).
171. D. K. Sparacin, C.-y. Hong, L. C. Kimerling, J. Michel, J. P. Lock, and K. K. Gleason, "Trimming of microring resonators by photo-oxidation of a plasma-polymerized organosilane cladding material," *Opt. Lett.* **30**, 2251-22532005/09/01 (2005).
172. J. Komma, C. Schwarz, G. Hofmann, D. Heinert, and R. Nawrodt, "Thermo-optic coefficient of silicon at 1550 nm and cryogenic temperatures," *Appl. Phys. Lett.* **101**, 041905 (2012).
173. M. Gnan, S. Thoms, D. S. Macintyre, R. M. De La Rue, and M. Sorel, "Fabrication of low-loss photonic wires in silicon-on-insulator using hydrogen silsesquioxane electron-beam resist," *Electron. Lett* **44**, 115-116 (2008).
174. 2015-06-20t08:18:09.799+02:00K. Padmaraju and K. Bergman, "Resolving the thermal challenges for silicon microring resonator devices," in *Nanophotonics* vol. 3, ed, (2014), p. 269.
175. J. Sun, E. Timurdogan, A. Yaacobi, E. S. Hosseini, and M. R. Watts, "Large-scale nanophotonic phased array," *Nature* **493**, 195-199 (2013).
176. Y. Kokubun, N. Funato, and M. Takizawa, "Athermal waveguides for temperature-independent lightwave devices," *Photonics Technology Letters, IEEE* **5**, 1297-1300 (1993).
177. Y. Kokubun, S. Yoneda, and S. Matsuura, "Temperature-independent optical filter at 1.55 μm wavelength using a silica-based athermal waveguide," *Electron. Lett* **34**, 367-369 (1998).
178. L. Jong-Moo, K. Duk-Jun, A. Hokyun, P. Sang-Ho, and K. Gyungock, "Temperature Dependence of Silicon Nanophotonic Ring Resonator With a Polymeric Overlayer," *Lightwave Technology, Journal of* **25**, 2236-2243 (2007).
179. V. Raghunathan, W. N. Ye, J. Hu, T. Izuhara, J. Michel, and L. Kimerling, "Athermal operation of Silicon waveguides: spectral, second order and footprint dependencies," *Opt. Express* **18**, 17631-176392010/08/16 (2010).
180. S. Grillanda, V. Raghunathan, V. Singh, F. Morichetti, J. Michel, L. Kimerling, A. Melloni, and A. Agarwal, "Post-fabrication trimming of athermal silicon waveguides," *Opt. Lett.* **38**, 5450-54532013/12/15 (2013).
181. C.-C. Lai, T.-Y. Wei, C.-Y. Chang, W.-S. Wang, and Y.-Y. Wei, "Gamma-ray irradiated polymer optical waveguides," *Appl. Phys. Lett.* **92**, 023303 (2008).
182. H. Haus and W. P. Huang, "Coupled-mode theory," *Proceedings of the IEEE* **79**, 1505-1518 (1991).

183. A. Yariv, "Universal relations for coupling of optical power between microresonators and dielectric waveguides," *Electron. Lett* **36**, 321-322 (2000).
184. V. R. Almeida, R. R. Panepucci, and M. Lipson, "Nanotaper for compact mode conversion," *Opt. Lett.* **28**, 1302-13042003/08/01 (2003).
185. C. Reichardt and T. Welton, "Appendix A. Properties, Purification, and Use of Organic Solvents," in *Solvents and Solvent Effects in Organic Chemistry*, ed: Wiley-VCH Verlag GmbH & Co. KGaA, 2010, pp. 549-586.
186. H. Lin, Z. Yi, and J. Hu, "Double resonance 1-D photonic crystal cavities for single-molecule mid-infrared photothermal spectroscopy: theory and design," *Opt. Lett.* **37**, 1304-1306 (2012).
187. J. Hu, "Ultra-sensitive chemical vapor detection using micro-cavity photothermal spectroscopy," *Opt. Express* **18**, 22174-22186 (2010).
188. P. T. Lin, V. Singh, J. Hu, K. Richardson, J. D. Musgraves, I. Luzinov, J. Hensley, L. C. Kimerling, and A. Agarwal, "Chip-scale Mid-Infrared chemical sensors using air-clad pedestal silicon waveguides," *Lab on a Chip* **13**, 2161-2166 (2013).
189. P. T. Lin, V. Singh, H.-Y. G. Lin, T. Tiwald, L. C. Kimerling, and A. M. Agarwal, "Low-Stress Silicon Nitride Platform for Mid-Infrared Broadband and Monolithically Integrated Microphotonics," *Adv. Opt. Mater.* **1**, 732-739 (2013).
190. D. Ahn, C. Hong, J. Liu, W. Giziewicz, M. Beals, L. Kimerling, and J. Michel, "High performance, waveguide integrated Ge photodetectors," *Opt. Express* **15**, 3916-3921 (2007).
191. A. Rogalski, "III-V Detectors," in *Infrared Detectors, Second Edition*, ed: CRC Press, 2010, pp. 309-365.
192. A. Rogalski, "Infrared Detectors for the Future," *Acta Phys. Pol., A* **116**, 389-406 (2009).
193. V. System S.A.*Infrared Detectors* (June 10). Available: http://www.vigo.com.pl/products/infrared-detectors
194. E. N. Lewis, P. J. Treado, R. C. Reeder, G. M. Story, A. E. Dowrey, C. Marcott, and I. W. Levin, "Fourier Transform Spectroscopic Imaging Using an Infrared Focal-Plane Array Detector," *Anal. Chem.* **67**, 3377-33811995/10/01 (1995).
195. P. J. Treado, I. W. Levin, and E. N. Lewis, "Indium Antimonide (InSb) Focal Plane Array (FPA) Detection for Near-Infrared Imaging Microscopy," *Appl. Spectrosc.* **48**, 607-6151994/05/01 (1994).
196. T. Zens, W. C., "3-12 μm Multi-spectral Infrared Detector Arrays (MIDAS)," Doctor of Philosophy, Materials Science and Engineering, Massachusetts Institute of Technology, Cambridge, MA (2011).
197. A. Rogalski and J. Rutkowski, "Temperature dependence of the RoA product for lead chalcogenide photovoltaic detectors," *Infrared Physics* **21**, 191-199 (1981).

198. R. Dalven, "A review of the semiconductor properties of PbTe, PbSe, PbS and PbO," *Infrared Physics* **9**, 141-184 (1969).
199. H. Holloway and J. N. Walpole, "MBE techniques for IV–VI optoelectronic devices," *Progress in Crystal Growth and Characterization* **2**, 49-94 (1981).
200. P. J. McCann and D. Zhong, "Liquid phase epitaxy growth of Pb1−xSnxSe1−yTey alloys lattice matched with BaF2," *J. Appl. Phys.* **75**, 1145-1150 (1994).
201. I. Melngailis and T. C. Harman, "Chapter 4 Single-Crystal Lead-Tin Chalcogenides," in *Semiconductors and Semimetals*. vol. Volume 5, R. K. Willardson and C. B. Albert, Eds., ed: Elsevier, 1970, pp. 111-174.
202. J. N. Humphrey and R. L. Petritz, "Photoconductivity of Lead Selenide: Theory of the Mechanism of Sensitization," *Phys. Rev.* **105**, 1736-1740 (1957).
203. R. F. Egerton and C. Juhasz, "The effect of oxygen on epitaxial PbTe, PbSe and PbS films," *Thin Solid Films* **4**, 239-253 (1969).
204. K. Seetharama Bhat and V. Damodara Das, "Electrical-conductivity changes in PbTe and PbSe films on exposure to the atmosphere," *Physical Review B* **32**, 6713-6719 (1985).
205. D. E. Bode and H. Levinstein, "Effect of Oxygen on the Electrical Properties of Lead Telluride Films," *Phys. Rev.* **96**, 259-265 (1954).
206. Z. Dashevsky, R. Kreizman, and M. P. Dariel, "Physical properties and inversion of conductivity type in nanocrystalline PbTe films," *J. Appl. Phys.* **98**, 094309 (2005).
207. F. Briones, D. Golmayo, and C. Ortiz, "The role of oxygen in the sensitization of photoconductive PbSe films," *Thin Solid Films* **78**, 385-395 (1981).
208. D. E. Bode, T. H. Johnson, and B. N. McLean, "Lead Selenide Detectors for Intermediate Temperature Operation," *Applied Optics* **4**, 327-3311965/03/01 (1965).
209. A. Muñoz, J. Meléndez, M. C. Torquemada, M. T. Rodrigo, J. Cebrián, A. J. de Castro, J. Meneses, M. Ugarte, F. López, G. Vergara, J. L. Hernández, J. M. Martín, L. Adell, and M. T. Montojo, "PbSe photodetector arrays for IR sensors," *Thin Solid Films* **317**, 425-428 (1998).
210. V. Ambegaokar, B. I. Halperin, and J. S. Langer, "Hopping conductivity in disordered systems," *Phys. Rev. B: Condens. Matter* **4**, 2612-2620 (1971).
211. R. L. Petritz, "Theory of Photoconductivity in Semiconductor Films," *Phys. Rev.* **104**, 1508-1516 (1956).
212. J. C. Slater, "Barrier Theory of the Photoconductivity of Lead Sulfide," *Phys. Rev.* **103**, 1631-1644 (1956).
213. E. L. Dereniak and G. D. Boreman, *Infrared Detectors and Systems*: Wiley Interscience (1996).

214. A. Gassenq, N. Hattasan, L. Cerutti, J. B. Rodriguez, E. Tournié, and G. Roelkens, "Study of evanescently-coupled and grating-coupled GaInAsSb photodiodes integrated on a silicon photonic chip," *Opt. Express* **20**, 11665-11672 (2012).
215. V. Singh, T. Zens, W., J. Hu, J. Wang, J. D. Musgraves, K. Richardson, L. C. Kimerling, and A. Agarwal, "Evanescently coupled mid-infrared photodetector for integrated sensing applications: Theory and design," *Sensor Actuat. B: Chem* **185**, 195-200 (2013).
216. *Selecting IR Transmitting Materials* (June 10) International Crystal Laboratories. Available: http://www.internationalcrystal.net/ti_sec1.htm
217. N. R. Newbury, "Searching for applications with a fine-tooth comb," *Nat Photon* **5**, 186-188 (2011).
218. D. K. Armani, T. J. Kippenberg, S. M. Spillane, and K. J. Vahala, "Ultra-high-Q toroid microcavity on a chip," *Nature* **421**, 925-928 (2003).
219. P. Del/'Haye, A. Schliesser, O. Arcizet, T. Wilken, R. Holzwarth, and T. J. Kippenberg, "Optical frequency comb generation from a monolithic microresonator," *Nature* **450**, 1214-1217 (2007).
220. T. J. Kippenberg, S. M. Spillane, and K. J. Vahala, "Kerr-Nonlinearity Optical Parametric Oscillation in an Ultrahigh-$Q$ Toroid Microcavity," *Phys. Rev. Lett.* **93**, 083904 (2004).
221. A. A. Savchenkov, A. B. Matsko, V. S. Ilchenko, I. Solomatine, D. Seidel, and L. Maleki, "Tunable Optical Frequency Comb with a Crystalline Whispering Gallery Mode Resonator," *Phys. Rev. Lett.* **101**, 093902 (2008).
222. J. S. Levy, A. Gondarenko, M. A. Foster, A. C. Turner-Foster, A. L. Gaeta, and M. Lipson, "CMOS-compatible multiple-wavelength oscillator for on-chip optical interconnects," *Nat Photon* **4**, 37-40 (2010).
223. T. J. Kippenberg, R. Holzwarth, and S. A. Diddams, "Microresonator-Based Optical Frequency Combs," *Science* **332**, 555-559April 29, 2011 (2011).
224. Y. K. Chembo and N. Yu, "Modal expansion approach to optical-frequency-comb generation with monolithic whispering-gallery-mode resonators," *Physical Review A* **82**, 033801 (2010).
225. A. B. Matsko, A. A. Savchenkov, W. Liang, V. S. Ilchenko, D. Seidel, and L. Maleki, "Mode-locked Kerr frequency combs," *Opt. Lett.* **36**, 2845-28472011/08/01 (2011).
226. R. Igreja and C. J. Dias, "Analytical evaluation of the interdigital electrodes capacitance for a multi-layered structure," *Sensors and Actuators A: Physical* **112**, 291-301 (2004).

227. S. Schaur and B. Jakoby, "An efficient method for modeling planar interdigitated electrodes for capacitive sensing," in *Sensors, 2011 IEEE*, 2011, pp. 1970-1973.
228. A. S. Sudbo, "Improved formulation of the film mode matching method for mode field calculations in dielectric waveguides," *Pure and Applied Optics: Journal of the European Optical Society Part A* **3**, 381 (1994).
229. A. S. Sudbo, "Film mode matching: a versatile numerical method for vector mode field calculations in dielectric waveguides," *Pure and Applied Optics: Journal of the European Optical Society Part A* **2**, 211 (1993).
230. D. F. G. Gallagher and T. P. Felici, "Eigenmode expansion methods for simulation of optical propagation in photonics: pros and cons," 2003, pp. 69-82.
231. A. Taflove, *Computational Electrodynamics: The Finite-Difference Time-Domain Method*. Norwood, MA: Artech House, Inc. (1995).
232. C. Gmachl, F. Capasso, R. Kohler, A. Tredicucci, A. L. Hutchinson, D. L. Sivco, J. N. Baillargeon, and A. Y. Cho, "Mid-infrared tunable quantum cascade lasers for gas-sensing applications," *Circuits and Devices Magazine, IEEE* **16**, 10-18 (2000).